UC San Diego

UC San Diego Electronic Theses and Dissertations

Title

High-resolution paleoceanography and modeling of abrupt warming events on greenhouse earth

Permalink

https://escholarship.org/uc/item/05v3p9xs

Author

Turner, Sandra Kirtland

Publication Date

2012

Peer reviewed|Thesis/dissertation

eScholarship.org Powered by the California Digital Library
University of California

UNIVERSITY OF CALIFORNIA, SAN DIEGO

High-Resolution Paleoceanography and Modeling of Abrupt Warming Events on Greenhouse Earth

A dissertation submitted in partial satisfaction of the requirements for the degree Doctor of Philosophy

in

Oceanography

by

Sandra Kirtland Turner

Committee in charge:

Professor Richard D. Norris, Chair
Professor Christopher D. Charles
Professor Ralph F. Keeling
Professor Jeffrey Severinghaus
Professor Mark H. Thiemens

2012

Copyright

Sandra Kirtland Turner, 2012

All rights reserved.

The Dissertation of Sandra Kirtland Turner is approved, and it is acceptable in quality and form for publication on microfilm and electronically:

_____

_____

_____

_____

_____

Chair

University of California, San Diego

2012

To Timothy Allen Ray, an Explorer

and a dear friend.

TABLE OF CONTENTS

SIGNATURE PAGE iii
DEDICATION iv
TABLE OF CONTENTS v
LIST OF FIGURES vii
LIST OF TABLES x
ACKNOWLEDGEMENTS xi
MATERIAL SUBMITTED FOR PUBLICATION xvi
VITAE xvii
ABSTRACT OF THE DISSERTATION xviii
CHAPTER 1: Introduction to the Dissertation 1
1.1 Outline of the Dissertation 7
1.2 References 9
CHAPTER 2: A South Pacific Source of Deep Water during the Paleocene 11
2.1 Introduction 13
2.2 Methods 15
2.2.1 Site Description 15
2.2.2 Seismic Reflection Data 17
2.2.3 Stable Isotope Data 17
2.2.4 Age Model 18
2.3 Results and Discussion 20
2.3.1 Is the Campbell 'Drift' a Paleogene Drift? 20
2.3.2 Global Ocean Stable Isotope Compilation 23
2.3.3 Possible Site of Deep Water Formation 28
2.4 Conclusions 29
2.5 References 31
2.6 Appendix 36
CHAPTER 3: Comparison of Hyperthermal Events from the Late Paleocene to the Early-Middle Eocene: Is there a Common Link? 44
3.1 Introduction 46
3.2 Methods 50
3.3 Results 55
3.4 Discussion 75
3.4.1 Causes of inter-site variability 75
3.4.2 Significance of event shape 82
3.4.3 How many hyperthermals were there? 85
3.4.4 Long-term hyperthermal sequence 94
3.5 Conclusions 99
3.6 References 100
3.7 Appendix 104

CHAPTER 4: A Synthesis of Carbon Isotope Excursions in Greenhouse Climates 140
4.1 Introduction 142
4.2 Datasets 146
4.3 Evaluation of Carbon Isotope Excursions 151
4.3.1 Effects of CIE Duration 153
4.3.2 Controls on CIE size 154
4.3.3 Comparison of CIEs 157
4.3.4 The Toarcian and PETM events 158
4.3.5 Hyperthermal Shape 160
4.4 Comparison of CIEs to background $\delta^{13}C$ variability 168
4.5 Evidence for warming during CIEs 177
4.6 Dissolution and weathering during CIEs 179
4.7 Biotic change during CIEs 182
4.8 Anoxia and changes in productivity and organic matter burial 184
4.9 Importance of shallow epicontinental seas? 187
4.10 Concluding remarks: What is a hyperthermal event? 191
4.11 References 192
CHAPTER 5: Evaluating the Sedimentary Record of a Small Eocene Hyperthermal using an Earth System Model of Intermediate Complexity 212
5.1 Introduction 214
5.2 Methods 215
5.3 Results 229
5.3.1 Excursion in BIOGEM 229
5.3.2 Excursion in SEDGEM 231
5.3.3 Timing of the CIE 237
5.3.4 Diagnosed Carbon Input 239
5.4 Discussion 244
5.4.1 Backing out the CIE magnitude 245
5.4.2 Diagnosing carbon input and removal 250
5.4.3 Factors controlling sedimentary CIE expression 257
5.4.4 Leads and lags in carbonate burial and $\delta^{13}C$ 259
5.5 Conclusions 261
5.6 References 263
CHAPTER 6: Conclusion to the Dissertation 266
6.1 Major conclusions 268
6.2 References 271

LIST OF FIGURES

Figure 2-1. Paleogeographic reconstruction for the mid-Paleocene (60 Ma) showing the location of records used in this study..... 16
Figure 2-2. Multichannel seismic reflection profile of Ewing 9201 showing a cross-section of the Campbell sediment drift.. 21
Figure 2-3. Paleocene composite of multisite benthic foraminiferal (all Nuttalides truempyi) $\delta^{13}C$ and $\delta^{18}O$ records. 24
Figure 3-1. Long-term climatic context of late Paleocene to early-middle Eocene hyperthermal events. 48
Figure 3-2. Records of estimated wt% $CaCO_3$ from ODP Sites 1258, 1267, and 1210 used in inter-site correlations. 52
Figure 3-3. CIE size (‰) plotted against CIE duration (kyr) determined from bulk carbonate stable isotope data for Events A-L, C22rH2, C22nH2, C22nH3, C21rH1, and C21rH5.. 56
Figure 3-4. Bulk carbonate CIE size (‰) plotted against bulk carbonate OIE (oxygen isotope excursion) size (‰)..... 58
Figure 3-5. CIE size (‰) plotted against CIE duration (kyr) determined from benthic foraminiferal stable isotope data for Events H1, H2, C22rH1, C22rH2, C22rH3, C22nH1, C22nH2, C22nH3, C22nH4, C21rH1, C21rH2, C21rH3, C21rH4, C21rH5, and C21rH6.. 59
Figure 3-6. Benthic foraminiferal CIE size (‰) plotted against benthic foraminiferal OIE (oxygen isotope excursion) size (‰)..... 60
Figure 3-7. High-resolution records of events C22rH2, C22nH2, C22nH3, C21rH1, and C21rH5 from ODP Site 1258, 1267, and 1210. 61
Figure 3-8. Comparison of benthic versus bulk carbonate records of carbon and oyxgen isotopes and event duration for multiple hyperthermals.. 66
Figure 3-9. High-resolution records of bulk carbonate carbon isotopes at ODP Sites 1258, 1267, and 1210 plotted against estimated wt% $CaCO_3$ for events C22rH2, C22nH2, C22nH3, C21rH1, and C21rH5. 69
Figure 3-10. High-resolution records of bulk carbonate carbon isotopes at ODP Sites 1263, 1265, 1267, and 1262 plotted against estimated wt% $CaCO_3$ for events H1 (Elmo) and H2..... 72
Figure 3-11. Benthic foraminiferal carbon isotope excursion magnitude plotted against normalized wt% $CaCO_3$ decrease. 74
Figure 3-12. Comparison of individual site characteristics with the size and duration of carbon isotope excursions from all available bulk and benthic records 77
Figure 3-13. Comparison of the shapes of the C22r-C21r hyperthermal events from a single site (ODP Site 1258). 83

Figure 3-14. Detrended long-term carbon isotope records for the early Eocene from DSDP 550, DSDP 577, ODP 1051A, ODP 1051B, ODP 690, ODP 1262, and for the early-middle Eocene from ODP Site 1258. 86
Figure 3-15. Threshold model of orbitally-paced methane hydrate release and abrupt warming events during the early-middle Eocene. 95
Figure 3-A1. Long-term carbon isotope records for the early Eocene from DSDP 550, DSDP 577, ODP 1051A, ODP 1051B, ODP 690, ODP 1262, and for the early-middle Eocene from ODP Site 1258 105
Figure 4-1. Ranges in CIE size ($\delta^{13}C$ ‰) plotted against absolute age for each event listed in Table 1.. 152
Figure 4-2. Ranges in CIE duration (in kyr) plotted against absolute age for each event listed in Table 1. 154
Figure 4-3. Individual CIE records from bulk carbonate for each event of the 44 listed in Table 1 that can be identified at multiple sites.. 161
Figure 4-4. 2.5 Myr intervals of $\delta^{13}C$ from sites with temporal resolution of ~15 kyr or greater..... 172
Figure 5-1. Seafloor carbonate distribution used as the initial condition in cGENIE experiments. 218
Figure 5-2. Spatially prescribed detrital flux forcing (in mol cm^{-2} yr^{-1}) used to generate initial conditions in cGENIE experiments. 219
Figure 5-3. Model schematic of the GENIE SEDGEM model.. 220
Figure 5-4. Site location and data used to force model atmospheric CO_2 $\delta^{13}C$. 224
Figure 5-5. Locations of model sites plotted against model depth.. 225
Figure 5-6. Illustration of the iterative process of backing out the 'true' atmospheric CO_2 $\delta^{13}C$ excursion. 228
Figure 5-7. Spatial record of the CIE in surface dissolved inorganic carbon $\delta^{13}C$.. 230
Figure 5-8. Global distribution of the size of the carbon isotope excursion in core-top sediment $CaCO_3$.. 232
Figure 5-9. Comparison of core-top CIE and sediment core CIE from a single model site..... 233
Figure 5-10. Comparison of model-derived sediment core benthic foraminiferal $\delta^{13}C$ record with actual benthic foraminiferal $\delta^{13}C$ data. 235
Figure 5-11. CIE size versus normalized change in wt% $CaCO_3$ for three model sites. 236
Figure 5-12. Comparison of CIE timing in various model tracers..... 238
Figure 5-13. Records of model sediment core benthic foraminiferal $\delta^{13}C$ plotted against model sediment core wt% $CaCO_3$. 240
Figure 5-14. Diagnosed carbon addition/removal when forcing atmospheric CO_2 $\delta^{13}C$ to match the 1.60‰ excursion.. 242
Figure 5-15. Results of flux forcing experiment, where a pulse of organic carbon (-25‰) is applied to the atmosphere at a constant rate..... 243

Figure 5-16. Comparison of the global ocean DIC concentration during the inversion experiment and during the flux forcing experiment..... 255

LIST OF TABLES

Table 2-A1. Benthic foraminiferal carbon and oxygen stable isotope data from ODP Sites 1121 and 1124. 36
Table 2-A2. Tie points used to construct age models for Paleocene stable isotope compilation. 40
Table 3-1. Summary of site charactersitics for all the sites used to obtain stable isotope data for hyperthermals. 54
Table 3-2. Comparison of CIE sizes to 2σ values calculated from de-trended long-term carbon isotope records 91
Table 3-A1. High-resolution bulk carbonate carbon and oyxgen isotope data for Events C22rH2, C22nH2, C22nH3, C21rH1, and C21rH5 from ODP Sites 1258, 1267, and 1210. 110
Table 4-1. List of all 'hyperthermal' events evaluated with absolute ages provided from the literature. 148

ACKNOWLEDGEMENTS

My time in graduate school has been enriching mostly because of the professional and personal relationships I have formed over the years. I have many people to thank for helping me to embark on my scientific career and complete my dissertation.

First, I must thank Richard Norris, for being an encouraging, inspirational, and fun advisor. I arrived at Scripps with a slightly unconventional plan for interdisciplinary study, and Dick has supported me every step of the way. Whenever I've felt stuck on a given idea, a talk with Dick is always enough to make me newly motivated. We've come up with some great ideas that I'm sure will continue in many fruitful research projects over the coming years. On top of supporting me in research, Dick has also taken me on a handful of the 'greatest adventures of our lives'—from sliding down a giant, booming sand dune in Nevada to terrifying car rides on winding mountain roads in New Zealand. Dick is a constant reminder that behind all the deadlines, grant writing, and paper submissions, science is really about a passion to understand the natural world. It is a lesson that I will never forget.

Second, I'd like to thank my 'pseudo-advisors,' Phil Sexton and Andy Ridgwell. I met Phil during my first year at Scripps, when he was a post-doc in the Norris lab. The inspiration for my dissertation came from work that Phil had recently completed on hyperthermals in the early-middle Eocene, and since the

moment when we designed the outline for my qualifying exam, Phil has been a constant mentor and friend. He's helped me with so many aspects of research, from identifying foraminifera to editing manuscripts. Our Skype chats, which often go on for hours, always represent a time when I clarify the details behind my ideas. I look forward to working with him much more in the future.

I met Andy Ridgwell while attending his workshop on the GENIE model at Pennsylvania State University. I'd already been excited by all his excellent publications, but after the workshop, I was hooked on GENIE. I never could have expected Andy to be so helpful in teaching me how to use the model for my research. He's hosted me three times at the University of Bristol and responded to countless email queries in amazing time. Andy is one of the brightest researchers I've ever met, and I can honestly say that I've never been more excited about science than while visiting and working in Bristol. The modeling I've learned through him has profoundly affected the direction in which I hope to take my career, and I am extremely grateful for all his time and effort. Finally, I'd like to thank him for my introduction to English cider!

I'm lucky to have a committee of extremely impressive scientists, whom I greatly admire. In particular, I'd like to thank Chris Charles for his extensive help in teaching me how to run the mass spec and patiently helping me with error messages and confusing data. I'd like to thank Jeff Severinghaus and Ralph Keeling for their Biogeochemistry course, which was a very motivational class for me in my first year at Scripps, when I was new to the field and searching for my

passion. I'd like to thank Mark Thiemens for taking the time to be a thoughtful committee member and highlighting issues that I often haven't considered.

If it weren't for two professors of mine back at Georgetown University, I never would have ended up at Scripps. First, I have to thank Hiroshi Nakai for introducing me to scientific research as his research assistant in the Department of Biochemistry and Molecular Biology. Though my area of research has changed greatly from those days, the research habits I learned then will always stay with me. Second, I have to thank Timothy Beach, who helped me articulate my career goals in interdisciplinary science and policy and suggested that I apply to Scripps in the first place.

There are so many people in the broader SIO community to whom I am indebted. I would like to thank all the current and former members of the Norris lab for being teachers, colleagues, and friends—Pincelli Hull was virtually another advisor for me and helped make the many hours I spent at the microscope much more entertaining. I thank Jill Leonard-Pingel for our many conversations about science career (and life) planning. I thank Lauren Freeman for her help with Matlab, and I thank Elizabeth Siebert for helping me through the stress of finishing a Ph.D. and for taking over the role of youngest scientist in the lab.

I would like to thank all my professors at Scripps for providing me with a solid foundation from which to pursue my own research interests. I would like to thank the Scripps Environmental Science and Policy group for providing an opportunity to consider the broader implications of my scientific research, and for

helping me keep in touch with my roots in science policy. On the same note, I'd like to thank the San Diego chapters of Citizens Climate Lobby, especially founder Marshall Saunders and Executive Director Mark Reynolds, for inspiring me to continue to engage with policymakers and the public.

I must thank the National Science Foundation for funding the majority of my graduate career through a Graduate Research Fellowship. I'd like to thank Cheryl Peach, Hubert Staudigel and the GK-12 program for support this past year as well. I'd like to thank the Philanthropic Educational Organization for a generous scholarship award that allowed me to travel to the U.K. for research.

I'd like to thank the SIO Graduate Department and the GRD administrative office for their support with all the logistical details of graduate school and research, and for financial support for conferences and other work travel.

I'd like to thank all my friends at Scripps for making it my home over the past years. I was lucky to have an incredible group of students start school with me in 2006—from group projects and study sessions to TGs and pool nights at Rock Bottom, they made graduate school a wonderful experience. In particular, I'd like to thank Jared Kluesner, Peter Barry, Jonathon Bent, Adam Radich, and Bill Sinko—who've been there for me through it all. I'd especially like to thank Jared, who not only helped me with Chapter 2 of my thesis, but also helped me through countless computer frustrations over the years.

Finally, I'd like to thank my friends and family. I'd like to thank Waffiyah Mian (even though she convinced most people I studied Shamu) and Nilou

Khonsari for being my constant cheerleaders. I'd like to thank my sister for being my original partner for beach explorations and marine life rescue. I'd like to thank my parents for always believing in me and being the best role models I have. It would take pages to do justice to their unconditional love and support. Saving the best for last, I have to thank my husband, Kyle, for keeping me sane and making it all worthwhile.

MATERIAL SUBMITTED FOR PUBLICATION

The data chapters (2-5) of this dissertation are in preparation and/or have been submitted previously for publication.

Chapter 2, in full, has been submitted for publication, and is currently under revision. The material may appear in Geology, 2012, Kirtland Turner, S., Norris, R.D., and Kluesner, J. A South Pacific Source of Deep Water during the Paleocene. I am the primary investigator and author of this paper.

Chapter 3, in part, is currently being prepared for submission for publication. I am the primary investigator and author of this paper in collaboration with co-authors Philip Sexton and Richard Norris.

Chapter 4, in part, is currently being prepared for submission for publication. I am the primary investigator and author of this paper in collaboration with co-author Richard Norris.

Chapter 5, in part, is currently being prepared for submission for publication. I am the primary investigator and author of this paper in collaboration with Andy Ridgwell.

VITAE

2006	Bachelor of Science in Foreign Service, Georgetown University School of Foreign Service
2006-2007	Regents Fellow, University of California, San Diego
2008-2011	National Science Foundation Graduate Student Fellow
2010	Master of Science in Oceanography, Scripps Institution of Oceanography, University of California, San Diego
2012	Doctor of Philosophy in Oceanography, Scripps Institution of Oceanography, University of California, San Diego

ABSTRACT OF THE DISSERTATION

High-Resolution Paleoceanography and Modeling of Abrupt Warming Events on Greenhouse Earth

by

Sandra Kirtland Turner

Doctor of Philosophy in Oceanography

University of California, San Diego, 2012

Professor Richard D. Norris, chair

In this dissertation I investigate the paleoceanography and paleoclimatology of greenhouse climates, with a focus on the preservation of abrupt warming events, or hyperthermals, in the sedimentary record. My research focuses on the integrative use of high-resolution datasets combined with data-model integration.

I begin by investigating patterns of global overturning circulation in the warm Paleocene epoch, a time when previous studies have suggested weak

deep-ocean aging gradients and sluggish circulation. Using a new benthic foraminiferal stable isotope dataset from the high-latitude South Pacific, I demonstrate that deep waters formed in the Southern Pacific (probably around the Ross Sea) at least intermittently during the Paleocene. I also suggest a number of distinct reorganizations of overturning during this epoch.

I continue by assessing the potential connections between a series of postulated hyperthermal events in the early-middle Eocene with the sequence of hyperthermals in the late Paleocene to early Eocene that bracket the Paleocene-Eocene Thermal Maximum (~56 Ma). Through a detailed comparison of the structure of all the suggested events in this interval, I demonstrate the similarity of most events, with the PETM and the subsequent Elmo event ~2 Myr later appearing as outliers. I also use a new method for identifying whether events appear significantly different from background variability. Finally, I adapt a threshold model to suggest that a common mechanism is plausible for all events.

I extend my analysis of the multiple hyperthermal events of the Paleocene-Eocene to synthesize records of all possible hyperthermal events from ~250 to ~40 Ma. I primarily compare records of bulk carbonate carbon isotopes, but also assess other environmental consequences of each event. This study represents the first such synthesis of postulated hyperthermals.

Finally, I use the GENIE model to assess the degree to which an individual deep-sea sedimentary record records the magnitude of environmental perturbation represented by an early-middle Eocene hyperthermal. I develop a

method to ‘back’ out the true excursion size by utilizing the sedimentary model in GENIE. I use model results to compare the range of and controls on inter-site variability in the size, timing, and overall duration of the event.

CHAPTER 1

Introduction to the Dissertation

Today, anthropogenic activities have cumulatively released ~300 billion tons (Gt) (1 Gt = 10^{15} g C) of carbon to the atmosphere. Most of this release has occurred over the last 60 years, as rates of carbon release have increased exponentially. Continuing this trajectory, total emissions will exceed 1000 Gt C by the end of the century without major mitigation efforts. Many reports on climate change pay special attention to the year 2100; it is often used as the target for determining the potential significance of impacts. Reports show predictions for total warming by the century's end, total change in sea level, total loss of Arctic sea ice and high altitude glaciers, etc. Yet the true impacts of anthropogenic global warming will far outlast the year 2100. In their 2009 paper, Archer et al., noted that "in practice, the tail is generally thrown out of [greenhouse warming potential] calculations by truncating the integral at 100 years, a timescale that we argue arises from our own lifetimes rather than anything intrinsic about the carbon cycle."

This "tail" is precisely what makes the CO_2-problem unique compared to other types of human pollution—CO_2 has a very long-lasting impact on the climate system. However, there is broad misunderstanding of the true time-scale of the impact of fossil fuel carbon on the climate. Archer et al., 2009, point out that even the 2007 Intergovernmental Panel on Climate Change Report may underestimate the extent of this long tail of elevated atmospheric CO_2 concentration by suggesting that 80% of the excess CO_2 is removed over centuries (Solomon et al., 2007).

In truth, depending on the ultimate magnitude of the CO_2 perturbation, a consistent result of coupled climate-carbon cycle models is that the climate impacts of elevated atmospheric CO_2 will persist for tens, if not hundreds of thousands of years (Archer et al., 1997; Archer et al., 1998; Archer, 2005; Ridgwell and Hargreaves, 2007; Tyrell et al., 2007; Lenton and Britton, 2006; Archer et al., 2009; Goodwin and Ridgwell, 2010). Archer et al., 2009, succinctly summarize the discrepancy between the oft-repeated description of climate change as a century-scale problem and the understanding among carbon cycle researchers that the effects will persist much longer. They note that estimates for an atmospheric lifetime of CO_2 that range from decades to centuries only address the first mechanism of CO_2 drawdown—largely equilibration with the oceans. While the process of 'ocean invasion' (the dissolution and transport of CO_2 through the oceans) happens on a timescale of hundreds of years, the residual CO_2 in the atmosphere after this process may be as high as 40% (Archer et al., 2009). The most significant CO_2 drawdown processes (in terms of the total excess CO_2 removed) are the so-called sedimentary feedbacks, namely seafloor and terrestrial carbonate neutralization. Together, these processes restore the pH of the oceans and allow further ocean invasion to occur, but after their completion, perhaps 6-10% of the anthropogenic CO_2 will still remain in the atmosphere, removed only by the very slow, hundreds of thousands of years process of silicate weathering (Goodwin and Ridgwell, 2010).

While 6-10% may sound small, if total anthropogenic emissions reach 5,000 Gt (a number often cited for available fossil fuel reserves considering conventional extraction methods), this represents an excess of as much as 500 Gt of carbon in the atmosphere compared to pre-industrial concentrations. Today, there is an excess of ~200 Gt C in the atmosphere, and many would argue that we have already begun to see the climate impacts of this change.

Yet, while we have a good understanding of the thermodynamics of the carbonate system that allow the estimates above, the geological record provides some of the most compelling evidence for the long-lasting consequences of abrupt atmospheric CO_2 loading. Studying the geologic record of rapid warming events provides a complete snapshot of the feedbacks that operate to magnify and eventually recover from the initial perturbation.

In the early 1990s, the discovery of massive warming at the Paleocene/Eocene boundary, combined with indications of the release of massive quantities of isotopically depleted carbon to the oceans and atmosphere over perhaps a few tens of thousands of years, provided a possible analog for modern climate change (Kennett and Stott, 1991). Since the initial discovery, records of the Paleocene/Eocene Thermal Maximum (PETM) have proliferated across the globe. The characteristic features of the PETM—an isotopic excursion of the carbon isotopic composition of the atmosphere and oceans, widespread dissolution of carbonates in the deep sea, and warming of 5-7°C globally—are considered hallmarks of hyperthermal events. However, there are still many

active debates regarding aspects of the event that are important in order to fully exploit the PETM to assess climate sensitivity, potential feedbacks, and the timescale of recovery. Uncertainties in paleo-boundary conditions like geography and atmospheric composition, combined with complex regional responses to a global perturbation and the myriad local processes that influence the PETM record at any single site, conspire to impede a straightforward application of climate models to study the event. In fact, while the sheer size of the PETM makes its occurrence recognizable in multiple settings, the environmental impact of such extreme change further complicates the fidelity of records. Though multiple studies have provided hypotheses, the amount of carbon released at the P/E boundary, the source or isotopic composition of that carbon, and the duration of each stage of the event are still active research questions.

More recently, increasing resolution of records of warm-Earth paleoclimates (in particular the Paleocene and Eocene epochs), has led to the discovery of multiple events with hyperthermal-like features. These small hyperthermal events are the motivation behind the primary question addressed in this dissertation: how ubiquitous are abrupt warming events in warm background climates without the existence of permanent, large ice sheets?

The scientific opportunities offered by studying multiple hyperthermals of various sizes are two-fold. First, the existence of multiple events provides a spectrum across which it is possible to assess the potential range of environmental impacts. Though estimates for the absolute magnitude of carbon

release at the PETM are imprecise, a range of 4000-6000 Gt C is most likely. This estimate suggests that the PETM is most comparable with a modern worst-case scenario where human activity releases nearly the total available fossil fuel reservoir (of ~5000 Gt C), though the modern scenario is occurring on a considerably faster timescale. Multiple events of various sizes may help generate understanding of the fundamental dynamics operating over geologically short timescales in a warm climate, a step beyond studying what originally appeared to be a one-off event. For instance, how much range is there in the recovery timescales between events, and do the same set of feedbacks appear to operate consistently? When Archer et al., 2009, assessed the climate feedbacks associated with abrupt carbon release and warming, they found that up to 50% of climate feedbacks in some models were a function of biological response—a particularly difficult system to model. However, if productivity increase, say, is a consistent feature during multiple hyperthermal recoveries, the case is stronger for its parameterization in climate models.

The second advantage of studying multiple hyperthermals involves the impossibility of extracting completely unbiased information from any single record of an event. The source in which a record is generated (i.e. bulk carbonate, shell material, organic compounds) as well as site-specific characteristics (latitude, water depth, sediment composition, sediment accumulation rate) all influence the record ultimately measured. The more abrupt warming events, the more likely it is to develop a systematic understanding of the biases involved in preserving

such abrupt perturbations, with the ultimate goal of producing a consistent mechanism to quantitatively address such biases before interpreting the fidelity of a given record.

1.1 Outline of the Dissertation

This dissertation attempts to utilize multiple methods to study variability in greenhouse Earth climates. In particular, I combine the development and interpretation of sedimentary records (especially stable isotopes) with the use of an Earth system model of intermediate complexity called c-GENIE (Grid-Enabled Integrated Earth system model).

Chapter 2 addresses a classic problem in studying warm epochs: whether overturning circulation was significantly weaker and/or dominated by convection in the low latitudes (by the formation of so-called 'warm saline deep waters'). We provide the first record of deep-sea conditions from a high-latitude Southern Pacific site in the Paleocene, demonstrating the possibility of a nearby site of deep-water formation, which we suggest was the Ross Sea.

In Chapter 3, I combine high-resolution records of a series of hyperthermal events recently identified from the early-middle Eocene, with records of previously identified hyperthermals from the late Paleocene to early Eocene to systematically assess the extent of inter-site variability in the magnitude and duration of recorded events. I suggest a method for determining whether an individual event is sufficiently large relative to background variability to qualify as

a hyperthermal. Finally, I suggest a connection between the events of the early-middle Eocene and the late Paleocene-early Eocene.

Chapter 4 goes one step further in synthesizing records of multiple hyperthermal events. Here, I compile and compare records of 44 separate events occurring between ~250 to ~40 Ma. All events are predominately identified through the existence of a carbon isotope excursion—I compare these recorded carbon isotope excursions for each event from bulk carbonate datasets in order to assess the range in sizes and shapes of identified events. I also assess additional common environmental changes associated with each event—from the development of anoxia to associated biotic change.

Finally, in Chapter 5 I use the GENIE model to assess a small hyperthermal event from the early-middle Eocene through its carbon isotope excursion. The sedimentary module of GENIE allows me to develop an iterative method to back out an estimated 'true' size for the excursion in the atmosphere and dissolved inorganic carbon implied by the sedimentary record. I use these model results to assess the causes of inter-site variability, with a particular focus on the influence of sedimentation rate differences in altering the apparent size and timing of an event.

Cumulatively, these chapters represent an effort to extract as much relevant information as possible from records of abrupt carbon release and warm climates. The goals are to understand the fundamental characteristics of large-scale environmental change on a greenhouse Earth, while also considering the

small-scale, site-specific processes that affect our ability to fully utilize records of Earth's climatic past.

1.2 References

Archer, D., (2005), The fate of fossil fuel in geologic time, *Journal of Geophysical Research*, Vol. 110, C09S05, doi:10.1029/2004JC002625.

Archer, D., Kheshgi, H., and E. Maier-Riemer, (1997), Multiple timescales for neutralization of fossil fuel CO_2, *Geophysics Research Letters*, Vol. 24, pp. 405-408, doi: 10.1029/97GL00168.

Archer, D., Kheshgi, H., and E. Maier-Reimer, (1998), Dynamics of fossil fuel CO_2 neutralization by marine $CaCO_3$, *Global Biogeochemical Cycles*, Vol. 12, pp. 259-276, doi:10.1029/98BG00744.

Archer, D., Eby, M., Brovkin, V., Ridgwell, A., Cao, L., Mikolajewicz, U., Caldeira, K., Matsumoto, K., Munhoven, G., Montenegro, A., and K. Tokos, (2009), Atmospheric lifetime of fossil fuel carbon dioxide, *Annual Reveiws of Earth and Planetary Scienes*, Vol. 37, pp. 117-134, doi:10.1146/annurev.earth.031208.100206.

Goodwin, P. and A. Ridgwell, (2010), Ocean-atmosphere partitioning of anthropogenic carbon dioxide on multimillennial timescales, *Global Biogeochemical Cycles*, Vol. 24, GB2014, 13 pp., doi:10.1029/2008GB003449

Kennett J.P. and and L.D. Stott, (1991), Abrupt deep sea warming, paleoceanographic changes and benthic extinctions at the end of the Paleocene, *Nature*, Vol. 353, pp. 319-322, doi:10.1038/353225a()

Lenton, T.M. and C. Britton, (2006), Enhanced carbonate and silicate weathering accelerates recovery from fossil fuel CO_2 perturbations, *Global Biogeochemical Cycles*, Vol. 20, GB3009, doi:10.1029/2005GB002678.

Ridgwell A. and J.C. Hargreaves, (2007), Regulation of atmospheric CO_2 by deep sea sediments in an Earth System Model, *Global Biogeochemical Cycles*, Vol. 21, GB2008, doi:10.1029/2006GB002764.

Solomon, S., Qin, D., Manning, M., Chen, Z., Marquis, M., Aeryt, K.B., Tignor, M., and H.L. Miller (eds.), (2007), Contribution of Working Group I to the Fourth Assessment Report of the Intergovernmental Panel on Climate Change, 2007, Cambridge University Press, Cambridge, United Kingdom and New York, NY, USA.

Tyrrell, T., Shepherd, J.G., and S. Castle, (2007), The long-term legacy of fossil fuels, *Tellus*, Vol. 59, pp. 664-672, doi:10.1111/j.1600-0889.2007.00290.x.

CHAPTER 2

A South Pacific Source of Deep Water during the Paleocene

The formation of deep waters is critical for the redistribution of heat and nutrients in the global ocean, but details of how this system operated in the warm Paleocene Epoch are controversial. Previous studies have separately suggested deep water formation at various high latitude sites (particularly in the South Atlantic), as well as the existence of low-latitude deep water formation. However, the lack of a high latitude Pacific site has hampered reconstructions of overturning, especially as the Pacific must have dominated the characteristics of the global Paleocene ocean as a result of its sheer size. A new Paleocene stable isotope record from the South Pacific shows that deep waters formed in this region during the early Danian and Selandian. Additionally, a seismic reflection profile indicates the presence of a contourite drift offshore of the Campbell Plateau, New Zealand, suggesting that deep waters originated in the nearby Ross Sea. Our results provide physical evidence of strong deep current velocities and suggest that deep convection occurred at multiple high latitude sites in the Paleocene.

2.1 Introduction

In an integral part of the modern thermohaline circulation, cold, dense waters formed in the North Atlantic and around Antarctica sink, fill the global ocean, and eventually upwell to the surface in a few thousand years, resulting in substantial aging gradients in the deep ocean. Yet, it is not clear that the oceans have always worked this way, particularly during past warm periods. Indeed, isotopic evidence demonstrates that circulation in the Paleocene (55-65 Ma on the BKSA95 timescale) was marked by relatively weak inter-ocean deep water gradients compared to today. Researchers have suggested greater ocean heat transport to explain extreme warmth at high latitudes (e.g. Barron, 1987; Lyle, 1997), but more recent modeling studies have suggested such an increase is unrealistic (Huber and Sloan, 2001, Heinemann et al., 2009), and that deep current velocities were similar to modern despite reduced temperature gradients (Huber and Sloan, 2001; Bice and Marotzke, 2003). Conversely, the apparent lack of sediment drifts older than Oligocene age and the discovery of Atlantic shales of Paleocene age have led to the suggestion that circulation was sluggish (Davies et al., 2001; Tucholke and Vogt, 1979). Further, researchers have invoked reduced inter-ocean isotopic gradients observed through detailed reconstructions of Palecene deep water sites as evidence for weak circulation (Cramer et al., 2009).

Records of $\delta^{13}C$ from sites of intermediate to deep depths have been extensively used to reconstruct sites of formation and flow paths of deep water,

by comparing values at a given site to the mean ocean value (Curry and Lohman, 1982; Shackleton et al., 1983; Katz and Miller, 1991; Pak and Miller, 1992; Corfield and Cartlidge, 1992; Corfield, 1994; Quillévéré, 2002; Nunes and Norris, 2006). Young waters recently isolated from the surface are depleted in organic carbon and have a relatively positive $\delta^{13}C$, while older waters acquire relatively negative $\delta^{13}C$ signatures as they accumulate remineralized organic matter. Through comparison of global $\delta^{13}C$ records, most authors have suggested a Southern Atlantic source of deep water throughout most of the Paleocene, with possible periodic influence of a North Atlantic source (Pak and Miller, 1992; Corfield and Cartlidge, 1992; Mountain and Miller, 1992; Corfield and Norris, 1998; Quillévéré et al., 2002; Nunes and Norris, 2006). In the Selandian through Thanetian, a noted collapse of inter-ocean $\delta^{13}C$ gradients and homogenous deep ocean temperature and salinity have led to the suggestion that overturning circulation was halothermal, or driven by the evaporation-induced density increase of warm waters at low latitudes (referred to as warm saline deep water, WSDW) (Brass et al., 1982; Kennett and Stott, 1990; Pak and Miller, 1992; MacLeod and Huber, 1996). Changes in the inferred strength and source of deep water flow during the Paleocene are of particular interest given the potential links between changes in circulation and changes in climate, with both modeling and proxy studies suggesting that there may be large and abrupt changes in global circulation during transient climatic events (Bice and Marotzke, 2003; Tripati and Elderfield, 2005; Nunes and Norris, 2006).

Despite numerous reconstructions of Paleocene deep water gradients, a lack of records from the high-latitude Pacific has hampered detailed reconstruction of overturning patterns. While the Pacific Ocean must have dominated the mean-ocean signal of the Paleocene due to its shear size, the best Paleocene Pacific records are from equatorial paleo-latitudes, given that Southern Pacific sites tend to be carbonate-poor. Scher and Martin (2004) used neodymium isotopes from the tropical Pacific to infer evidence of bipolar deep convection in the North Pacific and Southern Ocean from ~65-45 Ma, but the data cannot determine which sector of the Southern Ocean produced deep waters (Thomas et al., 2004; Thomas et al., 2008). While equatorial sites can help reconstruct differences in water chemistry and temperature between major ocean basins, they cannot definitively distinguish where deep waters formed. Here, we use new $\delta^{13}C$ and $\delta^{18}O$ records from the South Pacific to improve reconstructions of global deep water gradients and isolate a possible southern Pacific source of deep water.

2.2 Methods

2.2.1 Site Description

The Campbell Plateau is a submerged continental block southeast of the South Island, New Zealand. At the base of the plateau sits the Campbell 'drift,' a 850 x 170 km feature originally interpreted as a Neogene drift associated with the

development of the modern deep western boundary current (see Figure 2-1) (Carter and McCave, 1997). However, drilling during Ocean Drilling Program (ODP) Leg 181 on the edge of the Campbell 'drift' revealed the feature to be of Paleocene age, with less than 10 meters of Pleistocene clay overlying Paleocene material (Carter et al., 1999). This led to the re-interpretation of the 'drift' as an eroded pelagic apron formed from sediments off the Campbell Plateau (Carter et al., 2004).

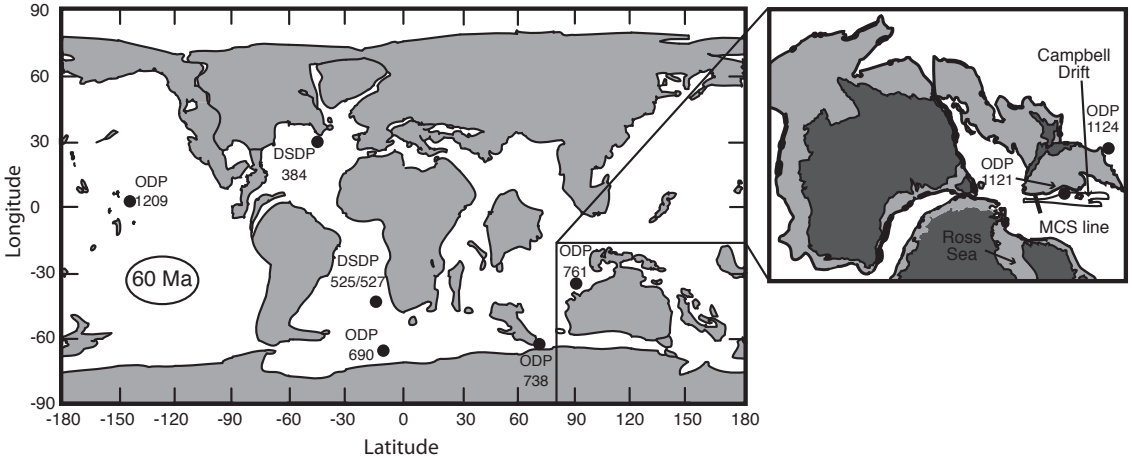


Figure 2-1. Paleogeographic reconstruction for the mid-Paleocene (60 Ma) showing the location of records used in this study. Reconstruction modified from a paleomap created using the web-based ODSN software. Inset (box) shows a detailed reconstruction of the Southwest Pacific (60 Ma) from S. Cande, including the location of the Campbell Drift and the seismic line Ewing 9201 described in this study.

At the edge of the drift near the base of the Plateau, ODP Hole 1121B (50°53.876'S, 176°59.862'E) recovered approximately 140 meters of Paleocene sediments with an average sedimentation rate of 3-4 cm/kyr. Hole 1124C

(39°29.901'S, 176°31.894'E) off the North Island, New Zealand, also recovered sediments of Paleocene-Cretaceous age. Both holes are in deep water (4000 meters), and therefore near the modern carbonate compensation depth (CCD). The paleodepth estimate for hole 1121B is about 3500 m and 2000-3000 m for hole 1124C--approximately at the depth of the Paleocene CCD (Carter et al., 1999).

2.2.2 Seismic Reflection Data

To test the interpretation of the Campbell 'drift' as an eroded pelagic apron, we obtained a multi-channel seismic line from Steve Cande that had been collected by the R/V Ewing as it transited over the Campbell 'drift' during the EW9201 cruise in 1992 (from 53°50.9392'S, 174°22.4946'E to 55°16.3181'S, 174°40.1100'E). We processed MCS data using Seismic Unix and SIOSEIS, employing noisy channel muting, bandpass filtering, predictive deconvolution, normal move-out correction, stacking, water column muting, and time-varied gain.

2.2.3 Stable Isotope Data

We generated $\delta^{13}C$ and $\delta^{18}O$ data from the benthic foraminifer *Nuttalides truempyi* at 50 cm spacing from ODP sites 1121B and 1124C, with additional intervals at 1121B sampled at 10 cm spacing (Appendix Table A1). Benthic

foraminifera are present but relatively low in abundance (typically only around 10 specimens (>150 microns) were available to analyze per 2 cm. sample). However, Wei et al (2005) concluded that diagenesis/dissolution was not significant because of the lack of systematic variation of $\delta^{18}O$ measures of bulk sediment with sediment wt% $CaCO_3$. Benthic foraminifera samples were analyzed at the UC, Santa Cruz stable isotope lab on a GVI Prism Isotope Ratio Mass Spectrometer with dual inlet automated carbonate device, with measurement precision of ± 0.04 ‰ for $\delta^{13}C$ and ± 0.06 ‰ for $\delta^{18}O$. All data are corrected to VPDB using NBS-19 as a standard. Combined, holes 1124C and 1121B provide a record of the Paleocene from approximately 57-65 Ma, though there are a few considerable gaps—most notably from ~60.2-63.2 Ma in hole 1124C. In addition to incomplete core recovery in both holes, an insufficient quantity of benthic foraminifera in some intervals also accounts for data gaps.

2.2.4 Age Model

For holes 1121B and 1124C, we have developed age models using biostratigraphic and magnetostratigraphic markers identified by the shipboard party and dated using the geological timescale from Berggren et al., 1995 (BKSA95). For hole 1121B, use of minimal tie points and linear interpolation between select biostratigraphic datums (primarily calcareous nannoplankton) yields a linear sedimentation rate of 4.0 cm/kyr from 32-94 mbsf and a linear

sedimentation rate of 3.04 cm/kyr from 94-133 mbsf. For hole 1124C we use a 0.93 cm/kyr sedimentation rate for the shallower Paleocene sections and a 0.84 cm/kyr sedimentation rate for deeper sections, separated by an unconformity at ~448 mbsf representing ~3 myr. For hole 1121B, two published age models exist (from Hollis, 2002 and Wei et al., 2005), but these disagree substantially on the sedimentation rate during the latest Paleocene (3 cm/kyr versus 17 cm/kyr). The high sedimentation rate inferred by Wei et al. (2005) is based on a calibration of features in a bulk $\delta^{13}C$ record from 1121B to records from DSDP 577 (Shatsky Rise, Central Pacific). We have selected the linear sedimentation rate age model in order to use minimal calibration points. However, for hole 1121B, age control provided by the biostratigraphic datums is sufficient to ensure that the top of the core is no younger than 57 Ma, and the base of the core is at least ~59.9 Ma, though may be as old as ~60.7 Ma.

In order to compare data from sites 1121 and 1124 to a global composite, we compiled Paleocene stable isotope data generated from *Nuttalides truempyi* at the following sites: DSDP 384 (J-Anomaly Ridge, North Atlantic from Berggren and Norris, 1997), ODP 1209 (Shatsky Rise, Central Pacific, from Westerhold et al., in press), DSDP 525/527 (Walvis Ridge, South Atlantic, from Shackleton et al., 1984 and Thomas and Shackleton, 1996), ODP 738 (Kerguelen Plateau, South Atlantic from Barrera and Huber, 1991), ODP 690 (Maud Rise, South Atlantic from Kennett and Stott, 1990), and ODP 761 (Wombat Plateau, Indian Ocean, Quillévéré et al., 2002). These sites all have paleodepths >1500 m, and

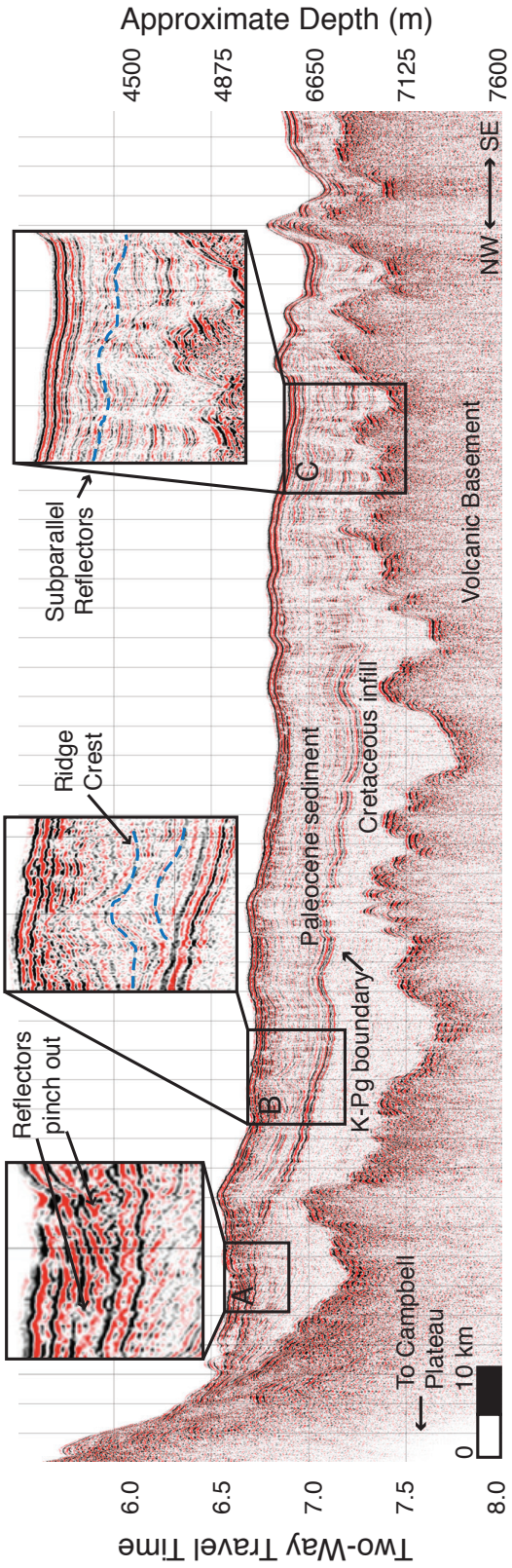
Sites DSDP 384 and DSDP 527 have paleodepths >2500 m. We have reassessed age models for all sites based on biostratigraphic (calcareous nanoplankton and planktonic foraminifera) and magnetostratigraphic datums plotted on the Berggren 1995 timescale. For sites where the Paleocene/Eocene Thermal Maximum and Cretaceous/Paleogene boundary are recorded (DSDP 577, ODP 1209, DSDP 525/527, ODP 690), they are also used as tie-points dated at 55.5 Ma and 65 Ma, respectively (see Appendix Table A2).

2.3 Results and Discussion

2.3.1 Is the Campbell 'Drift' a Paleogene Drift?

The seismic profile (see Figure 2-2) perpendicular to the edge of the Campbell Plateau reveals a lenticular sedimentary feature at the base of the Plateau overlying volcanic basement, sedimentary infill, and a prominent reflector (likely an erosional surface corresponding to the K/Pg boundary). Unlike the low amplitude infill interpreted as Cretaceous non-marine clastics below this reflector (Carter et al., 1999), the overlying sedimentary body has an internal structure that is much more complicated and contains features indicative of a contourite drift (Figure 2-2). The most prominent feature is a ridge crest (or channel levee) directly overlying the relatively flat K/Pg boundary reflector and onlapped by younger Paleogene sediments. Reflectors within the ridge crest show evidence of upslope migration, with a thinner sedimentary package accumulating towards the

Figure 2-2. Multichannel seismic reflection profile of Ewing 9201 showing a cross-section of the Campbell sediment drift. Drilling on nearby ODP Site 1121 demonstrate that the Campbell Drift is largely composed of Paleocene age sediments. Boxes demonstrate characteristic features suggesting that the Campbell Drift is a contourite drift formed by a deep western boundary current flowing along the Campbell Plateau: A) shows reflectors pinching out, reflecting that the main body of the drift accumulated offshore and terminates before reaching the base of the Plateau, B) traced line demonstrates the existence of a ridge crest formed from continuous overlay of upslope migrating downlapping reflectors, and C) traced line demonstrates the existence of sub-parallel reflectors in the sedimentary body that do not correspond to the basement structure.

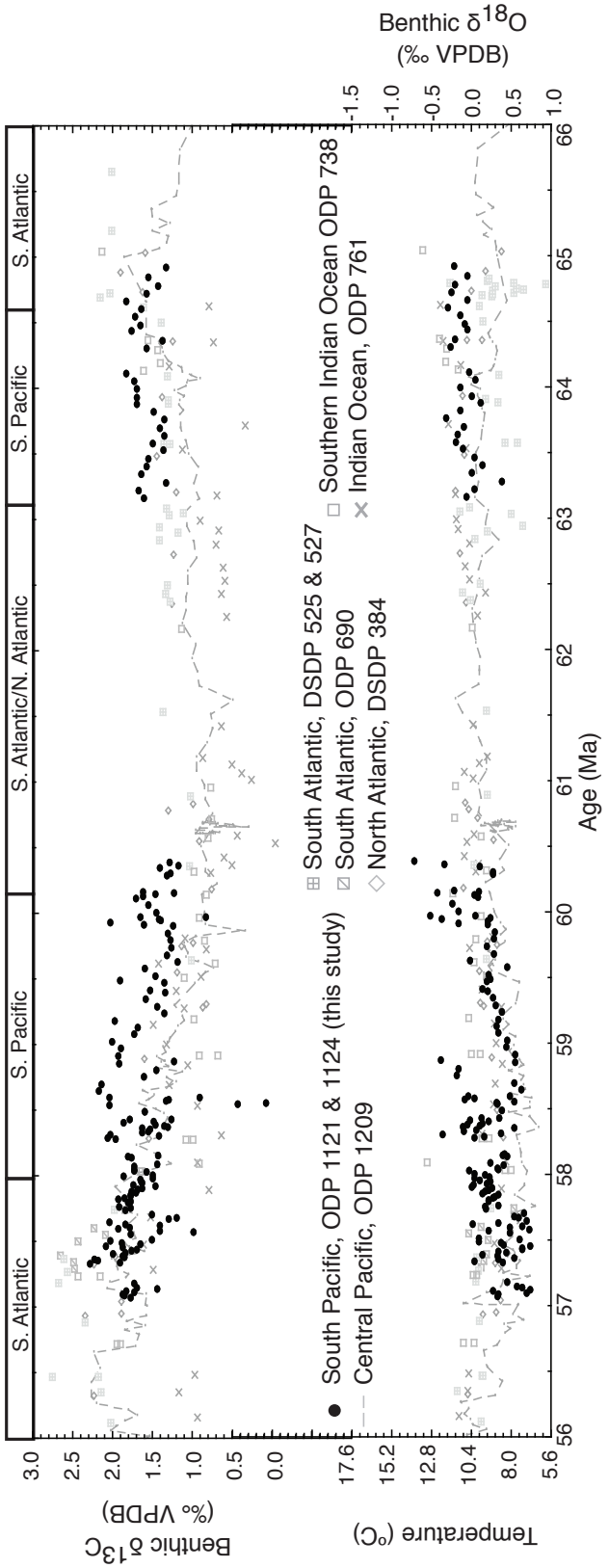

Approximate Depth (m)
4500
4875
6650
7125
7600
NW
SE
Two-Way Travel Time
6.0
6.5
7.0
7.5
8.0
0
10 km
To Campbell Plateau
Volcanic Basement
Cretaceous infill
Paleocene sediment
K-Pg boundary
Subparallel Reflectors
Ridge Crest
Reflectors pinch out
A
B
C

flat unconformity. Throughout the drift, reflectors are subparallel to the acoustic basement and the interpreted K-Pg sequences pinch out before reaching the base of the Campbell Plateau, though some modern deep western boundary current activity may be responsible for erosion of sediments. Site 1121 was drilled at the edge of the drift, and so did not recover the highly expanded Paleocene section further offshore (where Paleocene sediments reach almost 500 m thickness), yet sedimentation rates from 1121 (3-4 cm/kyr) are still well above pelagic rates of ~1 cm/kyr and consistent with drift sedimentation.

2.3.2 Global Ocean Stable Isotope Compilation

In order to asses the relative strength of deep water formation at various sites, we compare $\delta^{13}C$ values in the global composite to an inferred mean ocean value, represented by ODP Site 1209 in the equatorial Pacific (shown in Figure 2-3 as a dashed grey line) as a result of the Pacific's dominance of the global ocean. Previous studies have argued that the principal loci of deep water formation in the early Danian and Thanetian (approx. 65-64 and 58-55 Ma) was in the South Atlantic and have noted that the relative collapse in $\delta^{13}C$ gradients during the late Danian and Selandian (from approx. 64-58 Ma) may suggest the possible weakening of overturning strength or the development of a low-latitude Pacific or Tethys source (Katz and Miller, 1991, Pak and Miller, 1992, Corfield,

Figure 2-3. Paleocene composite of multisite benthic foraminiferal (all Nuttalides truempyi) δ13C and δ18O records plotted against age in millions of years. New data from this study (ODP Sites 1121B and 1124C in the Southwest Pacific) are plotted in black. Grey dashed line shows data from ODP Site 1209 in the Equatorial Pacific (data from Westerhold et al., in press) and is used here to represent mean ocean values. Data is plotted based on ocean basin, with all sites in a given ocean plotted as the same shape to highlight inter-ocean gradients. All sites chosen for this composite had paleodepths greater than at least 1500 meters and all data has been re-plotted using the most up-to-date biomagnetostratigraphy available for each site on the Berggren 1995 timescale. Temperature is calculated using the linear equations of Bemis et al (1998) after adjusting δ18O values to Cibicidoides following the corrections given by Katz et al (2003) and using a δ18O for seawater of -1.27 ‰. Data source: DSDP 384 (J-Anomaly Ridge, North Atlantic from Berggren and Norris, 1997), ODP 1209 (Shatsky Rise, Central Pacific, from Westerhold et al., in press), DSDP 525/527 (Walvis Ridge, South Atlantic, from Shackleton et al., 1984 and Thomas and Shackleton, 1996), ODP 738 (Kerguelen Plateau, South Atlantic from Barrera and Huber, 1991), ODP 690 (Maud Rise, South Atlantic from Kennett and Stott, 1990), and ODP 761 (Wombat Plateau, Indian Ocean, Quillévéré et al., 2002).


S. Atlantic
S. Pacific
S. Atlantic/N. Atlantic
S. Pacific
S. Atlantic
Benthic δ13C (‰ VPDB)
Temperature (°C)
Benthic δ18O (‰ VPDB)
Age (Ma)
South Pacific, ODP 1121 & 1124 (this study)
Central Pacific, ODP 1209
South Atlantic, DSDP 525 & 527
South Atlantic, ODP 690
North Atlantic, DSDP 384
Southern Indian Ocean ODP 738
Indian Ocean, ODP 761

1994, Quillévéré, et al., 2002). Our revised composite suggests that the Southwest Pacific had the heaviest carbon isotope values at times during the Danian and Selandian, consistent with intermittent deep water formation in the southern Pacific for a total of about 4 million years.

In the Danian (~64.7-63.2 Ma), our new $\delta^{13}C$ data show that the South Pacific is ~0.3-0.8 ‰ heavier than the mean ocean value and slightly more positive (~0.3 ‰) than the South Atlantic and North Atlantic. The large decline in $\delta^{13}C$ values after the K/Pg boundary at both South and North Atlantic sites is accompanied by an increase in $\delta^{13}C$ values from the South Pacific, suggesting a possible reorganization of circulation and the establishment of multiple sites of overturning—potentially in the North Atlantic and at various sites around Antarctica. Our lack of recovery in the late Danian and early Selandian (~63.2-60.4 Ma) prohibits interpretation of South Pacific deep water formation in this interval, during which South Atlantic sites continue to have the heaviest $\delta^{13}C$ values. In the late Selandian and Thanetian, the global composite of Quillévéré et al., 2002, mistakenly used planktonic foraminiferal $\delta^{13}C$ values from Site 690 to establish global benthic $\delta^{13}C$ gradients, causing the Southern Atlantic to appear significantly heavier (by >1 ‰) than other sites from ~58.3-56 Ma, whereas our revised composite demonstrates that South Atlantic $\delta^{13}C$ actually decreases at ~60 Ma and is either equal to or lighter than the global mean until ~58 Ma. During this interval (~60.4-58 Ma), the South Pacific has the heaviest $\delta^{13}C$ values by as much as 0.5 ‰. Within this interval there are episodic decreases in gradient

strength—notably at ~59.8 and ~58 Ma. At 58 Ma, the decrease in gradient coincides with the transition of heaviest $\delta^{13}C$ values from the South Pacific to the South Atlantic, with South Atlantic $\delta^{13}C$ reaching the most positive values from ~57.5-56 Ma. While our South Pacific $\delta^{13}C$ records show the increasing trend common at other sites, likely reflecting the Paleocene Carbon Isotope Maximum (PCIM), the increase is substantially less pronounced. This may be a function of the declining significance of the South Pacific as a source of deep water beginning around 58 Ma. The addition of this new South Pacific dataset to our revised composite alters the previous interpretation of minimal aging gradients in the mid-Paleocene followed by the late Paleocene establishment of strong overturning in the South Atlantic and demonstrates that aging gradients at times during the Selandian (at least as early as 60.4 Ma) were approximately as large as those in the later Paleocene.

Our $\delta^{18}O$ records from the South Pacific generally show values similar to (or slightly warmer than) the global average throughout the early and mid-late Paleocene. An increasing trend of ~1 ‰ from the Selandian to Thanetian (~61-57.5 Ma), records the long term cooling recognized at other sites (Quillévéré et al., 2002). Temperatures, based on calculations from $\delta^{18}O$ following the paleotemperature equation of Bemis et al., 1998, with all *N. truempyi* $\delta^{18}O$ values first corrected to *Cibicidoides* following the correction given by Katz et al., 2003, and using a $\delta^{18}O$ of seawater of -1.27‰, range from as high as 13 °C in the Selandian to 6-7 °C by the end of our record (and the height of the Paleocene

carbon isotope maximum). The large range in $\delta^{18}O$ values in our dataset from Site 1121 compared to the global composite—especially from 57.4-58.9 Ma—is at least partially a result of the larger number of measurements from Site 1121 compared to other sites in this interval. Another explanation might be that this site intermittently records an intermediate water mass. Scatter from 59.9-60.4 likely reflects a lack of age control in the lowest 10 m of the core, given the range (from 60-64) in biostratigraphic datums in this interval (Carter et al., 1999).

2.3.3 Possible Site of Deep Water Formation

Today, the bulk of Southern-component deep water forms in the southern and western Weddell Sea with smaller contributions to Southern component deep water from other sites around Antarctica, including the Ross Sea in the Pacific sector. In the Weddell Sea, newly formed deep water flows northward on the western side of the basin and exits through gaps in the South Scotia Ridge, with bottom currents reaching speeds of 10-15 cm/s (Pudsey, 1992). In the northern Weddell Sea and the southern Scotia Sea, multiple studies have described various drift deposits up to 1 km thickness, formed by deposition of sediment from suspension in the nephloid layer and best developed along the western sides of the basins (Pudsey 1992; Howe et al. 1998; Camerlenghi et al., 2001; Maldonado et al., 2003).

During the Paleocene, paleogeographic reconstructions demonstrate that the location of Australia and the Tasman Rise formed a barrier to circum-Antarctic flow (see Figure 2-1); thus, any deep western boundary current emanating from the Ross Sea would be constrained to flow along the Campbell Plateau. Combined with positive $\delta^{13}C$ values recorded from the South Pacific during the mid-Paleocene, the existence of a sediment drift along the base of the Campbell Plateau suggests that the Ross Sea may have been an important site of deep convection similar to the Weddell Sea today. Comparable to the modern sediment deposits formed in the path of newly formed bottom water flowing out of the Weddell Sea, we suggest Ross Sea deep water flowing out of the basin could have formed the Campbell Drift. The Paleocene age of sediments recovered from the Campbell Drift as well as seismic reflection evidence indicating a mode of formation consistent with strong deep boundary currents, demonstrate that the Campbell 'drift' is a sediment drift recording outflow of deep water formed in the Ross Sea.

2.4 Conclusions

Stable isotope and seismic data provide compelling evidence that the Pacific sector of the Southern Ocean (in particular, the Ross Sea) was a site of deep convection during the early Danian and Selandian for a total of approximately 4 Myr. While inter-ocean carbon isotopic gradients were

undoubtedly reduced compared to the modern throughout the entire Paleocene, our data reject the story of a large-scale collapse in gradients for the Selandian followed by the establishment of a strong, South Atlantic deep water source in the Thanetian. Rather, Paleocene overturning circulation appears to have been characterized by multiple episodes of pronounced reorganization (notably at ~58 Ma), with reversals in the primary loci of deep water formation and also with intervals where it is likely that deep water formation occurred in both the northern and southern hemispheres and the Atlantic and Pacific oceans. In particular, our revised $\delta^{13}C$ composite further reduces the likelihood of a low-latitude warm saline deep water mass during the Selandian and demonstrates that high-latitude sites had the most positive $\delta^{13}C$ values throughout the Paleocene. Rather than a sluggish ocean, it appears that convection was active during the warm Paleocene, with reduced gradients more likely due to multiple active sites of overturning than to a reduction in the intensity of deep convection.

Chapter 2, in full, has been submitted for publication, and is currently under revision. The material may appear in Geology, 2012, Kirtland Turner, S., Norris, R.D., and Kluesner, J. A South Pacific Source of Deep Water during the Paleocene. I am the primary investigator and author of this paper.

2.5 References

Barron, E.J., (1987), Eocene equator-to-pole surface ocean temperatures: A significant climate problem, *Paleoceanography*, Vol. 2, pp. 729-739, doi:10.1029/PA002i006p00729.

Bemis, B.E., Spero, H.J., Bijma, J., and D.W. Lea, (1998), Reevaluation of the oxygen isotopic composition of planktonic foraminifera: Experimental results and revised paleotemperature equations, *Paleoceanography*, Vol. 13, No.2, pp. 150-160, doi:10.1029/98PA00070.

Berggren, W.A., Kent, D.V., Swisher, C.C., III, and M.P. Aubry, (1995), A revised Cenozoic geochronology and chronostratigraphy, In Berggren, W.A., Kent, D.V., Aubry, M.-P., and J. Hardenbol, (Eds.), *Geochronology, Time Scales, and Global Stratigraphic Correlation: Special Publication of the Society of Sedimentary Geology,* Vol. 35, pp.129-212.

Berggren, W.A., Aubry, M. P., van Fossen, M., Kent, D.V., Norris, R.D., and F. Quillévéré, (2000), Integrated Paleocene calcareous plankton magnetobiochronology and stable isotope stratigraphy: DSDP Site 384 (NW Atlantic Ocean*), Paleogeography, Paleoclimatology, Paleoecology*, Vol. 159, pp. 1-51, doi:10.1016/S0031-0182(00)00031-6.

Bice, K.L., and J. Marotzke, (2003), Numerical evidence against reversed thermohaline circulation in the warm Paleocene/Eocene ocean, *Journal of Geophysical Research*, Vol. 106, pp. 529-542, doi:10.1029/2000J000561.

Brass, G.W., Southam, J.R., and W.H. Peterson, (1982), Warm saline bottom water in the ancient ocean, *Nature,* Vol. 296, pp. 620-623, doi:10.1038/296620a0.

Camerlenghi, A., Domack, E., Rebesco, M., Gilbert, R., Ishman, S., Leventer, A., Brachfeld, S. and A. Drake, (2001), Glacial morphology and post-glacial contourites in northern Prince Gustav Channel (NW Weddell Sea, Antarctica), *Marine Geophysical Research*, Vol. 22, pp. 417-443, doi:10.1023/A:1016399616365.

Carter, L., and I.N. McCave, (1997), The sedimentary regime beneath the Deep Western Boundary Current inflow to the Southwest Pacific, *Journal of Sedimentary Research*, Vol. 67, pp. 1005-1017, doi:10.1306/D42686B22B26-11D7864800102C1865D.

Carter, L., Carter, R.M., and I.N. McCave, (2004), Evolution of the sedimentary system beneath the deep Pacific inflow off eastern New Zealand, *Marine Geology*, Vol. 205, pp. 9-27, doi:10.1016/S0025-3227(04)00016-7.

Corfield, R.M., and J.E., Cartlidge, (1992), Oceanographic and climatic implications of the Palaeocene carbon isotope maximum, *Terra Nova*, Vol. 4, pp. 443-455, doi:10.1111/j.1365-3121.1992.tb00578.x.

Corfield, R.M., (1994), Paleocene oceans and climate: An isotopic perspective, *Earth Science Reviews*, Vol. 37, pp. 225-252, doi:10.1016/00128252(94)900030-2.

Corfield, R.M., and R.D. Norris, (1996), Deep water circulation in the Paleocene Ocean, In R.W. O'B. Knox, R.M. Corfield, and R.E. Dunay, (Eds.), *Correlation of the Early Paleogene in Northwest Europe*, Geological Society Special Publication, London, No. 101, pp. 443-456.

Corfield, R.M., and R.D. Norris, (1998), The oxygen and carbon isotopic context of the Paleocene/Eocene epoch boundary, In M Aubry, S.G. Lucas, and W.A. Berggren, (Eds.), *Late Paleocene-Early Eocene Climatic and Biotic Events in the Marine and Terrestrial Record*, New York, Columbia University Press, pp. 124-138.

Cramer, B.S., Toggweiler, J.R., Wright, J.D., Katz, M.E., and K.G. Miller, (2009), Ocean overturning since the Late Cretaceous: Inferences from a new benthic foraminiferal isotope compilation, *Paleoceanography*, Vol. 24, PA4216, doi:10.1029/2008PA001683.

Curry, W.B, and G.P. Lohmann, (1982), Carbon isotopic changes in benthic foraminifera from the western South Atlantic: Reconstruction of glacial abyssal circulation patterns, *Quaternary Research*, Vol. 18, pp. 218-235.

Davies, R., Cartwright, J., Pike, J., and C. Line, (2001), Early Oligocene initiation of North Atlantic Deep Water formation, *Nature*, Vol. 410, pp. 917-920, doi:10/1038/35073551.

De Boer, A.M., Sigman, D.M., Toggweiler, J.R., and J.L Russel, (2007), Effect of global ocean temperature change on deep ocean ventiliation, *Paleoceanography*, Vol. 22, PA2210, doi:10.1029/2005PA001242.

Feely, R.A., Talley, L.D., Johnson, G.C., Sabine, C.L., and R. Wanninkhof, (2005), Repeat hydrography cruises reveal chemical changes in the North

Atlantic*, EOS Transactions*, American Geophysical Union, Vol. 86, pp. 299, doi:10.1029/2005EO420003.

Heinemann, M., Jungclaus, J.H., and J. Marotzke, (2009), Warm Paleocene/Eocene climate as simulated in ECHAM5/MPI-OM, *Climates of the Past*, Vol. 5, pp. 785-802, doi:10.5194/cp-5-785-2009.

Hollis, C.J., (2002), Biostratigraphy and paleoceanographic significance of Paleocene radiolarians from offshore eastern New Zealand, *Marine Micropaleontology*, Vol. 46, pp. 265-316, doi:10.1016/SO377-8398(02)00066X.

Honjo, S., (1996), Fluxes of Particles to the Interior of the Open Oceans, In V. Ittekkot, P. Schafer, S. Honjo, and P.J. Depetris, (Eds.), *Particle Flux in the Ocean*, New York, John Wiley & Sons Ltd., pp. 91-154.

Howe, J.A., Livermore, R.A., and A. Maldonado, (1998), Mudwave activity and current-controlled sedimentation in Powell Basin, northern Weddell Sea, Antarctica, *Marine Geology*, Vol. 149, pp. 229-241, doi:10.1016/S00253227(98)00036-X.

Huber, M., and L.C. Sloan, (2001), Heat transport, deep waters, and thermal gradients: coupled simulation of an Eocene Greenhouse Climate, *Geophysical Research Letters*, Vol. 28, pp. 3481-3484, doi:10.1029/2001GL012943.

Katz, M.E., and K.G. Miller, (1991), Early Paleogene benthic foraminiferal assemblages and stable isotopes in the Southern Ocean, In Ciesielsi, P.F., Kristoffersen, Y., et al., *Proceedings of the Ocean Drilling Program Scientific Results*, Vol. 114: College Station, TX, pp 23-28, doi:10.2973/odp.proc.sr.114.173.1991.

Katz, M.E., Katz, D.R., Wright, J.D., Miller, K.G., Pak, D. K., Shackleton, N.J., and E. Thomas, (2003), Early Cenozoic benthic foraminiferal isotopes: Species reliability and interspecies correction factors, *Paleoceanography*, Vol. 18, No. 1024, doi:10.1029/2002PA000798.

Kennett, J.P., and L.D. Stott, (1990), Proteus and Proto-Oceanus: Paleogene oceans as revealed from Antarctic stable isotopic results: ODP Leg 113, In Barker, P.F, Kennett, J.P., et al., *Proceedings of the Ocean Drilling Program Scientific Results*, Vol. 113: College Station, TX, pp. 865-880, doi:10.2973/odp.proc.sr.113.188.1990.

Lyle, M., (1997), Could early Cenozoic thermohaline circulation have warmed the poles? *Paleoceanography*, Vol. 12, pp. 161-167, doi:10.1029/96/PA03330.

Macleod, K.G., and B.T. Huber, (1996), Reorganization of deep ocean circulation accompanying a Late Cretaceous extinction event, *Nature*, Vol. 380, pp. 422-425, doi:10.1038/380422a0.

Maldonado, A., Barnolas, A., Bohoyo, F., Galindo-Zaldivar, J., Hernandez Molina, J.,Lobo, F., Rodriguez-Fernandez, J., Somoza, L., and J.T. Vazquez, (2003), Contourite deposits in the central Scotia Sea: the importance of the Anarctic Circumpolar Current and the Weddell Gyre flows, *Palaeogeography, Palaeoclimatology,Palaeoecology*, Vol. 198, pp. 187-221, doi:10.1016/S0031-0182(03)00401-2.

Mountain, G.S., and K.G. Miller, (1992), Seismic and geologic evidence for early Paleogene deepwater circulation in the western North Atlantic, *Paleoceanography*, Vol. 7, pp. 423-239, doi:10.1029/92PA01268.

Norris, R.D., Kroon, D., Huber, B.T., and J. Erbacher, (2001), Cretaceous Palaeogene ocean and climate change in the subtropical North Atlantic, *Geological Society, London, Special Publications*, Vol. 183, p. 1-22, doi:10.1144/GSL.SP.2001.183.01.

Nunes, F., and R.D. Norris, (2006), Abrupt reversal in ocean overturning during the Palaeocene/Eocene warm period, *Nature*, Vol. 439, pp. 60-63, doi:10.1038/nature04386.

Pak, D.K., and K.G. Miller, (1992), Paleocene to Eocene benthic foraminiferal isotopes and assemblages: implications for deepwater circulation, *Paleoceanography*, Vol. 7, pp. 405-422, doi:10.1029/92PA01234.

Pudsey, C.J., (1992), Late Quaternary changes in Antarctic Bottom Water velocity inferred from sediment grain size in Northern Weddell Sea, *Marine Geology*, Vol. 107, pp. 910, doi:10.1016/0025-3227(92)90066-2.

Quillévéré, F., Aubry, M., Norris, R.D., and W.A. Berggren, (2002), Paleocene oceanography of the eastern subtropical Indian Ocean: An integrated magnetobiostratigraphic and stable isotope study of ODP Hole 761B (Wombat Plateau), *Paleogeography, Paleoclimatology, Paleocecology*, Vol.184, pp. 371-405, doi:10/1016/S0031-0182(02)00275-4.

Scher, H.D., and E.E. Martin, (2004), Circulation in the Southern Ocean during the Paleogene inferred from neodymium isotopes, *Earth and Planetary Science Letters*, Vol. 228, pp. 391-405, doi:10.1016/j.epsl.2004.10.016.

Shackleton, N.J., Imbrie, J., and M.A. Hall, (1983), Oxygen and carbon isotope record of East Pacific core V19-30: implications for the formation of deep water in the late Pleistocene, North Atlantic, *Earth and Planetary Science Letters*, Vol. 65, pp. 233-244, doi:10.1016/0012-821X(83)90162-0.

Shipboard Scientific Party, 1999, Site 1121: the Campbell "Drift," In Carter, R.M., McCave, I.N., Richter, C., Carter, L., et al., *Proceedings of the Ocean Drilling Program, Initial Reports, 181*: College Station, TX (Ocean Drilling Program), pp. 1-62, doi:10.2973/odp.proc.ir.181.104.2000.

Thomas, D., (2004), Evidence for deep-water production in the North Pacific Ocean during the early Cenozoic warm interval, *Nature*, Vol. 430, pp. 65-68, doi:10.1038/nature02639.

Thomas, D.J, Lyle, M., Moore Jr. T.C., and D.K.Rea, (2008), Paleogene deepwater mass composition of the tropical Pacific and implications for thermohaline circulationin a greenhouse world, *Geochemistry, Geophysics, Geosystems*, Vol. 9, Q02002, doi:10.1029/2007GC001748.

Tripati, A., and H. Elderfield, (2005), Deep-sea temperature and circulation changes at the Paleocene-Eocene Thermal Maximum, *Science*, Vol. 308, pp. 1894-1898, doi:10.1126/science.1109202.

Tucholke, B.E., and P.R. Vogt, (1979), Western North Atlantic: sedimentary evolution and aspects of tectonic history, In Tucholke, B.E., Vogt, P.R., et al., *Initial Reports Depp Sea Drilling Program*, 43: Washington, DC, pp. 791-825, doi:10.2973/dsdp.proc.43.140.1979.

Wei, K.Y., Mii, H.S, Shu, I.T., and Y.J Lin, (2005), Uppermost Cretaceous to middle Oligocene carbon and oxygen isotope stratigraphy of Southwest Pacific: Holes 1121B and 1124C, ODP Leg 181, *New Zealand Journal of Geology and Geophysics*, Vol. 48, pp. 15-26, doi:0028-8306/05/4801-0015.

Westerhold, T., Rohl, U., Donner, B., McCarren, H.K., and J.C. Zachos, (2011), A complete high-resolution Paleocene benthic stable isotope record for the central Pacific (ODP Site 1209), *Paleoceanography*, Vol. 26, PA2216 doi:10.1029/2010PA002092

2.6 Appendix

Table 2-A1. Benthic foraminiferal carbon and oxygen stable isotope data from ODP Sites 1121 and 1124 generated from *N. truempyi*.

Sample ID	Depth (mbsf)	Age (Ma)	$\delta^{13}C$	$\delta^{18}O$
ODP Site 1121B				
6X-1 12-14	32.82	57.07	1.78	0.32
6X-1 62-64	33.32	57.08	1.86	0.33
6X-1 110-112	33.8	57.10	1.88	0.69
6X-2 10-12	34.3	57.11	1.74	0.27
6X-2 66-68	34.86	57.12	1.83	0.74
6X-2 110-112	35.3	57.13	1.45	0.63
6X-3 10-12	35.8	57.15	1.7	0.57
6X-CC 7-9	37.08	57.18	1.74	0.45
7X-1 59-61	42.89	57.32	2.29	0.39
7X-1 110-112	43.4	57.34	1.91	0.04
7X-2 10-12	43.9	57.35	2.19	0.33
7X-2 60-62	44.4	57.36	2.23	0.54
7X-2 110-112	44.9	57.37	1.86	0.32
7X-3 10-12	45.4	57.39	1.88	0.13
7X-3 60-62	45.9	57.40	2	0.44
7X-3 110-112	46.4	57.41	1.85	0.34
7X-4 10-12	46.9	57.42	1.77	0.64
7X-4 59-61	47.39	57.43	1.7	0.64
7X-4 110-112	47.9	57.45	1.88	0.74
7X-5 10-12	48.4	57.46	2.09	0.4
7X-5 60-62	48.9	57.47	1.66	0.37
7X-5 110-112	49.4	57.49	1.89	0.09
7X-6 10-12	49.9	57.50	2.04	0.6
7X-6 59-61	50.39	57.51	1.51	0.09
8X-1 10-12	52.1	57.55	1.78	0.48
8X-1 60-62	52.6	57.57	0.99	0.21
8X-1 110-112	53.1	57.58	1.41	0.72
8X-2 10-12	53.6	57.59	1.93	0.48
8X-2 60-62	54.1	57.60	1.79	0.64
8X-2 110-112	54.6	57.62	1.41	0.01
8X-3 10-12	55.1	57.63	1.85	0.34
8X-3 60-62	55.6	57.64	2.05	0.69
8X-4 10-12	56.6	57.67	1.3	0.59
8X-4 60-62	57.1	57.68	1.2	0.54
8X-5 10-12	58.1	57.70	1.51	0.66
8X-6 10-12	59.45	57.74	1.85	0.18
8X-6 60-62	59.95	57.75	1.78	0.17
8X-6 110-112	60.45	57.76	1.92	0.34

Table 2-A1, Continued.

Sample ID	Depth (mbsf)	Age (Ma)	$\delta^{13}C$	$\delta^{18}O$
9X-1 10-12	61.7	57.79	1.81	0.21
9X-1 59-61	62.19	57.80	1.78	0.21
9X-1 110-112	62.7	57.82	1.93	0.27
9X-2 10-12	63.2	57.83	1.86	0.29
9X-2 60-62	63.7	57.84	1.78	0.34
9X-2 110-112	64.2	57.86	1.78	0.13
9X-3 10-12	64.7	57.87	1.71	0.17
9X-3 60-62	65.2	57.88	1.77	0.21
9X-3 110-112	65.7	57.89	1.69	0.26
9X-4 10-12	66.2	57.91	1.63	0.00
9X-4 60-62	66.7	57.92	1.47	0.02
9X-4 110-112	67.2	57.93	1.75	0.19
9X-5 10-12	67.7	57.94	1.63	0.23
9X-5 60-62	68.2	57.96	1.65	0.10
9X-5 110-112	68.7	57.97	1.66	0.04
9X-6 10-12	69.2	57.98	1.50	0.22
9X-6 60-62	69.7	57.99	1.87	0.17
9X-6 110-112	70.2	58.01	1.50	0.04
9X-CC 10-12	71.13	58.03	1.58	-0.03
10X-1 10-12	71.3	58.03	1.74	0.34
10X-1 60-62	71.8	58.05	1.74	0.32
10X-2 10-12	72.8	58.07	1.73	0.40
10X-2 60-62	73.3	58.08	1.45	0.23
10X-3 110-112	75.3	58.13	1.77	0.45
10X-4 10-12	75.59	58.14	1.81	0.39
10X-4 60-62	76.09	58.15	1.43	0.41
11X-1 10-12	81	58.28	1.97	0.04
11X-1 60-62	81.5	58.29	2.07	0.16
11X-1 110-112	82	58.30	1.42	-0.36
11X-2 10-12	82.5	58.31	2.04	0.37
11X-2 60-62	83	58.33	1.64	-0.1
11X-2 112-114	83.52	58.34	1.56	0.06
11X-3 10-12	84	58.35	1.53	0.54
11X-3 64-66	84.54	58.36	1.63	-0.11
11X-3 116-118	85.06	58.38	1.36	-0.05
11X-4 10-12	85.5	58.39	1.47	0.14
11X-4 60-62	86	58.40	1.87	0.21
11X-4 110-112	86.5	58.41	1.49	-0.02
11X-5 12-14	87.02	58.43	1.27	0.12
12X-1 110-112	91.6	58.54	0.43	0.31
12X-2 10-12	92.1	58.55	0.08	0.53
12X-2 60-62	92.6	58.57	1.34	-0.09
12X-2 110-112	93.1	58.58	1.3	0.04

Table 2-A1, Continued.

Sample ID	Depth (mbsf)	Age (Ma)	$\delta^{13}C$	$\delta^{18}O$
12X-3 12-14	93.62	58.59	0.91	-0.04
12X-3 60-62	94.1	58.87	1.23	-0.39
14X-CC 17-19	109.87	59.49	1.91	0.23
15X-1 115-117	120.55	59.91	1.61	-0.17
15X-2 10-12	121	59.93	2.03	0.2
15X-2 57-59	121.47	59.94	1.4	-0.38
15X-2 110-112	122	59.96	0.83	0.05
15X-CC 10-12	122.14	59.97	1.66	-0.52
16X-1 14-16	126.14	60.13	1.62	0.04
16X-1 60-62	126.6	60.14	1.47	-0.43
16X-1 106-108	127.06	60.16	1.62	-0.22
17X-1 10-12	130.1	60.28	1.32	0.27
17X-1 62-64	130.62	60.30	1.28	0.27
17X-2 10-12	131.6	60.34	1.41	0.1
17X-2 60-62	132.1	60.36	1.18	-0.34
17X-2 112-114	132.62	60.38	1.29	-0.72
ODP Site 1124C				
45X-1 10-12	429.1	58.37	1.31	0.1
45X-1 64-66	429.64	58.43	1.79	0.35
45X-1 114-116	430.14	58.48	1.6	0.38
45X-2 11-13	430.61	58.53	2.05	0.32
45X-2 68-70	431.18	58.59	2.05	0.48
45X-2 115-117	431.65	58.64	2.18	0.62
45X-3 12-14	432.12	58.70	2.15	0.53
45X-3 66-68	432.66	58.75	1.61	-0.19
45X-3 114-116	433.14	58.80	1.46	-0.16
45X-4 10-12	433.6	58.85	1.92	0.55
45X-4 60-62	434.1	58.91	1.93	0.55
45X-4 112-114	434.62	58.96	1.9	0.43
45X-5 15-17	435.15	59.02	2.01	0.45
45X-5 63-65	435.63	59.07	1.74	0.34
45X-5 114-118	436.14	59.13	1.69	0.31
45X-6 12-14	436.62	59.18	1.98	0.34
45X-6 63-65	437.13	59.23	1.36	0.38
45X-6 113-115	437.63	59.29	1.45	0.3
45X-7 14-16	438.14	59.34	1.59	0.27
45X-CC 12-14	438.59	59.39	1.35	0.2
46X-1 9-11	438.79	59.41	1.54	0.13
46X-1 60-62	439.3	59.47	1.36	0.19
46X-1 110-112	439.8	59.52	1.47	0.21
46X-2 10-12	440.3	59.57	1.6	0.45
46X-2 57-59	440.77	59.63	1.19	-0.02
46X-2 107-109	441.27	59.68	1.32	0.28

Table 2-A1, Continued.

Sample ID	Depth (mbsf)	Age (Ma)	$\delta^{13}C$	$\delta^{18}O$
46X-3 10-12	441.8	59.74	1.27	0.19
46X-3 64-66	442.34	59.79	1.28	0.28
46X-3 113-115	442.83	59.85	1.31	0.29
46X-4 10-12	443.3	59.90	1.25	0.2
46X-4 63-65	443.83	59.95	1.42	0.23
46X-4 110-112	444.3	60.00	1.46	-0.17
46X-5 10-12	444.8	60.06	1.56	-0.24
46X-5 60-62	445.3	60.11	1.71	0.08
46X-CC 16-18	445.7	60.16	1.23	0.09
47X-1 10-12	448.4	63.16	1.61	-0.07
47X-1 60-62	448.9	63.22	1.68	0.04
47X-1 109-111	449.39	63.28	1.34	0.38
47X-2 10-12	449.9	63.34	1.65	0
47X-2 60-62	450.4	63.40	1.58	0.13
47X-2 110-112	450.9	63.46	1.56	0.03
47X-3 14-16	451.44	63.52	1.37	-0.11
47X-3 62-64	451.92	63.58	1.5	-0.2
47X-3 108-110	452.38	63.64	1.36	-0.18
47X-4 8-10	452.88	63.69	1.41	-0.1
47X-4 64-66	453.44	63.76	1.36	-0.32
47X-4 110-112	453.9	63.82	1.49	-0.14
47X-5 14-16	454.44	63.88	1.7	0.11
47X-5 56-58	454.86	63.93	1.7	0
47X-5 110-112	455.4	63.99	1.7	-0.14
47X-6 10-12	455.9	64.05	1.73	0.05
47X-6 60-62	456.4	64.11	1.83	-0.03
48X-1 10-12	458	64.30	1.58	-0.26
48X-1 60-62	458.5	64.36	1.38	-0.21
48X-1 118-120	459.08	64.43	1.77	-0.05
48X-2 6-8	459.46	64.48	1.66	-0.09
48X-2 60-62	460	64.54	1.72	-0.14
48X-2 110-112	460.5	64.60	1.65	-0.3
48X-3 10-12	461	64.66	1.83	-0.05
48X-3 60-62	461.5	64.72	1.58	-0.25
48X-3 110-112	462	64.78	1.44	-0.21
48X-4 14-16	462.54	64.84	1.56	-0.05
48X-4 74-76	463.14	64.92	1.33	-0.22

Table 2-A2. Tie points used to construct age models for Paleocene stable isotope compilation (Figure 2-3).

Age Models		
Datum	**Depth**	**Age**
ODP Site 1121 (from [1]Carter et al, 1999; [2]Hollis et al., 2002)		
FAD Heliolithus riedeli[1]	35.74	57.30
FAD Pterocodon poculum[2]	36.9	57.60
FAD Aspis velutochlamydosaurus[2]	75.4	58.40
FAD Heliolithus kleinpelli[1]	82.05	58.40
FAD Sethochytris babylonis[2]	93.8	59.00
FAD Plectodiscus circularis[2]	93.8	59.00
FAD Buryella pentadica[2]	93.8	59.00
FAD Cassideus aff. mariae[2]	93.8	59.50
FAD Fasciculithus tympaniformis[1]	115.26	59.70
FAD Fasciculithus ulii[1]	134.42	59.90
FAD Chiasmolithus bidens[1]	134.42	60.70
FAD Buryella tetradica tetradica[2]	121.4	61.00
FAD Buryella foremanae[2]	134.42	63.00
FAD Chiasmolithus danicus[1]	134.42	63.80
FAD Buryella granulata[2]	134.42	64.20
ODP Site 1124 (from Carter et al., 1999)		
LAD Gavelinella beccariiformis	429.1	55.00
LAD Hornibrookina teuriensis	429.28	58.30
FAD Fasciculithus tympaniformis	442.2	59.70
FAD Chiasmolithus bidens	438.62	60.70
LAD Aragonia ouezzanensis	438.7	55.00
FAD Morozovella conicotruncata	438.7	60.90
FAD Morozovella angulata	438.7	61.00
FAD Morozovella praecursoria	438.7	61.20
FAD Morozovella trinidadensis	438.7	63.00
FAD Sphenolithus primus	445.83	60.60
FAD Cruciplacolithus tenuis	460.39	64.50
FAD Globbanomalina compresa	457.6	63.50
LAD Globoconusa daubjergensis	457.6	63.00
LAD Globigerina fringa	457.6	63.00
FAD Hornibrookina teuriensis	463.32	64.90
ODP Site 1209 (from Bralower, 2005)		
PETM (peak)	217.99	55.50
FAD Discoaster multiradiatus	228.05	56.30
FAD Discoaster mohleri	233.719	57.50
FAD Heliolithus kleinpellii	236.485	58.40
FAD Sphenolithus anarrhopus	236.485	58.40
FAD Fasciculithus tympaniformis	244.01	59.70
FAD Fasciculithus spp.	245.015	59.90

Table 2-A2, Continued.

Datum	Depth	Age
FAD Chiasmolithus bidens	246.853	60.70
FAD Sphenolithus primus	250.596	60.60
FAD Ellipsolithus macellus	253.558	62.20
FAD Chiasmolithus danicus	256.719	63.80
FAD Cruciplacolithus tenuis	260.785	64.50
K/T boundary	261.86	65.00
ODP Site 761 (from Quillevere et al., 2002)		
FAD Morozovella subbotinae	125.5	55.90
LAD Globanomalina pseudomendardii	125.5	55.90
Chron C25n/C25r	128	56.39
LCO Acarinina subsphaerica	130.3	57.10
FAD Heliolithus riedelii	132.445	57.30
FAD Discoaster mohleri	134	57.50
FAD Heliolithus kleinpelli	140.475	58.40
FAD Acarinina subsphaerica	148.25	59.20
FAD Fasciculithus tympaniformis	155.5	59.70
FAD Igorina albeari	158.75	60.00
FAD Sphenolithus primus	162.75	60.60
FAD Igorina pusilla	162.95	61.00
FAD Morozovella angulata	162.95	61.00
ODP Site 761 (from Quillevere et al., 2002)		
FAD Praemurica uncinata	165.5	61.20
Chron C27n/C27r	166.05	61.27
FAD Ellipsolithus macellus	167	62.20
Chron C27r/C28n	171.025	62.49
FAD Praemurica inconstans	173.75	63.00
Chron C28n/C28r	175.455	63.63
FAD Chiasmolithus danicus	176.01	63.80
ODP Site 690 (from Quillevere et al., 2002)		
FAD Tribrachiatus bramlettei	148.9	55.00
PETM (peak)	170.65	55.50
Chron C24r/C25n	185.475	55.90
FAD Discoaster multiradiatus	185.8	56.20
Chron C25n/C25r	195.94	56.39
FAD Discoaster nobilis	192.25	56.90
FAD Heliolithus riedelli	198.35	57.30
FAD Discoaster mohleri	205.24	57.50
ODP Site 738 (from Huber, 1991; Wei and Thierstein, 1991)		
FAD Discoaster sublodoensis	227.03	49.70
FAD Acarinina pentacamerata	259.7	52.30
FAD Discoaster lodoensis	264.43	52.85
FAD Morozovella gracilis	285.3	54.70
FAD Discoaster multiradiatus	302.65	56.20

Table 2-A2, Continued.

Datum	Depth	Age
FAD Discoaster mohleri	326.75	57.50
FAD Heliolithus kleinpellii	334.95	58.40
FAD Acarinina mckannai	337.75	59.10
FAD Chiasmolithus bidens	351.5	60.70
FAD Prinsius martinii	360.68	62.20
FAD Chiasmolithus danicus	364.6	63.80
FAD Cruciplacolithus tenuis	376.39	64.50
FAD Biantholithus sparsus	377.16	65.00
DSDP 527 (from [1]Boersma, 1984; [2]Shackleton et al., 1984)		
FAD Nannotetrina fulgens	146.02	43.10
FAD Discoaster sublodoensis[2]	152.74	49.70
LAD Tribrachiatus orthostylus	160.34	50.60
FAD Discoaster lodoensis	170.5	52.85
FAD Tribrachiatus orthostylus	182.34	53.64
DSDP 527 (from [1]Boersma, 1984; [2]Shackleton et al., 1984)		
LAD Tribrachiatus contortus	182.34	54.17
FAD Tribrachiatus contortus	189	54.37
PETM	201.07	55.50
FAD Discoaster multiradiatus	220.75	56.20
FAD Heliolitus riedeli	231.96	57.30
FAD Discoaster mohleri	235.08	57.50
FAD H. kleinpelli	245.43	58.40
FAD Fasciculithus tympaniformis	249.78	59.70
FAD Morozovella conicotruncata[1]	258.5	60.90
FAD Morozovella pusilla pusilla[1]	258.5	61.00
FAD Chiasmolithus danicus	271.1	63.80
FAD Cruciplacolithus tenuis	276.19	64.50
FAD Planorotalites eugubinus[1]	279.9	64.70
K/T boundary	280.02	65.00
DSDP 525 (from Boersma, 1984; Shackleton et al., 1984)		
FAD Tribrachiatus contortus	387.84	54.37
PETM	392.81	55.50
FAD Discoaster multiradiatus	401.88	56.20
FAD Heliolithus riedeli	413.13	57.30
FAD Discoaster mohleri	419.63	57.50
FAD Heliolithus kleinpellii	428.35	58.40
FAD Fasciculithus tympaniformis	433.95	59.70
FAD Cruciplacolithus tenuis	449.3	64.50
ODP Site 384 (from Berggren et al., 2000		
FAD Discoaster multiradiatus	100.75	56.20
FAD Discoaster okadai	109.61	56.80

Table 2-A2, Continued.

Datum	Depth	Age
FAD Discoaster nobilis	109.61	56.90
FAD Heliolithus riedeli	120.58	57.30
FAD Discoaster mohleri	122.68	57.50
FAD Sphenolithus anarrhopus	126.04	58.40
FAD Heliolithus kleinpelli	127.16	58.40
FAD Chiasmolithus consuetus	138.94	59.70
FAD Fasciculithus tympaniformis	138.94	59.70
FAD Sphenolithus primus	146.02	60.60
FAD Fasciculithus ulii	146.92	59.90
FAD Ellipsolithus macellus	157.26	62.20
FAD Chiasmolithus danicus	163.59	63.80

CHAPTER 3

Comparison of Hyperthermal Events from the Late Paleocene to the Early-Middle Eocene: Is there a Common Link?

Multiple hyperthermals, or abrupt warming events, occur through the late Paleocene to early Eocene (~57.5-53 Ma). The largest of these events is the Paleocene-Eocene Thermal Maximum (PETM, ~56 Ma). While most studies assume that this regular sequence of hyperthermals terminated with the Early Eocene Climatic Optimum, there is also evidence for small, regularly paced hyperthermal events in the early-middle Eocene (~50-47.5 Ma). Here, we provide the first multi-site stable isotope records of these early-middle Eocene hyperthermals that demonstrate that they are global events similar to those from the late Paleocene-early Eocene. We also provide a detailed comparison of the structure of individual hyperthermal events to demonstrate that it is possible to identify hyperthermals through a statistical assessment of their departure from background variability rather than through a qualitative description of common features. Our detailed comparison suggests that not all named hyperthermals from the late Paleocene through early-middle Eocene represent major global anomalies in the carbon cycle and climate. We assess causes for inter-site variability in order to demonstrate how site-specific environmental characteristics generate heterogeneity in the apparent size and duration of events. Finally, we suggest how a common mechanism may explain orbital pacing of carbon release during both the late Paleocene-early Eocene hyperthermals and the early-middle Eocene events.

3.1 Introduction

Bracketing the massive warming of the PETM, multiple studies have recorded a ~4.4 million year sequence of quasi-regularly paced 'hyperthermal' events, or brief episodes of intense global warming during the Early Eocene, ending with the late Early Eocene Climatic Optimum (EECO, 51-53 Ma) (Zachos et al., 2010; Galeotti et al., 2010; Westerhold et al., 2009; Westerhold et al., 2007; Niccolo et al, 2007; Lourens et al., 2005; Cramer et al., 2003). During these hyperthermal events, warming correlates with abrupt negative carbon isotope excursions and carbonate dissolution horizons, suggesting the release of large quantities of isotopically light carbon to the oceans and atmosphere during relatively rapid ($<10^4$ years) intervals. As global temperatures rise from the late Paleocene through the early Eocene, there is a trend after the PETM towards smaller, more closely spaced events (Zachos et al., 2010; Lunt et al., 2011). The quasi-periodic occurrence of these events, coupled with their generally decreasing size, has led to proposals that hyperthermals (possibly excepting the PETM) were driven by repeated, orbitally-forced releases of carbon from a perturbable reservoir (such as methane hydrates, peat, or permafrost) (Lunt et al., 2011; Zachos et al, 2010; DeConto et al., 2012). Under this scenario, rising temperatures might account for the depletion of the buried carbon reservoirs by the height of the EECO, resulting in the end of the hyperthermal sequence.

Recently, Sexton et al., 2011, has shown that regular hyperthermal events are not confined to the Early Eocene interval bracketing the PETM. Using a

record from the equatorial Atlantic (Demerara Rise, ODP Site 1258) spanning the middle Eocene interval 50-47.6 Ma, Sexton et al., 2011, found the repeat occurrence of 13 rapid, brief carbon isotope excursions (CIEs), which appear to correlate with warming of 2-4°C and decreases in carbonate preservation at Demerara Rise (Sexton et al., 2011). Decreases in carbonate preservation at two other sites in the southern Atlantic and central Pacific (Walvis Ridge, ODP Site 1267 and Shatsky Rise, ODP Site 1210) appear to correlate with the $\delta^{13}C$ excursions identified from Demerara, suggesting that events are global. Spacing of 100-400 kyr between $\delta^{13}C$ events raised the possibility of orbital pacing (Sexton et al., 2011). The Demerara benthic isotope record represents the only complete isotopic record from this interval of comparable resolution to those that record the PETM-bracketing sequence in the early Eocene. Mirroring that succession, the events of Sexton et al., 2011, occur at the onset of long-term global cooling following the end of the EECO, with cooling of roughly 5°C over the entire 2.4-myr record (Figure 3-1). As a result, these events raise the possibility that the common mechanism responsible for the early Eocene hyperthermals continued to operate (or re-started) following the height of early Eocene warmth.

The primary difficulty in attempting to determine the frequency of these events, and the total duration of the interval over which the inferred carbon-release mechanism operated, is that some perturbations are difficult to distinguish from background variability. Given differences in the amplitude of this background variability (or even the difficulty of defining background variability)

among different sites, simply identifying 'hyperthermals' is a non-trivial exercise. As a result, not all sites that record the late Paleocene to early-middle Eocene show clear evidence of the same number of hyperthermals, and this is not always a function of obvious stratigraphic gaps in such records. It is necessary to both clarify the total number of hyperthermals that occurred over this interval and obtain a good estimate of their true magnitude in order to determine if periodic

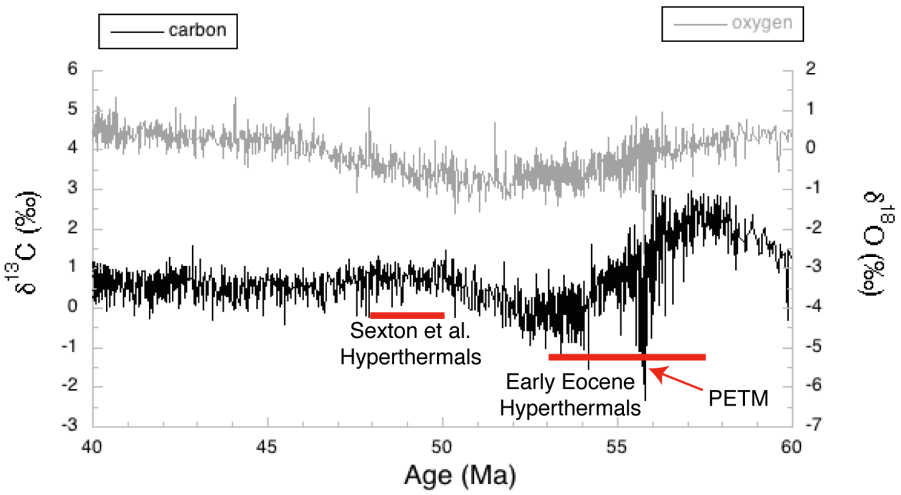


Figure 3-1. Long-term climatic context of the events discussed in this paper. Benthic foraminiferal $\delta^{13}C$ and $\delta^{18}O$ compilation is from Cramer et al., 2009. Red lines indicate the time intervals of the A-L events identified from the early Eocene and the C22r-C21r events of the early-middle Eocene. The largest hyperthermal, the PETM, is indicated by an arrow**.**

orbital forcing triggered events and to provide constraints on the rate of recharge and total mass of potential carbon reservoirs.

Here, we assess multi-site deep-sea records of the hyperthermals bracketing the PETM (Events A-L following the Cramer et al., 2003, terminology)

as well as the 13 events from the early-middle Eocene (Chron 22r-Chron 21r) identified by Sexton et al., 2011. For each postulated event, excluding the PETM, we compare the event's apparent structure (particularly the magnitude and duration) from bulk carbonate and benthic foraminiferal stable isotope records at each site. We also assess the relative size of these events compared to background variability from each site for the longer-term interval. We use bulk carbonate and benthic stable isotope records from the following sites: ODP 1262 (Stap et al., 2009; Stap et al., 2010; Zachos et al., 2010), ODP 1263 (Stap et al., 2009; Stap et al., 2010), ODP 1265 (Stap et al., 2009; Stap et al., 2010a; Stap et al., 2010b), ODP 1267 (Stap et al., 2009; this study), ODP 1051 (Cramer et al., 2003), DSDP 550 (Cramer et al., 2003), DSDP 577 (Cramer et al., 2003), ODP 690 (Cramer et al., 2003; Stap et al., 2010), ODP 1258 (Sexton et al., 2011; this study), and ODP 1210 (this study). Although some events have also been identified from shallow water or restricted basin sections, we exclude these records here and consider only deep-sea (>1500 m paleodepth) sites (e.g. Niccolo et al., 2007; Galeotti et al., 2010). These deep-sea sites have the greatest completeness for records of the Paleocene-Eocene and are most often used in the identification of hyperthermal events.

In order to assess the hyperthermals identified by Sexton et al., 2011, we have developed very high-resolution (3 kyr or less) bulk carbonate stable isotope ($\delta^{13}C$ and $\delta^{18}O$) records across five of the largest events identified from the Demerara benthic isotope record from ODP Sites 1258, 1267, and 1210. We

have also generated preliminary benthic stable isotope data from a few events at ODP Sites 1210 and 1267. We will use results from these high-resolution datasets to comment on the remaining eight hyperthermal events identified only from benthic foraminifera at Demerara Rise.

Our results demonstrate the large influence of inter-site variability on records of hyperthermal events. We compare details of the magnitude and duration of recorded hyperthermals with site characteristics (paleodepth, wt% $CaCO_3$, and sedimentation rate) in order to assess factors controlling inter-site variability. We suggest additional factors that may explain large differences in the relative magnitude and duration of events between sites, including discrepancies in age models, deep ocean circulation patterns, changes in the carbonate compensation depth (CCD), and orbital effects. In particular, we note the difficulty in identifying hyperthermal events from a single site. Finally, we discuss the carbon cycle and climate implications of the long-term series of hyperthermals bracketing the PETM, including the early-middle Eocene hyperthermals typically excluded from such consideration.

3.2 Methods

To assess multiple hyperthermal events from the late Paleocene through early-middle Eocene, we compiled records of the A-L hyperthermals from deep-sea sites. For each site where a given event has been identified, we assess the magnitude and duration of the carbon isotope excursion and the magnitude of the

oxygen isotope excursion (if apparent). We use age models from the original studies for each record. We calculate the magnitude of each carbon isotope excursion by the difference between the most positive point at the start of an event (oldest material) after which values begin to decline and the point at which minimum value are recorded. We calculate duration by the difference between the identified starting point and the point at which $\delta^{13}C$ returns to values approximately as positive as the starting point. These calculations are somewhat subjective, but different choices for the starting/ending points would not change calculations of the magnitude and duration by more than a few hundredths of a per mil or a few thousand years, respectively.

To compare multi-site expression of the hyperthermals from Sexton et al., 2011, we selected 5 prominent hyperthermal events from the Demerara Rise, ODP 1258, benthic isotope record for high-resolution analysis (C22rH2, C22nH2, C22nH3, C21rH1, and C21rH5). Our criteria were that: 1) events have coincident minima in $\delta^{13}C$ and $\delta^{18}O$, 2) more than one data point marks the excursion event, and 3) $\delta^{13}C$ excursions are of a large magnitude relative to others in the record (approaching 1.0 ‰). In order to determine correlative intervals to analyze at additional sites, we used estimated wt% $CaCO_3$ records from Sites 1210 and 1267 plotted on a common age model, developed by hanging each record on the Last Appearance Datum (LAD) of *Discoaster lodoensis*. We also tuned clear, correlatable events in the Site 1210 and 1267 estimated wt% $CaCO_3$ records to the astronomically calibrated estimated wt% $CaCO_3$ record from ODP Site 1258

(Sexton et al., 2011). Each interval selected for analysis at Sites 1210 and 1267 corresponded to a distinct decrease in estimated wt% $CaCO_3$. Sexton et al., 2011, used a minimum number of tie points during the tuning process, so we analyzed samples from intervals at Sites 1210 and 1267 that bracketed each entire wt% $CaCO_3$ decrease, even if this meant that the assigned ages for the selected interval at each site differed slightly (Figure 3-2).

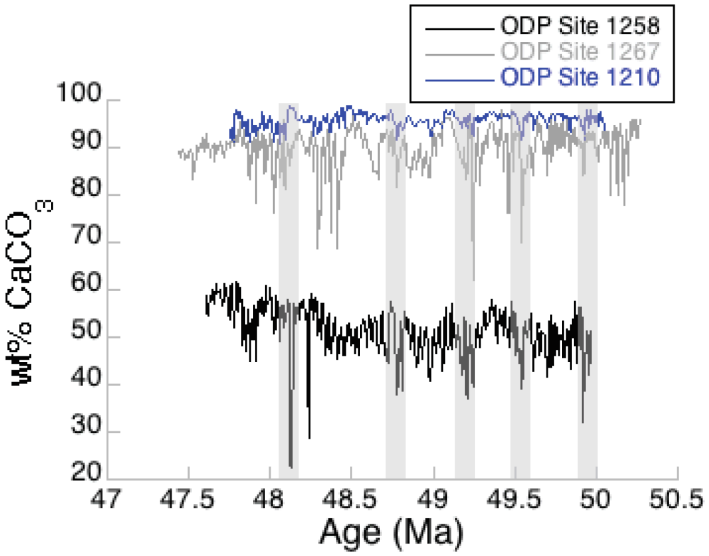


Figure 3-2. Records of estimated wt% $CaCO_3$ from ODP Sites 1258, 1267, and 1210 (after Sexton et al., 2011). Inter-site correlations for these three sites were developed based on the common occurrence of the LAD of *D. lodoensis* and further tuned using features of the wt% $CaCO_3$ records common to all three sites. Grey bars indicate the 5 events selected for high-resolution analysis.

We generated stable carbon and oxygen isotope measurements from bulk sediment samples collected at 1-cm spacing across each of the 5 events at Sites 1258, 1267, and 1210 (total of 1,181 samples) using an automated common acid bath carbonate preparation device attached to a Finnigan MAT 252 Mass

Spectrometer at Scripps Institution of Oceanography. Replicate analysis of an in-house standard (n=916) over the period of time when samples were run yielded machine error of 0.08 ‰ for $\delta^{18}O$ and 0.07 ‰ for $\delta^{13}C$. Benthic foraminiferal stable isotope data for ODP Sites 1210 and 1267 was generated at the National Oceanography Centre, University of Southampton, U.K., using a Europa Geo 20-20 mass spectrometer equipped with an automatic carbonate preparation system. For each sample, between 10-15 mono-specific samples (*Nuttalides truempyi* or *Oridorsalis umbonatus*) were analyzed. External analytical precision, based on replicate analyses of in-house standards calibrated to NBS-19, is better than ±0.1‰ for $\delta^{18}O$ and $\delta^{13}C$. All data are reported relative to the Vienna Peedee Belemnite standard (VPDB). For reporting *O. umbonatus* data, these are first corrected to *N. truempyi* by the correction factors of Katz et al., 2003, i.e. adding 0.47‰ for carbon isotope data and subtracting 0.36‰ for oxygen isotope data. (For complete bulk datasets, see Appendix, Table A1).

In order to analyze available isotope data in the context of local environmental characteristics, we have also assembled relevant parameters describing each site (Table 1). We report both sedimentation rate and wt% $CaCO_3$ as averages from long-term records at each site rather than determining them separately for each event. Detailed wt% $CaCO_3$ records are available only from ODP Sites 1210, 1258, 1262, 1263, 1265, and 1267 for Events H1, H2, and the middle-Eocene events of Sexton et al., 2011.

Table 3-1. Summary of site characteristics for all the sites used to obtain stable isotope data considered in this study.

Site	Location	Events Recorded	Paleodepth	Sedimentation Rate	wt% $CaCO_3$	Source
DSDP 550	North Atlantic	C1, C2, D1, D2, E1, F, H1, H2, I1, I2, J, K, L	4300 m	2.3 cm/kyr	30-60 % (avg. 45%)	DSDP Initial Reports Vol. 80
DSDP 577	Central Pacific	A, B1, B2, C1, C2, D1, F, H1, H2, I1, I2, J, K	2500 m	0.27 cm/kyr	~90%	DSDP Initial Reports Vol. 86
ODP 1051A	North Atlantic	A, B1, B2, C1, C2, D1, G, H1, H2, I1, I2, J	2300 m	2.7 cm/kyr	37-72% (avg. 52%)	ODP Initial Reports Vol. 171B
ODP 1051B	North Atlantic	C1, C2, D1, D2, E1, E2, F, G	2300 m	3.1 cm/kyr	37-72% (avg. 52%)	ODP Initial Reports Vol. 171B
ODP 690	South Atlantic	A, B1, B2, C1, C2, D1, D2, E1, E2, F, G, H1	2000 m	2.4 cm/kyr	60-90%	ODP Initial Reports Vol. 113
ODP 1262	South Atlantic	B1, B2, C1, C2, D1, D2, E1, E2, F, H1, H2, I1, I2, J	3600 m	1.2 cm/kyr	85%	Stap et al., 2009; Zachos et al., 2005; Zachos et al., 2010
ODP 1263	South Atlantic	H1, H2	1500 m	1.7 cm/kyr	93%	Stap et al., 2009; Zachos et al., 2005
ODP 1265	South Atlantic	H1, H2	2000 m	1.6 cm/kyr	92%	Stap et al., 2009; Zachos et al., 2005

Table 3-1, Continued.

Site	Location	Events Recorded	Paleodepth	Sedimentation Rate	wt% $CaCO_3$	Source
ODP 1267 (early Eocene)	South Atlantic	H1, H2	3000 m	1.1 cm/kyr	92%	Stap et al., 2009; Zachos et al., 2005
ODP 1267 (middle Eocene)	South Atlantic	C22rH2, C22nH2, C22nH3, C21rH1, C21rH5	3000 m	0.6 cm/kyr	90%	ODP Initial Reports Vol. 208; Sexton et al., 2011
ODP 1258	Central Atlantic	C22rH1, C22rH2, C22rH3, C22nH1, C22nH2, C22nH3, C22nH4, C21rH1, C21rH2, C21rH3, C21rH4, C21rH5, C21rH6	3000 m	0.8 cm/kyr	51%	Sexton et al., 2006
ODP 1210	Central Pacific	C22rH2, C22nH2, C22nH3, C21rH1, C21rH5	2000 m	0.7 cm/kyr	96%	ODP Initial Reports Vol. 198; Sexton et al., 2011

3.3 Results

Bulk carbonate stable isotope records have been used extensively to identify the existence of hyperthermal events (i.e. Cramer et al., 2003; Lourens et al., 2005; Stap et al., 2009; Zachos et al., 2010). Benthic foraminiferal records

are comparatively rare for the smaller hyperthermal events of the early Eocene—aside from the PETM, the only benthic foraminiferal records are for Events H1 (also known as Elmo, Eocene Thermal Maximum-2, or ETM2) and H2. Figure 3-3 shows the magnitude and duration of hyperthermals identified from high-resolution bulk carbonate stable isotope data. There is no correlation between size and duration for these events. All events except for H1 are smaller in magnitude than 1‰, and all events are between 20-200 kyr in duration. Inter-site variability (indicated by the ±1σ error bars from the mean of all available records for each event) is large relative to the size of the recorded CIEs. The average CIE size is 0.48‰ and the average 1σ is 0.14‰. The amount of variability in the

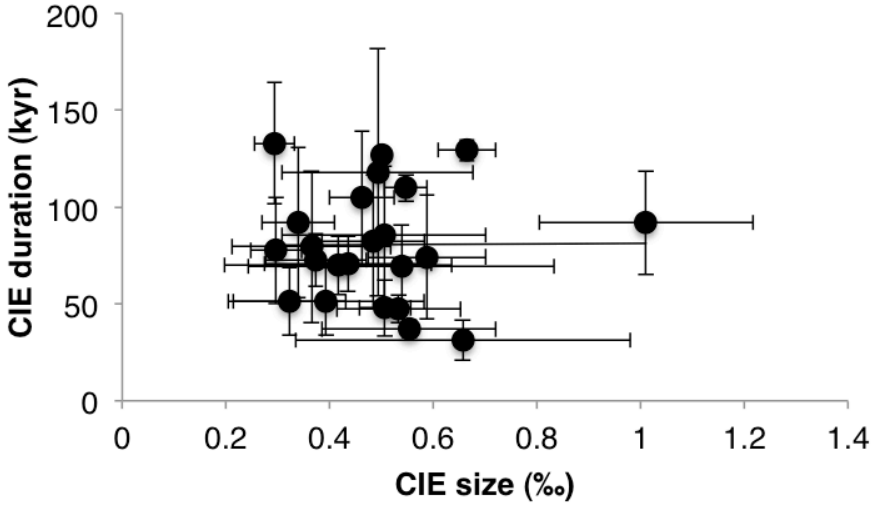


Figure 3-3. CIE size (‰) plotted against CIE duration (kyr) determined from bulk carbonate stable isotope data for Events A-L, C22rH2, C22nH2, C22nH3, C21rH1, and C21rH5. Error bars are ±1σ determined from all deep-sea expressions of each event. The single event with a mean CIE size greater than 1‰ is the H1 (Elmo) event.

duration of each event across all available sites is similarly large; average duration is 79 kyr with an average 1σ of 23 kyr. From this plot, Elmo appears an outlier compared to the other events.

Hyperthermals are typically assumed to represent increased greenhouse gas loading in the atmosphere and oceans—driving warming as well as carbonate dissolution. To assess the relationship between the amount of warming and the size of the carbon cycle perturbation, we compare $\delta^{18}O$ excursions and $\delta^{13}C$ excursions from bulk carbonate (Figure 3-4). Bulk carbonate $\delta^{18}O$ excursions predominantly reflect the temperature history of some relatively undefined portion of the water column—most likely the upper ocean recorded in calcareous nannofossils—so we cannot directly convert these excursions to temperature changes. Further, the oxygen isotope fractionation in the formation of carbonate is more complicated than carbon isotope fractionation because oxygen is also exchanged with the ocean water in addition to the dissolved carbon species (Zeebe, 2007).

However, there is a weakly positive correlation between the magnitude of excursions in $\delta^{18}O$ and $\delta^{13}C$ for each event recorded at each site. Bulk carbonate $\delta^{18}O$ datasets show less variability than $\delta^{13}C$ datasets (based on 1σ calculated from long-term records), and oxygen isotope excursions are typically smaller than carbon isotope excursions (slope of best fit line line <1 in Figure 3-4), suggesting that bulk carbonate $\delta^{18}O$ is a less sensitive recorder of environmental changes in the water column. Other workers have suggested that $\delta^{18}O$ records are more

often compromised by diagenesis compared to $\delta^{13}C$ records, so bulk carbonate $\delta^{18}O$ are often relatively neglected in studies identifying hyperthermals (Cramer et al., 2003, Zachos et al., 2010, Galeotti et al., 2010). We find it is not uncommon for $\delta^{18}O$ to fail to record evidence of an excursion identified from $\delta^{13}C$ data. Out of the 95 records of the early-middle Eocene CIEs included in Figure 3-3, 22 show no clear $\delta^{18}O$ excursion corresponding with the identified CIE.

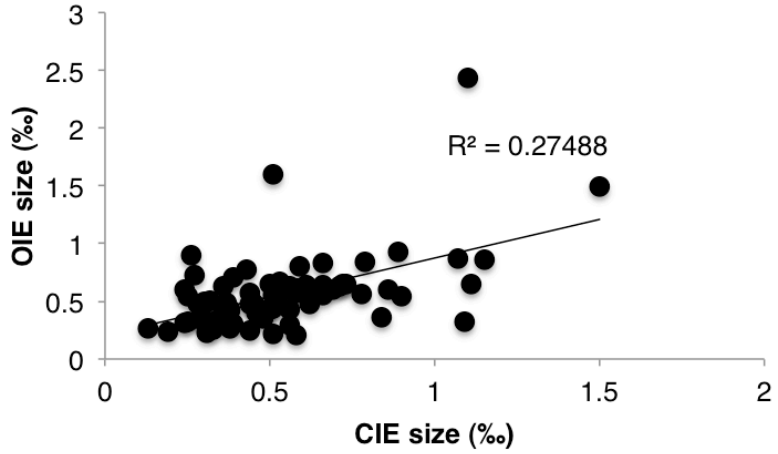


Figure 3-4. Bulk carbonate CIE size (‰) plotted against bulk carbonate OIE (oxygen isotope excursion) size (‰).

While there are comparatively few benthic foraminiferal records for each event, these records are more reliable indicators of water chemistry than bulk datasets, 1) because the benthic foraminifer records indicate the chemistry of a specified portion of the water column (i.e. the sediment-water interface) and 2) mono-specific records mean there is a consistent offset from equilibrium fractionation of carbonate from seawater. With bulk records, it is impossible to

verify the precise composition of nannofossils that make up an individual sample or to understand how changing populations may affect the record. The goal in all these samples (both bulk and benthic) is to approximate changes in the isotopic composition of dissolved inorganic carbon—benthic foraminifera are arguably the most useful tracers for such an approximation (e.g. Zachos et al., 2001).

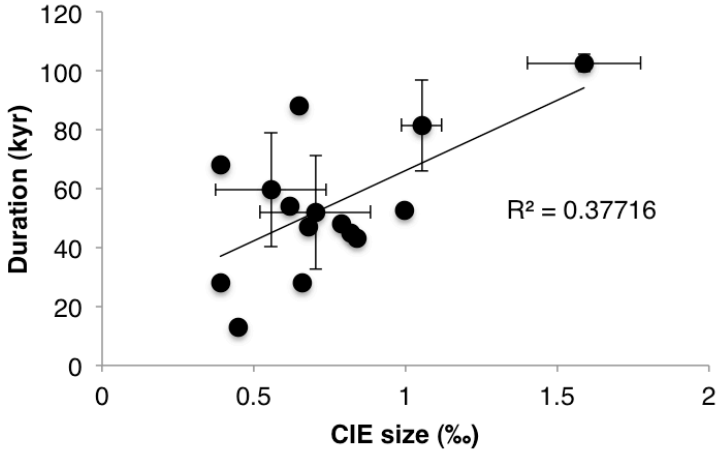


Figure 3-5. CIE size (‰) plotted against CIE duration (kyr) determined from benthic foraminiferal stable isotope data for Events H1, H2, C22rH1, C22rH2, C22rH3, C22nH1, C22nH2, C22nH3, C22nH4, C21rH1, C21rH2, C21rH3, C21rH4, C21rH5, and C21rH6. Error bars are ±1σ determined from all deep-sea expressions of each event. The single event with a mean CIE size greater than 1.5‰ is the H1 (Elmo) event.

A comparison of the overall magnitude and duration of all available benthic foraminiferal records for the early-middle Eocene hyperthermals (excluding the PETM) does show a positive correlation between the size and duration of events (Figure 3-5). In addition, there is also a much stronger correlation between the size of the correlative excursions in $\delta^{18}O$ and $\delta^{13}C$ (Figure 3-6). This is most

likely a function of the generally larger benthic oxygen isotope excursions compared to bulk oxygen isotope excursions as well as the likelihood that benthic $\delta^{18}O$ records are providing a better estimate of temperature change throughout than event than bulk carbonate $\delta^{18}O$.

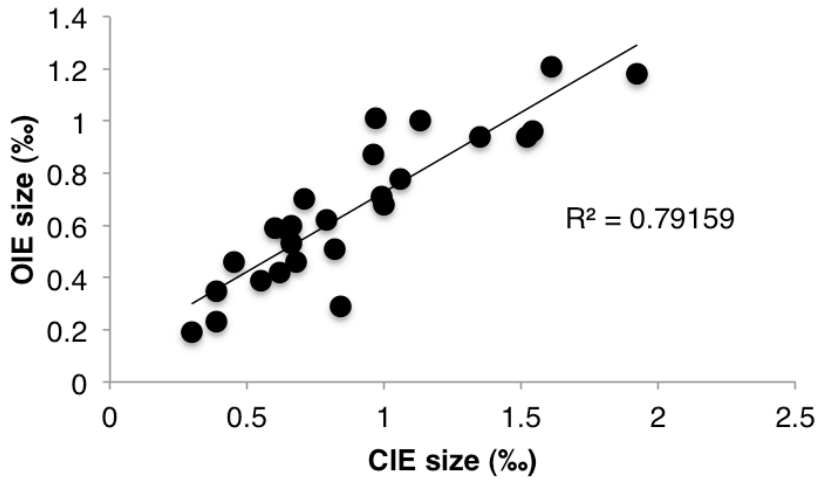
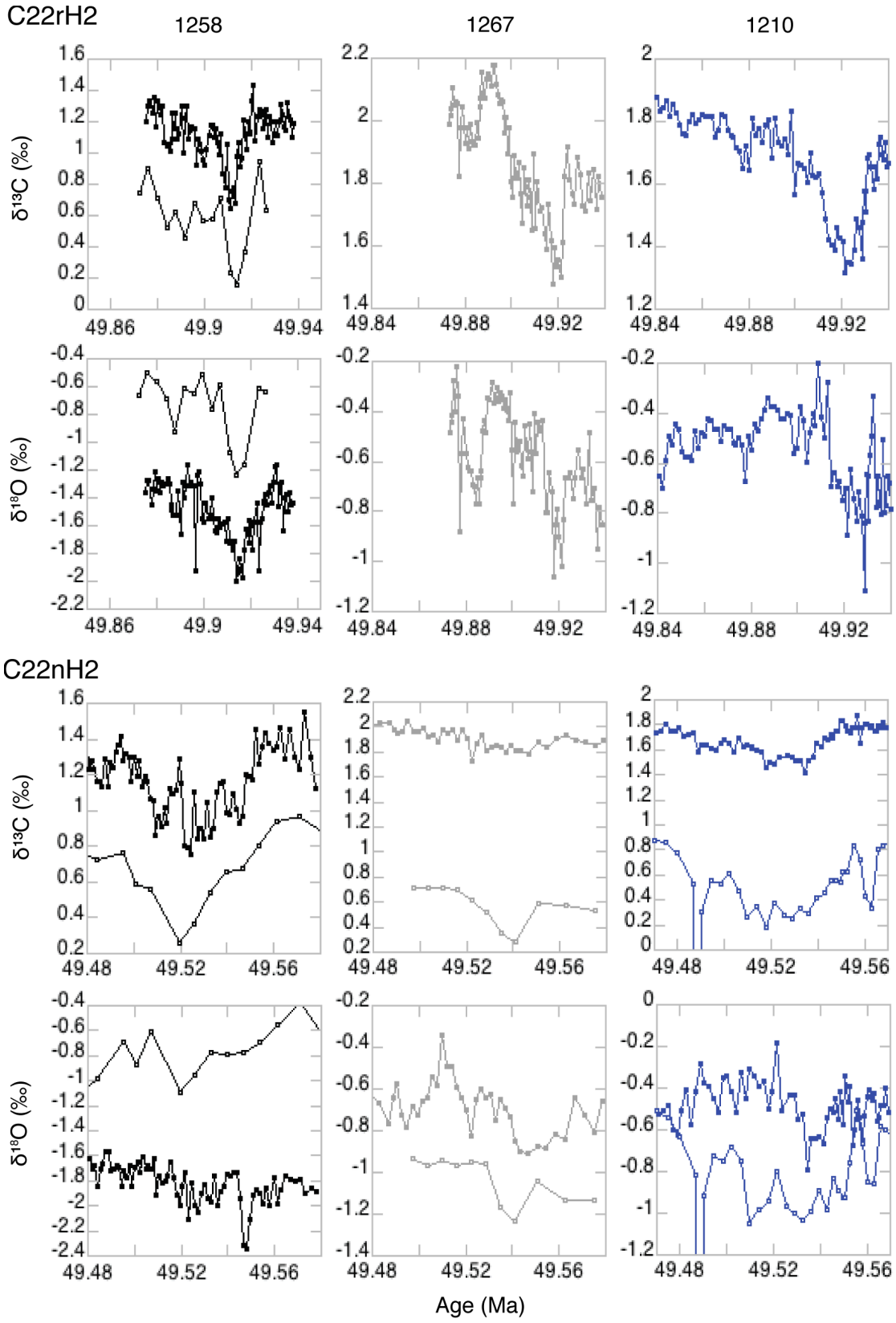


Figure 3-6. Benthic foraminiferal CIE size (‰) plotted against benthic foraminiferal OIE (oxygen isotope excursion) size (‰).

For a more detailed analysis of the inter-site variation for individual events, we analyze high-resolution bulk carbonate stable isotope data generated in this study for events C22rH2, C22nH2, C22nH3, C21rH1, and C21rH5 from three sites (ODP Sites 1258, 1267, and 1210). We compare these records to the original (lower-resolution) benthic foraminifer stable isotope records from Site 1258 and lower resolution benthic foraminiferal stable isotope records from Site 1210 and 1267 where available (Figure 3-7). We test the inter-site correlations developed from estimated wt% $CaCO_3$ records (Figure 3-2) by plotting all stable

Figure 3-7. High-resolution records of events (from top to bottom) C22rH2, C22nH2, C22nH3, C21rH1, and C21rH5 from ODP Site 1258 (black), 1267 (grey) and 1210 (blue). Bulk records (closed circles) are of higher resolution than benthic records (open squares) where they exist. For each event, both carbon isotopes and oxygen isotopes are plotted. All records are plotted over a 100 kyr interval except for C22nH3 at ODP Site 1210, which is plotted over 120 kyr.


C22rH2
1258
1267
1210
δ13C (‰)
δ18O (‰)
C22nH2
Age (Ma)

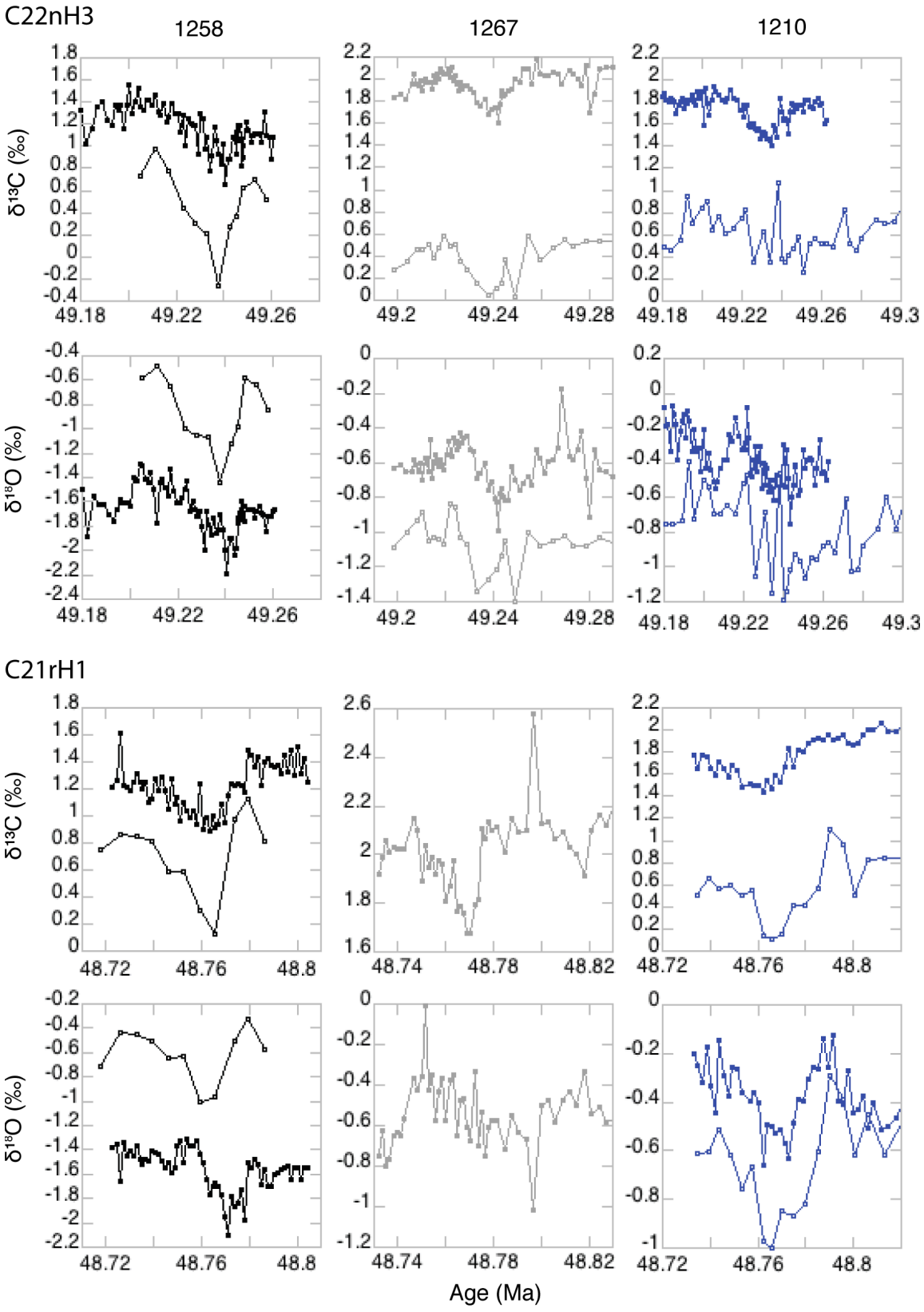


Figure 3-7, Continued.

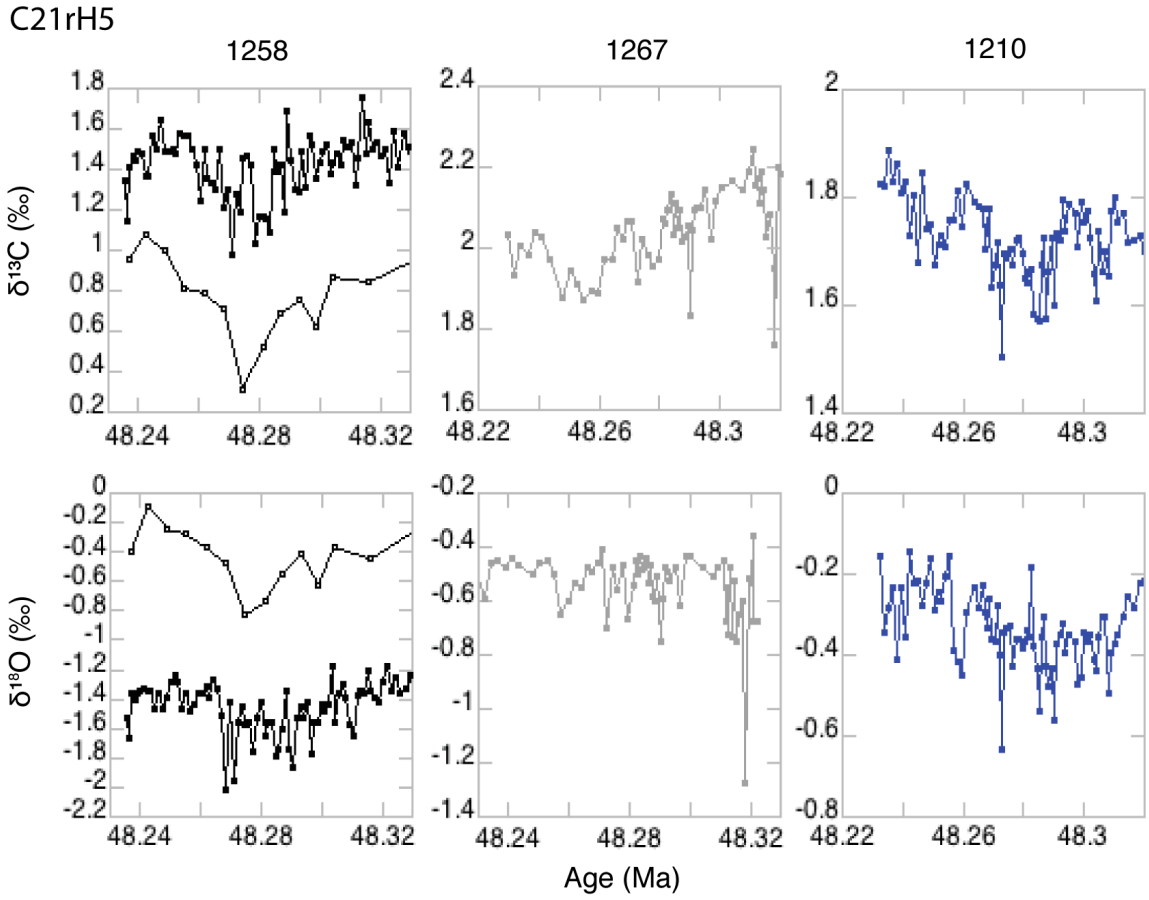


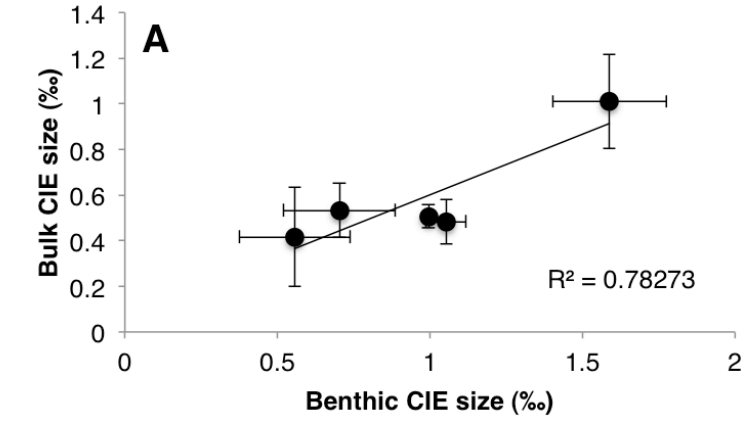
Figure 3-7, Continued.

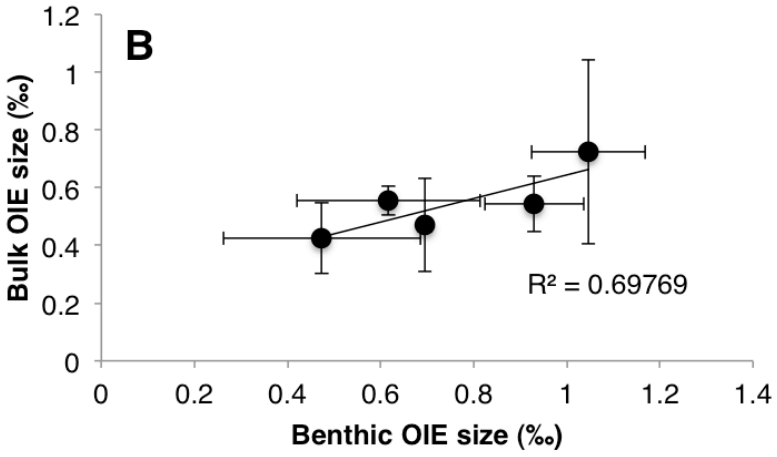
isotope records on our original age models, without any tuning based on feature in the isotopic data. Such tuning could actually introduce additional error since 1) wt% $CaCO_3$ decreases and isotope excursions are always synchronous at a given site and 2) site-specific characteristics can influence both the magnitude and apparent timing of the event (see Chapter 5). There is a large amount of inter-site variability for each event, though more so for some events.

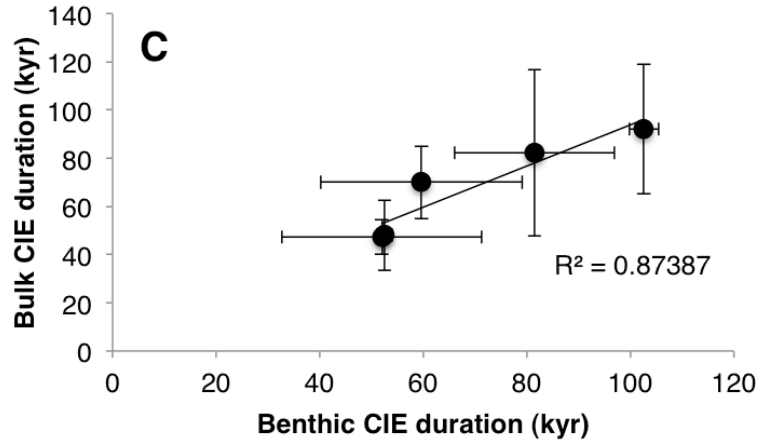
C22rH2 is perhaps the clearest of the five events. The bulk carbonate carbon and oxygen isotope records are very similar to benthic records for the event at ODP Site 1258 in both magnitude and duration. Additionally, the carbon and oxygen isotope excursions are apparent in bulk carbonate records from ODP Site 1267 and 1210, and are broadly similar in shape and overall duration. Excursions are also relatively clear in both bulk and benthic carbon and oxygen isotopes at all three sites for both C22nH3 and C21rH1. In contrast, C22nH2 shows no obvious bulk carbonate CIE at ODP Site 1267, though a benthic CIE is clear, and oxygen isotope records are difficult to interpret at all three sites (with either inconsistent results between bulk and benthic records, or no clear excursion at all). Excursions are also particularly difficult to identify for C21rH1 at ODP Site 1267, though there is a long-term decreasing trend in the bulk carbonate carbon isotopes, which may correspond to the onset of the excursion, which appears relatively slow in the benthic foraminiferal carbon isotope record from ODP Site 1258.

To summarize results of our inter-site records for these five events, we compare bulk to benthic carbon isotope excursion size, oxygen isotope excursion size, and duration. We include only events where both bulk and benthic data exist from multiple sites, so in addition to three of the C22r-C21r events, we also use records of the Elmo and H2 events, since both have multi-site benthic foraminiferal records (Figure 3-8).

Figure 3-8. For each plot A-C, black markers indicate the mean for each event and error bars indicate ±1σ calculated from records for all available sites. A) Benthic CIE size (‰) vs. bulk carbonate CIE size (‰) for Elmo, H2, C22nH2, C22nH3, and C21rH1. B) Benthic OIE size (‰) vs. bulk carbonate OIE size (‰) for Elmo, H2, C22nH2, C22nH3, and C21rH1. C) Benthic CIE duration (kyr) vs. bulk carbonate CIE duration (kyr) for Elmo, H2, C22nH2, C22nH3, and C21rH1.


A
Bulk CIE size (‰)
Benthic CIE size (‰)
R² = 0.78273
0
0.2
0.4
0.6
0.8
1
1.2
1.4
0
0.5
1
1.5
2


B
Bulk OIE size (‰)
Benthic OIE size (‰)
R² = 0.69769
0
0.2
0.4
0.6
0.8
1
1.2
0
0.2
0.4
0.6
0.8
1
1.2
1.4

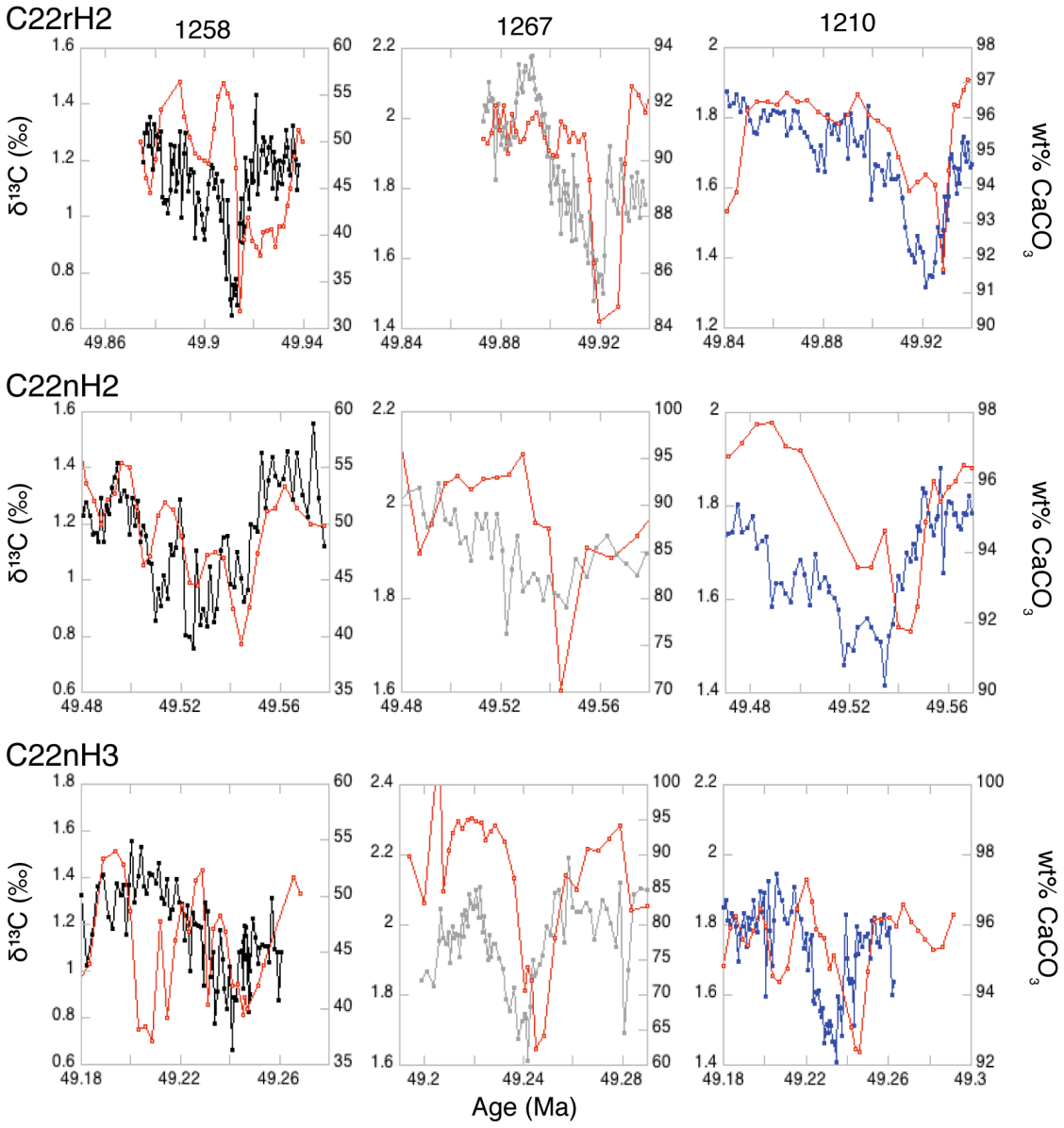

C
Bulk CIE duration (kyr)
Benthic CIE duration (kyr)
R² = 0.87387
0
20
40
60
80
100
120
140
0
20
40
60
80
100
120

Comparing benthic foraminiferal to bulk carbonate records shows that there is generally good agreement between benthic foraminifera and bulk carbonate for the characteristic size and duration of a given event, though the correlation is the weakest for oxygen isotope records. This is consistent with our expectation that bulk carbonate oxygen isotope records tend to be the least reliable indicators of an event. Benthic carbon isotope excursions are generally larger at a given site than bulk carbonate carbon isotope excursions, though there are a few examples of bulk carbonate CIEs exceeding benthic foraminiferal CIEs in magnitude (H1 at ODP Site 1263, C22nH2 at ODP Sites 1210 and 1267, C22nH3 at ODP Site 1267). Our results support the use of bulk carbonate records to determine the relative size of different events where benthic foraminiferal data are unavailable.

We also compare, for all sites where available, changes in wt% $CaCO_3$ corresponding to each carbon isotope excursion (Figure 3-9). A common feature among most events is that the minimum in wt% $CaCO_3$ occurs before the most negative carbon isotope values are reached. This is not an artifact of age models, core splices, or inter-site correlations because plots show bulk carbon isotope data and estimated wt% $CaCO_3$ records for the exact same intervals of core.

The only other sites for which there are detailed records of wt% $CaCO_3$ corresponding with isotope data are from the Walvis Ridge transects of Elmo and H2 from Stap et al., 2009. Again, wt% $CaCO_3$ and bulk carbonate carbon isotope data follow the same age model for the same samples. For these events, the

Figure 3-9. High-resolution records of bulk carbonate carbon isotopes at ODP Sites 1258 (black lines), 1267 (grey lines), and 1210 (blue lines) plotted against estimated wt% $CaCO_3$ (red lines) for each site for events C22rH2, C22nH2, C22nH3, C21rH1, and C21rH5.


C22rH2
1258
1267
1210
C22nH2
C22nH3
δ13C (‰)
wt% CaCO3
Age (Ma)

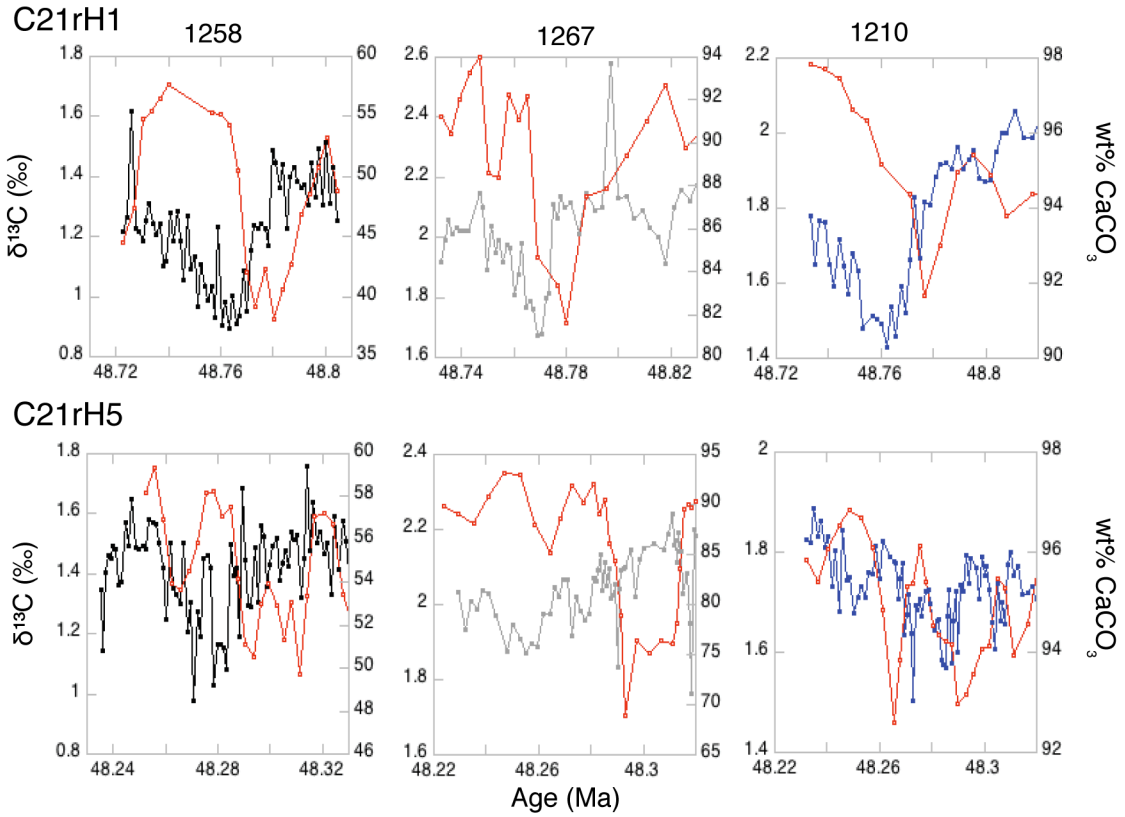


Figure 3-9, Continued.

lead of the carbonate minima compared to the carbon isotope excursion is apparent for H2, but not for the Elmo event (Figure 3-10). For Elmo, carbon isotope and wt% $CaCO_3$ records either show synchronous minima, or the wt% $CaCO_3$ minima are slightly delayed. Decreases in wt% $CaCO_3$ are considerably larger for Elmo than the other hyperthermals, suggesting a connection between the size of the recorded wt% $CaCO_3$ decrease and its temporal lead.

Stap et al., 2009, suggested that the wt% $CaCO_3$ decreases associated with Elmo equated to large amounts of dissolution (as much as 96% at Walvis sites). In contrast, the smaller wt% $CaCO_3$ decreases associated with the other

hyperthermals (including H2), do not indicate large amounts of dissolution.

Rather, we suggest that they are the result of decreased carbonate accumulation

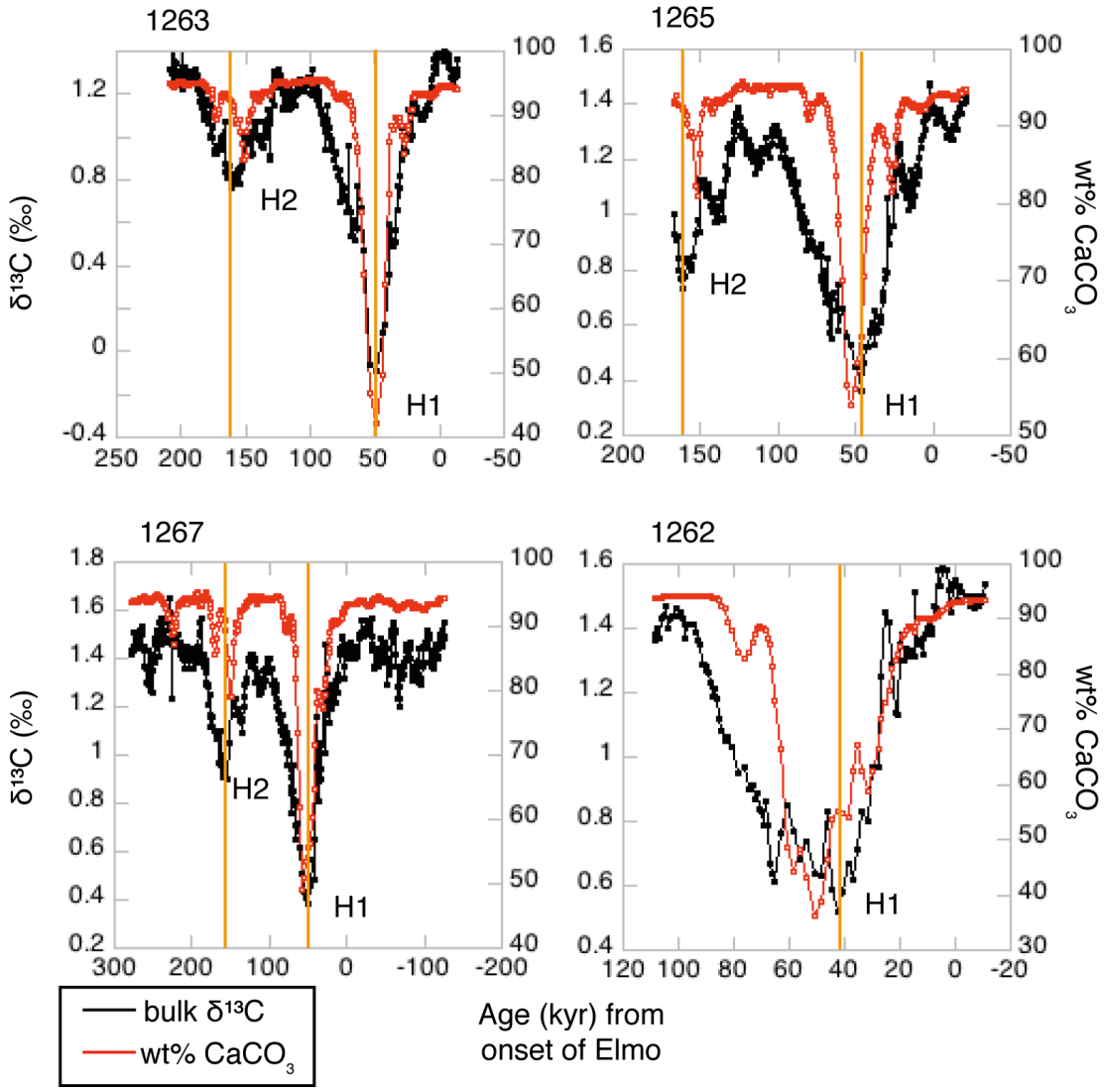


Figure 3-10. High-resolution records of bulk carbonate carbon isotopes at ODP Sites 1263, 1265, 1267, and 1262 (black lines) plotted against estimated wt% $CaCO_3$ (red lines) for each site for events H1 (Elmo) and H2. All data are from Stap et al., 2009. Orange lines indicate the peak of the carbon isotope excursions for H1 and H2.

on the seafloor related to decreased sea surface production. Changes resulting from conditions at the sea surface may be expected to register much more rapidly than changes in the whole ocean dissolved inorganic carbon isotopic composition, explaining the lead in reduced wt% $CaCO_3$ compared to the carbon isotope excursion for the small events.

In contrast, extensive dissolution is the result of changes in the carbonate compensation depth, which should have a longer timescale, comparable to that required for recording the isotopic change. When extensive dissolution occurs, this will make the wt% $CaCO_3$ minima correspond to the carbon isotope minima. Further, the wt% $CaCO_3$ records for Elmo (Figure 3-10) show small decreases in wt% $CaCO_3$, followed by short-lived recoveries, preceding the main wt% $CaCO_3$ decrease at ODP Sites 1263, 1265, and 1267. These small decreases may represent the early signal of reduced carbonate production and export from the sea surface, in contrast to the dissolution indicated by the subsequent wt% $CaCO_3$ decrease.

To compare the magnitude of wt% $CaCO_3$ decrease between sites with different initial wt% $CaCO_3$ values and to compare the wt% $CaCO_3$ decrease to the size of the carbon isotope excursion, we calculate the magnitude of the normalized wt% $CaCO_3$ decrease at each site as

$$\Delta_n \text{ wt\% } CaCO_3 = \frac{\text{wt\% } CaCO_{3\,(initial)} - \text{wt\% } CaCO_{3\,(final)}}{\text{wt\% } CaCO_{3\,(initial)}}$$

As explained by Panchuk, 2007, the benefit of this method (as opposed to simply calculating the change in wt% $CaCO_3$ at each site) is that the normalized wt% $CaCO_3$ decrease can account for the different amount of dissolution suggested by two sites with the same magnitude of wt% $CaCO_3$ decrease but different initial wt% $CaCO_3$.

There is a positive correlation between the size of the carbon isotope excursion and the magnitude of the normalized wt% $CaCO_3$ decrease at a given site (Figure 3-11). However, the strength of this positive correlation derives from the inclusion of data for Elmo. Excluding all Elmo records from cross-plots of benthic carbon isotope excursion magnitude and normalized wt% $CaCO_3$ decrease results in no correlation between the two (R^2=0.0074).

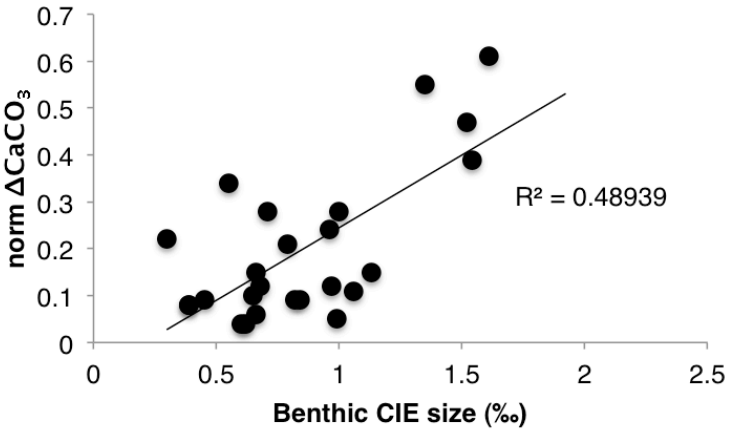


Figure 3-11. Benthic foraminiferal carbon isotope excursion magnitude plotted against normalized wt% $CaCO_3$ decrease at each individual site from which both types of data are available (these are for events H1, H2, C22nH2, C22nH3, and C21rH1).

The weak correlation suggests that using the magnitude of normalized wt% $CaCO_3$ decrease alone is a poor predictor of the size of a carbon isotope excursion, especially for smaller events that do not cause extensive dissolution. Researchers should therefore use caution in interpreting magnetic susceptibility records or Fe intensity data derived from X- ray fluorescence scanning to suggest the relative magnitude of isotopic change that may be indicated by peaks in these proxies. Finally, we find that for individual events, the magnitude of normalized wt% $CaCO_3$ decrease is consistently greatest at the deepest sites.

3.4 Discussion

3.4.1 Causes of inter-site variability

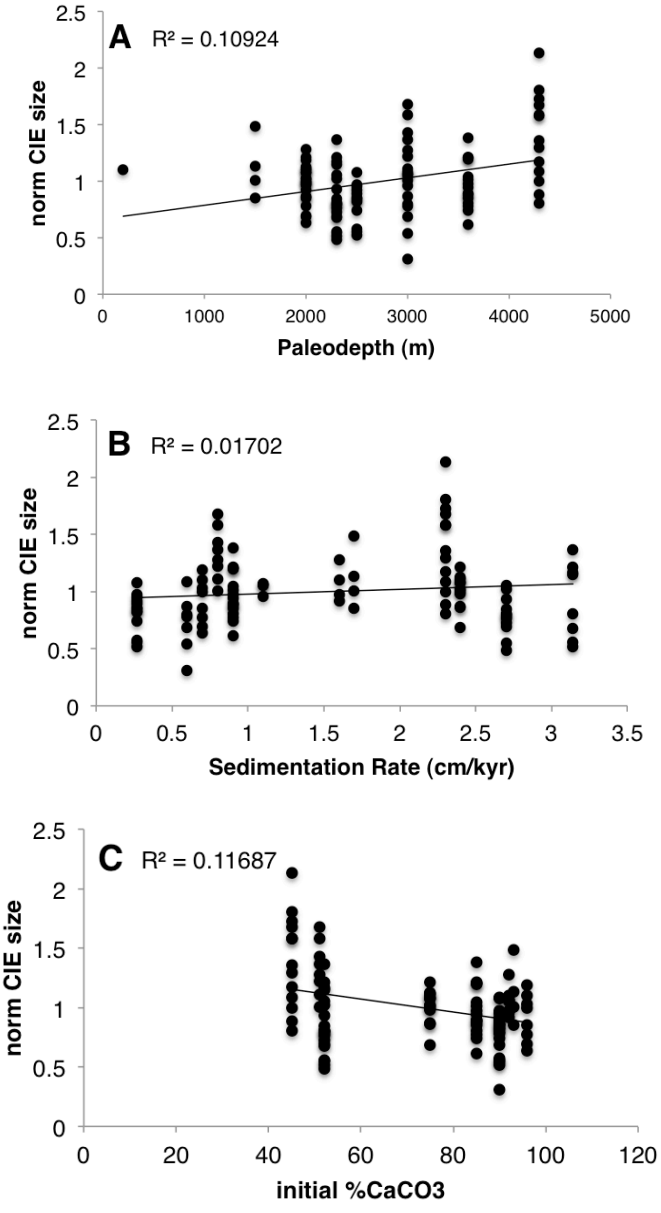
A primary result from both our assessment of multi-site records of the A-L hyperthermals and our new multi-site datasets for events C22rH2, C22nH2, C22nH3, C21rH1, and C21rH5 is that there is a great deal of inter-site variability in the sedimentary expression of various events apparent from both bulk carbonate and benthic foraminiferal datasets. The extent of inter-site variability for individual events in the magnitude of the carbon isotope excursion is slightly smaller for benthic foraminiferal records than for bulk carbonate, especially when considered relative to the size of the recorded excursion. For instance, in comparing only events where both bulk carbonate and benthic foraminiferal data exist, the average 1σ for benthic CIEs represents 13% of the size of the mean

benthic CIE. In contrast, the average 1σ for bulk carbonate CIEs represents 23% of the size of the mean bulk CIE. The same relationship holds for comparison of the magnitude of oxygen isotope excursions and the duration of events between benthic and bulk carbonate records—i.e. bulk records show more inter-site variability compared to benthic records.

In order to assess possible site-specific controls on the shape (magnitude and duration) of the carbon isotope excursions recorded at each site, we compare the magnitude and duration of carbon isotope excursions from each site, normalized to the mean magnitude and duration from all sites for a given event, to paleodepth, sedimentation rate, and initial wt% $CaCO_3$. By normalizing each site's record of an event's magnitude and duration to the mean magnitude and duration of that event from all available sites, we are able to correct for the fact that we do not have records of each event from a full range of sites with different conditions. In these analyses, we include both bulk and benthic records (Figure 3-12).

Overall, correlations between site characteristics and the magnitude and duration of carbon isotope excursions is relatively weak, and there are no correlations between duration and site characteristics with an R^2 >0.1. The strongest correlation is between the magnitude of the carbon isotope excursion and the initial wt% $CaCO_3$ (R^2 = 0.11687). Sites with higher wt% $CaCO_3$ record relatively smaller excursions. There is also a positive correlation between paleodepth and CIE magnitude (R^2 = 0.10924), where greater paleodepths are

Figure 3-12. Comparison of individual site characteristics with the size and duration of carbon isotope excursions from all available bulk and benthic records. Both CIE magnitude and duration for each record are normalized to the mean size and duration of that event calculated from all available sites. A site where the CIE has the exact same magnitude as the mean CIE from all sites would have a normalized CIE magnitude of 1. A) Paleodepth versus normalized CIE size. B) Sedimentation rate versus normalized CIE size. C) Initial wt% $CaCO_3$ versus normalized CIE size. D) Paleodepth versus normalized CIE duration. E) Sedimentation rate versus normalized CIE duration. F) Initial wt% $CaCO_3$ versus normalized CIE duration.


A
R² = 0.10924
norm CIE size
Paleodepth (m)
B
R² = 0.01702
norm CIE size
Sedimentation Rate (cm/kyr)
C
R² = 0.11687
norm CIE size
initial %CaCO3

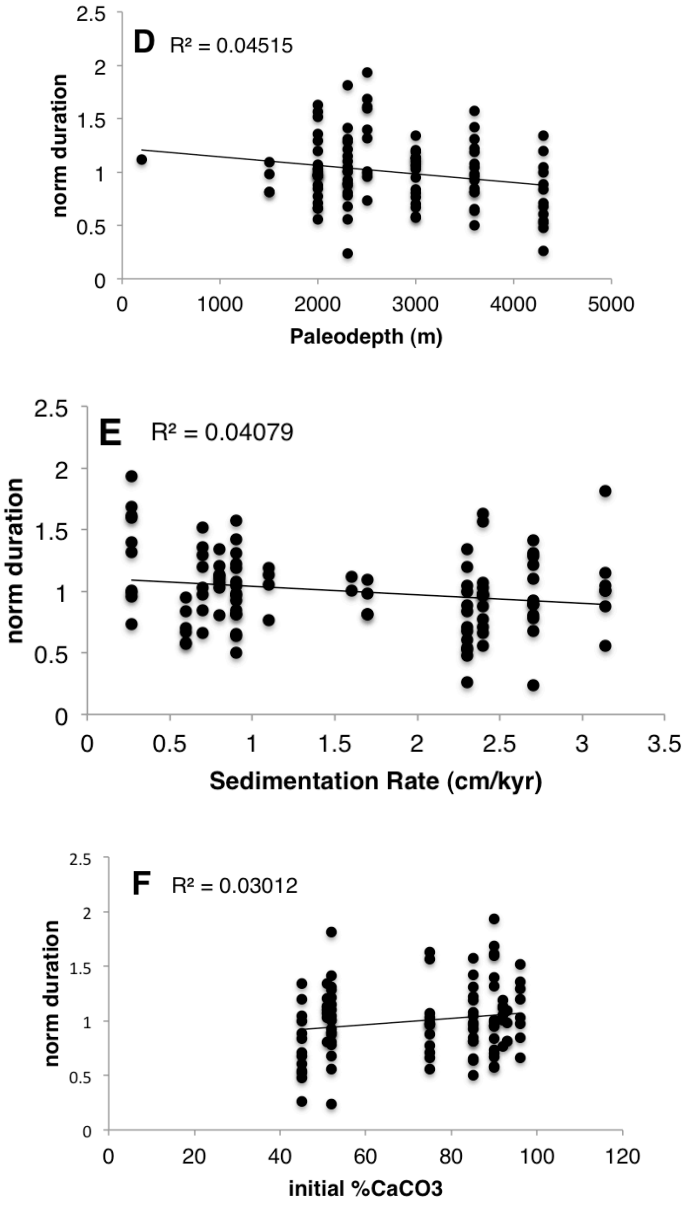


Figure 3-12, Continued.

associated with larger CIEs (greater paleodepths typically correspond to lower initial wt% $CaCO_3$.

Though the correlations are weak, this result is counterintuitive. For the PETM, the opposite is generally true—shallower sites and sites on carbonate

platforms and continental margins record some of the largest CIEs (i.e. Panchuk, 2007; John et al., 2008; Robinson, 2010). Depth transects for the PETM and Elmo developed from Walvis Ridge in the Southern Atlantic (data from these sites for Elmo and H2 have been used in analyses here) show larger CIEs at shallower sites (Zachos et al., 2005; Stap et al., 2009). For H2, the relationship between depth and CIE size from the Walvis Ridge transect is less conclusive.

The explanation for the depth-size relationship for the PETM and Elmo is usually that the more extensive dissolution at deeper sites means that sediments do not record the most depleted isotopic values (Zachos et al., 2005; Panchuk, 2007; Stap et al., 2009). Specifically, Panchuk, 2007, finds that the most significant factor in the recorded size of the PETM at a given site is the delay between the recovery of the isotopic composition of dissolved inorganic carbon and the resumption of sedimentation after the dissolution pulse has ceased. Given that dissolution is significantly less substantial for the smaller hyperthermals compared to Elmo and the PETM, the likeliest explanation for the counter-intuitive relationship between paleodepth, initial wt% $CaCO_3$, and CIE size is that without substantial dissolution, paleodepth and the amount of carbonate available for dissolution are much less significant factors in recording the true CIE size.

A more surprising result is the lack of correlation between sedimentation rate and carbon isotope excursion size or duration. Panchuk, 2007, suggested that bioturbation is a significant factor in the size of the PETM CIE recorded at a

given site, since bioturbation returns older, isotopically heavy carbonate to the sediment surface during an event, damping the apparent excursion size. By mixing depleted carbonate down the sediment column, bioturbation might also increase the apparent duration of an event. If bioturbation intensity were equivalent at every site, sedimentation rate would control the impact of bioturbation on the sediment record by determining the total age of the mixed layer of sediment.

Sedimentation rate is likely the most uncertain of all our calculated site characteristics for the hyperthermal events assessed here. We calculate the sedimentation rate for each site by a linear line of best fit through age-depth plots for each site over 2-4 myr intervals (for ODP Site 1267, which we use for both the H1 and H2 events as well as the C22r-C21r events, we calculate sedimentation rate separately for these two intervals). This method ignores shorter-term changes in sedimentation rate, which are both likely and potentially larger (for instance, we use an average sedimentation rate for ODP Site 1210 of 0.7 cm/kyr, but during the interval over which hyperthermals occur, our age models suggest sedimentation rates vary between 0.3-1.5 cm/kyr and for ODP Site 1267, the early-middle Eocene average sedimentation rate of 0.6 cm/kyr masks variations between 0.2-1.8 cm/kyr.

Further, the age models on which sedimentation rates are based add uncertainty. All the age models used for the datasets presented here are based on astronomically tuning cycles present in physical property data (estimated wt%

$CaCO_3$, magnetic suceptibiliy, and Fe intensity) (Cramer et al., 2003; Stap et al., 2009, Zachos et al., 2010; Sexton et al., 2011). Such methods do not always agree on either the orbital frequency represented by sediment cycles or with alternative methods for age model calibration (including extraterrestrial ^{3}He). However, separately assessing inter-site records for individual events does suggest that the site with the lowest sedimentation rate (DSDP Site 577, with a sedimentation rate of ~0.3 cm/kyr) consistently records the smallest early Eocene carbon isotope excursions compared to other sites. In general, it is reasonable to assume that higher sedimentation rate sites will yield less biased records of hyperthermals.

3.4.2 Significance of event shape

Assessing records of hyperthermal events in detail (i.e. Figure 3-7) demonstrates the wide variety of event shapes. The characteristic shape of the PETM is asymmetrical—there is a very abrupt onset (perhaps <10 kyr) followed by a plateau of depleted isotopic values for a few tens of thousands of years, and a recovery over approximately 100 kyr (Cohen et al., 2007). In contrast, Elmo has a more symmetrical shape, with an extended onset over around 50 kyr and a recovery of equal duration (Stap et al., 2009; Stap et al., 2010). For the remaining A-L and C22r-C21r hyperthermals, there are all sorts of event shapes—some have relatively rapid onsets and slow recoveries, some are almost perfectly

symmetrical, and others have recoveries that appear more abrupt than their onsets.

Given that event shape is determined by the relative duration of onset, peak, and recovery, the inferred shape of an event is highly dependent on the assigned age model. Just as disagreement over the duration of the PETM derives from differences in the calculated length of the long recovery interval between astronomical versus ^{3}He-based age models (Norris and Rohl, 1999; Farley and Elgroth, 2003; Rohl et al., 2007), changes in sedimentation rate throughout an event can greatly impact apparent event shape. Differences in site-specific characteristics can also alter event shape based on, for example, inter-site differences in mixing intensity and dissolution.

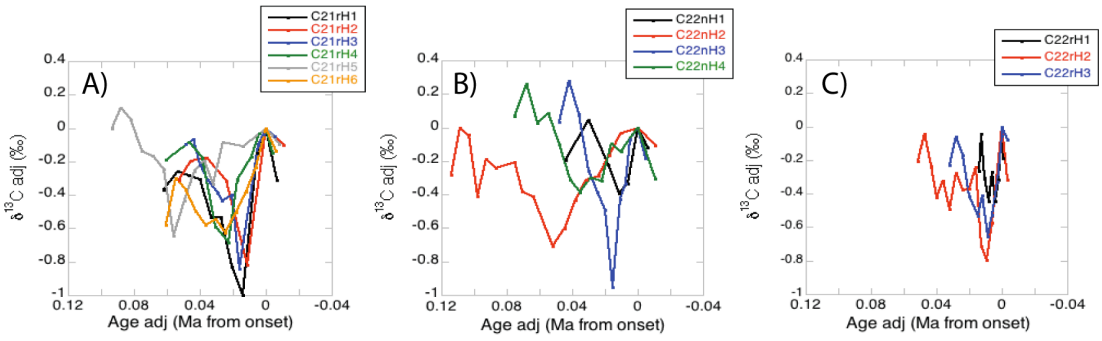


Figure 3-13. Comparison of the shapes of the C22r-C21r hyperthermal events from a single site (ODP Site 1258). All carbon isotope records are adjusted so that the onset of an event is at 0 ‰ and 0 Ma. All benthic data are from Sexton et al., 2011. A) C21r events 1-6. B) C22n events 1-4. C) C22r events 1-3.

To provide an example of the range of shapes among different events at a single site, where a consistent age model is used for each event, we analyze all

13 benthic foraminiferal $\delta^{13}C$ records from events C22r-C21r in detail using datasets from Sexton et al., 2011 (Figure 3-13). We adjust records for each event to a common starting point (time=0, $\delta^{13}C$=0 ‰). We identify the starting point for each event as the point of most positive $\delta^{13}C$ before values begin to decline towards the excursion. In each case, we select the end of the event as where $\delta^{13}C$ reaches a value at least as positive as the starting point.

Roughly, it is possible to group the events into two characteristic shapes—those with durations of less than 48 kyr (the mean duration for all events) and an abrupt onset to excursion values (less than half the event's total duration), and those with a duration of more than 48 kyr and a slow onset (more than half the event's total duration). Events C22rH1, C22rH2, C22rH3, C22nH1, C22nH3, C21rH1, C21rH2, C21rH3, C21rH4 fall into the first category, and C22nH2, C22nH4, and C21rH5 fall into the second. C21rH6 is the only event that does not fit this classification, with a total duration of more than 48 kyr, but an onset less than half of the total duration.

It is unlikely that the age model overly impacts the differences in shape between these 13 events, since event shapes persist when plotting each carbon isotope record against depth rather than calculated age. In addition, the few events with relatively slow onsets show many more data points between the onset of the event and the peak of the excursion compared to events with relatively rapid onsets—demonstrating the slow onsets are not imposed by the age model.

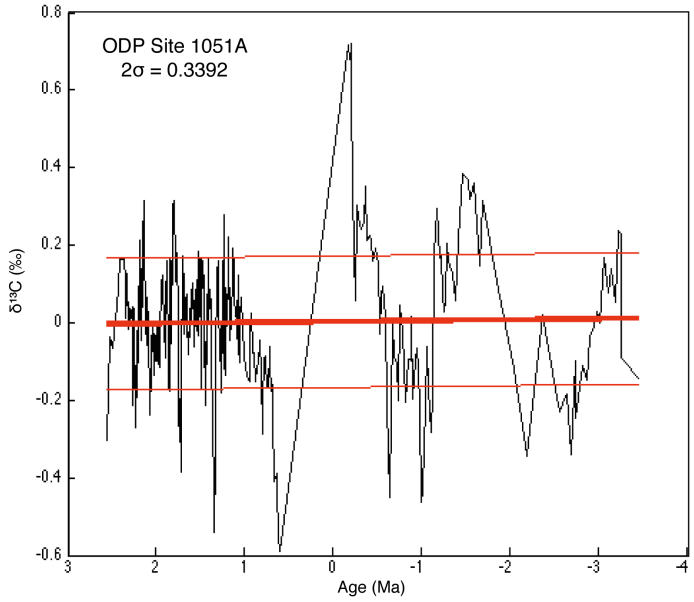
Where we have generated additional very high-resolution bulk carbonate records, the carbon isotope data supports the description of event shape inferred from analysis of the lower resolution benthic foraminiferal carbon isotope records. This suggests our assessment of event shape is not strongly affected by aliasing.

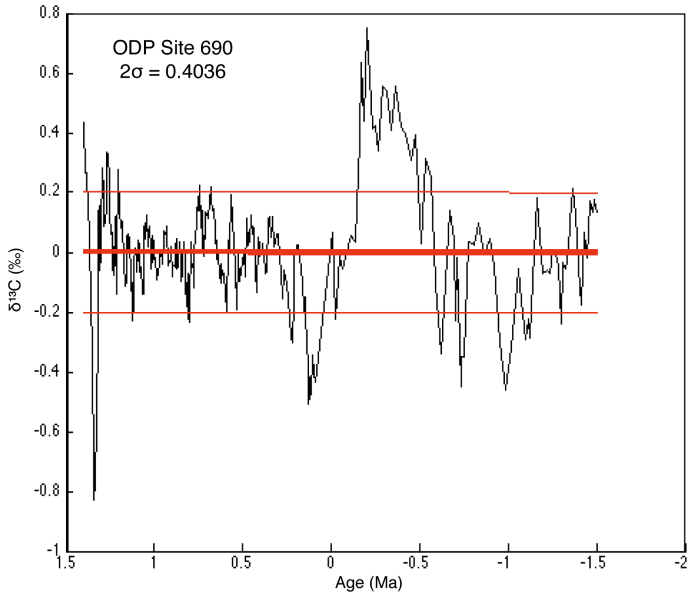
3.4.3 How many hyperthermals were there?

Our high-resolution bulk carbonate stable isotope records for events C22rH2, C22nH2, C22nH3, C21rH1, and C21rH5 typically show smaller excursions compared to benthic foraminiferal records from the same site, and benthic foraminiferal isotope records for C22nH2, C22nH3, and C21rH1 from ODP Sites 1210 and 1267 also show smaller excursion than those originally identified at ODP Site 1258. The smallest of the five events selected for high resolution, multi-site analysis, C21rH5, shows a benthic foraminiferal CIE of 0.65‰ at ODP Site 1258 and a bulk carbonate CIE of 0.66‰; however, bulk carbonate CIEs are less than 0.3‰ at Sites 1210 and 1267. At such a small size, it becomes difficult to confidently identify an event from background variability.

We attempt to define criteria for identifying hyperthermals from background variability in carbon isotope records. To do this, we use the long-term benthic foraminiferal $\delta^{13}C$ record from ODP Site 1258 for the C22r-C21r hyperthermals, and for the A-L hyperthermals, we use long-term bulk carbonate carbon isotope records from DSDP 550, DSDP 577, ODP 1051A, ODP 1051B, ODP 690, and ODP 1262. We define unusual short-term variability as excursions that exceed a magnitude of 2σ, calculated from each record after removing

Figure 3-14. Long-term carbon isotope records for the early Eocene from DSDP 550, DSDP 577, ODP 1051A, ODP 1051B, ODP 690, ODP 1262 (bulk carbonate, from Cramer et al., 2003), and for the early-middle Eocene from ODP Site 1258 (benthic foraminifera, from Sexton et al., 2011). Early Eocene records are plotted on age models relative to the timing of the PETM from Cramer et al., 2003, and the early-middle Eocene record is plotted on the age model from Sexton et al., 2011. Center red lines indicate lines of best fit for de-trended records and envelope indicates ±1σ calculated from de-trended record. We de-trend each record using a polynomial line of best fit (best fit lines shown in Figure 3-A1).


ODP Site 1051A
2σ = 0.3392
δ13C (‰)
Age (Ma)


ODP Site 690
2σ = 0.4036
δ13C (‰)
Age (Ma)

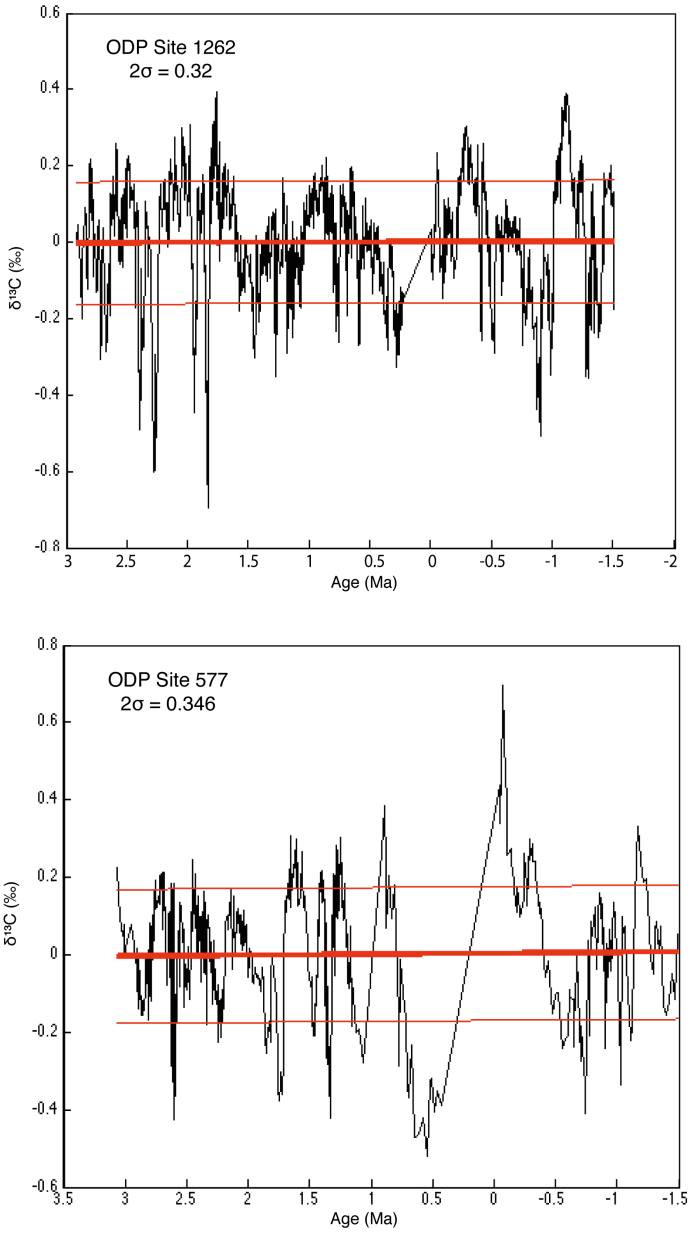


Figure 3-14, Continued.

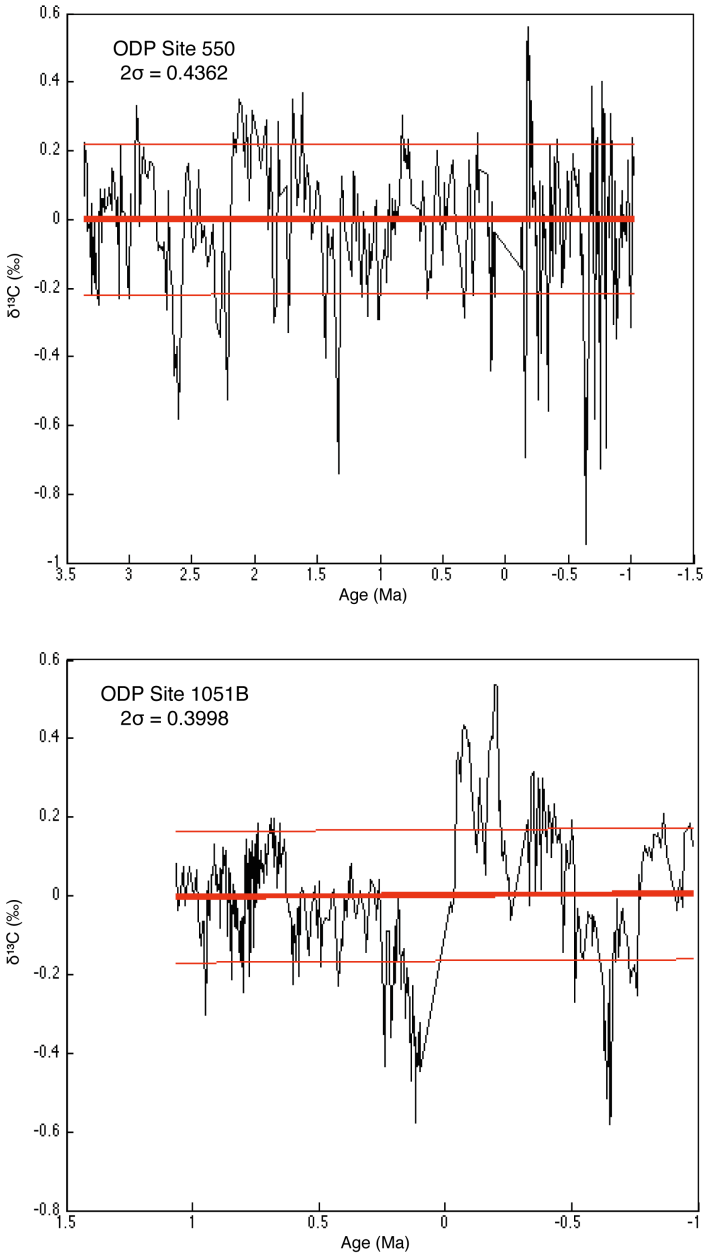


Figure 3-14, Continued.

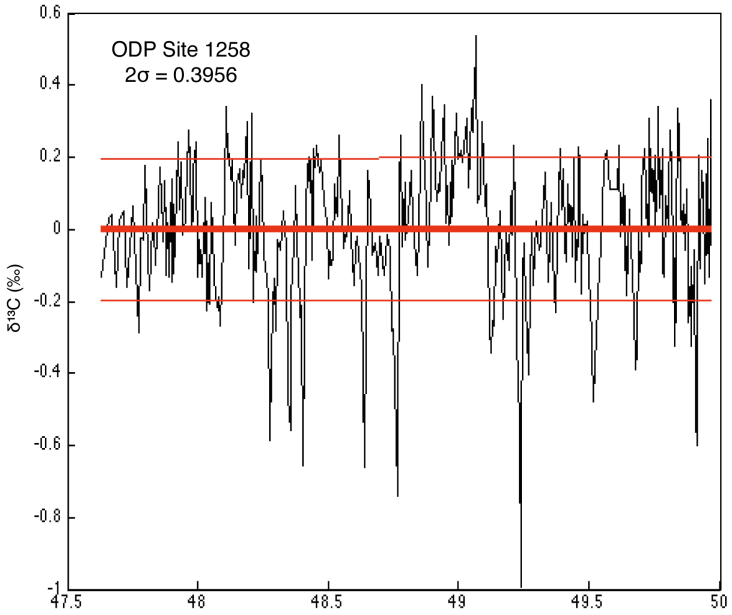


Figure 3-14, Continued.

long-term trends from the data by de-trending datasets using a polynomial line of best fit with order based on the length of each record (see Figure 3-14 and Figure 3-A1). Before de-trending early Eocene records, we remove the carbon isotope data corresponding to the PETM, since this event is an extreme outlier from background variability. If an 'event' fails to exceed this threshold, it grades into background variability, and it becomes difficult to justify it as an anomaly.

When we compare assessed CIE sizes to the 2σ values for each site, we eliminate different events from each site (see Table 2). This highlights the degree of inter-site variability in records of hyperthermals. Our analysis suggests removing some events from consideration as anomalies: events A and G are eliminated from all site, and events D1, E1, E2, and F are eliminated from more

than half of the sites from which they were originally identified. In the record from Sexton et al., 2011, events C22nH2 and C22nH4 fail to pass the threshold and C22rH1 is very close, suggesting that there are perhaps only 10 events that justify the label of 'hyperthermal' in this record.

Table 3-2. Comparison of CIE sizes to 2σ values calculated from de-trended long-term carbon isotope records.

Site	Identified CIEs	CIEs failing to pass 2σ threshold
DSDP 550	C1, C2, D1, D2, E1, E2, F, H1, H2, I1, I2, J, K,L	E2, H2
DSDP 577	A, B1, B2, C1, C2, D1, F, H1, H2, I1, I2, J, K	A, C2, D1, F, I2
ODP 1051A	A, B1, B2, C1, C2, D1, G, H1, H2, I1, I2, J	A, B2, C1, D1, G, I2, J
ODP 1051B	C1, C2, D1, D2, E1, E2, F, G	C1, D2, E1, F, G
ODP 690	A, B1, B2, C1, C2, D1, E1, E2, F, G, H1	A, D1, E1, E2, F, G
ODP 1262	B1, B2, C1, C2, D1, D2, E1, E2, F, H1, H2, I1, I2, J	C2, E1, E2
ODP 1258	C21r-C22r	C22nH1, C22nH4

From Table 2, it appears that some sites are better recorders of hyperthermals than others. This raises the question of whether variability that passes the threshold at a single site is justifiably a hyperthermal event, or if some sites are more sensitive recorders of short-term variability. Aside from previously discussed site characteristics, including paleodepth, sedimentation rate, and carbonate content, other inter-site differences may explain the appearance of more short-term excursions appearing to pass the threshold for defining anomalies at some sites compared to others. For example, a site's position

relative to the location of bottom water formation may make an event a particularly sensitive recorder to changes in overturning strength.

Lunt et al., 2010, used a fully coupled atmosphere-ocean general circulation model configured for the Eocene to demonstrate the sensitivity of overturning circulation to changes in seasonality in a high CO_2 world, with the transition from minimum to maximum precession-modulated eccentricity (for maximum southern hemisphere seasonality) driving a slow-down in deep water formation in the southern Atlantic. In addition to causing intermediate water warming, such a slowdown could alter the chemistry of a nearby site's overlying water mass. Sites far from the location of overturning at the 'end' of the deep water flow path may not record such transitions as strongly as nearby sites.

Lunt et al., 2010, suggested that this mechanism could explain the intensity of deep-sea dissolution at Walvis Ridge in the South Atlantic during the PETM compared to other sites, but it could also explain regional differences in the number of apparent hyperthermals during the early Eocene. Transitions between two different water masses bathing a site (such as corrosive, relatively negative $\delta^{13}C$ bottom water and relatively younger bottom waters) could explain both isotopic excursions and estimated % $CaCO_3$ decreases.

Another variable factor among sites is the position of the CCD. Studies have demonstrated regional differences in the position of the CCD before and across the PETM (Panchuk et al., 2008; Zeebe et al., 2009). Differences in both the depth of the CCD at a given site (influencing the site's carbonate content) but

also in the extent of CCD shoaling and the rate of recovery of the CCD at a given location (influencing the magnitude of changes in carbonate content) can influence the size of the recorded excursion (i.e. Panchuk, 2007). Further, sites may respond differently to orbitally paced changes in the export ratio of carbonate to organic carbon from the sea surface. Models attempting to assess the presence of orbital forcing in carbon isotope records typically involve parameterizing fluctuations in this ratio (Palike et al., 2006; Russon et al., 2010). However, orbital forcing varies with latitude, so it is likely that the latitude of different sites will influence the magnitude of changes in this ratio and thus influence the threshold for identifying an anomalous event.

Finally, inaccuracies in age models and inter-site correlations might also explain the mismatch between events identified at each site. Identifying extreme events like the PETM at multiple sites may be relatively straightforward, but when events are small and the timescales separating events are shorter than the age-depth tie-points available from bio- or magnetostratigraphy, cycle counting can introduce errors by inaccurately representing the number of cycles or the dominant orbital frequency recorded at a given site. Differences in sedimentation rate between sites can further affect cycle counting by acting as a filter on the frequencies preserved.

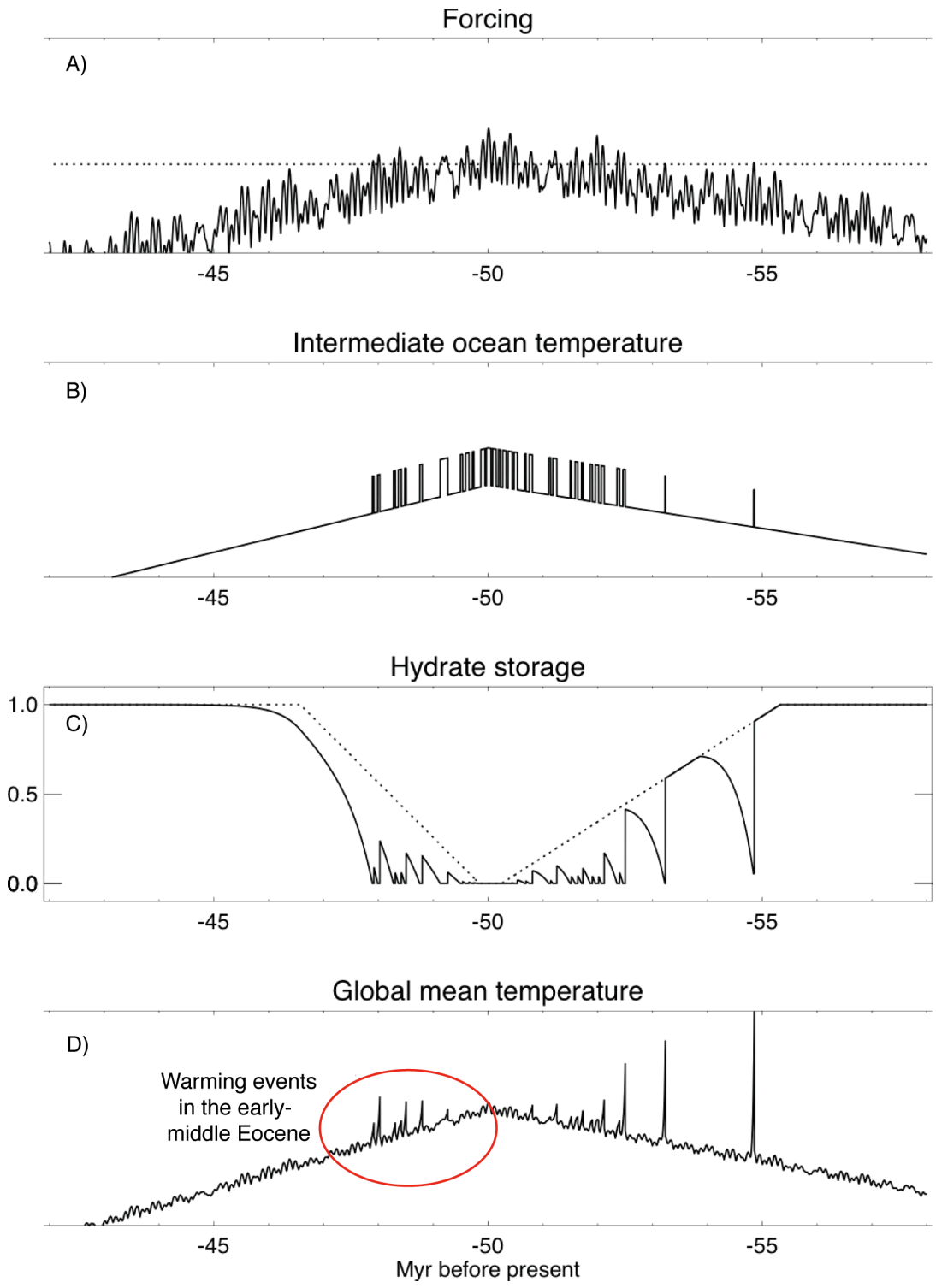
Inter-site differences in the number of apparent hyperthermal events suggest using caution in identifying an isotope excursion recognized at a single site as a global hyperthermal event. As a first criterion, it is important to establish

that the identified event is truly anomalous in the context of that site's background variability. Inter-site expressions of an event are important to assess its occurrence, particularly in order to rule out the original record as unusual as a result of local characteristics. In particular, records of an event from widely spaced sites unlikely to be influenced by local or regional changes in an individual water mass would provide the strongest evidence that an event is global.

3.4.4 Long-term hyperthermal sequence

Competing hypotheses for the mechanism to explain the occurrence of repeated hyperthermal events in the early Eocene include repeated, orbitally paced releases of carbon from methane hydrates, permafrost carbon, or peat (Lunt et al., 2011, DeConto et al., 2012, Zachos et al., 2010). However, all of these hypotheses address only the sequence of hyperthermals in the early Eocene. Sexton et al., 2011, separately suggested that release of dissolved organic carbon from a deep abyssal ocean reservoir could drive the C22r-C21r hyperthermals. However, the overall similarity in size and duration between the early Eocene and early-middle Eocene hyperthermals suggests that a common mechanism to explain all of them is plausible. Most records of the early Eocene sequence of hyperthermals leading up to the EECO stop around 52.5 Ma, and there are currently no high-resolution records from ~52.5-50 Ma (the interval between event L and event C22rH1). Many of the hypothesized mechanisms for

Figure 3-15. Threshold model of orbitally-paced methane hydrate release and abrupt warming events during the early-middle Eocene adapted from Lunt et al., 2011. A) Eccentricity forcing derived from the eccentricity component of the astronomical solution from Laskar et al., 2004, for the interval 40-58 Ma combined with a linear warming trend for the interval 58-50 Ma, followed by a linear cooling trend from 50-40 Ma. Dotted line indicates the threshold where eccentricity forcing will result in a slowdown of overturning circulation and intermediate water warming (threshold defined by GCM model results from Lunt et al., 2011). B) Intermediate ocean temperatures reflecting background warming/cooling trend and abrupt increases in intermediate ocean temperature as a result of eccentricity maxima-induced slow-down in overturning circulation. C) Storage of methane hydrates—total potential storage is based on background temperature and is smaller for warmer climate. Release events occur when forcing crosses the threshold in A. D) Global mean temperature, reflecting the occurrence of abrupt warming events corresponding to times when forcing crosses the threshold in A. The magnitude of each abrupt warming event is related to the size of the available hydrate reservoir (itself a function of background temperature).


Forcing
A)
-45
-50
-55
Intermediate ocean temperature
B)
-45
-50
-55
Hydrate storage
1.0
0.5
0.0
C)
-45
-50
-55
Global mean temperature
D)
Warming events
in the early-
middle Eocene
-45
-50
-55
Myr before present

the multiple hyperthermals of the early Eocene suggest that the sequence ended when temperatures became too warm to allow the maintenance of a sufficiently large, perturbable carbon reservoir (Lunt et al., 2011; DeConto et al., 2012). None of these studies suggests that hyperthermals might be expected to restart once global temperature cooled slightly at the end of the EECO.

We used the threshold model of Lunt et al., 2011, to test whether it is conceptually plausible to link the occurrence of repeated warming events during background cooling following peak warmth at the height of the EECO to the repeated events during the warming trend preceding the EECO. Lunt et al., 2011, developed the threshold model using the observation from general circulation model results that eccentricity forcing (causing variations in seasonality) could lead to changes in overturning circulation and intermediate water warming. The threshold to this circulation switch was dependent on background climate, simulated as a function of CO_2 driven warming. This finding provided a mechanism to explain repeated releases from a hydrate reservoir, which increased in frequency as a result of the background warming trend of the early Eocene, yet decreased in magnitude as the potential available hydrate reservoir diminished in size. Lunt et al., 2011, emphasized that the model is not conceptually exclusive to hydrates as the carbon source; a similar mechanism could account for orbitally-paced release of carbon from another reservoir—such as permafrost, dissolved organic carbon, or peat.

We modified the orbital forcing in the threshold model to add eccentricity forcing until 44 Ma, and followed the linear warming trend with a linear cooling trend (to simulate the end of the EECO). The modified forcing produced a series of events imposed on the cooling trend in addition to those previously identified for the warming trend of the early Eocene. The events superimposed on the cooling trend are closely spaced because as temperatures cool, the climate is still close to the threshold for carbon release and can cross it at practically every eccentricity maxima (Figure 3-15). As the temperatures decline, the potential carbon reservoir refills, but at some point, background temperatures decline to a level where the reservoir is stable despite eccentricity forcing.

While this model is highly tunable—especially in terms of the rate of recharge of the perturbable carbon reservoir and the rate of warming and cooling across the early-middle Eocene, our results suggest that it is logical to extend hypotheses for the early Eocene hyperthermals to include those recorded in the early-middle Eocene. In addition to similar structure in terms of magnitude and duration, these events occur in an interval where the combination of large changes in global temperature and orbital forcing may have led to major instability in the global carbon cycle, resulting in climate-carbon cycle interactions of a magnitude more commonly associated with Plio-Pleistocene glaciations.

3.5 Conclusions

We have demonstrated that the more commonly known sequence of hyperthermals in the early Eocene extends into the early-middle Eocene by identifying that at least some of the C22r-C21r hyperthermals are global and similar in size and duration to the A-L hyperthermals. Records of hyperthermal events show considerable inter-site variability, which is not a simple function of any single site characteristic, but rather a complicated function of factors including the site's latitude, paleodepth, position relative to sites of deep water formation, the local depth of the lysocline, the rain ratio of carbonate to organic carbon exported from the sea surface, total sedimentary carbonate content, and sedimentation rate. As a result of these variations, it is not always possible to conclusively identify an event at every site, even when no obvious stratigraphic gaps are present.

Some of the early-middle Eocene hyperthermals are so small that they grade into background variability. Defining a threshold for identifying events at individual sites, we have demonstrated that some of the previously identified events may not justifiably be termed hyperthermals. In particular, events A, G, C22nH1, and C22nH4 are most likely not major global events. If carbon cycle variability in the Eocene represents a continuum of scales, then perhaps the hyperthermal terminology is misleading. While the PETM, and probably Elmo, are clearly outliers among the carbon cycle and climate variability of this interval, the

smaller events appear more as nodes in orbital forcing of the carbon and climate cycle.

Chapter 3, in part, is currently being prepared for submission for publication. I am the primary investigator and author of this paper in collaboration with co-authors Philip Sexton and Richard Norris.

3.6 References

Cohen, A.S. Coe, A.L, Kemp, D.B, (2007), The late Palaeocene-Early Eocene and Toarcian (Early Jurassic) carbon isotope excursions: a comparison of their time scales, associated environmental changes, causes and consequences, *Journal of the Geological Society London*, Vol. 164, pp.1093-1108, doi:10.1144/0016-76492006-123.

Cramer, B.S., Wright, J.D., Kent, D.V., and M.P. Aubry, (2003), Orbital climate forcing of d13C excursions in the late Paleocene-early Eocene (chrons C24n-C25n), *Paleoceanography*, Vol. 18, No. 1097, 25 pp., doi:10.1029/2003PA000909.

Cramer, B.S., Toggweiler, J.R., Wright, J.D., Katz, M.E., and K.G. Miller, (2009), Ocean overturning since the Late Cretaceous: Inferences from a new benthic foraminiferalisotope compilation, *Paleoceanography*, Vol. 24, PA4216, 14 pp., doi:10.1029/2008PA001683.

DeConto, R.M., Galeotti, S., Pagani, M., Tracy, D., Schaefer, K., Zhang, T., Pollard, D., and D.J. Beerling, (2012), Past extreme warming events linked to massive carbon release From thawing permafrost, *Nature*, Vol. 484, doi:10.1038/nature10929.

Farley, K.A., and S.F. Eltgroth, (2003), An alternative age model for the Paleocene Eocene thermal maximum using extraterrestrial 3He, *Earth and Planetary Science Letters*, Vol. 208, No. 3–4, pp. 135-148, doi:10.1016/S0012821X(03)000177.

Galeotti, S., Krishnan, S., Pagani, M., Lanci, L., Gaudio, A., Zachos, J.C., Monechi, S., Morelli, G., and L. Lourens, (2010), Orbital chronology of Early Eocene hyperthermals from the Contessa Road section, central Italy, *Earth and Planetary Science Letters*, Vol. 290, No. 1-2, pp. 192-200, doi:10.1016/j.epsl.2009.12.021.

John, C.M., Bohaty, S.M., Zachos, J.C., Sluijs, A., Gibbs, S., Brinkhuis, H., and T.J. Bralower, (2008), North American continental margin records of the Paleocene Eocene thermal maximum: implications for global carbon and hydrological cycling, *Paleoceanography*, Vol 23, PA2217, 20 pp. doi:10.1029/2007PA001465.

Katz, M.E., Katz, D.R., Wright, J.D., Miller, K.G., Pak, D.K., Shackleton, N.J., and E. Thomas, (2003), Early Cenozoic benthic foraminiferal isotopes: Species reliability and interspecies correction factors, *Paleoceanography*, Vol. 18, No. 1024, 12 pp., doi:10.1029/2002PA000798.

Lourens, L.J., Sluijs, A., Kroon, D., Zachos, J.C., Thomas, E., Rohl, U., Bowles, J. and I. Raffi, (2005), Astronomical pacing of late Palaeocene to early Eocene global warming events, *Nature*, Vol. 435, pp. 1083-1087, doi:10.1038/nature03814.

Lunt, D.J., Valdes, P.J., Dunkley Jones, T., Ridgwell, A., Haywood, A.M., Schmidt, D.N., Marsh, R., and Maslin, M, (2010), CO_2-driven ocean circulation changes as an Amplifier of Paleocene-Eocene thermal maximum hydrate destabilization, *Geology*, Vol. 38, No., 10, doi:10.1130/G31184.1.

Lunt, D.J., Ridgwell, A. and Sluijs, A. Zachos, J., Hunter, S., and A. Haywood, (2010), Orbital pacing of methane hydrate destabilization during the Paleogene, *Nature Geoscience,* Vol. 4, pp. 775–778 doi:10.1038/ngeo1266.

Niccolo, M.J., Dickens, G.R., Hollis, C.J., and J.C. Zachos, (2007), Multiple early Eocene hyperthermals: Their sedimentary expression on the New Zealand continental margin and in the deep sea, *Geology*, Vol. 35, No. 8, pp. 699-702, doi:10.1130/G23648A.1.

Norris, R.D., and U. Rohl, (1999), Carbon cycling and chronology of climate warming during the Palaeocene/Eocene transition, *Nature*, Vol. 401, pp. 775-778, doi:10.1038/44545.

Robinson, S.A., (2010), Shallow-water carbonate record of the Paleocene

Eocene Thermal Maximum from a Pacific Ocean guyot, *Geology*, Vol. 39, No 1.pp. 51-54. doi:10.1130/G31422.1.

Palike, H., Norris, R.D., Herrle, J.O., Wilson, P.A., Coxall, H.K., Lear, C.H., Shackleton, N.J., Tripati, A.K., and B.S. Wade, (2006), The Heartbeat of the Oligocene Climate System, *Science*, Vol. 314, No. 5807, pp. 1894-1898, doi:10.1126/science.1133822.

Panchuk, K., (2007), Investigating the Paleocene/Eocene Carbon Cycle Perturbation: An Earth System Model Approach, Ph.D. Dissertation, The Pennsylvania State University.

Panchuk, K., Ridgwell, A. and Kump, L.R. (2008). Sedimentary response to Paleocene Eocene Thermal Maximum carbon release: A model-data comparison. *Geology* 36:4 315-318. doi: 10.1130/G24474A.1

Rohl, U., Westerhold, T., Bralower, T.J., and J.C. Zachos, (2007). On the duration of the Paleocene-Eocene thermal maximum. *Geochemistry, Geophysics, Geosystems*, Vol 8, Q12002, 13 pp., doi:10.1029/2007GC001784.

Russon, T., Paillard, D., and M. Elliot, (2010), Potential origins of 400-500 kyr periodicities in the ocean carbon cycle: A box model approach. *Global Biogeochemical Cycles,* Vol. 24, GB2013, 16 pp., doi:10.1029/2009GB003586.

Sexton, P.F., Wilson, P.A., and R.D. Norris, (2006), Testing the Cenozoic multisite composite $\delta^{18}O$ and $\delta^{13}C$ curves: New monospecific Eocene records from a single locality, Demerara Rise (Ocean Drilling Program Leg 207), *Paleoceanography*, Vol. 21, PA2019, 17 pp., doi:10.1029/2005PA001253.

Sexton, P.N., Norris, R.D., Wilson, P.A., Palike, H., Westerhold, T., Rohl, U., Bolton, C.T., and S. Gibbs, (2011), Multiple Eocene 'hyperthermal' events driven by ocean ventilation, *Nature,* Vol. 471, pp. 349-353. doi:10.1038/nature09826.

Shipboard Scientific Party, 1985. Site 550, In Graciansky, P.C. de, Poag, C.W., et al. (1985), *Initial Reports of the Deep Sea Drilling Program, Leg 80*: Washington (U.S), doi:10.2973/dsdp.proc.80.104.1985.

Shipboard Scientific Party, 1985. Site 577, In Graciansky, P.C. de, Poag, C.W., et al. (1985), *Initial Reports of the Deep Sea Drilling Program, Leg 80*:

Washington (U.S), doi:10.2973/dsdp.proc.86.104.1985.

Shipboard Scientific Party, 1988. Site 690, In Barker, P.E., Kennet, J.P., et al. (1988), *Proceedings of the Ocean Drilling Program, Leg 113*: College Station, Texas (Ocean Drilling Program), pp. 13-32, doi:10/2973/odp.proc.ir.113.107.1988.

Shipboard Scientific Party, 1998. Site 1051, In Norris, R.D., Kroon, D., Klaus, A., et al. (1998), *Proceedings of the Ocean Drilling Program, Leg 171B*: College Station, Texas (Ocean Drilling Program), pp. 93-169, doi:10/2973/odp.proc.ir.171B.105.1998.

Shipboard Scientific Party, 2002. Site 1210, In Bralower, T.J., Premoli Silva, I., Malone, M.J., et al. (2002), *Proceedings of the Ocean Drilling Program, Leg 198*: College Station, Texas (Ocean Drilling Program), pp. 1-89, doi:10/2973/odp.proc.ir.198.106.2002.

Shipboard Scientific Party, 2004, Site 1267, In Zachos, J.C., Kroon, D. Blum, P., et al. (2004), *Proceedings of the Ocean Drilling Program, Leg 208*: College Station, Texas (Ocean Drilling Program), pp. 1-77, doi:10/2973/odp.proc.ir.208.108.2004.

Stap, L., Sluijs, A., Thomas, E., and L. Lourens, (2009), Patterns and magnitude of deep sea carbonate dissolution during Eocene Thermal Maximum 2 and H2, Walvis Ridge, southeastern Atlantic Ocean, *Paleoceanography,* Vol. 24, PA1211, 13 pp., doi:10.1029/2008PA001655.

Stap, L., L.J. Lourens, E. Thomas, A. Sluijs, S. Bohaty, and J.C. Zachos, (2010), High-resolution deep-sea carbon and oxygen isotope records of Eocene Thermal Maximum 2 and H2, *Geology*, Vol. 38, No. 7, pp. 607-610. doi:10.1130/G30777.1

Westerhold, T., Rohl, U., Laskar, J., Raffi, I., Bowles, J., Lourens, L.J., and J.C. Zachos, (2007), On the duration of magnetochrons C24r and C25n and the timing of early Eocene global warming events: Implications from the OceanDrilling Program Leg 208 Walvis Ridge depth transect *Paleoceanography*, Vol. 22, PA2201, 19 pp., doi:10.1029/2006PA001322.

Westerhold., T., and U. Rohl, (2009), High resolution cyclostratigraphy of the early Eocene - new insights into the origin of the Cenozoic cooling trend. *Climates of the Past*, Vol. 5, pp. 309-327. doi:10.5194/cp-5-309-2009.

Zachos, J.C., M. Pagani, L. Sloan, E. Thomas, and K. Billups, (2001), Trends,

Rhythms, and Aberrations in Global Climate 65 Ma to Present, *Science,* Vol. 292, No. 5517, pp. 686-693, doi:10.1126/science.1059412**.**

Zachos, J.C., Rohl, U., Schellenberg, S.A., Sluijs, A., Hodell, D.A., Kelly, D.C., Thomas, E, Nicolo, M.,Raffi, I., Lourens, L.J., McCarren, M., and D. Kroon, (2005), Rapid acidification of the ocean during the Paleocene Eocene Thermal Maximum, *Science,* Vol. 308, No. 5728, pp. 1611-1615 doi:10.1126/science.1109004.

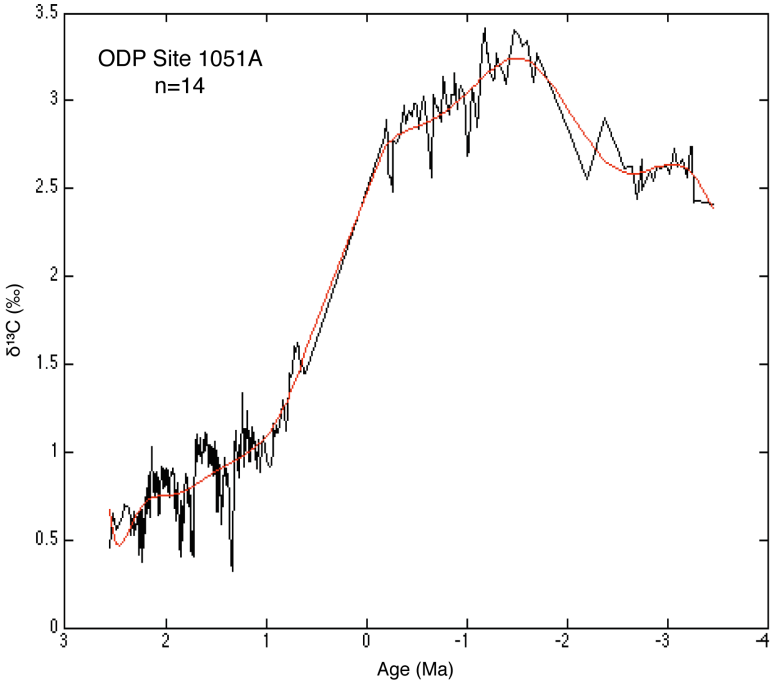
Zachos, J.C., McCarren, H., Murphy, B., Röhl, U., and T. Westerhold, (2010), Tempo and scale of late Paleocene and early Eocene carbon isotope cycles: Implications for the origin of hyperthermals, *Earth and Planetary Science Letters*, Vol. 299, No. 1–2, pp. 242-249, doi:10.1016/j.epsl.2010.09.004.

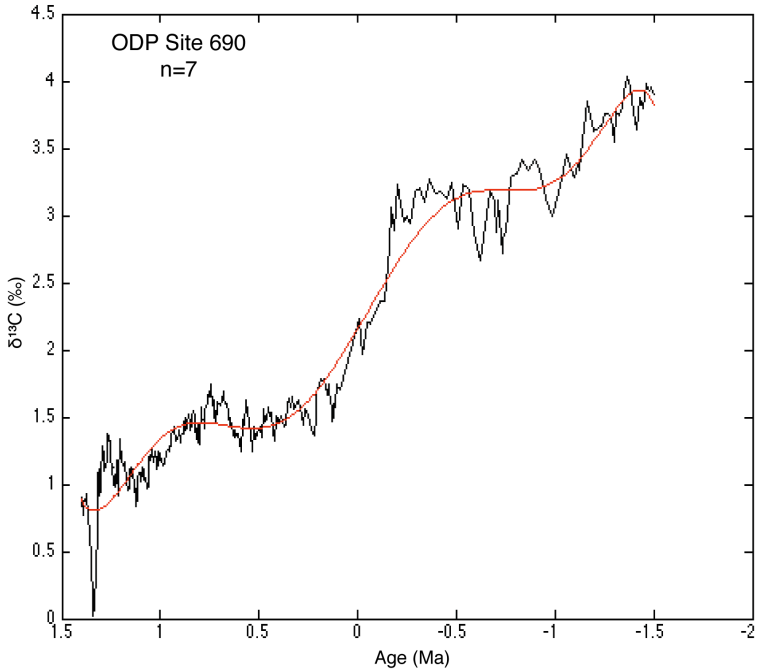
Zeebe, R.E., (2007), An expression for the overall oxygen isotope fractionation between the sum of dissolved inorganic carbon and water, *Geochemistry, Geophysics, Geosystems*, Vol. 8, No.9, QO9002, doi:10.1029/2007GC001663.

Zeebe, R.E., Zachos, J.C., and G.R. Dickens, (2009), Carbon dioxide forcing alone insufficient to explain Palaeocene-Eocene Thermal Maximum warming, *Nature Geoscience*, Vol. 2, pp. 576-580, doi:10.1038/ngeo578.

3.7 Appendix

Figure 3-A1. Long-term carbon isotope records for the early Eocene from DSDP 550, DSDP 577, ODP 1051A, ODP 1051B, ODP 690, ODP 1262 (bulk carbonate, from Cramer et al., 2003), and for the early-middle Eocene from ODP Site 1258 (benthic foraminifera, from Sexton et al., 2011). Early Eocene records are plotted on age models relative to the timing of the PETM from Cramer et al., 2003, and the early-middle Eocene record is plotted on the age model from Sexton et al., 2011. Center red lines indicate polynomial lines of best fit with order specified for each record based on the record's length. We de-trend each record using these calculated lines of best fi in Figure 3-14.


ODP Site 1051A
n=14
δ13C (‰)
Age (Ma)
3.5
3
2.5
2
1.5
1
0.5
0
3
2
1
0
-1
-2
-3
-4


ODP Site 690
n=7
δ13C (‰)
Age (Ma)
4.5
4
3.5
3
2.5
2
1.5
1
0.5
0
1.5
1
0.5
0
-0.5
-1
-1.5
-2

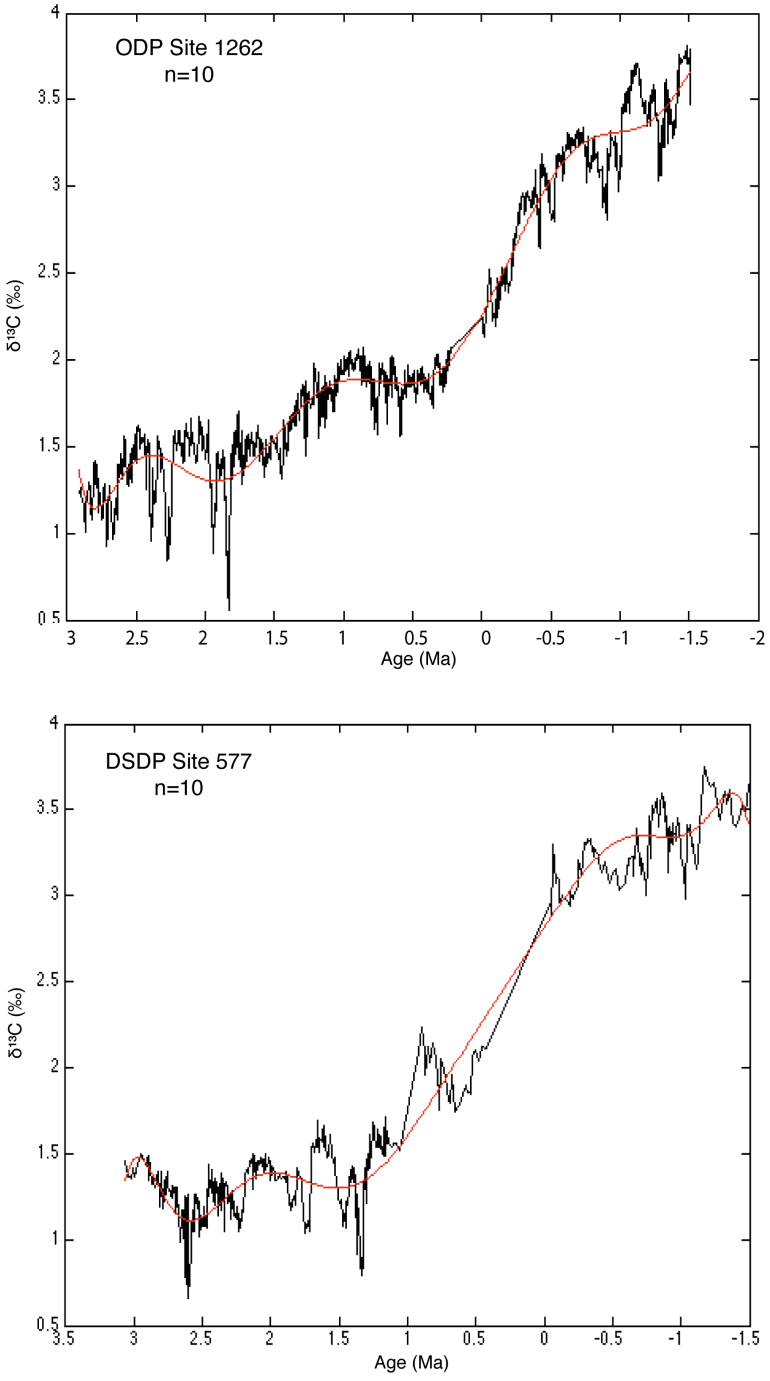


Figure 3-A1, Continued.

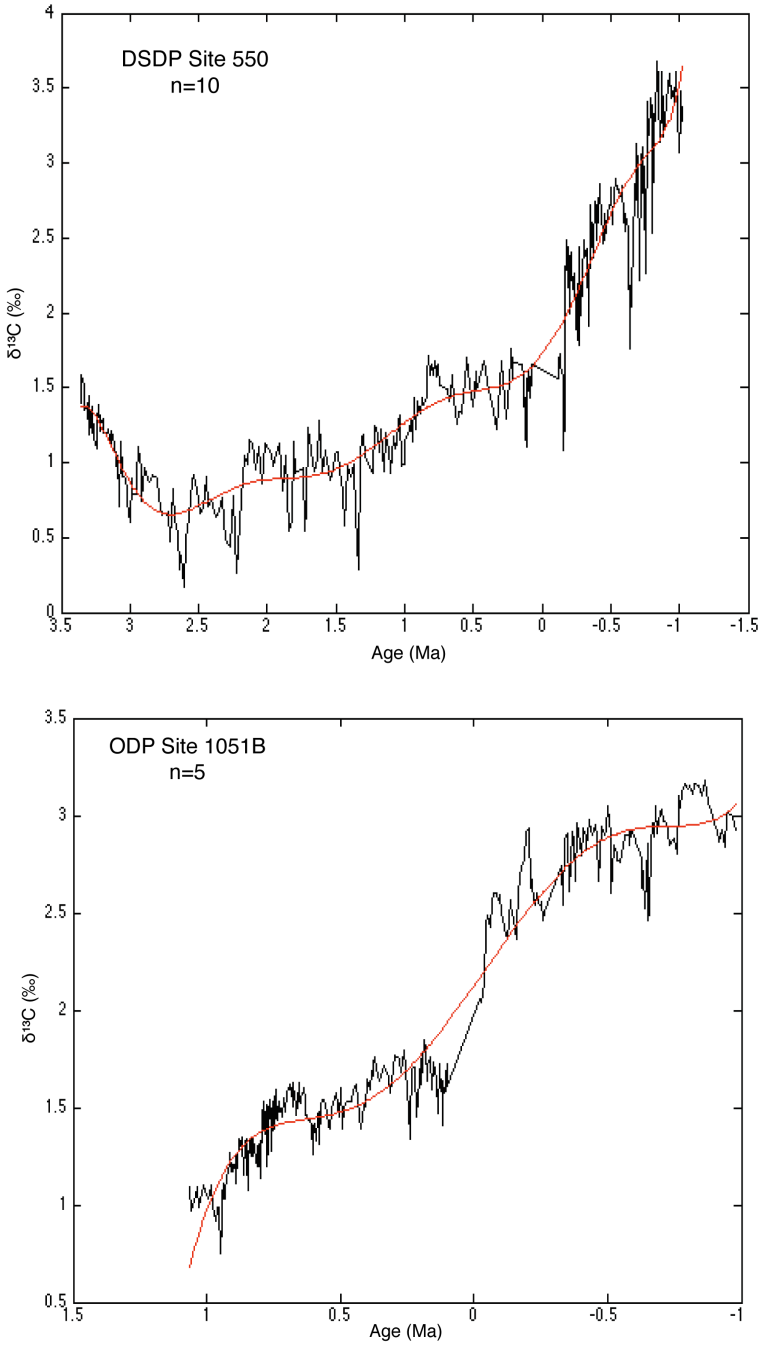


Figure 3-A1, Continued.

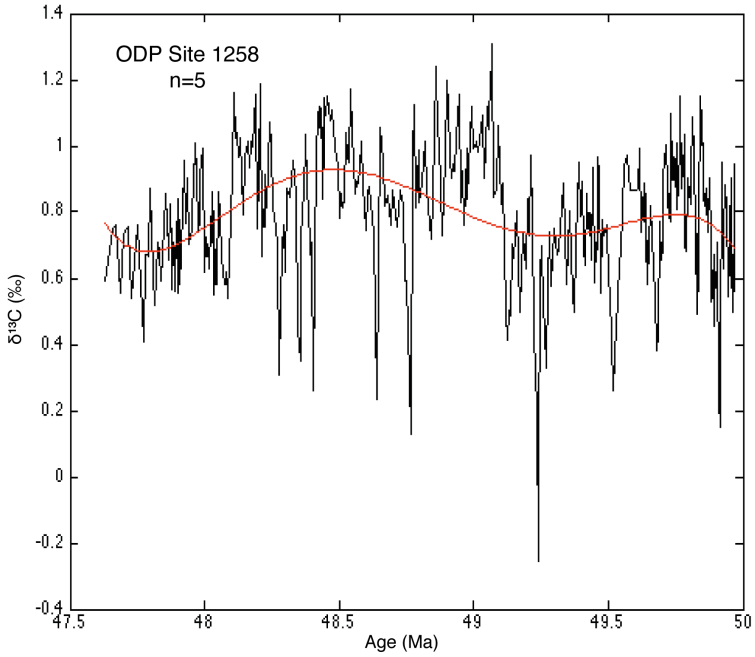


Figure 3-A1, Continued.

Table 3-A1. High-resolution bulk carbonate carbon and oxygen isotope data for Events C22rH2, C22nH2, C22nH3, C21rH1, and C21rH5 from ODP Sites 1258, 1267, and 1210.

Site	Hole	Core	Section	Top	Calculated Age (Ma)	$\delta^{13}C$ (‰)	$\delta^{18}O$ (‰)
C22rH2							
1258	A	7	3	136	49.8751	1.195	-1.358
1258	A	7	3	137	49.8759	1.298	-1.269
1258	A	7	3	138	49.8767	1.332	-1.275
1258	A	7	3	139	49.8775	1.252	-1.446
1258	A	7	3	140	49.8783	1.354	-1.338
1258	A	7	3	141	49.8791	1.166	-1.210
1258	A	7	3	142	49.8798	1.330	-1.351
1258	A	7	3	143	49.8806	1.290	-1.268
1258	A	7	3	144	49.8814	1.240	-1.359
1258	A	7	3	145	49.8822	1.302	-1.288
1258	A	7	3	146	49.8830	1.068	-1.307
1258	A	7	3	147	49.8838	1.046	-1.305
1258	A	7	3	148	49.8845	1.057	-1.259
1258	A	7	3	149	49.8853	1.012	-1.303
1258	A	7	3	150	49.8861	1.093	-1.448
1258	A	7	4	0	49.8861	1.255	-1.483
1258	A	7	4	1	49.8869	1.153	-1.520
1258	A	7	4	2	49.8877	1.253	-1.520
1258	A	7	4	3	49.8885	1.091	-1.520
1258	A	7	4	4	49.8892	1.122	-1.351
1258	A	7	4	5	49.8900	1.303	-1.663
1258	A	7	4	6	49.8908	0.998	-1.282
1258	A	7	4	7	49.8916	1.224	-1.402
1258	A	7	4	8	49.8924	1.296	-1.317
1258	A	7	4	9	49.8931	1.088	-1.160
1258	A	7	4	10	49.8939	1.145	-1.317
1258	A	7	4	11	49.8947	1.166	-1.293
1258	A	7	4	12	49.8955	1.157	-1.313
1258	A	7	4	13	49.8963	0.922	-1.922
1258	A	7	4	14	49.8971	1.084	-1.234
1258	A	7	4	15	49.8979	1.061	-1.210
1258	A	7	4	16	49.8986	1.009	-1.301
1258	A	7	4	17	49.8994	0.954	-1.549
1258	A	7	4	18	49.9002	0.917	-1.577
1258	A	7	4	19	49.9010	1.027	-1.439
1258	A	7	4	20	49.9018	1.114	-1.551
1258	A	7	4	21	49.9025	1.181	-1.528
1258	A	7	4	22	49.9033	1.175	-1.396
1258	A	7	4	23	49.9041	1.101	-1.555
1258	A	7	4	24	49.9049	1.154	-1.636

Table 3-A1, Continued.

Site	Hole	Core	Section	Top	Calculated Age (Ma)	$\delta^{13}C$ (‰)	$\delta^{18}O$ (‰)
1258	A	7	4	25	49.9057	1.071	-1.653
1258	A	7	4	26	49.9064	0.985	-1.546
1258	A	7	4	27	49.9072	1.124	-1.609
1258	A	7	4	28	49.9080	0.872	-1.590
1258	A	7	4	29	49.9087	0.776	-1.577
1258	A	7	4	30	49.9095	1.056	-1.713
1258	A	7	4	31	49.9102	0.704	-1.552
1258	A	7	4	32	49.9109	0.645	-1.726
1258	A	7	4	33	49.9116	0.759	-1.718
1258	A	7	4	34	49.9122	0.720	-1.753
1258	A	7	4	35	49.9128	0.778	-1.777
1258	A	7	4	36	49.9135	0.682	-1.711
1258	A	7	4	37	49.9141	0.976	-2.002
1258	A	7	4	38	49.9147	1.062	-1.932
1258	A	7	4	39	49.9153	0.907	-1.835
1258	A	7	4	40	49.9160	0.964	-1.918
1258	A	7	4	41	49.9166	1.208	-1.972
1258	A	7	4	42	49.9172	1.126	-1.771
1258	A	7	4	43	49.9179	1.026	-1.631
1258	A	7	4	44	49.9185	1.197	-1.667
1258	A	7	4	45	49.9191	1.120	-1.559
1258	A	7	4	46	49.9198	1.128	-1.723
1258	A	7	4	47	49.9204	1.334	-1.597
1258	A	7	4	48	49.9210	1.435	-1.769
1258	A	7	4	49	49.9216	1.082	-1.575
1258	A	7	4	51	49.9229	1.236	-1.440
1258	A	7	4	52	49.9235	1.281	-1.919
1258	A	7	4	53	49.9242	1.267	-1.576
1258	A	7	4	54	49.9248	1.158	-1.554
1258	A	7	4	55	49.9254	1.189	-1.439
1258	A	7	4	56	49.9260	1.248	-1.431
1258	A	7	4	57	49.9267	1.283	-1.378
1258	A	7	4	58	49.9273	1.101	-1.452
1258	A	7	4	59	49.9279	1.232	-1.367
1258	A	7	4	60	49.9286	1.195	-1.313
1258	A	7	4	61	49.9292	1.062	-1.437
1258	A	7	4	62	49.9298	1.119	-1.290
1258	A	7	4	63	49.9304	1.200	-1.179
1258	A	7	4	64	49.9311	1.115	-1.167
1258	A	7	4	65	49.9317	1.195	-1.464
1258	A	7	4	66	49.9323	1.215	-1.305
1258	A	7	4	67	49.9330	1.306	-1.306
1258	A	7	4	68	49.9336	1.247	-1.285

Table 3-A1, Continued.

Site	Hole	Core	Section	Top	Calculated Age (Ma)	$\delta^{13}C$ (‰)	$\delta^{18}O$ (‰)
1258	A	7	4	69	49.9342	1.167	-1.641
1258	A	7	4	70	49.9348	1.149	-1.402
1258	A	7	4	71	49.9355	1.323	-1.376
1258	A	7	4	72	49.9361	1.229	-1.494
1258	A	7	4	73	49.9367	1.206	-1.366
1258	A	7	4	74	49.9374	1.097	-1.455
1258	A	7	4	75	49.9380	1.185	-1.441
C22nH2							
1258	B	6	3	1	49.4616	1.203	-1.518
1258	B	6	3	2	49.4627	1.285	-1.666
1258	B	6	3	3	49.4637	1.400	-1.617
1258	B	6	3	4	49.4648	1.240	-1.591
1258	B	6	3	5	49.4659	1.360	-1.679
1258	B	6	3	6	49.4669	1.403	-1.753
1258	B	6	3	7	49.4680	1.238	-1.804
1258	B	6	3	8	49.4690	1.328	-1.736
1258	B	6	3	9	49.4701	1.397	-1.811
1258	B	6	3	10	49.4711	1.507	-1.817
1258	B	6	3	11	49.4722	1.314	-1.780
1258	B	6	3	12	49.4732	1.290	-1.646
1258	B	6	3	13	49.4743	1.373	-1.700
1258	B	6	3	14	49.4754	1.559	-1.827
1258	B	6	3	15	49.4764	1.258	-1.682
1258	B	6	3	16	49.4775	1.281	-1.752
1258	B	6	3	17	49.4785	1.432	-1.789
1258	B	6	3	18	49.4797	1.364	-1.678
1258	B	6	3	19	49.4808	1.233	-1.624
1258	B	6	3	20	49.4819	1.275	-1.700
1258	B	6	3	21	49.4831	1.232	-1.674
1258	B	6	3	22	49.4842	1.164	-1.846
1258	B	6	3	23	49.4853	1.167	-1.709
1258	B	6	3	24	49.4865	1.138	-1.668
1258	B	6	3	25	49.4876	1.291	-1.562
1258	B	6	3	26	49.4888	1.138	-1.569
1258	B	6	3	27	49.4899	1.265	-1.715
1258	B	6	3	28	49.4910	1.237	-1.702
1258	B	6	3	29	49.4922	1.328	-1.675
1258	B	6	3	30	49.4933	1.364	-1.693
1258	B	6	3	31	49.4945	1.416	-1.847
1258	B	6	3	32	49.4956	1.281	-1.723
1258	B	6	3	33	49.4968	1.321	-1.768
1258	B	6	3	34	49.4979	1.297	-1.677

Table 3-A1, Continued.

Site	Hole	Core	Section	Top	Calculated Age (Ma)	$\delta^{13}C$ (‰)	$\delta^{18}O$ (‰)
1258	B	6	3	35	49.4991	1.165	-1.844
1258	B	6	3	36	49.5002	1.295	-1.691
1258	B	6	3	37	49.5013	1.192	-1.652
1258	B	6	3	38	49.5025	1.283	-1.728
1258	B	6	3	39	49.5036	1.135	-1.609
1258	B	6	3	40	49.5048	1.194	-1.704
1258	B	6	3	41	49.5059	1.159	-1.683
1258	B	6	3	42	49.5071	1.066	-1.712
1258	B	6	3	43	49.5083	1.058	-1.627
1258	B	6	3	44	49.5095	0.858	-1.920
1258	B	6	3	45	49.5107	0.972	-1.767
1258	B	6	3	46	49.5119	0.910	-1.811
1258	B	6	3	47	49.5131	1.019	-1.801
1258	B	6	3	48	49.5144	0.934	-1.754
1258	B	6	3	49	49.5156	1.128	-1.653
1258	B	6	3	50	49.5168	1.092	-1.776
1258	B	6	3	51	49.5180	1.117	-1.916
1258	B	6	3	52	49.5193	1.288	-2.003
1258	B	6	3	53	49.5206	1.155	-1.842
1258	B	6	3	54	49.5220	0.802	-1.736
1258	B	6	3	55	49.5234	0.798	-2.106
1258	B	6	3	56	49.5248	0.756	-1.821
1258	B	6	3	57	49.5262	1.106	-1.996
1258	B	6	3	58	49.5276	0.842	-2.052
1258	B	6	3	59	49.5289	0.898	-1.901
1258	B	6	3	60	49.5303	0.837	-1.824
1258	B	6	3	61	49.5317	1.048	-1.947
1258	B	6	3	62	49.5331	0.850	-1.963
1258	B	6	3	63	49.5345	0.897	-1.763
1258	B	6	3	64	49.5359	1.106	-1.996
1258	B	6	3	65	49.5373	1.150	-1.891
1258	B	6	3	66	49.5387	1.160	-1.844
1258	B	6	3	67	49.5400	0.985	-1.746
1258	B	6	3	68	49.5414	0.976	-1.759
1258	B	6	3	69	49.5428	1.099	-1.729
1258	B	6	3	70	49.5442	1.006	-1.738
1258	B	6	3	71	49.5456	0.925	-1.937
1258	B	6	3	72	49.5470	0.967	-2.322
1258	B	6	3	73	49.5484	1.198	-2.341
1258	B	6	3	74	49.5498	1.190	-2.106
1258	B	6	3	75	49.5511	1.173	-1.911
1258	B	6	3	76	49.5525	1.453	-1.870
1258	B	6	3	77	49.5539	1.256	-1.903

Table 3-A1, Continued.

Site	Hole	Core	Section	Top	Calculated Age (Ma)	$\delta^{13}C$ (‰)	$\delta^{18}O$ (‰)
1258	B	6	3	78	49.5553	1.356	-1.990
1258	B	6	3	79	49.5567	1.438	-1.865
1258	B	6	3	80	49.5581	1.372	-1.996
1258	B	6	3	81	49.5596	1.341	-1.774
1258	B	6	3	82	49.5611	1.359	-1.978
1258	B	6	3	83	49.5629	1.462	-1.874
1258	B	6	3	84	49.5650	1.286	-1.764
1258	B	6	3	85	49.5670	1.456	-1.786
1258	B	6	3	86	49.5691	1.302	-1.805
1258	B	6	3	87	49.5712	1.226	-1.791
1258	B	6	3	88	49.5733	1.556	-1.903
1258	B	6	3	89	49.5755	1.295	-1.857
1258	B	6	3	90	49.5778	1.120	-1.887
C22nH3							
1258	A	6	5	110	49.0897	1.432	-1.245
1258	A	6	5	111	49.0911	1.472	-1.188
1258	A	6	5	112	49.0925	1.296	-1.315
1258	A	6	5	113	49.0939	1.440	-1.061
1258	A	6	5	114	49.0953	1.376	-1.117
1258	A	6	5	115	49.0967	1.350	-1.286
1258	A	6	5	116	49.0981	1.309	-1.156
1258	A	6	5	117	49.0995	1.345	-1.283
1258	A	6	5	118	49.1008	1.442	-1.232
1258	A	6	5	119	49.1022	1.430	-1.310
1258	A	6	5	120	49.1036	1.664	-1.476
1258	A	6	5	121	49.1050	1.344	-1.247
1258	A	6	5	122	49.1064	1.313	-1.340
1258	A	6	5	123	49.1077	1.359	-1.332
1258	A	6	5	124	49.1091	1.291	-1.368
1258	A	6	5	125	49.1104	1.447	-1.415
1258	A	6	5	126	49.1117	1.408	-1.415
1258	A	6	5	127	49.1130	1.432	-1.304
1258	A	6	5	128	49.1143	1.410	-1.310
1258	A	6	5	129	49.1156	1.307	-1.361
1258	A	6	5	130	49.1169	1.394	-1.414
1258	A	6	5	131	49.1182	1.394	-1.417
1258	A	6	5	132	49.1194	1.151	-1.382
1258	A	6	5	133	49.1207	1.312	-1.418
1258	A	6	5	134	49.1220	1.413	-1.478
1258	A	6	5	135	49.1232	1.451	-1.480
1258	A	6	5	136	49.1245	1.357	-1.532
1258	A	6	5	137	49.1258	1.377	-1.419

Table 3-A1, Continued.

Site	Hole	Core	Section	Top	Calculated Age (Ma)	$\delta^{13}C$ (‰)	$\delta^{18}O$ (‰)
1258	A	6	5	138	49.1271	1.294	-1.340
1258	A	6	5	139	49.1283	1.396	-1.626
1258	A	6	5	140	49.1296	1.255	-1.525
1258	A	6	5	141	49.1309	1.345	-1.525
1258	A	6	5	142	49.1321	1.452	-1.488
1258	A	6	5	143	49.1334	1.202	-1.466
1258	A	6	5	144	49.1347	1.414	-1.599
1258	A	6	5	145	49.1360	1.444	-1.593
1258	A	6	5	146	49.1372	1.341	-1.578
1258	A	6	5	147	49.1385	1.349	-1.558
1258	A	6	5	148	49.1398	1.414	-1.641
1258	A	6	5	149	49.1410	1.412	-1.457
1258	A	6	5	150	49.1423	1.495	-1.497
1258	A	6	6	1	49.1436	1.483	-1.486
1258	A	6	6	2	49.1449	1.396	-2.013
1258	A	6	6	3	49.1461	1.337	-1.666
1258	A	6	6	4	49.1474	1.439	-1.615
1258	A	6	6	5	49.1487	1.365	-1.661
1258	A	6	6	6	49.1502	1.559	-1.679
1258	A	6	6	7	49.1517	1.394	-1.628
1258	A	6	6	8	49.1534	1.373	-1.607
1258	A	6	6	9	49.1552	1.484	-1.610
1258	A	6	6	10	49.1571	1.304	-1.549
1258	A	6	6	11	49.1590	1.456	-1.575
1258	A	6	6	12	49.1609	1.299	-1.517
1258	A	6	6	13	49.1629	1.262	-1.348
1258	A	6	6	14	49.1651	1.328	-1.419
1258	A	6	6	15	49.1673	1.341	-1.486
1258	A	6	6	16	49.1694	1.247	-1.484
1258	A	6	6	17	49.1716	1.327	-1.416
1258	A	6	6	18	49.1738	1.489	-1.582
1258	A	6	6	19	49.1759	1.404	-1.632
1258	A	6	6	20	49.1781	1.279	-1.596
1258	A	6	6	21	49.1803	1.324	-1.503
1258	A	6	6	22	49.1824	1.023	-1.880
1258	A	6	6	23	49.1846	1.158	-1.553
1258	A	6	6	24	49.1868	1.364	-1.622
1258	A	6	6	25	49.1889	1.410	-1.619
1258	A	6	6	26	49.1909	1.230	-1.708
1258	A	6	6	27	49.1929	1.184	-1.754
1258	A	6	6	28	49.1945	1.375	-1.660
1258	A	6	6	29	49.1957	1.325	-1.581
1258	A	6	6	30	49.1969	1.371	-1.613

Table 3-A1, Continued.

Site	Hole	Core	Section	Top	Calculated Age (Ma)	$\delta^{13}C$ (‰)	$\delta^{18}O$ (‰)
1258	A	6	6	31	49.1981	1.156	-1.608
1258	A	6	6	32	49.1992	1.368	-1.615
1258	A	6	6	33	49.2004	1.555	-1.638
1258	A	6	6	34	49.2016	1.296	-1.399
1258	A	6	6	35	49.2028	1.408	-1.425
1258	A	6	6	36	49.2040	1.532	-1.293
1258	A	6	6	37	49.2052	1.360	-1.304
1258	A	6	6	38	49.2064	1.331	-1.414
1258	A	6	6	39	49.2076	1.418	-1.437
1258	A	6	6	40	49.2088	1.414	-1.353
1258	A	6	6	41	49.2099	1.378	-1.495
1258	A	6	6	42	49.2111	1.464	-1.781
1258	A	6	6	43	49.2123	1.314	-1.440
1258	A	6	6	44	49.2135	1.287	-1.414
1258	A	6	6	45	49.2147	1.391	-1.486
1258	A	6	6	46	49.2159	1.224	-1.552
1258	A	6	6	47	49.2171	1.265	-1.327
1258	A	6	6	48	49.2183	1.395	-1.510
1258	A	6	6	49	49.2195	1.296	-1.605
1258	A	6	6	50	49.2206	1.289	-1.611
1258	A	6	6	51	49.2218	1.133	-1.573
1258	A	6	6	52	49.2230	1.283	-1.493
1258	A	6	6	53	49.2241	1.003	-1.426
1258	A	6	6	54	49.2251	1.250	-1.671
1258	A	6	6	55	49.2262	1.199	-1.590
1258	A	6	6	56	49.2272	1.195	-1.662
1258	A	6	6	57	49.2283	1.187	-1.724
1258	A	6	6	58	49.2293	0.937	-1.674
1258	A	6	6	59	49.2302	1.296	-1.798
1258	A	6	6	60	49.2312	1.254	-1.999
1258	A	6	6	61	49.2321	0.975	-1.680
1258	A	6	6	62	49.2331	1.080	-1.791
1258	A	6	6	63	49.2340	0.778	-1.866
1258	A	6	6	64	49.2350	0.912	-1.730
1258	A	6	6	65	49.2360	1.176	-1.862
1258	A	6	6	66	49.2369	1.050	-1.826
1258	A	6	6	67	49.2379	0.927	-1.707
1258	A	6	6	68	49.2388	0.836	-1.833
1258	A	6	6	69	49.2398	1.018	-1.993
1258	A	6	6	70	49.2407	0.660	-2.196
1258	A	6	6	71	49.2417	0.885	-1.899
1258	A	6	6	72	49.2427	0.876	-1.904
1258	A	6	6	73	49.2436	1.083	-2.037

Table 3-A1, Continued.

Site	Hole	Core	Section	Top	Calculated Age (Ma)	$\delta^{13}C$ (‰)	$\delta^{18}O$ (‰)
1258	A	6	6	74	49.2446	1.087	-1.978
1258	A	6	6	75	49.2455	0.927	-1.770
1258	A	6	6	76	49.2456	1.123	-1.738
1258	A	6	6	77	49.2457	1.194	-1.698
1258	A	6	6	78	49.2460	1.072	-1.747
1258	A	6	6	79	49.2466	1.051	-1.667
1258	A	6	6	80	49.2471	1.054	-1.696
1258	A	6	6	81	49.2476	0.824	-1.718
1258	A	6	6	82	49.2482	0.903	-1.757
1258	B	6	1	135	49.2465	1.189	-1.591
1258	B	6	1	136	49.2474	1.069	-1.641
1258	B	6	1	137	49.2484	1.003	-1.636
1258	B	6	1	138	49.2493	1.224	-1.666
1258	B	6	1	139	49.2503	1.146	-1.670
1258	B	6	1	140	49.2513	1.033	-1.662
1258	B	6	1	141	49.2522	1.102	-1.729
1258	B	6	1	142	49.2532	1.115	-1.680
1258	B	6	1	143	49.2541	1.108	-1.638
1258	B	6	1	144	49.2551	1.107	-1.697
1258	B	6	1	145	49.2560	1.038	-1.711
1258	B	6	1	146	49.2570	1.310	-1.843
1258	B	6	1	147	49.2580	1.091	-1.718
1258	B	6	1	148	49.2589	1.080	-1.718
1258	B	6	1	149	49.2599	0.876	-1.676
1258	B	6	1	150	49.2608	1.081	-1.667
C21rH1							
1258	A	6	3	130	48.7226	1.218	-1.376
1258	A	6	3	131	48.7243	1.265	-1.349
1258	A	6	3	132	48.7259	1.617	-1.659
1258	A	6	3	133	48.7274	1.228	-1.332
1258	A	6	3	134	48.7288	1.216	-1.444
1258	A	6	3	135	48.7301	1.187	-1.411
1258	A	6	3	136	48.7314	1.252	-1.454
1258	A	6	3	137	48.7327	1.309	-1.371
1258	A	6	3	138	48.7340	1.244	-1.478
1258	A	6	3	139	48.7354	1.205	-1.524
1258	A	6	3	140	48.7367	1.244	-1.482
1258	A	6	3	141	48.7380	1.101	-1.492
1258	A	6	3	142	48.7393	1.120	-1.402
1258	A	6	3	143	48.7406	1.278	-1.420
1258	A	6	3	144	48.7420	1.184	-1.439
1258	A	6	3	145	48.7433	1.287	-1.496

Table 3-A1, Continued.

Site	Hole	Core	Section	Top	Calculated Age (Ma)	$\delta^{13}C$ (‰)	$\delta^{18}O$ (‰)
1258	A	6	3	146	48.7446	1.186	-1.551
1258	A	6	3	147	48.7459	1.055	-1.503
1258	A	6	3	148	48.7472	1.271	-1.593
1258	A	6	3	149	48.7486	1.091	-1.542
1258	A	6	3	150	48.7499	1.135	-1.373
1258	A	6	4	1	48.7512	0.965	-1.327
1258	A	6	4	2	48.7525	1.106	-1.502
1258	A	6	4	3	48.7538	1.035	-1.306
1258	A	6	4	4	48.7552	0.990	-1.365
1258	A	6	4	5	48.7565	1.036	-1.360
1258	A	6	4	6	48.7578	0.932	-1.330
1258	A	6	4	7	48.7591	1.232	-1.439
1258	A	6	4	8	48.7605	0.902	-1.504
1258	A	6	4	9	48.7618	0.982	-1.640
1258	A	6	4	10	48.7632	0.892	-1.767
1258	A	6	4	11	48.7645	1.005	-1.699
1258	A	6	4	12	48.7659	0.910	-1.676
1258	A	6	4	13	48.7672	0.934	-1.695
1258	A	6	4	14	48.7686	1.086	-1.764
1258	A	6	4	15	48.7700	0.949	-1.951
1258	A	6	4	16	48.7714	1.153	-2.098
1258	A	6	4	17	48.7727	1.239	-1.777
1258	A	6	4	18	48.7741	1.225	-1.871
1258	A	6	4	19	48.7755	1.242	-1.839
1258	A	6	4	20	48.7769	1.227	-1.725
1258	A	6	4	21	48.7782	1.172	-1.976
1258	A	6	4	22	48.7796	1.489	-1.511
1258	A	6	4	23	48.7810	1.446	-1.551
1258	A	6	4	24	48.7823	1.363	-1.472
1258	A	6	4	25	48.7837	1.441	-1.523
1258	A	6	4	26	48.7851	1.225	-1.682
1258	A	6	4	27	48.7865	1.398	-1.556
1258	A	6	4	28	48.7878	1.431	-1.701
1258	A	6	4	29	48.7892	1.381	-1.697
1258	A	6	4	30	48.7906	1.362	-1.603
1258	A	6	4	31	48.7919	1.375	-1.586
1258	A	6	4	32	48.7933	1.308	-1.557
1258	A	6	4	33	48.7947	1.448	-1.546
1258	A	6	4	34	48.7961	1.331	-1.529
1258	A	6	4	35	48.7974	1.492	-1.639
1258	A	6	4	36	48.7988	1.304	-1.553
1258	A	6	4	37	48.8002	1.514	-1.544
1258	A	6	4	38	48.8015	1.312	-1.644

Table 3-A1, Continued.

Site	Hole	Core	Section	Top	Calculated Age (Ma)	$\delta^{13}C$ (‰)	$\delta^{18}O$ (‰)
1258	A	6	4	39	48.8029	1.428	-1.542
1258	A	6	4	40	48.8043	1.255	-1.551
C21rH5							
1258	B	5	3	25	48.2354	1.347	-1.534
1258	B	5	3	26	48.2363	1.144	-1.669
1258	B	5	3	27	48.2372	1.407	-1.366
1258	B	5	3	28	48.2381	1.464	-1.409
1258	B	5	3	29	48.2391	1.449	-1.365
1258	B	5	3	30	48.2401	1.492	-1.345
1258	B	5	3	31	48.2411	1.481	-1.322
1258	B	5	3	32	48.2422	1.363	-1.339
1258	B	5	3	33	48.2434	1.372	-1.343
1258	B	5	3	34	48.2447	1.571	-1.463
1258	B	5	3	35	48.2460	1.495	-1.364
1258	B	5	3	36	48.2473	1.650	-1.467
1258	B	5	3	37	48.2486	1.490	-1.397
1258	B	5	3	38	48.2499	1.484	-1.283
1258	B	5	3	39	48.2512	1.495	-1.232
1258	B	5	3	40	48.2525	1.480	-1.277
1258	B	5	3	41	48.2538	1.583	-1.465
1258	B	5	3	42	48.2551	1.569	-1.356
1258	B	5	3	43	48.2564	1.568	-1.481
1258	B	5	3	44	48.2577	1.504	-1.443
1258	B	5	3	45	48.2590	1.422	-1.353
1258	B	5	3	46	48.2604	1.248	-1.354
1258	B	5	3	47	48.2617	1.505	-1.310
1258	B	5	3	48	48.2630	1.352	-1.384
1258	B	5	3	49	48.2643	1.333	-1.273
1258	B	5	3	50	48.2656	1.298	-1.334
1258	B	5	3	51	48.2669	1.505	-1.508
1258	B	5	3	52	48.2682	1.208	-2.010
1258	B	5	3	53	48.2695	1.305	-1.428
1258	B	5	3	54	48.2708	0.976	-1.950
1258	B	5	3	55	48.2721	1.276	-1.561
1258	B	5	3	56	48.2734	1.191	-1.451
1258	B	5	3	57	48.2747	1.452	-1.573
1258	B	5	3	58	48.2760	1.464	-1.555
1258	B	5	3	59	48.2773	1.418	-1.760
1258	B	5	3	60	48.2786	1.029	-1.534
1258	B	5	3	61	48.2799	1.166	-1.426
1258	B	5	3	62	48.2811	1.163	-1.650
1258	B	5	3	63	48.2824	1.153	-1.563

Table 3-A1, Continued.

Site	Hole	Core	Section	Top	Calculated Age (Ma)	$\delta^{13}C$ (‰)	$\delta^{18}O$ (‰)
1258	B	5	3	64	48.2835	1.084	-1.564
1258	B	5	3	65	48.2847	1.496	-1.792
1258	B	5	3	66	48.2859	1.392	-1.737
1258	B	5	3	67	48.2870	1.421	-1.604
1258	B	5	3	68	48.2882	1.190	-1.337
1258	B	5	3	69	48.2894	1.684	-1.747
1258	B	5	3	70	48.2906	1.445	-1.866
1258	B	5	3	71	48.2917	1.296	-1.533
1258	B	5	3	72	48.2929	1.290	-1.447
1258	B	5	3	73	48.2941	1.486	-1.527
1258	B	5	3	74	48.2952	1.307	-1.423
1258	B	5	3	75	48.2964	1.563	-1.776
1258	B	5	3	76	48.2976	1.523	-1.563
1258	B	5	3	77	48.2988	1.358	-1.558
1258	B	5	3	78	48.2999	1.433	-1.433
1258	B	5	3	79	48.3011	1.492	-1.488
1258	B	5	3	80	48.3023	1.521	-1.434
1258	B	5	3	81	48.3034	1.379	-1.177
1258	B	5	3	82	48.3046	1.436	-1.558
1258	B	5	3	83	48.3058	1.479	-1.359
1258	B	5	3	84	48.3069	1.426	-1.297
1258	B	5	3	85	48.3081	1.542	-1.397
1258	B	5	3	86	48.3093	1.513	-1.570
1258	B	5	3	87	48.3105	1.532	-1.653
1258	B	5	3	88	48.3116	1.320	-1.374
1258	B	5	3	89	48.3128	1.452	-1.340
1258	B	5	3	90	48.3140	1.761	-1.361
1258	B	5	3	91	48.3152	1.475	-1.211
1258	B	5	3	92	48.3164	1.638	-1.345
1258	B	5	3	93	48.3177	1.505	-1.390
1258	B	5	3	94	48.3191	1.539	-1.426
1258	B	5	3	95	48.3205	1.465	-1.284
1258	B	5	3	96	48.3220	1.501	-1.182
1258	B	5	3	97	48.3234	1.331	-1.338
1258	B	5	3	98	48.3248	1.590	-1.254
1258	B	5	3	99	48.3262	1.413	-1.364
1258	B	5	3	100	48.3276	1.576	-1.334
1258	B	5	3	101	48.3291	1.510	-1.240
1258	B	5	3	102	48.3305	1.345	-1.489
1258	B	5	3	103	48.3321	1.279	-1.589
1258	B	5	3	104	48.3337	1.306	-1.400
1258	B	5	3	105	48.3354	1.367	-1.308

Table 3-A1, Continued.

Site	Hole	Core	Section	Top	Calculated Age (Ma)	$\delta^{13}C$ (‰)	$\delta^{18}O$ (‰)
C22rH2							
1267	B	18	5	5	49.8731	1.990	-0.482
1267	B	18	5	6	49.8737	2.037	-0.414
1267	B	18	5	7	49.8744	2.019	-0.445
1267	B	18	5	8	49.8750	2.103	-0.277
1267	B	18	5	9	49.8757	2.051	-0.401
1267	B	18	5	10	49.8764	2.059	-0.222
1267	B	18	5	11	49.8770	2.055	-0.340
1267	B	18	5	12	49.8777	1.825	-0.881
1267	B	18	5	13	49.8783	1.976	-0.566
1267	B	18	5	14	49.8790	2.042	-0.427
1267	B	18	5	16	49.8803	1.926	-0.567
1267	B	18	5	17	49.8810	1.977	-0.623
1267	B	18	5	18	49.8816	1.911	-0.634
1267	B	18	5	19	49.8823	1.988	-0.637
1267	B	18	5	20	49.8829	1.934	-0.692
1267	B	18	5	21	49.8835	1.925	-0.698
1267	B	18	5	22	49.8842	1.924	-0.772
1267	B	18	5	23	49.8848	1.994	-0.665
1267	B	18	5	24	49.8855	1.945	-0.769
1267	B	18	5	25	49.8862	2.047	-0.640
1267	B	18	5	26	49.8868	2.073	-0.667
1267	B	18	5	27	49.8875	2.154	-0.478
1267	B	18	5	28	49.8881	2.089	-0.438
1267	B	18	5	29	49.8888	2.074	-0.483
1267	B	18	5	30	49.8894	2.134	-0.349
1267	B	18	5	31	49.8901	2.152	-0.355
1267	B	18	5	33	49.8914	2.111	-0.282
1267	B	18	5	34	49.8921	2.177	-0.370
1267	B	18	5	35	49.8927	2.178	-0.346
1267	B	18	5	36	49.8933	2.116	-0.302
1267	B	18	5	37	49.8940	2.085	-0.361
1267	B	18	5	38	49.8946	2.053	-0.322
1267	B	18	5	39	49.8953	2.068	-0.339
1267	B	18	5	40	49.8960	2.059	-0.384
1267	B	18	5	41	49.8966	2.009	-0.350
1267	B	18	5	42	49.8973	1.963	-0.373
1267	B	18	5	43	49.8979	2.013	-0.395
1267	B	18	5	44	49.8986	1.892	-0.437
1267	B	18	5	45	49.8992	1.976	-0.323
1267	B	18	5	46	49.8999	1.808	-0.556
1267	B	18	5	47	49.9006	1.757	-0.772

Table 3-A1, Continued.

Site	Hole	Core	Section	Top	Calculated Age (Ma)	$\delta^{13}C$ (‰)	$\delta^{18}O$ (‰)
1267	B	18	5	48	49.9012	1.888	-0.446
1267	B	18	5	49	49.9019	1.814	-0.563
1267	B	18	5	50	49.9025	1.816	-0.541
1267	B	18	5	51	49.9031	1.864	-0.517
1267	B	18	5	52	49.9038	1.765	-0.615
1267	B	18	5	53	49.9044	1.671	-0.656
1267	B	18	5	54	49.9051	1.851	-0.456
1267	B	18	5	55	49.9058	1.787	-0.544
1267	B	18	5	56	49.9064	1.730	-0.586
1267	B	18	5	57	49.9071	1.812	-0.452
1267	B	18	5	58	49.9078	1.758	-0.558
1267	B	18	5	59	49.9086	1.649	-0.724
1267	B	18	5	60	49.9094	1.896	-0.411
1267	B	18	5	61	49.9102	1.653	-0.569
1267	B	18	5	62	49.9111	1.808	-0.441
1267	B	18	5	63	49.9119	1.709	-0.476
1267	B	18	5	64	49.9128	1.720	-0.439
1267	B	18	5	66	49.9144	1.637	-0.803
1267	B	18	5	67	49.9152	1.587	-0.806
1267	B	18	5	68	49.9160	1.732	-0.646
1267	B	18	5	69	49.9169	1.617	-0.724
1267	B	18	5	70	49.9177	1.478	-1.062
1267	B	18	5	71	49.9185	1.596	-0.855
1267	B	18	5	72	49.9194	1.534	-0.787
1267	B	18	5	73	49.9202	1.553	-0.900
1267	B	18	5	74	49.9211	1.499	-1.022
1267	B	18	5	75	49.9219	1.609	-0.833
1267	B	18	5	76	49.9229	1.822	-0.663
1267	B	18	5	77	49.9238	1.919	-0.665
1267	B	18	5	78	49.9249	1.810	-0.641
1267	B	18	5	79	49.9260	1.767	-0.750
1267	B	18	5	80	49.9271	1.731	-0.662
1267	B	18	5	81	49.9283	1.882	-0.555
1267	B	18	5	82	49.9294	1.830	-0.665
1267	B	18	5	83	49.9306	1.729	-0.633
1267	B	18	5	84	49.9317	1.710	-0.767
1267	B	18	5	85	49.9328	1.834	-0.485
1267	B	18	5	86	49.9340	1.747	-0.758
1267	B	18	5	87	49.9351	1.844	-0.707
1267	B	18	5	88	49.9363	1.717	-0.947
1267	B	18	5	89	49.9374	1.821	-0.783
1267	B	18	5	90	49.9386	1.754	-0.855

Table 3-A1, Continued.

Site	Hole	Core	Section	Top	Calculated Age (Ma)	$\delta^{13}C$ (‰)	$\delta^{18}O$ (‰)
C22nH2							
1267	A	17	6	20	49.4752	2.037	-0.563
1267	A	17	6	21	49.4764	2.109	-0.534
1267	A	17	6	22	49.4775	2.050	-0.575
1267	A	17	6	23	49.4787	2.007	-0.619
1267	A	17	6	24	49.4829	2.027	-0.665
1267	A	17	6	25	49.4870	2.037	-0.763
1267	A	17	6	26	49.4888	1.980	-0.643
1267	A	17	6	27	49.4905	1.953	-0.577
1267	A	17	6	28	49.4923	1.963	-0.728
1267	A	17	6	29	49.4949	2.048	-0.786
1267	A	17	6	30	49.4975	1.969	-0.684
1267	A	17	6	31	49.4996	1.961	-0.726
1267	A	17	6	32	49.5017	1.990	-0.655
1267	A	17	6	33	49.5038	1.920	-0.638
1267	A	17	6	34	49.5059	1.932	-0.539
1267	A	17	6	35	49.5080	1.881	-0.583
1267	A	17	6	36	49.5101	1.982	-0.342
1267	A	17	6	37	49.5122	1.949	-0.490
1267	A	17	6	38	49.5142	1.980	-0.488
1267	A	17	6	39	49.5163	1.889	-0.590
1267	A	17	6	40	49.5184	1.982	-0.642
1267	A	17	6	41	49.5205	1.903	-0.696
1267	A	17	6	42	49.5226	1.725	-0.826
1267	A	17	6	43	49.5246	1.864	-0.648
1267	A	17	6	44	49.5267	1.936	-0.597
1267	A	17	6	45	49.5288	1.815	-0.638
1267	A	17	6	46	49.5309	1.835	-0.625
1267	A	17	6	47	49.5330	1.853	-0.748
1267	A	17	6	48	49.5351	1.840	-0.654
1267	A	17	6	49	49.5372	1.796	-0.690
1267	A	17	6	50	49.5393	1.847	-0.733
1267	A	17	6	51	49.5414	1.812	-0.848
1267	A	17	6	52	49.5435	1.805	-0.904
1267	A	17	6	53	49.5465	1.782	-0.908
1267	A	17	6	54	49.5506	1.884	-0.876
1267	A	17	6	55	49.5546	1.846	-0.887
1267	A	17	6	56	49.5587	1.909	-0.813
1267	A	17	6	57	49.5628	1.933	-0.839
1267	A	17	6	58	49.5668	1.895	-0.640
1267	A	17	6	59	49.5709	1.874	-0.724
1267	A	17	6	60	49.5749	1.850	-0.806
1267	A	17	6	61	49.5789	1.896	-0.655

Table 3-A1, Continued.

Site	Hole	Core	Section	Top	Calculated Age (Ma)	$\delta^{13}C$ (‰)	$\delta^{18}O$ (‰)
C22nH3							
1267	A	17	5	12	49.1987	1.841	-0.627
1267	A	17	5	13	49.2011	1.867	-0.609
1267	A	17	5	14	49.2035	1.825	-0.649
1267	A	17	5	15	49.2059	1.956	-0.650
1267	A	17	5	16	49.2067	2.048	-0.583
1267	A	17	5	17	49.2074	1.961	-0.608
1267	A	17	5	19	49.2089	1.946	-0.651
1267	A	17	5	20	49.2097	1.981	-0.606
1267	A	17	5	21	49.2105	1.893	-0.700
1267	A	17	5	22	49.2112	1.995	-0.575
1267	A	17	5	23	49.2120	1.964	-0.602
1267	A	17	5	24	49.2127	1.977	-0.648
1267	A	17	5	25	49.2135	1.969	-0.466
1267	A	17	5	26	49.2143	1.910	-0.692
1267	A	17	5	27	49.2150	2.031	-0.598
1267	A	17	5	28	49.2158	1.968	-0.555
1267	A	17	5	29	49.2165	2.041	-0.594
1267	A	17	5	30	49.2173	1.996	-0.624
1267	A	17	5	31	49.2180	2.088	-0.586
1267	A	17	5	32	49.2187	2.061	-0.615
1267	A	17	5	33	49.2195	2.046	-0.641
1267	A	17	5	34	49.2202	2.053	-0.556
1267	A	17	5	35	49.2210	2.099	-0.477
1267	A	17	5	36	49.2218	2.019	-0.551
1267	A	17	5	37	49.2225	2.108	-0.566
1267	A	17	5	38	49.2233	1.981	-0.453
1267	A	17	5	39	49.2240	2.026	-0.480
1267	A	17	5	40	49.2248	1.954	-0.523
1267	A	17	5	41	49.2256	1.899	-0.502
1267	A	17	5	42	49.2263	1.970	-0.430
1267	A	17	5	43	49.2271	1.909	-0.482
1267	A	17	5	44	49.2278	1.945	-0.460
1267	A	17	5	45	49.2286	1.945	-0.443
1267	A	17	5	46	49.2301	1.904	-0.527
1267	A	17	5	47	49.2316	1.874	-0.534
1267	A	17	5	48	49.2331	1.786	-0.687
1267	A	17	5	49	49.2347	1.754	-0.663
1267	A	17	5	50	49.2363	1.822	-0.605
1267	A	17	5	51	49.2379	1.675	-0.761
1267	A	17	5	52	49.2395	1.727	-0.707
1267	A	17	5	53	49.2406	1.745	-0.810

Table 3-A1, Continued.

Site	Hole	Core	Section	Top	Calculated Age (Ma)	$\delta^{13}C$ (‰)	$\delta^{18}O$ (‰)
1267	A	17	5	54	49.2413	1.735	-0.822
1267	A	17	5	55	49.2419	1.611	-0.994
1267	A	17	5	56	49.2425	1.766	-0.780
1267	A	17	5	57	49.2432	1.852	-0.798
1267	A	17	5	58	49.2438	1.902	-0.747
1267	A	17	5	59	49.2445	1.854	-0.793
1267	A	17	5	60	49.2451	1.864	-0.819
1267	A	17	5	61	49.2465	1.888	-0.814
1267	A	17	5	62	49.2478	1.912	-0.618
1267	A	17	5	63	49.2494	1.998	-0.703
1267	A	17	5	64	49.2511	1.970	-0.758
1267	A	17	5	65	49.2528	2.093	-0.719
1267	A	17	5	66	49.2546	2.100	-0.678
1267	A	17	5	67	49.2563	1.952	-0.729
1267	A	17	5	68	49.2581	2.190	-0.525
1267	A	17	5	69	49.2598	2.051	-0.576
1267	A	17	5	70	49.2615	2.038	-0.665
1267	A	17	5	71	49.2633	2.038	-0.596
1267	A	17	5	72	49.2650	2.062	-0.585
1267	A	17	5	73	49.2668	2.040	-0.518
1267	A	17	5	74	49.2685	1.958	-0.171
1267	A	17	5	76	49.2719	2.071	-0.561
1267	A	17	5	77	49.2736	2.044	-0.586
1267	A	17	5	78	49.2754	2.003	-0.521
1267	A	17	5	79	49.2771	1.938	-0.421
1267	A	17	5	80	49.2789	2.122	-0.686
1267	A	17	5	81	49.2806	1.690	-0.914
1267	A	17	5	82	49.2823	1.869	-0.522
1267	A	17	5	83	49.2845	2.089	-0.644
1267	A	17	5	84	49.2872	2.103	-0.649
1267	A	17	5	85	49.2898	2.101	-0.677
1267	A	17	5	86	49.2929	2.128	-0.672
1267	A	17	5	87	49.2960	2.198	-0.511
1267	A	17	5	88	49.2991	2.219	-0.569
C21rH1							
1267	A	17	4	25	48.7321	1.919	-0.749
1267	A	17	4	26	48.7336	1.990	-0.626
1267	A	17	4	27	48.7351	2.058	-0.797
1267	A	17	4	28	48.7365	2.013	-0.766
1267	A	17	4	29	48.7380	2.033	-0.652
1267	A	17	4	30	48.7395	2.023	-0.631
1267	A	17	4	31	48.7410	2.022	-0.648

Table 3-A1, Continued.

Site	Hole	Core	Section	Top	Calculated Age (Ma)	$\delta^{13}C$ (‰)	$\delta^{18}O$ (‰)
1267	A	17	4	32	48.7425	2.024	-0.570
1267	A	17	4	35	48.7469	2.148	-0.368
1267	A	17	4	36	48.7484	2.098	-0.425
1267	A	17	4	37	48.7499	1.893	-0.361
1267	A	17	4	38	48.7513	2.036	-0.009
1267	A	17	4	39	48.7528	1.950	-0.427
1267	A	17	4	40	48.7543	1.991	-0.352
1267	A	17	4	41	48.7558	1.919	-0.579
1267	A	17	4	42	48.7573	1.977	-0.430
1267	A	17	4	43	48.7587	1.964	-0.369
1267	A	17	4	44	48.7602	1.809	-0.573
1267	A	17	4	45	48.7617	1.874	-0.376
1267	A	17	4	46	48.7632	1.978	-0.346
1267	A	17	4	47	48.7647	1.765	-0.653
1267	A	17	4	48	48.7661	1.788	-0.472
1267	A	17	4	49	48.7676	1.761	-0.468
1267	A	17	4	50	48.7691	1.674	-0.605
1267	A	17	4	51	48.7706	1.678	-0.674
1267	A	17	4	52	48.7721	1.796	-0.334
1267	A	17	4	53	48.7735	1.812	-0.702
1267	A	17	4	54	48.7750	2.109	-0.535
1267	A	17	4	55	48.7765	2.066	-0.752
1267	A	17	4	56	48.7780	2.135	-0.605
1267	A	17	4	57	48.7795	2.102	-0.574
1267	A	17	4	58	48.7817	2.117	-0.574
1267	A	17	4	59	48.7847	2.012	-0.717
1267	A	17	4	60	48.7877	2.148	-0.549
1267	A	17	4	61	48.7907	2.092	-0.634
1267	A	17	4	62	48.7938	2.098	-0.665
1267	A	17	4	63	48.7968	2.580	-1.016
1267	A	17	4	64	48.7999	2.130	-0.504
1267	A	17	4	65	48.8029	2.135	-0.475
1267	A	17	4	66	48.8059	2.062	-0.583
1267	A	17	4	67	48.8090	2.091	-0.472
1267	A	17	4	68	48.8120	2.030	-0.437
1267	A	17	4	69	48.8151	2.003	-0.497
1267	A	17	4	70	48.8181	1.913	-0.337
1267	A	17	4	71	48.8211	2.099	-0.539
1267	A	17	4	72	48.8242	2.160	-0.511
1267	A	17	4	73	48.8272	2.122	-0.582
1267	A	17	4	74	48.8303	2.186	-0.570
1267	A	17	4	75	48.8333	2.107	-0.621

Table 3-A1, Continued.

Site	Hole	Core	Section	Top	Calculated Age (Ma)	$\delta^{13}C$ (‰)	$\delta^{18}O$ (‰)
C21rH5							
1267	B	17	6	25	48.2295	2.034	-0.484
1267	B	17	6	26	48.2318	1.932	-0.591
1267	B	17	6	27	48.2341	2.008	-0.462
1267	B	17	6	28	48.2365	1.986	-0.446
1267	B	17	6	29	48.2388	2.037	-0.472
1267	B	17	6	30	48.2411	2.029	-0.442
1267	B	17	6	31	48.2434	1.972	-0.466
1267	B	17	6	33	48.2481	1.877	-0.500
1267	B	17	6	34	48.2504	1.944	-0.457
1267	B	17	6	35	48.2527	1.910	-0.447
1267	B	17	6	36	48.2550	1.872	-0.501
1267	B	17	6	37	48.2573	1.895	-0.646
1267	B	17	6	38	48.2597	1.889	-0.602
1267	B	17	6	39	48.2620	1.974	-0.532
1267	B	17	6	40	48.2643	1.974	-0.547
1267	B	17	6	41	48.2660	2.048	-0.474
1267	B	17	6	42	48.2677	2.021	-0.495
1267	B	17	6	43	48.2693	2.068	-0.459
1267	B	17	6	44	48.2710	2.068	-0.407
1267	B	17	6	45	48.2727	1.917	-0.704
1267	B	17	6	46	48.2744	2.023	-0.473
1267	B	17	6	47	48.2761	1.984	-0.555
1267	B	17	6	48	48.2777	1.957	-0.470
1267	B	17	6	49	48.2794	1.974	-0.664
1267	B	17	6	50	48.2811	2.070	-0.538
1267	B	17	6	51	48.2820	2.062	-0.453
1267	B	17	6	52	48.2829	2.093	-0.502
1267	B	17	6	53	48.2837	2.133	-0.433
1267	B	17	6	54	48.2845	2.036	-0.483
1267	B	17	6	55	48.2853	2.111	-0.442
1267	B	17	6	56	48.2861	2.051	-0.534
1267	B	17	6	57	48.2869	2.096	-0.470
1267	B	17	6	58	48.2877	2.016	-0.580
1267	B	17	6	59	48.2885	2.026	-0.600
1267	B	17	6	60	48.2893	2.053	-0.511
1267	B	17	6	61	48.2901	1.832	-0.753
1267	B	17	6	62	48.2909	2.043	-0.593
1267	B	17	6	63	48.2917	2.092	-0.477
1267	B	17	6	64	48.2925	2.098	-0.488
1267	B	17	6	65	48.2933	2.099	-0.529
1267	B	17	6	66	48.2951	2.147	-0.471

Table 3-A1, Continued.

Site	Hole	Core	Section	Top	Calculated Age (Ma)	$\delta^{13}C$ (‰)	$\delta^{18}O$ (‰)
1267	B	17	6	67	48.2968	2.022	-0.619
1267	B	17	6	68	48.2986	2.119	-0.433
1267	B	17	6	69	48.3005	2.152	-0.437
1267	B	17	6	71	48.3041	2.164	-0.471
1267	B	17	6	73	48.3078	2.144	-0.505
1267	B	17	6	74	48.3095	2.189	-0.477
1267	B	17	6	75	48.3112	2.243	-0.454
1267	B	17	6	76	48.3118	2.158	-0.679
1267	B	17	6	77	48.3124	2.173	-0.551
1267	B	17	6	78	48.3130	2.112	-0.729
1267	B	17	6	79	48.3135	2.191	-0.475
1267	B	17	6	80	48.3141	2.141	-0.733
1267	B	17	6	81	48.3147	2.143	-0.527
1267	B	17	6	82	48.3153	2.028	-0.754
1267	B	17	6	84	48.3164	2.085	-0.651
1267	B	17	6	86	48.3176	1.949	-0.600
1267	B	17	6	87	48.3182	1.761	-1.271
1267	B	17	6	89	48.3194	2.202	-0.518
1267	B	17	6	90	48.3200	2.183	-0.530
1267	B	17	6	91	48.3206	2.081	-0.359
1267	B	17	6	92	48.3213	2.133	-0.671
1267	B	17	6	93	48.3222	2.117	-0.676
C22rH2							
1210	B	17	6	36	49.8010	1.803	-0.804
1210	B	17	6	37	49.8022	1.820	-0.533
1210	B	17	6	38	49.8035	1.820	-0.609
1210	B	17	6	39	49.8047	1.819	-0.526
1210	B	17	6	40	49.8059	1.840	-0.458
1210	B	17	6	41	49.8071	1.815	-0.497
1210	B	17	6	42	49.8083	1.810	-0.453
1210	B	17	6	43	49.8095	1.856	-0.427
1210	B	17	6	44	49.8108	1.887	-0.440
1210	B	17	6	45	49.8120	1.893	-0.369
1210	B	17	6	46	49.8132	1.871	-0.420
1210	B	17	6	47	49.8144	1.829	-0.406
1210	B	17	6	48	49.8156	1.835	-0.439
1210	B	17	6	49	49.8168	1.723	-0.608
1210	B	17	6	50	49.8180	1.790	-0.491
1210	B	17	6	51	49.8192	1.782	-0.458
1210	B	17	6	52	49.8204	1.745	-0.612
1210	B	17	6	53	49.8216	1.721	-0.625
1210	B	17	6	54	49.8228	1.785	-0.543

Table 3-A1, Continued.

Site	Hole	Core	Section	Top	Calculated Age (Ma)	$\delta^{13}C$ (‰)	$\delta^{18}O$ (‰)
1210	B	17	6	55	49.8241	1.761	-0.535
1210	B	17	6	56	49.8253	1.748	-0.524
1210	B	17	6	57	49.8265	1.708	-0.631
1210	B	17	6	58	49.8277	1.769	-0.451
1210	B	17	6	59	49.8289	1.701	-0.624
1210	B	17	6	60	49.8301	1.767	-0.474
1210	B	17	6	61	49.8313	1.760	-0.573
1210	B	17	6	62	49.8325	1.749	-0.621
1210	B	17	6	63	49.8337	1.829	-0.629
1210	B	17	6	64	49.8349	1.867	-0.640
1210	B	17	6	65	49.8361	1.920	-0.574
1210	B	17	6	66	49.8374	1.871	-0.614
1210	B	17	6	67	49.8386	1.905	-0.619
1210	B	17	6	68	49.8398	1.863	-0.650
1210	B	17	6	69	49.8410	1.877	-0.651
1210	B	17	6	70	49.8423	1.833	-0.702
1210	B	17	6	71	49.8437	1.843	-0.590
1210	B	17	6	72	49.8451	1.867	-0.493
1210	B	17	6	73	49.8464	1.817	-0.529
1210	B	17	6	74	49.8478	1.854	-0.445
1210	B	17	6	75	49.8492	1.828	-0.463
1210	B	17	6	76	49.8505	1.791	-0.551
1210	B	17	6	77	49.8519	1.760	-0.575
1210	B	17	6	78	49.8532	1.753	-0.576
1210	B	17	6	79	49.8546	1.801	-0.587
1210	B	17	6	80	49.8560	1.823	-0.474
1210	B	17	6	81	49.8573	1.792	-0.542
1210	B	17	6	82	49.8587	1.807	-0.481
1210	B	17	6	83	49.8601	1.820	-0.490
1210	B	17	6	84	49.8614	1.815	-0.420
1210	B	17	6	85	49.8628	1.814	-0.426
1210	B	17	6	86	49.8641	1.818	-0.467
1210	B	17	6	87	49.8655	1.750	-0.463
1210	B	17	6	88	49.8669	1.772	-0.513
1210	B	17	6	89	49.8682	1.823	-0.453
1210	B	17	6	90	49.8696	1.817	-0.464
1210	B	17	6	91	49.8709	1.770	-0.465
1210	B	17	6	92	49.8723	1.757	-0.516
1210	B	17	6	93	49.8737	1.748	-0.527
1210	B	17	6	94	49.8750	1.716	-0.500
1210	B	17	6	95	49.8764	1.703	-0.526
1210	B	17	6	96	49.8778	1.651	-0.673
1210	B	17	6	97	49.8791	1.721	-0.495

Table 3-A1, Continued.

Site	Hole	Core	Section	Top	Calculated Age (Ma)	$\delta^{13}C$ (‰)	$\delta^{18}O$ (‰)
1210	B	17	6	98	49.8805	1.647	-0.546
1210	B	17	6	99	49.8818	1.810	-0.440
1210	B	17	6	100	49.8832	1.754	-0.471
1210	B	17	6	101	49.8846	1.780	-0.422
1210	B	17	6	102	49.8859	1.736	-0.389
1210	B	17	6	103	49.8873	1.787	-0.337
1210	B	17	6	104	49.8886	1.808	-0.372
1210	B	17	6	105	49.8900	1.683	-0.371
1210	B	17	6	106	49.8914	1.812	-0.385
1210	B	17	6	107	49.8927	1.734	-0.421
1210	B	17	6	108	49.8941	1.722	-0.422
1210	B	17	6	109	49.8955	1.746	-0.398
1210	B	17	6	110	49.8968	1.693	-0.411
1210	B	17	6	111	49.8982	1.834	-0.560
1210	B	17	6	112	49.8995	1.567	-0.539
1210	B	17	6	113	49.9009	1.666	-0.371
1210	B	17	6	114	49.9023	1.662	-0.427
1210	B	17	6	115	49.9036	1.650	-0.599
1210	B	17	6	116	49.9050	1.607	-0.478
1210	B	17	6	117	49.9064	1.698	-0.404
1210	B	17	6	118	49.9077	1.627	-0.453
1210	B	17	6	119	49.9091	1.625	-0.203
1210	B	17	6	120	49.9104	1.635	-0.418
1210	B	17	6	121	49.9118	1.570	-0.497
1210	B	17	6	122	49.9131	1.489	-0.273
1210	B	17	6	123	49.9145	1.420	-0.691
1210	B	17	6	124	49.9157	1.408	-0.637
1210	B	17	6	125	49.9168	1.389	-0.692
1210	B	17	6	126	49.9180	1.461	-0.671
1210	B	17	6	127	49.9192	1.428	-0.748
1210	B	17	6	128	49.9204	1.417	-0.701
1210	B	17	6	129	49.9216	1.315	-0.885
1210	B	17	6	130	49.9227	1.351	-0.623
1210	B	17	6	131	49.9239	1.344	-0.739
1210	B	17	6	132	49.9251	1.389	-0.831
1210	B	17	6	133	49.9263	1.489	-0.712
1210	B	17	6	134	49.9274	1.461	-0.814
1210	B	17	6	135	49.9286	1.360	-1.111
1210	A	18	2	111	49.9286	1.480	-0.842
1210	A	18	2	112	49.9293	1.576	-0.641
1210	A	18	2	113	49.9300	1.510	-0.835
1210	A	18	2	114	49.9306	1.577	-0.651
1210	A	18	2	115	49.9313	1.682	-0.568

Table 3-A1, Continued.

Site	Hole	Core	Section	Top	Calculated Age (Ma)	$\delta^{13}C$ (‰)	$\delta^{18}O$ (‰)
1210	A	18	2	116	49.9319	1.695	-0.492
1210	A	18	2	117	49.9326	1.658	-0.335
1210	A	18	2	119	49.9339	1.582	-0.776
1210	A	18	2	120	49.9346	1.655	-0.649
1210	A	18	2	121	49.9352	1.614	-0.752
1210	A	18	2	122	49.9359	1.728	-0.806
1210	A	18	2	123	49.9366	1.748	-0.504
1210	A	18	2	124	49.9372	1.696	-0.799
1210	A	18	2	125	49.9379	1.676	-0.767
1210	A	18	2	126	49.9385	1.731	-0.650
1210	A	18	2	127	49.9392	1.657	-0.676
1210	A	18	2	128	49.9398	1.667	-0.781
C22nH2							
1210	B	17	4	127	49.4671	1.735	-0.535
1210	B	17	4	128	49.4691	1.712	-0.603
1210	B	17	4	129	49.4710	1.740	-0.529
1210	B	17	4	130	49.4730	1.745	-0.505
1210	B	17	4	131	49.4749	1.802	-0.482
1210	B	17	4	132	49.4768	1.745	-0.601
1210	B	17	4	133	49.4788	1.754	-0.629
1210	B	17	4	134	49.4807	1.779	-0.512
1210	B	17	4	135	49.4827	1.711	-0.408
1210	B	17	4	136	49.4846	1.724	-0.578
1210	B	17	4	137	49.4866	1.734	-0.414
1210	B	17	4	138	49.4885	1.586	-0.287
1210	B	17	4	139	49.4905	1.636	-0.379
1210	B	17	4	140	49.4924	1.633	-0.393
1210	B	17	4	141	49.4944	1.614	-0.451
1210	B	17	4	142	49.4963	1.593	-0.517
1210	B	17	4	143	49.4982	1.655	-0.354
1210	B	17	4	144	49.5002	1.686	-0.340
1210	B	17	4	145	49.5021	1.654	-0.419
1210	B	17	4	146	49.5041	1.588	-0.513
1210	B	17	4	147	49.5060	1.697	-0.328
1210	B	17	4	148	49.5080	1.624	-0.453
1210	B	17	4	149	49.5099	1.646	-0.309
1210	B	17	4	150	49.5119	1.628	-0.345
1210	B	17	5	0	49.5119	1.615	-0.340
1210	B	17	5	1	49.5138	1.604	-0.391
1210	B	17	5	2	49.5157	1.578	-0.364
1210	B	17	5	3	49.5177	1.460	-0.497
1210	B	17	5	4	49.5196	1.504	-0.420

Table 3-A1, Continued.

Site	Hole	Core	Section	Top	Calculated Age (Ma)	$\delta^{13}C$ (‰)	$\delta^{18}O$ (‰)
1210	B	17	5	5	49.5216	1.491	-0.180
1210	B	17	5	6	49.5235	1.541	-0.505
1210	B	17	5	8	49.5272	1.561	-0.436
1210	B	17	5	9	49.5290	1.541	-0.433
1210	B	17	5	10	49.5308	1.516	-0.550
1210	B	17	5	11	49.5325	1.511	-0.523
1210	B	17	5	12	49.5343	1.417	-0.789
1210	B	17	5	13	49.5360	1.521	-0.644
1210	B	17	5	14	49.5378	1.548	-0.641
1210	B	17	5	15	49.5395	1.650	-0.636
1210	B	17	5	16	49.5412	1.621	-0.665
1210	B	17	5	17	49.5429	1.700	-0.544
1210	B	17	5	18	49.5446	1.681	-0.502
1210	B	17	5	19	49.5457	1.718	-0.520
1210	B	17	5	20	49.5467	1.688	-0.454
1210	B	17	5	21	49.5477	1.755	-0.552
1210	B	17	5	22	49.5487	1.747	-0.417
1210	B	17	5	23	49.5498	1.838	-0.578
1210	B	17	5	24	49.5508	1.827	-0.338
1210	B	17	5	25	49.5518	1.786	-0.465
1210	B	17	5	26	49.5528	1.755	-0.394
1210	B	17	5	27	49.5539	1.739	-0.679
1210	B	17	5	28	49.5549	1.772	-0.597
1210	B	17	5	29	49.5559	1.778	-0.462
1210	B	17	5	30	49.5570	1.880	-0.545
1210	B	17	5	31	49.5580	1.657	-0.646
1210	B	17	5	32	49.5590	1.783	-0.536
1210	B	17	5	33	49.5600	1.808	-0.441
1210	B	17	5	34	49.5611	1.807	-0.411
1210	B	17	5	35	49.5621	1.782	-0.462
1210	B	17	5	36	49.5631	1.786	-0.421
1210	B	17	5	37	49.5641	1.757	-0.560
1210	B	17	5	38	49.5652	1.749	-0.538
1210	B	17	5	39	49.5662	1.785	-0.487
1210	B	17	5	40	49.5672	1.781	-0.483
1210	B	17	5	41	49.5682	1.822	-0.404
1210	B	17	5	42	49.5693	1.784	-0.518
1210	B	17	5	43	49.5703	1.782	-0.471
1210	B	17	5	44	49.5713	1.794	-0.483
1210	B	17	5	45	49.5723	1.781	-0.520
1210	B	17	5	46	49.5734	1.779	-0.472
1210	B	17	5	47	49.5744	1.750	-0.476
1210	B	17	5	48	49.5754	1.830	-0.413

Table 3-A1, Continued.

Site	Hole	Core	Section	Top	Calculated Age (Ma)	$\delta^{13}C$ (‰)	$\delta^{18}O$ (‰)
1210	B	17	5	49	49.5766	1.836	-0.425
1210	B	17	5	50	49.5777	1.808	-0.451
1210	B	17	5	51	49.5788	1.772	-0.410
1210	B	17	5	52	49.5800	1.824	-0.470
1210	B	17	5	53	49.5811	1.767	-0.424
1210	B	17	5	54	49.5822	1.799	-0.444
1210	B	17	5	55	49.5834	1.789	-0.427
1210	B	17	5	56	49.5845	1.752	-0.437
1210	B	17	5	57	49.5856	1.747	-0.453
C22nH3							
1210	B	17	3	65	49.1015	1.950	-0.277
1210	B	17	3	66	49.1038	1.988	-0.218
1210	B	17	3	67	49.1062	2.028	-0.057
1210	B	17	3	68	49.1086	2.006	-0.002
1210	B	17	3	69	49.1110	1.866	-0.302
1210	B	17	3	70	49.1146	1.924	-0.113
1210	B	17	3	71	49.1183	1.783	-0.216
1210	B	17	3	72	49.1219	1.881	-0.019
1210	B	17	3	73	49.1256	1.908	0.022
1210	B	17	3	74	49.1292	1.912	0.014
1210	B	17	3	75	49.1329	1.957	0.034
1210	B	17	3	76	49.1365	1.777	-0.196
1210	B	17	3	77	49.1401	1.890	-0.032
1210	B	17	3	78	49.1438	1.886	0.070
1210	B	17	3	79	49.1474	1.896	0.024
1210	B	17	3	80	49.1511	1.821	-0.117
1210	B	17	3	81	49.1547	1.844	-0.090
1210	B	17	3	82	49.1584	1.799	-0.310
1210	B	17	3	83	49.1620	1.788	-0.184
1210	B	17	3	84	49.1657	1.743	-0.405
1210	B	17	3	85	49.1693	1.800	-0.284
1210	B	17	3	86	49.1729	1.795	-0.324
1210	B	17	3	87	49.1766	1.740	-0.484
1210	B	17	3	88	49.1778	1.746	-0.367
1210	B	17	3	89	49.1789	1.765	-0.337
1210	B	17	3	90	49.1801	1.852	-0.078
1210	B	17	3	91	49.1811	1.873	-0.186
1210	B	17	3	92	49.1821	1.811	-0.180
1210	B	17	3	93	49.1831	1.802	-0.330
1210	B	17	3	94	49.1840	1.834	-0.069
1210	B	17	3	95	49.1850	1.821	-0.120
1210	B	17	3	96	49.1860	1.798	-0.181

Table 3-A1, Continued.

Site	Hole	Core	Section	Top	Calculated Age (Ma)	$\delta^{13}C$ (‰)	$\delta^{18}O$ (‰)
1210	B	17	3	97	49.1870	1.696	-0.383
1210	B	17	3	98	49.1879	1.777	-0.217
1210	B	17	3	99	49.1889	1.796	-0.163
1210	B	17	3	100	49.1899	1.832	-0.117
1210	B	17	3	101	49.1909	1.738	-0.254
1210	B	17	3	102	49.1919	1.821	-0.106
1210	B	17	3	103	49.1928	1.786	-0.155
1210	B	17	3	104	49.1938	1.815	-0.337
1210	B	17	3	105	49.1948	1.870	-0.209
1210	B	17	3	106	49.1958	1.801	-0.319
1210	B	17	3	107	49.1967	1.780	-0.334
1210	B	17	3	108	49.1977	1.894	-0.311
1210	B	17	3	109	49.1987	1.838	-0.450
1210	B	17	3	110	49.1997	1.890	-0.213
1210	B	17	3	111	49.2007	1.594	-0.430
1210	B	17	3	112	49.2016	1.924	-0.429
1210	B	17	3	113	49.2026	1.784	-0.340
1210	B	17	3	114	49.2036	1.682	-0.445
1210	B	17	3	115	49.2046	1.813	-0.510
1210	B	17	3	116	49.2057	1.946	-0.549
1210	B	17	3	117	49.2067	1.891	-0.514
1210	B	17	3	118	49.2083	1.871	-0.432
1210	B	17	3	119	49.2098	1.815	-0.383
1210	B	17	3	120	49.2113	1.804	-0.379
1210	B	17	3	121	49.2128	1.838	-0.240
1210	B	17	3	122	49.2144	1.908	-0.278
1210	B	17	3	123	49.2159	1.840	-0.144
1210	B	17	3	124	49.2174	1.817	-0.246
1210	B	17	3	125	49.2189	1.733	-0.323
1210	B	17	3	126	49.2204	1.776	-0.290
1210	B	17	3	127	49.2212	1.672	-0.328
1210	B	17	3	128	49.2219	1.757	-0.077
1210	B	17	3	129	49.2227	1.773	-0.255
1210	B	17	3	130	49.2234	1.583	-0.465
1210	B	17	3	131	49.2241	1.577	-0.479
1210	B	17	3	132	49.2248	1.608	-0.385
1210	B	17	3	133	49.2255	1.604	-0.432
1210	B	17	3	134	49.2262	1.612	-0.308
1210	B	17	3	135	49.2269	1.555	-0.451
1210	B	17	3	136	49.2277	1.536	-0.367
1210	B	17	3	137	49.2284	1.563	-0.302
1210	B	17	3	138	49.2291	1.461	-0.551

Table 3-A1, Continued.

Site	Hole	Core	Section	Top	Calculated Age (Ma)	$\delta^{13}C$ (‰)	$\delta^{18}O$ (‰)
1210	B	17	3	139	49.2298	1.515	-0.401
1210	B	17	3	140	49.2305	1.491	-0.412
1210	B	17	3	141	49.2312	1.527	-0.525
1210	B	17	3	142	49.2319	1.512	-0.427
1210	B	17	3	143	49.2326	1.465	-0.569
1210	B	17	3	144	49.2334	1.467	-0.499
1210	B	17	3	145	49.2341	1.458	-0.552
1210	B	17	3	146	49.2348	1.407	-0.612
1210	B	17	3	147	49.2355	1.595	-0.497
1210	B	17	3	149	49.2369	1.561	-0.472
1210	B	17	4	0	49.2376	1.483	-0.620
1210	B	17	4	2	49.2391	1.831	-0.526
1210	B	17	4	3	49.2398	1.706	-0.300
1210	B	17	4	4	49.2405	1.644	-0.543
1210	B	17	4	5	49.2412	1.635	-0.401
1210	B	17	4	6	49.2419	1.646	-0.322
1210	B	17	4	7	49.2426	1.637	-0.486
1210	B	17	4	8	49.2433	1.513	-0.748
1210	B	17	4	9	49.2441	1.712	-0.596
1210	B	17	4	10	49.2448	1.795	-0.533
1210	B	17	4	11	49.2455	1.716	-0.414
1210	B	17	4	12	49.2462	1.775	-0.426
1210	B	17	4	13	49.2474	1.737	-0.586
1210	B	17	4	14	49.2485	1.765	-0.558
1210	B	17	4	15	49.2497	1.775	-0.329
1210	B	17	4	16	49.2509	1.705	-0.431
1210	B	17	4	17	49.2521	1.812	-0.385
1210	B	17	4	18	49.2532	1.822	-0.372
1210	B	17	4	19	49.2544	1.751	-0.381
1210	B	17	4	20	49.2556	1.736	-0.530
1210	B	17	4	21	49.2568	1.806	-0.434
1210	B	17	4	22	49.2579	1.831	-0.262
1210	B	17	4	23	49.2591	1.770	-0.458
1210	B	17	4	24	49.2603	1.790	-0.448
1210	B	17	4	25	49.2615	1.601	-0.499
1210	B	17	4	26	49.2626	1.636	-0.395
C21rH1							
1210	A	17	5	30	48.7330	1.780	-0.202
1210	A	17	5	31	48.7349	1.651	-0.251
1210	A	17	5	32	48.7367	1.766	-0.321
1210	A	17	5	33	48.7385	1.764	-0.176
1210	A	17	5	34	48.7403	1.651	-0.332

Table 3-A1, Continued.

Site	Hole	Core	Section	Top	Calculated Age (Ma)	$\delta^{13}C$ (‰)	$\delta^{18}O$ (‰)
1210	A	17	5	35	48.7421	1.592	-0.443
1210	A	17	5	36	48.7439	1.716	-0.147
1210	A	17	5	37	48.7458	1.647	-0.293
1210	A	17	5	38	48.7476	1.571	-0.377
1210	A	17	5	39	48.7494	1.681	-0.254
1210	A	17	5	40	48.7512	1.634	-0.264
1210	A	17	5	41	48.7530	1.480	-0.363
1210	A	17	5	43	48.7566	1.514	-0.394
1210	A	17	5	44	48.7585	1.505	-0.358
1210	A	17	5	45	48.7603	1.491	-0.406
1210	A	17	5	46	48.7621	1.431	-0.660
1210	A	17	5	47	48.7639	1.539	-0.494
1210	B	17	2	84	48.7657	1.460	-0.502
1210	B	17	2	85	48.7675	1.592	-0.528
1210	B	17	2	86	48.7694	1.522	-0.516
1210	B	17	2	87	48.7712	1.664	-0.567
1210	B	17	2	88	48.7730	1.828	-0.633
1210	B	17	2	89	48.7748	1.666	-0.487
1210	B	17	2	90	48.7766	1.815	-0.390
1210	B	17	2	91	48.7787	1.810	-0.396
1210	B	17	2	92	48.7808	1.885	-0.307
1210	B	17	2	93	48.7829	1.917	-0.254
1210	B	17	2	94	48.7850	1.920	-0.262
1210	B	17	2	95	48.7871	1.906	-0.138
1210	B	17	2	96	48.7892	1.961	-0.255
1210	B	17	2	97	48.7913	1.904	-0.126
1210	B	17	2	98	48.7934	1.930	-0.395
1210	B	17	2	99	48.7955	1.955	-0.411
1210	B	17	2	100	48.7976	1.879	-0.274
1210	B	17	2	101	48.7997	1.869	-0.441
1210	B	17	2	102	48.8018	1.877	-0.430
1210	B	17	2	103	48.8039	1.950	-0.378
1210	B	17	2	104	48.8061	2.000	-0.506
1210	B	17	2	105	48.8082	2.002	-0.406
1210	B	17	2	106	48.8113	2.058	-0.513
1210	B	17	2	107	48.8145	1.989	-0.501
1210	B	17	2	108	48.8177	1.988	-0.465
1210	B	17	2	109	48.8210	2.043	-0.401
1210	B	17	2	110	48.8243	1.930	-0.567
1210	B	17	2	111	48.8277	2.026	-0.292
1210	B	17	2	112	48.8310	2.012	-0.175
1210	B	17	2	113	48.8343	1.942	-0.336

Table 3-A1, Continued.

Site	Hole	Core	Section	Top	Calculated Age (Ma)	$\delta^{13}C$ (‰)	$\delta^{18}O$ (‰)
1210	B	17	2	114	48.8376	1.952	-0.160
1210	B	17	2	115	48.8409	1.989	-0.202
1210	B	17	2	116	48.8442	2.042	-0.162
1210	B	17	2	117	48.8476	1.922	-0.218
1210	B	17	2	118	48.8509	2.057	-0.145
1210	B	17	2	119	48.8542	1.943	-0.298
C21rH5							
1210	B	16	6	54	48.2322	1.824	-0.157
1210	B	16	6	55	48.2336	1.820	-0.345
1210	B	16	6	56	48.2350	1.888	-0.281
1210	B	16	6	57	48.2364	1.831	-0.234
1210	B	16	6	58	48.2378	1.863	-0.409
1210	B	16	6	59	48.2391	1.809	-0.234
1210	B	16	6	60	48.2405	1.831	-0.354
1210	B	16	6	61	48.2419	1.730	-0.146
1210	B	16	6	62	48.2433	1.804	-0.220
1210	B	16	6	63	48.2447	1.681	-0.217
1210	B	16	6	64	48.2461	1.845	-0.278
1210	B	16	6	65	48.2475	1.743	-0.224
1210	B	16	6	66	48.2488	1.749	-0.163
1210	B	16	6	67	48.2502	1.677	-0.287
1210	B	16	6	68	48.2516	1.711	-0.246
1210	B	16	6	69	48.2530	1.730	-0.266
1210	B	16	6	70	48.2544	1.708	-0.203
1210	B	16	6	71	48.2558	1.759	-0.156
1210	B	16	6	72	48.2572	1.757	-0.387
1210	B	16	6	73	48.2585	1.813	-0.418
1210	B	16	6	74	48.2599	1.747	-0.452
1210	B	16	6	75	48.2613	1.823	-0.297
1210	B	16	6	77	48.2641	1.790	-0.234
1210	B	16	6	78	48.2655	1.782	-0.286
1210	B	16	6	79	48.2663	1.779	-0.227
1210	B	16	6	80	48.2671	1.706	-0.294
1210	B	16	6	81	48.2680	1.747	-0.333
1210	B	16	6	82	48.2688	1.779	-0.262
1210	B	16	6	83	48.2696	1.633	-0.360
1210	B	16	6	84	48.2704	1.675	-0.369
1210	B	16	6	85	48.2712	1.717	-0.276
1210	B	16	6	86	48.2720	1.639	-0.398
1210	B	16	6	87	48.2729	1.504	-0.635
1210	B	16	6	88	48.2737	1.694	-0.345

Table 3-A1, Continued.

Site	Hole	Core	Section	Top	Calculated Age (Ma)	$\delta^{13}C$ (‰)	$\delta^{18}O$ (‰)
1210	B	16	6	89	48.2745	1.686	-0.336
1210	B	16	6	90	48.2753	1.705	-0.327
1210	B	16	6	91	48.2761	1.673	-0.430
1210	B	16	6	93	48.2778	1.722	-0.363
1210	B	16	6	94	48.2786	1.726	-0.363
1210	B	16	6	95	48.2794	1.697	-0.383
1210	B	16	6	96	48.2802	1.652	-0.366
1210	B	16	6	97	48.2810	1.643	-0.340
1210	B	16	6	98	48.2818	1.663	-0.358
1210	B	16	6	99	48.2827	1.666	-0.185
1210	B	16	6	100	48.2835	1.585	-0.375
1210	B	16	6	101	48.2843	1.574	-0.431
1210	B	16	6	102	48.2851	1.570	-0.541
1210	B	16	6	103	48.2859	1.673	-0.358
1210	B	16	6	104	48.2867	1.725	-0.304
1210	B	16	6	105	48.2876	1.577	-0.427
1210	B	16	6	106	48.2884	1.662	-0.479
1210	B	16	6	107	48.2892	1.723	-0.432
1210	B	16	6	108	48.2900	1.601	-0.559
1210	B	16	6	109	48.2910	1.733	-0.374
1210	B	16	6	110	48.2920	1.722	-0.350
1210	B	16	6	111	48.2929	1.795	-0.324
1210	B	16	6	112	48.2940	1.738	-0.395
1210	B	16	6	113	48.2950	1.788	-0.352
1210	B	16	6	115	48.2970	1.769	-0.364
1210	B	16	6	116	48.2980	1.707	-0.473
1210	B	16	6	117	48.2990	1.791	-0.457
1210	B	16	6	118	48.3000	1.753	-0.346
1210	B	16	6	119	48.3010	1.773	-0.366
1210	B	16	6	120	48.3020	1.725	-0.352
1210	B	16	6	121	48.3030	1.658	-0.411
1210	B	16	6	122	48.3040	1.607	-0.438
1210	B	16	6	123	48.3050	1.737	-0.356
1210	B	16	6	124	48.3060	1.663	-0.304
1210	B	16	6	125	48.3070	1.700	-0.308
1210	B	16	6	126	48.3080	1.656	-0.495
1210	B	16	6	127	48.3090	1.776	-0.392
1210	B	16	6	128	48.3101	1.800	-0.372
1210	B	16	6	129	48.3111	1.754	-0.348
1210	B	16	6	130	48.3129	1.772	-0.305
1210	B	16	6	131	48.3148	1.716	-0.254
1210	B	16	6	132	48.3166	1.719	-0.284

Table 3-A1, Continued.

Site	Hole	Core	Section	Top	Calculated Age (Ma)	$\delta^{13}C$ (‰)	$\delta^{18}O$ (‰)
1210	B	16	6	133	48.3185	1.730	-0.221
1210	B	16	6	134	48.3203	1.678	-0.203
1210	B	16	6	135	48.3222	1.770	-0.172
1210	B	16	6	136	48.3241	1.646	-0.172
1210	B	16	6	137	48.3260	1.730	-0.091
1210	B	16	6	138	48.3278	1.749	-0.165
1210	B	16	6	139	48.3297	1.749	-0.127
1210	B	16	6	140	48.3316	1.676	-0.306

CHAPTER 4

A Synthesis of Carbon Isotope Excursions in Greenhouse Climates

Records of greenhouse Earth climates (prior to the onset of widespread glaciation at ~34 Ma) have demonstrated the occurrence of numerous transient episodes of extreme warming corresponding to major disruptions of the carbon cycle. Called 'hyperthermals,' or sometimes carbon isotope excursions, for the characteristic signature of such events in the sedimentary record, these events provide plausible analogs for future greenhouse gas-induced warming and global change. Here, we synthesize records of potential hyperthermal events from ~250 to 40 Ma. We identify 44 potential hyperthermals based on identification of negative carbon isotope excursions. We compare carbon isotope excursions identified from sedimentary carbonate records to demonstrate that the Toarcian (~180 Ma) is the largest event, and that most events are comparatively small—only the Toarcian, PETM, Permian-Triassic boundary, Triassic-Jurassic boundary, and Aptian Ocean Anoxic event are show bulk carbonate carbon isotope excursions greater than 2‰. However, the 44 purported hyperthermals show a number of commonalities in terms of evidence for warming, extinction and/or biotic turnover, dissolution of carbonates, weathering, and anoxia. Finally, based on the temporal relationship between hyperthermal events and the existence of widespread anoxia-favoring geography, we suggest that such geography is a necessary precondition for the occurrence of hyperthermal events in geologic history.

4.1 Introduction

Records of carbon and oxygen stable isotopes from marine carbonates are the primary tools for reconstructing Earth's long-term climatic trends (Scholle and Arthur, 1980; Shackleton 1985; Zachos et al., 2001). Numerous authors have identified episodes of rapid change in the isotopic composition of oxygen (reflecting changes in temperature and ice volume) and carbon (reflecting changes in the carbon cycle). Zachos et al., 2001, illustrated the three most prominent climatic perturbations of the Cenozoic as the Paleocene-Eocene Thermal Maximum (PETM) at ~56 Ma, the onset of Antarctic glaciation at ~34 Ma, and glaciation at the Oligocene-Miocene boundary at ~23 Ma.

The abundance of high-resolution of records from the late Cenozoic spanning the glacial-interglacial cycles of the Plio-Pleistocene compared to the warm, early Cenozoic, has given the impression of reduced climatic and carbon cycle variability during warm climates. Continuing improvements to the resolution of proxy records from the early Cenozoic, in particular the Paleogene period, have revealed numerous fluctuations punctuating a warm, greenhouse climate. Records extending further, into the Jurassic and Cretaceous periods, have revealed a number of discrete ocean anoxic events (OAEs), coupled with extreme warmth. These records demonstrate that abrupt climatic variability is not unique to recent geologic time. It is not obvious that climates of greenhouse Earth were more equable than icehouse Earth.

Carbon has a long (10^5 years) residence time in the exogenic system (not

including the lithosphere). Over this timescale, the mass and isotopic composition of exogenic carbon is a function of the balance between input via volcanism/metamorphism and organic matter weathering and removal via sedimentary burial of organic carbon and carbonate (Kump and Arthur 1999; Berner 2003). Fluctuations in the isotopic composition of marine carbonates are generally interpreted to indicate deviations from steady state, with positive excursions representing increases in organic matter burial through some combination of increased productivity and/or increased organic matter preservation, and negative excursions representing the reverse. Unfortunately, a straightforward interpretation of measured carbonate isotopic values to determine changes in the burial ratio is complicated by the possibility of changes in either the isotopic composition of carbon inputs or the fractionation between organic carbon and carbonate through time (Kump and Arthur, 1999).

In contrast, shorter-term fluctuations are traditionally interpreted as transfers of organic carbon between reservoirs. Researchers explain the negative $\delta^{13}C$ excursion of 0.3-0.4‰ associated with the Last Glacial Maximum by the transfer of large quantities (300-700 Gt) of terrestrial organic carbon to the oceans-atmosphere (Curry et al., 1988; Bird et al., 1994; Sigman and Boyle, 2000). Large negative carbon isotopic excursions (CIEs) identified from earlier geologic intervals, in contrast, coincide with indications of intense, abrupt warming.

The most famous, well-studied example of these events is the PETM,

where an abrupt negative CIE of >3‰ corresponds with 5-6°C warming (Zachos et al., 2007; Dunkley Jones et al., 2010). Researchers have suggested that the massive size of the CIE during the PETM makes it improbable that transfer of carbon between exogenic reservoirs could be the cause—the mass of organic carbon required would be approximately equal to the entire present-day organic carbon reservoir—as a result, Dickens, 1995, suggested that the massive dissociation and release of methane hydrates might have been responsible. This source of sedimentary carbon is separate from the readily exchangeable exogenic system and its release represents massive disruption to the carbon cycle.

In addition to the CIE, the PETM shows evidence of intense dissolution of deep-sea carbonates, indicating shoaling of the lysocline and carbonate compensation depth, which provides additional constraints on the magnitude of the required carbon input (Zachos et al., 2005; Panchuk et al., 2008). The PETM is called a 'hyperthermal' event because of the magnitude of disruption to the carbon cycle and extent of warming at the end-Paleocene, which stands out as one of the major climatic events of the entire Cenozoic.

Over the past 20 years since the discovery of carbon injection and warming at the PETM, multiple authors have described additional carbon cycle perturbations, sometimes coupled with warming, which they have labeled as 'hyperthermals' comparable to, though smaller than, the PETM. The postulated causes of these events include smaller releases of carbon from a methane

hydrate reservoir or redistribution of dissolved organic carbon from the deep ocean (Zachos et al., 2008; Lourens et al., 2005; Niccolo et al., 2007; Sexton et al., 2010).

In addition, increasing resolution of carbon isotope records across OAEs demonstrate that rapid negative CIEs often preceded the positive CIEs typically associated with deposition of black shales or organic-rich sediments (Jenkyns, 2010). These negative CIEs have been attributed to volcanic CO_2 release as well as dissociation of methane hydrates and thermal metamorphism of organic matter (Hesselbo et al., 2000; Jahren et al., 2001; Jenkyns 2003; McElwain et al., 2005; Kuroda et al., 2007; Jenkyns, 2010). While some of these CIEs are clearly above-background in magnitude and correspond with evidence of warming and often carbonate dissolution, some of the identified 'hyperthermals' show relatively moderate environmental change. To date, there has been no comprehensive evaluation of events labeled as 'hyperthermals,' or attempts to assign criteria for the definition of a 'hyperthermal.'

This study seeks to synthesize records of 'hyperthermals' and assess their ubiquity during greenhouse intervals. We will also contrast 'hyperthermal' records with variability from the later Cenozoic. The Middle Eocene Climatic Optimum is the last identified 'hyperthermal' event at ~40 Ma (Bohaty and Zachos, 2003; Bohaty et al; 2009). Providing a lower bound on the occurrence of hyperthermals is more complicated because of the scarcity of deep-sea records earlier than the mid-Cretaceous due to seafloor subduction. The Toarcian OAE during the

Jurassic period (~183 Ma), is the oldest event that has been labeled as a 'hyperthermal,' though large negative CIEs have been identified earlier, including at the Triassic-Jurassic boundary (T/J ~200 Ma), the Permian-Triassic (P/T ~251 Ma), and from Proterozoic cap carbonates (Kennedy et al., 2001; Hesselbo et al., 2002; Payne et al., 2004). This study will not consider events before the Permian-Triassic, given the absence of pelagic calcifiers in earlier time periods (Ridgwell and Zeebe, 2005; Honisch et al., 2012).

4.2 Datasets

We have selected 44 potential 'hyperthermal' events from ~252-40 Ma for comparison (though some events counted as two distinct events may be considered a single event). The majority of the selected records are from the Paleogene—these are the events typically described as 'hyperthermals' in the literature—though we also include 5 Mesozoic OAEs that show negative CIEs before the positive CIEs more commonly associated with their occurrence (Table 1), as well as records of the CIEs associated with the T/J and P/T mass extinctions.

Our primary focus of comparison for each event is the CIE itself—researchers have frequently used the existence of a negative CIE as their main criteria for identification of a hyperthermal. It is possible to identify CIEs from multiple sources—both carbonates (including both bulk carbonate and foraminifera) and organic matter (including bulk and specific compounds). In

contrast, it is often more difficult to find unequivocal evidence for intense warming from the same proxy for each event. Oxygen isotopic compositions of foraminifera are more susceptible to diagenetic overprinting than carbon isotopes (Sexton et al., 2006), and using $\delta^{18}O$ from bulk carbonates to infer temperature change is complicated by the possibility of changes in fractionation of different species of calcareous nannoplankton. For organic matter, alternative temperature proxies are necessary, such as the TEX_{86} sea surface temperature proxy (Zachos et al., 2006).

The multiple sources available for recording $\delta^{13}C$ during each event are also problematic because different sources consistently record different magnitude excursions for a single event. The PETM has records from the largest number of sources, allowing comparison of the range of different magnitudes for a given, global event. In general, organic carbon records larger excursions than carbonate, with typical marine carbonate excursions between 2-3.5‰ (Zachos et al., 2007; Panchuk, 2007), but organic carbon excursions as large as 6‰ (Pagani et al., 2006).

Carbonate records are often compromised by dissolution, with the result that the peak of the CIE is not preserved, and by changes in pH during the event, which can alter the size of the excursion recorded through the carbonate ion effect (Panchuk, 2007; Pagani et al., 2006; Spero et al., 1997). For this reason, Pagani et al., 2006, suggested organic carbon records might provide better estimates for the CIE magnitude. However, other authors have cautioned against

the use of organic matter for determining CIE magnitude, since compositional changes of bulk organic matter (terrestrial versus marine) may compromise the primary signal (Corsetti et al., 2005). Studies have targeted carbon isotopic compositions of bulk organic matter as well as specific compounds, such as higher plant n-alkanes supposed to preserve an atmospheric signal; however, there is a possibility that hydrological cycle or other environmental changes could have affected fractionation in these sources (Bowen et al., 2004; Schouten et al., 2007). Schouten et al., 2007, demonstrated that angiosperms recorded a larger excursion than conifers during the PETM: evidence that terrestrial organic carbon records might not demonstrate the exact CIE magnitude in the atmosphere-oceans.

Table 4-1. List of all 'hyperthermal' events evaluated in this study with absolute ages provided from the literature. For Events A-L, ages are calculated relative to the PETM.

Event Name	Approximate Age (Ma)	Sources
Permian-Triassic Boundary Excursion	252.3	Meyer et al., 2011; Corsetti et al., 2005
Triassic-Jurassic Boundary Event	200	Palfy et al., 2008
Toarcian T-OAE	183	Hermoso et al., 2012; Jenkyns et al., 2010; Cohen et al., 2007; Kump et al., 2005; Jenkyns et al., 2003
Early Aptian OAE 1a (Selli Event)	120	Jenkyns et al., 1995; Menegatti et al., 1998; Bellanca et al., 2002
Early Albian OAE 1b (Paquier Event)	111	Herrle et al., 2003; Wagner et al., 2007; Erbacher et al., 1996
Late Albian OAE 1d (Breistroffer Event)	99.2	Wilson and Norris, 2001
Cenomanian-Turonian C/T OAE, OAE 2 (Bonarelli Event)	94	Voigt et al., 2006
Dan-C2 Event	65.1	Quillevere et al., 2008

Table 4-1, Continued.

Event Name	Approximate Age (Ma)	Sources
Latest Danian Event (Top Chron 27 Event)	61.75	Bornemann et al., 2009; Westerhold et al., 2011
Mid-Paleocene Biotic Event (Early-Late Paleocene Event)	58.4	Bernaola et al., 2007
'A' Event	57.5	Cramer et al., 2003; Zachos et al., 2010
'B1' Event	57.4	Cramer et al., 2003; Zachos et al., 2010
'B2' Event	57.3	Cramer et al., 2003; Zachos et al., 2010
'C1' Event	57	Cramer et al., 2003; Zachos et al., 2010
'C2' Event	56.9	Cramer et al., 2003; Zachos et al., 2010
'D1' Event	56.5	Cramer et al., 2003; Zachos et al., 2010
'D2' Event	56.4	Cramer et al., 2003; Zachos et al., 2010
Paleocene Thermal Maximum (PETM)	56	Bralower et al., 1997; Bains et al., 2003; Cohen et al., 2007; Zachos et al., 2005; Zachos et al., 2007; Pagani et al., 2006; Bowen et al., 2004
'E1' Event	55.9	Cramer et al., 2003
'E2' Event	55.8	Cramer et al., 2003
'F' Event	55.4	Cramer et al., 2003
'G' Event	55.1	Cramer et al., 2003
Eocene Thermal Maximum 2 (Elmo); 'H1' Event	54.6	Cramer et al., 2003; Lourens et al., 2005; Stap et al., 2009; Zachos et al., 2010
'H2' Event	54.5	Cramer et al., 2003; Lourens et al., 2005; Stap et al., 2009; Zachos et al., 2010
'I1' Event	54.2	Cramer et al., 2003; Zachos et al., 2010
'I2' Event	54.1	Cramer et al., 2003; Zachos et al., 2010
'J' Event	53.8	Cramer et al., 2003; Zachos et al., 2010
'K' or 'X' Event	53.4	Cramer et al., 2003
'L' Event	53.1	Cramer et al., 2003
C22rH1	49.97	Sexton et al., 2011
C22rH2	49.92	Sexton et al., 2011; this study
C22rH3	49.84	Sexton et al., 2011
C22nH1	49.69	Sexton et al., 2011
C22nH2	49.56	Sexton et al., 2011
C22nH3	49.25	Sexton et al., 2011; this study
C22nH4	49.16	Sexton et al., 2011

Table 4-1, Continued.

Event Name	Approximate Age (Ma)	Sources
C21rH1	48.78	Sexton et al., 2011; this study
C21rH2	48.65	Sexton et al., 2011
C21rH3	48.42	Sexton et al., 2011
C21rH4	48.38	Sexton et al., 2011
C21rH5	48.33	Sexton et al., 2011
C21rH6	48.11	Sexton et al., 2011
C19r Event	41.8	Edgar et al., 2007
Middle Eocene Climatic Optimum (MECO)	40	Bohaty and Zachos 2003; Bohaty et al., 2009

While bulk or foraminiferal carbonate records exist for all of the events assessed here, $\delta^{13}C$ records from bulk organic carbon are more common for the OAEs, given that most OAEs are characterized by organic-rich sediments and often show low carbonate content. Where records from multiple sources exist, we will evaluate the range of magnitudes for a given event; for detailed comparison of individual records, however, we use bulk carbonate datasets. In addition to assessing the absolute magnitude of the recorded CIE, we will also compare (where published age models are available) the total duration, rate of onset, and rate of recovery of each 'hyperthermal' as defined by the carbon isotope data.

Many CIEs are associated with multiple signs of rapid and intense environmental change. For some events, particularly the PETM, there are studies detailing global and regional impacts on biology, weathering, carbonate preservation and ocean carbonate chemistry, anoxia, and the hydrological cycle (e.g. Thomas et al., 2002; Zachos et al., 2005; Bowen et al., 2004; Sluijs et al., 2006). The Permain-Triassic and Triassic-Jurassic Boundary are well known episodes of mass extinction. For most postulated 'hyperthermals,' in contrast,

there is insufficient data to constrain the full environmental implications of the carbon cycle perturbation recorded. Still, there appear to be commonalities to many 'hyperthermals' beyond the record of the CIE. In general, these episodes coincide with evidence for warming and dissolution of carbonates, and many show some degree of biotic turnover. For each event, we will also assess the evidence for warming, extinction and/or biotic turnover, dissolution, weathering, anoxia, and evidence for the event's global occurrence.

Previous reviews have suggested links between the PETM and Toarcian events, and also suggested connections between the PETM and the smaller 'hyperthermals' that occur in a ~5 Myr bracketing interval (Cohen et al., 2007; Zachos et al., 2010; Lunt et al., 2011). This study will compare a much larger selection of events in an attempt to isolate criteria necessary for defining an event as a hyperthermal, which will be useful in seeking to understand the likelihood that a common mechanism is responsible for the occurrence of at least some of these events.

4.3 Evaluation of Carbon Isotope Excursions

CIEs associated with identified 'hyperthermals' demonstrate a large range in size—from bulk carbonate CIEs of <0.4‰ to bulk organic carbon CIEs of up to 8‰. Figure 4-1 shows the range of CIE magnitudes for the 44 events listed in Table 1. Larger ranges are partly a function of the number of records available for an individual event. The PETM, the most well studied event, shows a range

across all sources of 1-6‰, though a consensus has emerged around a CIE-size of ~4‰ (Dunkley-Jones et al., 2010). Many of the Paleogene events have fewer than 5 records (and most of the C22r-C21r events have isotope data from only a single site). In general, earlier events also have larger ranges. The largest range exists for the T/J (1.5-8‰), but van Schootbrugge et al., 2008, actually argue that no negative excursion occurred in the exogenic carbon pool at the T/J because 1) compositional changes can explain organic C $\delta^{13}C$ shifts, 2) there are bulk carbonate $\delta^{13}C$ records across the T/J that show no evidence of a negative CIE, and 3) diagnetic overprinting may explain negative CIEs from other bulk carbonate records.

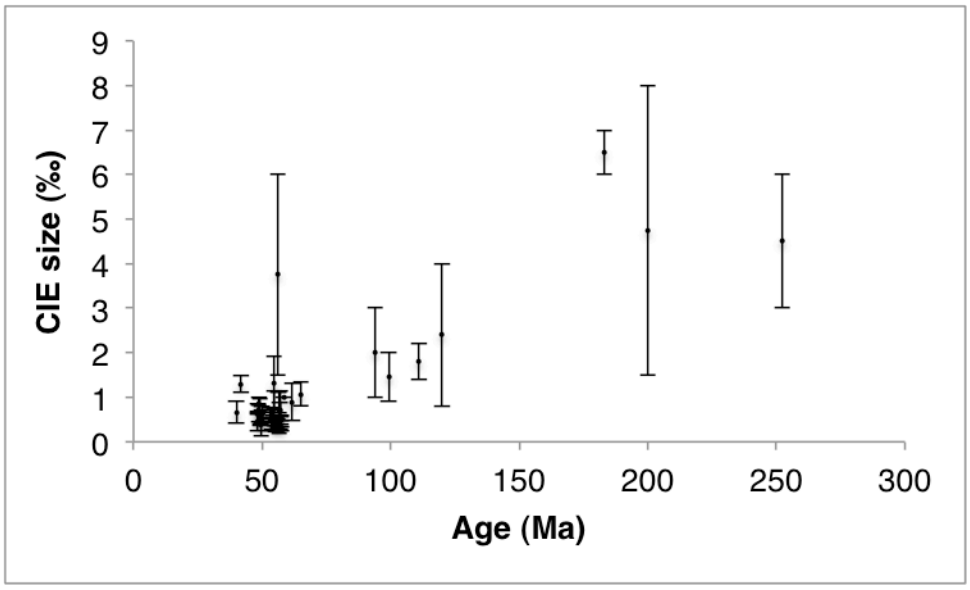


Figure 4-1. Ranges in CIE size ($\delta^{13}C$ ‰) plotted against absolute age for each event listed in Table 1. Sizes are taken from all available sources (including both carbonate and organic carbon records). Records are only excluded if diagnosis is obvious. Sources of records used are listed in Table 1.

4.3.1 Effects of CIE Duration

The durations of each CIE are generally more similar (Figure 4-2). Again, greater uncertainty exists for earlier events; in particular, estimates for the duration of the CIE at the P/T boundary range from 165 kyr to 2 Myr (Corsetti et al., 2005), and estimates for the duration of the T/J event range from 20-40kyr to ~600 kyr (Ruhl et al., 2011; Hesselbo et al., 2002). Excluding the large end of the range for these events, CIEs are typically no more than 300 kyr in duration (~300 kyr is the preferred estimate for the duration of the Toarcian based on astronomical cycle counts) (Kemp et al., 2005; Cohen et al., 2007). A large majority of events (38 of 44) are less than 150 kyr in duration. Further, some of the events with total durations greater than 150 kyr have either very abrupt (10-20 kyr) onsets (like the Toarcian and PETM), or may actually constitute two separate events (the LDE and TJ both exhibit double-peak isotopic excursions).

This upper limit of ~150 kyr is equivalent to the residence time of carbon in the exogenic system, suggesting CIEs represent carbon release events, with the timescale of recovery ultimately controlled by the rate of silicate weathering (though faster recoveries may indicate additional mechanisms of CO_2 drawdown). Events with a longer duration suggest multiple pulses of carbon or an extended duration of carbon release.

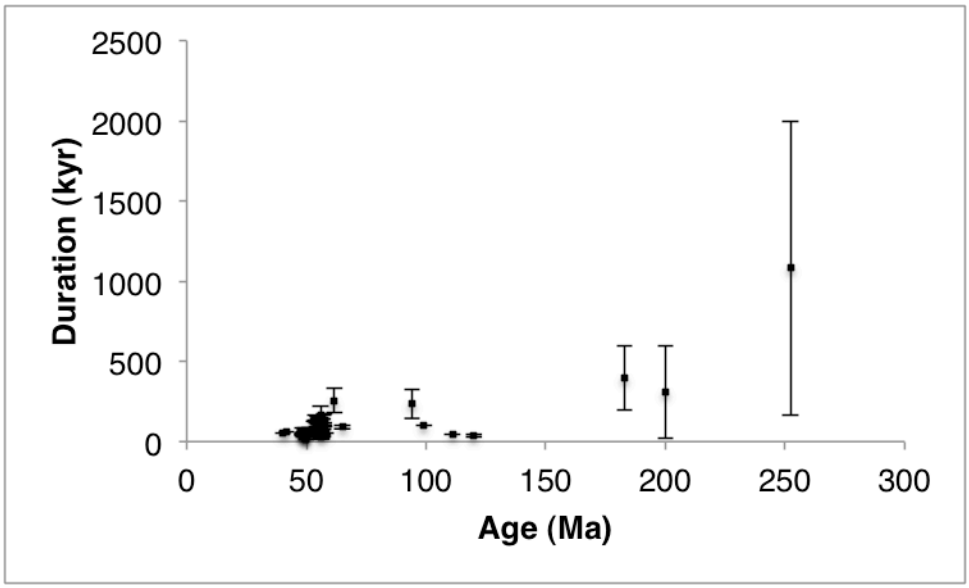


Figure 4-2. Ranges in CIE duration (in kyr) plotted against absolute age for each event listed in Table 1.

4.3.2 Controls on CIE size

The smallest CIE for a given event is typically associated with bulk and benthic foraminiferal carbonate from deep-sea sections (Kennett and Stott, 1991; Thomas et al., 1999, Zachos et al., 2003; Zachos et al., 2005). Zachos et al., 2005, demonstrated that dissolution was the most intense in the deep-sea during the PETM, suggesting the primary reason for the subdued CIEs is that the total loss of carbonate prevented the recording of peak excursion values. A carbonate ion effect may also reduce the apparent size of the excursion in carbonates—a decrease in the carbonate ion concentration in seawater, which is an expected effect of decreasing pH associated with massive carbon input to the atmosphere-oceans, will cause a positive shift in the isotopic composition of carbonates,

partially offsetting the negative excursion (Spero et al., 1997).

In contrast, the largest CIEs recorded for the PETM are from marine organic carbon, higher plant n-alkanes, and pedogenic (terrestrial) carbonates (Sluijs et al., 2006; Pagani et al., 2006; Bowen et al., 2004). This relationship—with larger CIEs recorded in organic carbon—occurs in Toarcian records as well (Cohen et al., 2007). The difference in magnitude between the carbonate and organic carbon excursions even occurs in individual sections (Jenkyns et al., 2001; Hesselbo et al., 2007). While organic carbon records are more common for earlier events, records for the large number of Paleogene events are only from bulk and benthic foraminiferal calcite. The source of these records may bias our interpretation of these CIEs towards smaller sizes.

Comparing bulk carbonate records alone is still an imperfect method of assessing relative CIE magnitude because individual site characteristics can impact the details of the size and shape of the recorded CIE. Sedimentation rate, by controlling the extent to which bioturbation 'smears' the signal, can exert a strong control on CIE-magnitude—Earth system modeling suggests that a 50% decrease in sedimentation rate can decrease the apparent CIE size by around a third (see Chapter 5).

Given that dissolution intensity is at least partly a function of depth, differences in paleodepth may also influence CIE size—Zachos et al., 2005, and Stap et al., 2009, use depth transects recording the PETM, ETM-2, and H2, which show that shallower sites record consistently larger excursions. Given that

records of OAEs, the T/J, and P/T are typically from shallow sites as a result of the subduction of old seafloor, our interpretation of these CIEs may be biased towards larger sizes. Additionally, dissolution intensity is a function of the amount of carbon released, so the influence of dissolution on the recorded excursion size will be greater for large excursions than for small, suggesting smaller excursions may not be as biased as larger ones that cause massive dissolution.

Larger carbon release events should also result in a larger range of recorded CIEs across different sites. This is consistent with model results demonstrating that larger carbon pulses (though with varying carbon isotopic compositions, all intended to simulate the negative 4‰ CIE of the PETM) show a wider range in surface dissolved inorganic carbon $\delta^{13}C$ excursions (Panchuk 2007).

Combined, inter-site characteristics and the size of carbon input during each event impact the degree to which a single site accurately records an individual event. In general, however, these effects will tend to reduce the apparent CIE-size—none of these proposed mechanisms would enhance CIE-size in carbonates relative to the 'true' excursion in the oceans-atmosphere. Diagenesis, in contrast, provides one possible mechanism for enhancing the apparent CIE size. Bralower et al., 1997, suggest diagenesis is responsible for the extremely large magnitude CIE (12‰) recorded in bulk carbonate at ODP Site 999 in the Caribbean for the PETM.

One oft-used method for assessing diagenetic overprinting is to generate

cross-plots of $\delta^{13}C$ and $\delta^{18}O$ values, with strong correlation taken as evidence of diagenesis. However, modern foraminiferal shell values of $\delta^{18}O$ and $\delta^{13}C$ almost always display this covariance, so covariant trends are not absolute indicators of diagenesis (Veizer et al., 1999). None of our selected records have evidence of diagenesis reported, so using the largest CIE recorded represents the best guess among bulk carbonate records of an individual event, while still serving as a minimum estimate of the event's true size.

4.3.3 Comparison of CIEs

In order to compare details of individual bulk carbonate CIEs, we have plotted adjusted $\delta^{13}C$ records against depth for each of our 44 events that has been identified from multiple sites (Figure 4-3). Using only bulk carbonate records requires the exclusion of a number of the proposed hyperthermals of Sexton et al., 2011, where benthic foraminiferal records from a single site provide the only isotopic evidence of occurrence. Bulk carbonate isotopic data identifying CIEs are available from multiple sites for three of these events, C22rH2, C22nH3, and C21rH1, so we include records from these three events in Figure 4-3. In addition, we exclude the Chron 19r event despite the availability of bulk carbonate data, because of its identification at only a single Atlantic site (Edgar et al., 2007). Similarly, we do not show a record for OAE-1d, since we were not able to find a bulk record clearly showing a preceding negative CIE (though foraminiferal data from ODP Site 1052 do show such an excursion, which we include in Figure 4-1)

(Wilson and Norris, 2001).

The one exception to our multi-site rule is the Mid-Paleocene Biotic Event. Though there is only one isotopic record for this event from a pelagic section in the Pyrenean Basin (Bernaola et al., 2007), correlatable sections in the Pacific, Atlantic, and Caribbean all show evidence for an unusually massive dissolution event (Westerhold et al., 2007).

Where multiple bulk carbonate records are available, we select the largest recorded excursion. Each event is shifted so that its onset occurs at zero, where we define onset as the maximum value after which values begin to decrease continuously towards the $\delta^{13}C$ minimum. We also include the estimated duration of each event (though not on separate axes, since detailed age models are not available for each record). The estimated ranges in duration are for all records of an event and are therefore not specific to the records plotted here.

4.3.4 The Toarcian and PETM events

The largest excursion in bulk carbonate, 6.3‰, is from the Toarcian (Hermoso et al., 2012). Like other records of the Toarcian CIE, there is a stepped decrease in isotopic values towards the excursion peak, which authors have interpreted as evidence for multiple pulses of carbon release (Hermoso et al., 2012, Jenkyns and Clayton, 1997; Jenkyns et al., 2001). The Toarcian record plotted here is from the Parris Basin at ~30°N, a sub-basin off of the north epicontinental seaway, with a paleodepth of just 100-200 meters (Hermoso et al.,

2009). This comparatively shallow depth suggests that the record has not been highly compromised by dissolution, as does its similarity to the $\delta^{13}C$ record from bulk organic carbon from the same locality (Hermoso et al., 2012).

In general, the shallow depths of most Toarcian carbonate records means that carbonate CIEs are much closer in magnitude to organic carbon CIEs than for the PETM. Counting of inferred orbital cycles suggests an absolute duration of ~300 kyr for the Toarcian, with the series of pulses to negative $\delta^{13}C$ values occurring over a total of ~60 kyr (Kemp et al., 2005). This timescale suggests the Toarcian has an asymmetrical shape—with a recovery interval longer than the onset. Though not clearly apparent in our selected Toarcian $\delta^{13}C$ record, others show an extended duration for the peak of the CIE—the $\delta^{13}C_{org}$ record from Yorkshire, England, used by Kemp et al., 2005, for their astronomical calculations showed a plateau in $\delta^{13}C$ values for ~120 kyr.

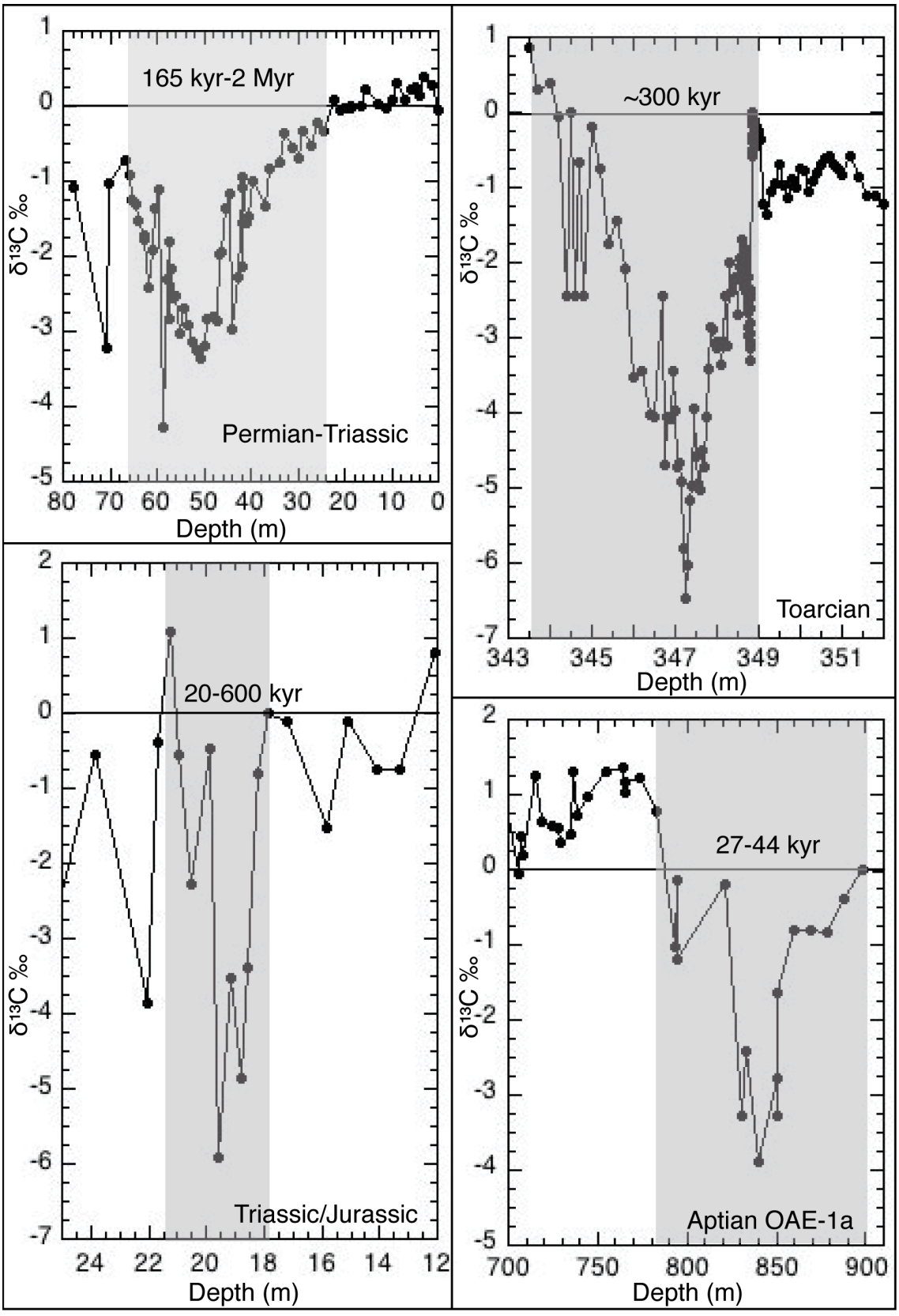
The Toarcian and PETM CIEs share multiple features—including a stepped onset and an asymmetrical shape, as well as a broadly similar timescale (the PETM has a duration of roughly 220 kyr) (Cohen et al., 2007). The PETM record in Figure 4-3, with a CIE of -3‰, is one of the largest identified in marine bulk carbonate, from ODP Site 1001 in the Caribbean with a paleodepth of 1500-2500 m (Bralower et al., 1997). Shallower sections, including a Pacific carbonate platform (Limalok Guyot, ODP Site 871) also show an ~-3‰ CIE (Robinson, 2010). The extremely abrupt onset, with no intermediate values, is typical of PETM records where, as at Site 1001, wt% $CaCO_3$ drops to zero during the

event. Even at sites where dissolution is less intense, the rate of onset for the PETM still appears extremely rapid, <10 kyr (Thomas et al., 2002; Sluijs et al., 2008; Dunkley-Jones et al., 2010). In contrast, most PETM records show a relatively extended recovery phase, which has often been used as evidence that silicate weathering was the primary mechanism responsible for removal of excess carbon.

4.3.5 Hyperthermal Shape

Event shapes are apparent from $\delta^{13}C$ records plotted against depth in Figure 4-3. However, changes in sedimentation rate are probable during an event, so age models should improve interpretation of the true shape. As a result of these events' relatively short duration, most age models are developed through orbital tuning, assuming regular cycles in proxy records represent specific orbital periods (typically precession). For the PETM, an age model developed for ODP Site 690 using extraterrestrial ^{3}He, assumed to be a constant sedimentation rate tracer, disagrees with orbital age models for the recovery phase at this site by more than 100 kyr (Farley and Eltgroth, 2003). Age models for the PETM from ODP Leg 208 sites in the South Atlantic agree with the Site 690 age models, suggesting a relatively more rapid recovery from excursion values, with sedimentation rates increasing during the recovery phase (Murphy et al., 2010). These alternative age models suggest that the PETM may not be as asymmetrical as previously assumed, with implications for the mode of recovery

Figure 4-3. Individual CIE records from bulk carbonate for each event of the 44 listed in Table 1 that can be identified at multiple sites. P/T record from Daijiang China, Meyer et al., 2011; T/J record from Hungary, Palfy et al., 2001; Toarcian record from Paris Basin, Hermoso et al., 2012; Aptian record Alison Guyot ODP Site 809, from Jenkyns et al., 2001; Albian record from; C/T record from Voigt et al., 2006; Dan C-2 record from Quillevere et al., 2008; LDE record from Borneman et al., 2009; MBE record from Zumaia, Spain, Bernaola et al., 2007; 'A' from ODP 609, Cramer et al., 2003; B1 from Cramer et al., 2003; B2 from Cramer et al., 2003; C1 from Cramer et al., 2003; C2 from Cramer et al., 2003; D1 from Cramer et al., 2003; PETM from Bralower et al., 1997; E1 from Cramer et al., 2003; E2 from Cramer et al., 2003; F from Cramer et al., 2003; G from Cramer et a., 2004; H1 and H2 from Stap et al., 2009; I1 and I2 from Cramer et al., 2003; K from Cramer et al., 2003; L from Cramer et al., 2003; C22rH2 from this study; C22nH3 from this study; C21rH1 from this study; MECO from Bohaty et al., 2009. Grey shaded boxes indicate the body of the CIE. All δ- values are plotted with the 'starting' value adjusted to 0‰ for comparison.


165 kyr-2 Myr
Permian-Triassic
δ13C ‰
Depth (m)
~300 kyr
Toarcian
δ13C ‰
Depth (m)
20-600 kyr
Triassic/Jurassic
δ13C ‰
Depth (m)
27-44 kyr
Aptian OAE-1a
δ13C ‰
Depth (m)

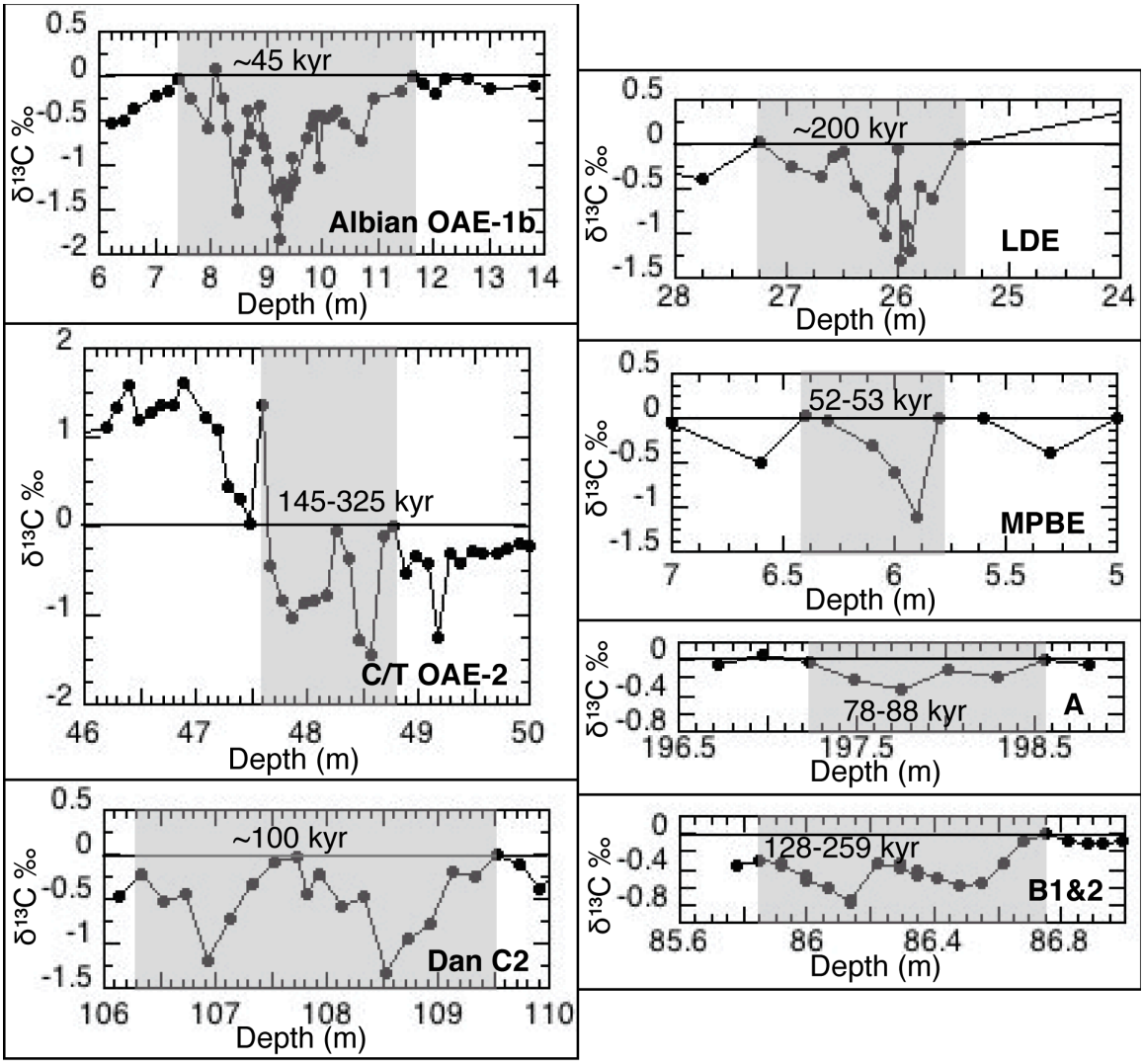


Figure 4-3, Continued.

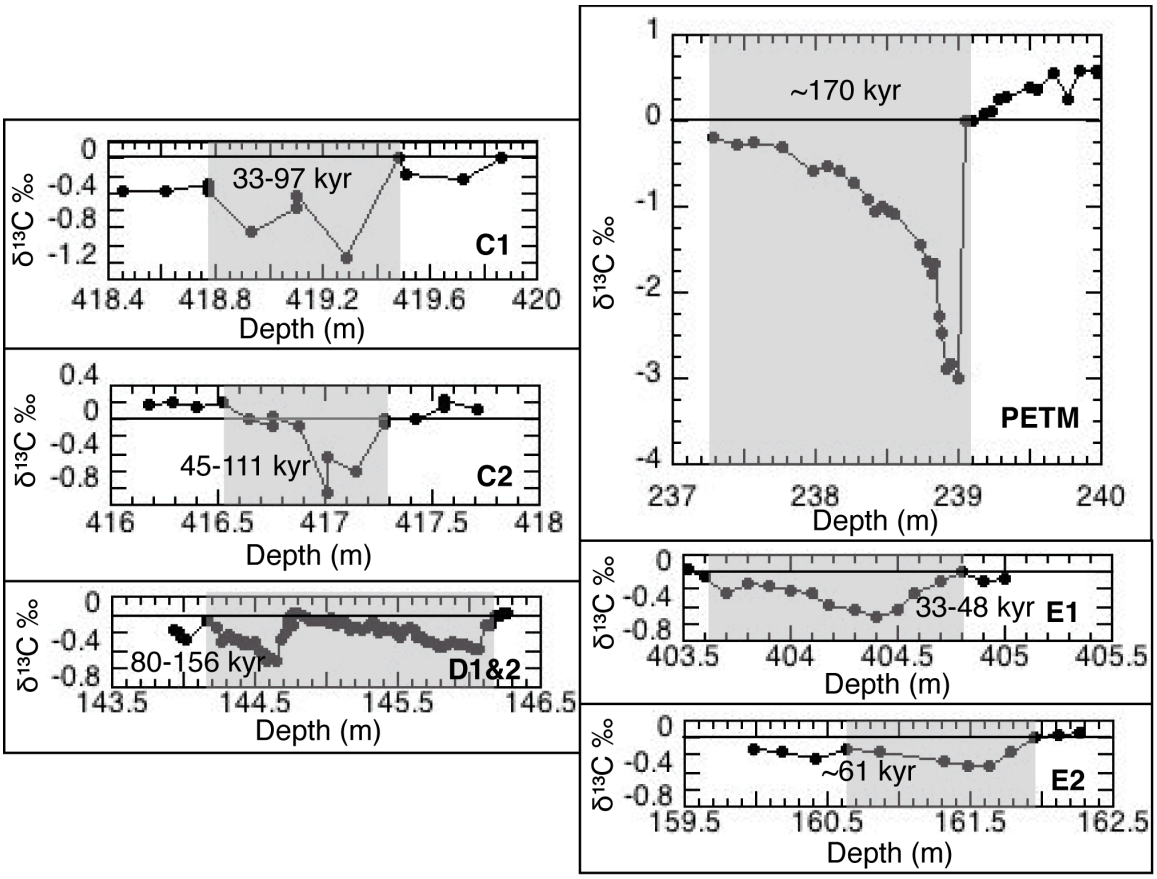


Figure 4-3, Continued.

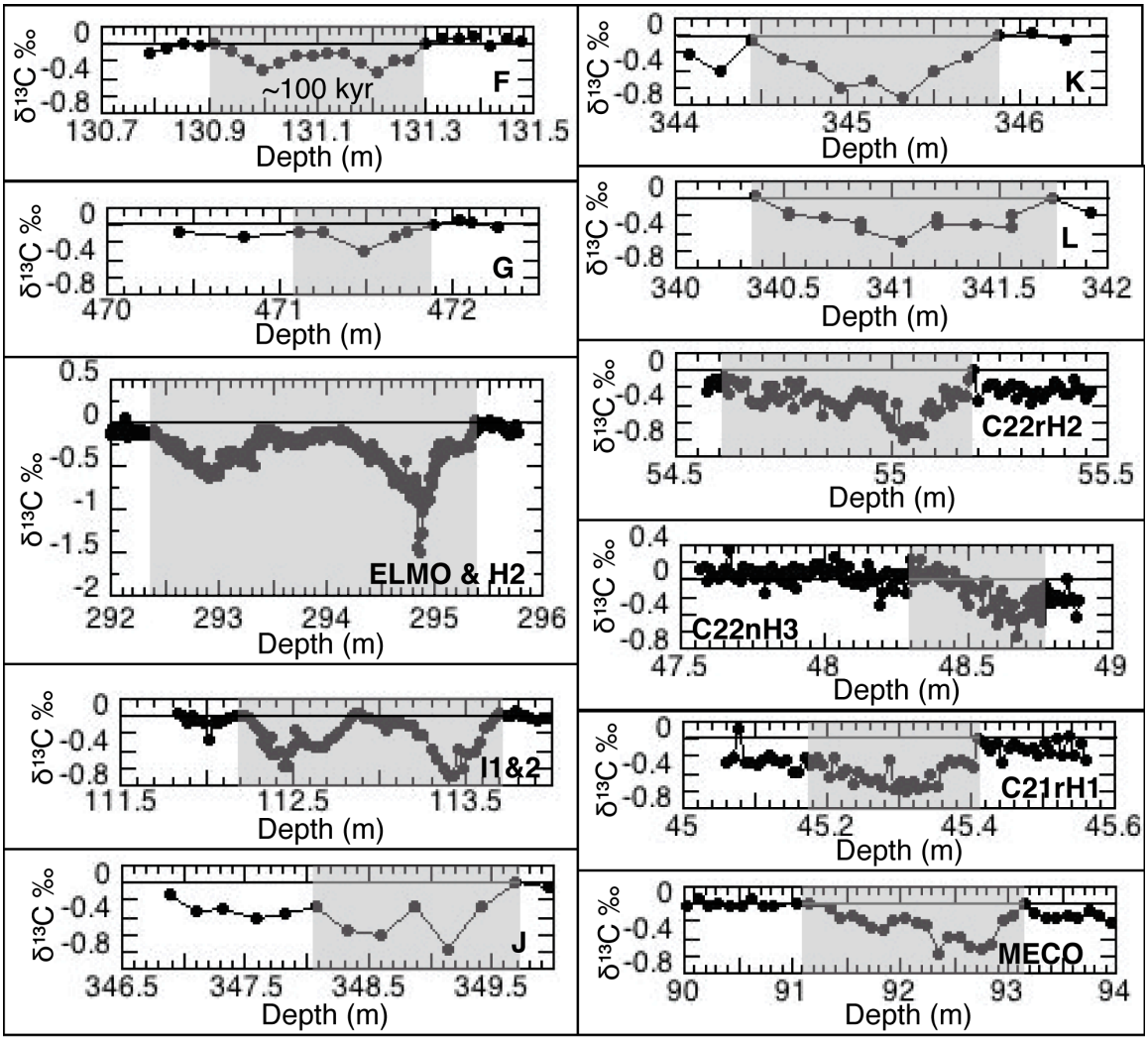


Figure 4-3, Continued.

In fact, most CIEs show a symmetrical shape, with rate of onset similar to rates of recovery. This is not simply a feature of small CIEs—the large excursions at the P/T and T/J boundaries are roughly symmetrical as well. Age models for the events in Figure 4-3 do not greatly alter their apparent shape, and all age models (with the exception of the PETM) are from orbital tuning. Age models may differ significantly depending on which orbital periods cycles are assumed to represent; this is particularly true for the earlier events, which show a wide range of estimates for their total duration.

For other events (and for the P/T and T/J as well, if shorter estimates are more accurate), onsets occur in less than 60 kyr. The apparent rapidity of onset, rather than the size of the CIE alone, is what makes these events unique from gradual trends common in $\delta^{13}C$ records. Rates of recovery are slightly longer. For Paleogene events, the PETM recovery appears to be the longest, with the remainder of recoveries occurring over less than 100 kyr. Timescales of recovery for the negative CIEs preceding the OAEs are more uncertain, but also appear rapid. For the pre-OAE events, values usually transition from the negative CIE directly into a large, extended positive excursion, associated with black shale deposition and enhanced productivity and/or organic matter preservation (Jenkyns, 2010).

Many of the records in Figure 4-3 show a double peak in $\delta^{13}C$. In some cases, these double peaks have been identified as separate events. Cramer et al., 2003, adopted the convention of labeling paired transients from the late

Paleocene to early Eocene with the same letter, parts ‘1’ and ‘2.’ For this study, in determining whether to plot these CIEs as individual events or double peak events, we assessed whether there was a clear recovery between each event based on the number of intervening ‘background’ values. When values appear to decline immediately following the recovery from the first excursion (using sites where the largest CIEs are recorded), we plot both excursions as a single event. Of the twelve transients Cramer et al., 2003, identified, six occurred as pairs. However, the double peak shape also occurs in the early Paleocene (Latest Danian Event and Dan-C2 event), for a number of the OAEs, and possibly at the T/J boundary.

These double peaks suggest that carbon input occurs in discrete pulses and also implies the operation of strong feedbacks during an event that could result in rapid and preferential drawdown of ^{12}C, such as enhanced organic matter preservation (Bowen and Zachos, 2010). Less common are records where $\delta^{13}C$ values plateau during the excursion, though this is at least partly a factor of sampling resolution. Extensive records exist for the PETM and Toarcian, and both show that the most negative values are maintained for an extended interval—perhaps 85-120 kyr (Cohen et al., 2007). The extended duration of peak excursion values also necessitates multiple pulses of carbon addition (Cui et al., 2011).

4.4 Comparison of CIEs to background $\delta^{13}C$ variability

Carbon cycle events identified as 'hyperthermals' clearly represent a spectrum in the degree of environmental impact. Figure 4-3 demonstrates that the majority of the identified events, in particular events A-L and the mid-late Eocene C22r-C21r events, are as much as an order of magnitude smaller than the large excursions associated with the Toarcian, T/J boundary, P/T boundary, Aptian OAE, and PETM. To identify all these events as 'hyperthermals' should suggest a degree of uniqueness—that the events are clearly distinguishable from typical amplitude variations in $\delta^{13}C$ records.

Variability in $\delta^{13}C$ records is often associated with orbital forcing of the carbon cycle (Woodruff and Savin; 1991; Flower and Kennett, 1995; Diester-Haas et al., 1996; Zachos et al., 1996; Zachos et al., 2001; Cramer et al., 2003; Palike et al., 2006). The long residence time of carbon in the exogenic system (10^5 years) acts as a filter on the $\delta^{13}C$ variability recorded in carbonates, such that long period orbital cycles are most identifiable (Cramer et al., 2003; Palike et al., 2006).

Carbon isotope records throughout the Cenozoic show prominent short eccentricity cycles (~100 kyr), which many authors have interpreted as evidence of a precessional influence on the carbon cycle, since eccentricity maxima are times of greatest precessional variability, and precession forcing has a stronger radiative impact than eccentricity forcing (Flower and Kennett, 1995; Diester-Haas et al., 1996; Zachos et al., 1996; Zachos et al., 2001; Cramer et al., 2003).

Others have identified longer-period cycles in $\delta^{13}C$, consistent with long period (400-500 kyr) eccentricity modulation of precession and long-period modulated obliquity (1.4 Myr). These cycles are generally interpreted as a function of changes in the burial ratio of organic carbon to carbonate and changes in total marine productivity (Woodruff and Savin, 1991; Palike et al., 2006; Russon et al., 2010). Zachos et al., 2010, suggested that cycles in the late Paleocene-early Eocene are the result of changes in amount of organic carbon buried on land.

The standard deviation for mean values of carbonate $\delta^{13}C$ for Cretaceous through Cenozoic bulk carbonate records is 0.3‰ (2σ of 0.6‰) (Shackleton, 1987; Hayes et al., 1999). For long-period (~400 kyr) fluctuations over the past 5 Myr, typical amplitude variability is 0.5-0.15‰ (Russon et al., 2010). However, studies from the Neogene, Oligocene, and Paleogene have all identified up to 1‰ fluctuations in the $\delta^{13}C$ of carbonates associated with orbital periods.

Whereas the amplitude of $\delta^{13}C$ and $\delta^{18}O$ variability in the Neogene (and Oligocene) has often been ascribed to the influence of ice-sheets as amplifiers of orbitally-induced climatic changes, Cramer et al., 2003, point out that equivalent variations are equally large in the Paleogene, when widespread ice sheets did not exit. Further, they suggest that ‘hyperthermals’ (though not the PETM), are climatic perturbations occurring at eccentricity maxima. Zachos et al., 2010, confirm this relationship between a number of Paleogene ‘hyperthermals’ and orbital cycles, noting that the PETM is out of phase with the long (405 kyr) eccentricity cycle, but possibly occurs at a short eccentricity maxima.

If ‘hyperthermals’ occur at eccentricity maxima, questions arise whether 1) they occur at all eccentricity maxima, and 2) whether a regular, orbitally-paced climatic cycle can be connected with larger events, including the PETM and the CIEs preceding the OAEs. The regular, orbitally-paced A-L CIEs identified in bulk carbonate records are also apparent in benthic foraminiferal $\delta^{13}C$, demonstrating a whole-ocean signal, and correspond with negative excursions in benthic foraminiferal $\delta^{18}O$, suggesting 1-4°C bottom water warming (Cramer et al., 2003). This is similar to the Chron 22r-21r events from Sexton et al., 2011, with 13 purported ‘hyperthermals’ in a 2.4 Myr interval, with power at the short and long eccentricity frequencies.

Not all of the A-L and C22r-C21r ‘hyperthermals’ are clearly larger in magnitude than short-term, orbitally-paced variability from the rest of the Cenozoic. Figure 4-4 shows selected benthic foraminiferal $\delta^{13}C$ records for 2.5 Myr time-slices through the Cenozoic (0-5 Myr from ODP Site 846, 10-12.5 Myr from ODP Site 574, 14-16.5 Myr from ODP Site 1171, 22.5-32.5 Myr from ODP Site 1218, 47.5-50 Myr from ODP Site 1258, and 57.5-65 Myr from ODP Site 1209). Each record is from an individual site, chosen because these sites have relatively high (approximately 15 kyr or less) resolution, sufficient for detecting longer period (excluding precession) orbital cyclicity.

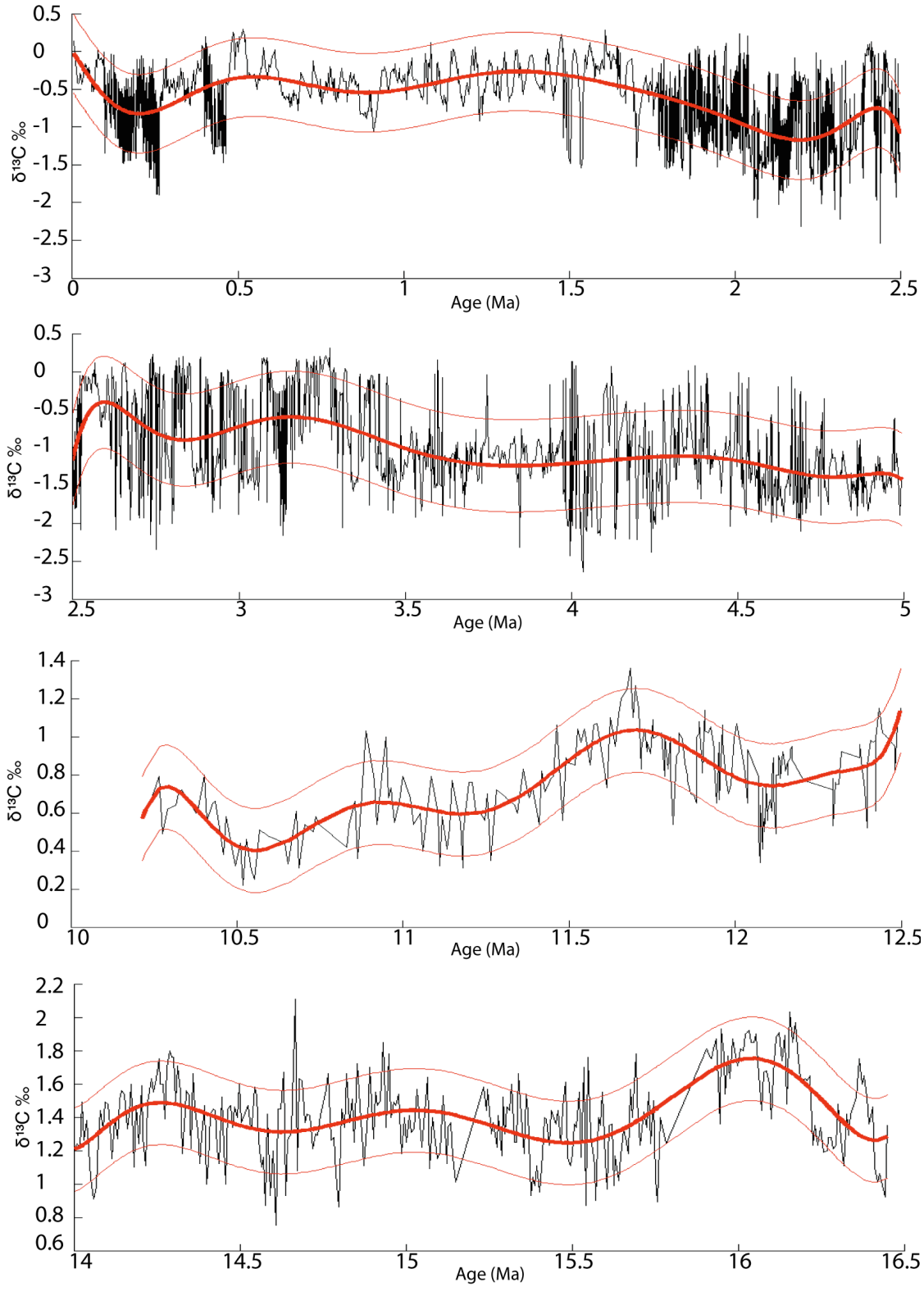
The highest resolution records (unsurprisingly) are from the 0-5 Myr interval, at ODP Site 846, which has very high sedimentation rates ranging from 1.5 to 7 cm/kyr (Mix et al., 1995). In contrast, the Paleocene records, from ODP

Site 1209, have sedimentation rates typically less than 1 cm/kyr (Westerhold et al., 2011). Low sedimentation rates should act as a filter on high-frequency variability, with greater time averaging, so it is impossible to make an absolute evaluation of $\delta^{13}C$ variability by comparing records for each interval from sites with different sedimentation rates. For this reason, we assess the amplitude of $\delta^{13}C$ variability relative to each individual interval. 4-4 shows the 95% confidence envelope for each 2.5 Myr timeslice (plotted as ±1σ from a least squared error line of best fit)—we calculate standard deviation from 2.5 Myr intervals because this is the length of the record from Sexton et al., 2011, identifying 13 'hyperthermals.'

We compare the $\delta^{13}C$ variability and magnitude of 'hyperthermals' from this interval with the variability of $\delta^{13}C$ from records with resolution equal to or better than the record from Sexton et al., 2011. The greatest σ values (~0.6) occur from records of the Pliocene-late Miocene, with very rapid, short-lived excursions of as much as 2‰. For the remainder of the Cenozoic, σ values are ~0.2, though individual excursions sometimes reach ~1‰. In Figure 4-4, the events that have been identified as hyperthermals are shaded in grey. We do not show the A-L hyperthermals because benthic foraminiferal records with orbital scale-resolution are still in progress for this interval from ODP Site 1262 (Littler et al., 2011).

The relative size of excursions compared to the 95% confidence envelope in a given interval, combined with the structure of each excursion (i.e. negative

Figure 4-4. 2.5 Myr intervals of $\delta^{13}C$ from sites with temporal resolution of ~15 kyr or greater. 0-5, 10-12.5, and 14-16.5 from Cramer et al., 2009; 22.5-32.5 from Palike et al., 2006; 47.5-50 from Sexton et al., 2011; and 57.5-65 from Westerhold et al., 2011. For each 2.5 Myr interval, we calculate the standard deviation and plot this as ± 1σ from a least squared error line of best fit calculated for that interval.


δ13C ‰
Age (Ma)
0.5
0
-0.5
-1
-1.5
-2
-2.5
-3
0
0.5
1
1.5
2
2.5
δ13C ‰
Age (Ma)
2.5
3
3.5
4
4.5
5
δ13C ‰
Age (Ma)
1.4
1.2
1
0.8
0.6
0.4
0.2
0
10
10.5
11
11.5
12
12.5
δ13C ‰
Age (Ma)
2.2
2
1.8
1.6
1.4
1.2
1
0.8
0.6
14
14.5
15
15.5
16
16.5

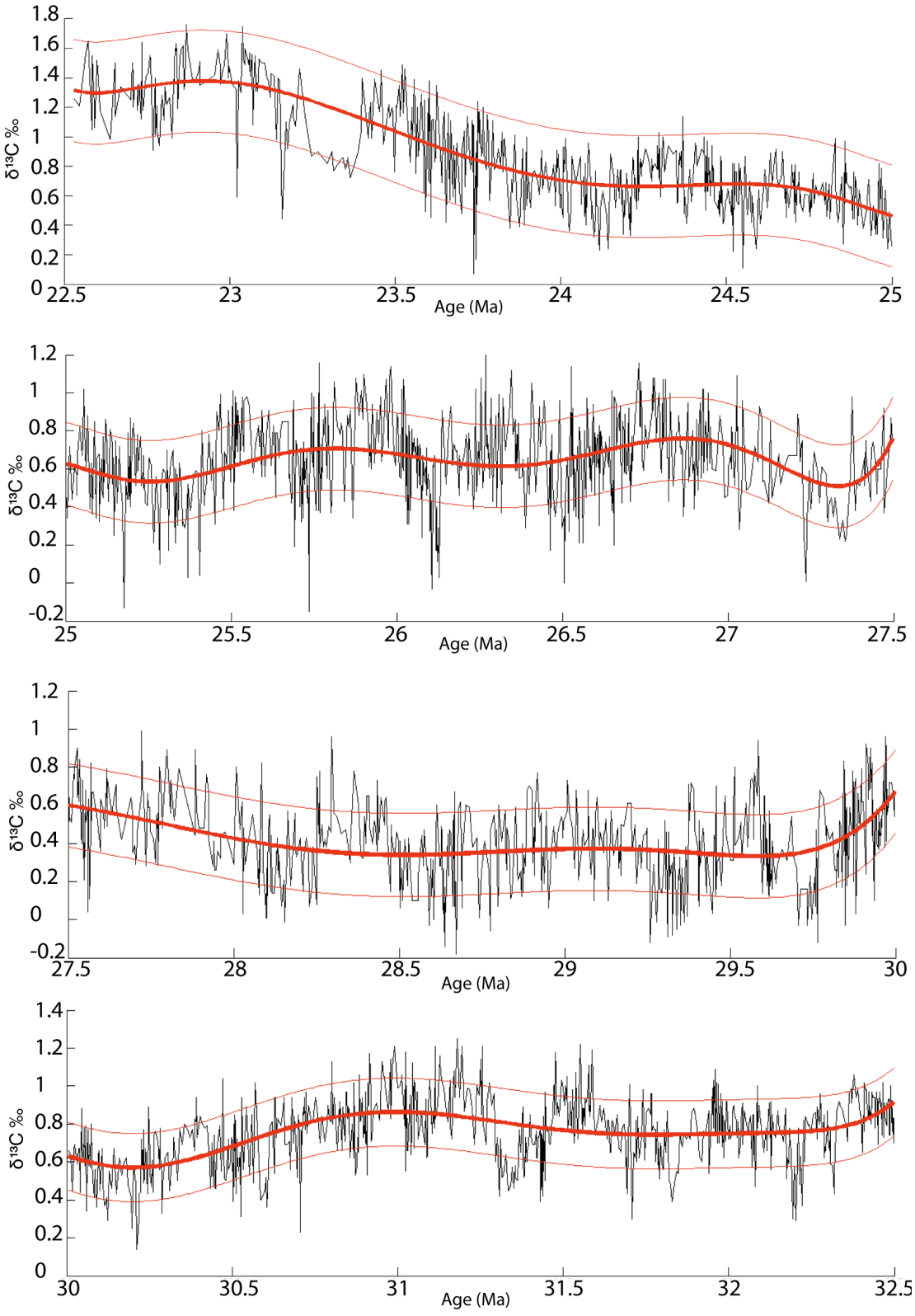


Figure 4-4, Continued.

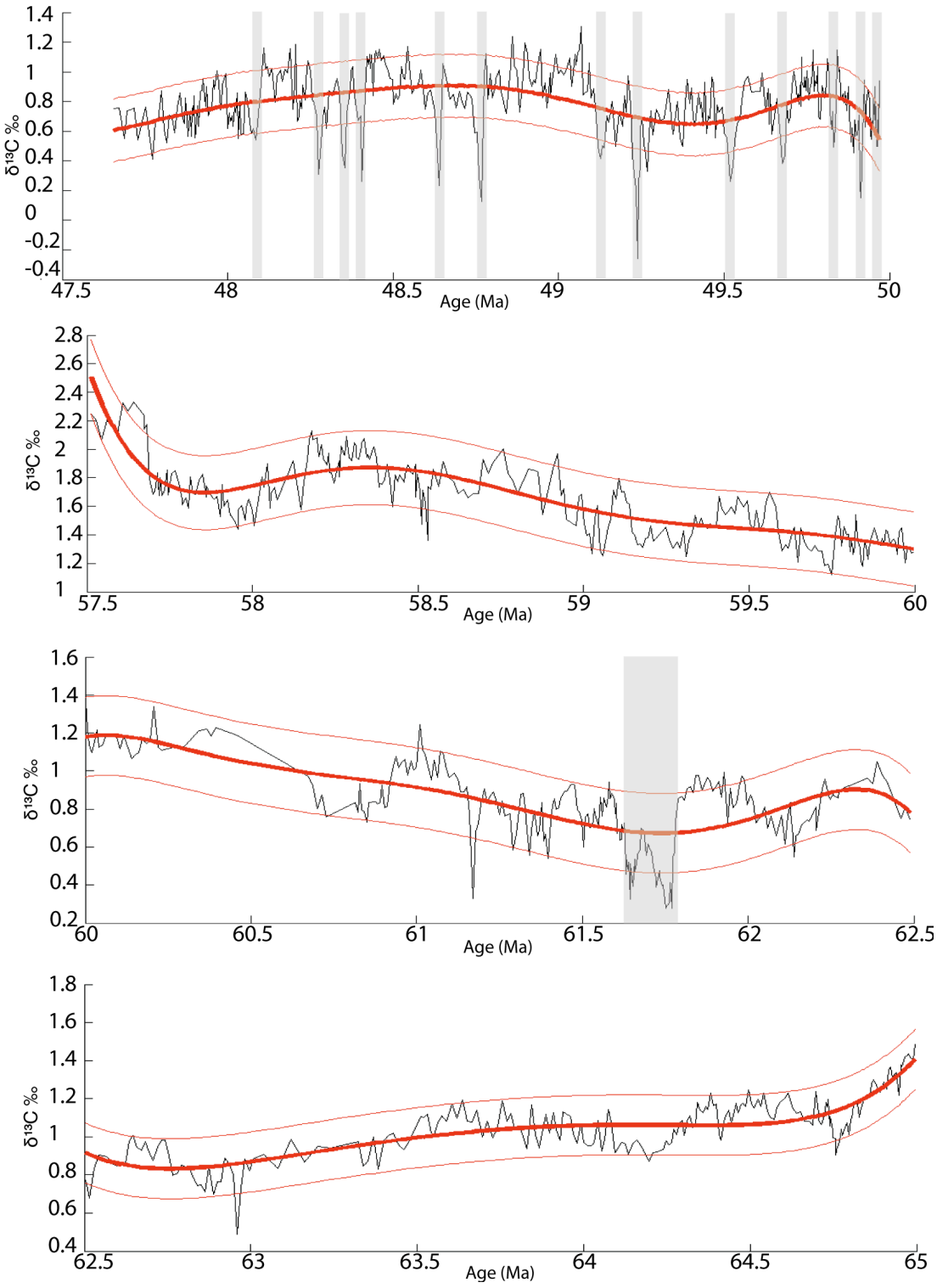


Figure 4-4, Continued.

values persist for at least a few thousand years), differentiate at least some of the 'hyperthermal' events of Sexton et al., 2011, from the short-term $\delta^{13}C$ fluctuations of the later Cenozoic (see Chapter 3 for more detail). While these records cannot provide an absolute size-requirement for an excursion to be considered unusual, decreases in $\delta^{13}C$ of less than 2σ do not seem sufficiently large to consider as CIEs.

Given the small size of so many of the purported 'hyperthermals' compared to Cenozoic short-term $\delta^{13}C$ variability, their significance is probably not as individual events, but that they represent such a strong carbon cycle-climate response to orbital forcing in an ice-free geologic interval. Lunt et al., 2011, suggested that the combination of a long-term warming trend from the late Paleocene to early Eocene (caused by rising CO_2), coupled with orbital forcing, could generate abrupt warming events through periodic destabilization of a methane hydrate reservoir. They noted that the use of methane hydrates as the perturbable reservoir was not exclusive: terrestrial or marine organic carbon could also act as the readily-exchangeable carbon source.

If most of the purported Paleogene 'hyperthermals' are not significantly larger in magnitude than short-term $\delta^{13}C$ variability characteristic throughout the Cenozoic, then why have so many authors identified specific, individual 'events' from this interval, but not from the Pliocene, when CIEs of this magnitude were common? First, Plio-Pleistocene records show an inverse relationship between $\delta^{13}C$ and $\delta^{18}O$, with negative CIEs corresponding to evidence of colder

temperatures and higher ice volumes. In the earlier Cenozoic, the opposite is true—lower $\delta^{13}C$ tends to coincide with lower $\delta^{18}O$. Second, while variation is greater in Plio-Pleistocene records, this means that few cycles stand out, while the CIEs in the early Cenozoic appear relatively more rare. Still, it is clear that 'hyperthermals' should be identified relative to the variability apparent in a surrounding interval. For instance, the P/T boundary excursion is not obviously different than the other huge swings in $\delta^{13}C$ records for the Early Triassic (Payne et al., 2004). The relative size of a CIE compared to background variability is arguably more significant than the absolute magnitude of the excursion.

4.5 Evidence for warming during CIEs

The term 'hyperthermal' derives from indications for abrupt warming coincident with CIEs. All the CIEs identified here correspond with evidence of warming. In general, the amount of warming scales with the size of the CIE—the A-L, 22r-C21r, LDE and Dan C2 events show deep-sea warming of 1-4°C, while temperatures increased by more than 5°C during the PETM (Cramer et al., 2003; Dunkley-Jones et al., 2010). Relating the timing of temperature changes to OAEs can be difficult, but all OAEs correspond with evidence for warming, with estimates of 6-7°C for the Toarcian and C/T events, and approximately 8°C for the Aptian and Albian events (Jenkyns, 2010; Ando et al., 2008; Voigt et al., 2006; Bailey et al., 2003; Herrle et al., 2003). Estimates are up to 10°C temperature increase at the T/J boundary and 5-6°C at the P/T (Korte et al.,

2009; Kidder and Worsley, 2004).

It is difficult to directly compare estimates of warming because of the variety of proxies used to deduce temperature change. Temperature estimates are derived from $\delta^{18}O$ of calcite (including bulk carbonate and shells of foraminifera, belemnites, and oysters), Mg/Ca of calcite, and TEX_{86}, each of which reconstructs temperature change in a different environment. For instance, estimates derived from benthic foraminiferal calcite may be influenced by changes in overturning circulation.

The most straightforward use of decreases in $\delta^{18}O$ as indicators of warming are from benthic foraminiferal records from the ice-free Paleogene. Bulk $\delta^{18}O$ records are generally interpreted to reflect temperature signals, but differential fractionation and/or changing nannoplankton abundances prohibit a direct estimate of paleotemperatures, and $\delta^{18}O$ is also more susceptible to diagenesis than bulk $\delta^{13}C$, though this should impact overall values more than short-term trends (Zachos et al., 2010). The $\delta^{18}O$ paleotemperature estimates for OAEs and earlier events generally come from bulk carbonate (or shells of belemnites and oysters), whereas benthic foraminiferal records are available for temperature estimates for the Paleogene. However, the observation that negative CIEs correspond with temperature increase appears robust—differentiating the pre-Neogene negative CIEs from carbon cycle oscillations from the more recent past.

4.6 Dissolution and weathering during CIEs

CIEs commonly occur with decreases in wt% $CaCO_3$, or increases in Fe concentration, typically interpreted as evidence for the decreased accumulation of carbonates and/or dissolution of previously deposited carbonate. These geochemical changes suggest the occurrence of ocean acidification—or more precisely a reduction in the saturation state of seawater with respect to calcite. However, it is not possible to quantify the extent of reduced saturation from individual records of carbonate accumulation.

The most successful attempts to constrain the extent of lysocline and/or CCD shoaling are for the PETM (Zachos et al., 2005; Panchuk et al., 2008; Zeebe et al., 2009), but this is a function of the large number of wt% $CaCO_3$ records available to constrain the depth of the initial and final CCD. The amount of dissolution varies widely for PETM sites—normalized decreases in wt% $CaCO_3$ (corrected for the initial wt% $CaCO_3$) vary from 0-1, with systematic differences between the Atlantic and Pacific (Panchuk, 2007; Panchuk et al., 2008). Also for the PETM, deep sites consistently experienced greater dissolution than shallow sites (Zachos et al., 2005), suggesting that uncertainties in paleodepth for hyperthermal records can bias estimates of the severity of reduced carbonate saturation. For the OAEs, T/J, and P/T events, the lack of deep seafloor also restricts estimates of carbonate dissolution (e.g. Honisch et al., 2012).

For the PETM, inter-site variation in the magnitude of normalized

carbonate decrease does not simply correspond with inter-site variation in the magnitude of the recorded CIE. Similarly, the magnitude of normalized carbonate decrease does not always scale with CIE size for different events. For instance, the Fe increase and wt% $CaCO_3$ decrease associated with the MPBE at ODP Site 1209 in the Pacific is almost as large as for the PETM at the same site (Westerhold et al., 2009), though the only available isotopic data for the MPBE suggests a substantially smaller CIE.

Further, using records of sedimentary Fe content to estimate dissolution during an event may be complicated by the likelihood of changes in dust accumulation associated with CIEs. Woodard et al., 2011, demonstrate an influence of orbital cycles on dust flux and show that Fe content variations cannot be explained by dissolution or changes in carbonate production alone. Along with the timing of many Paleogene hyperthermals, peaks in dust flux occur during eccentricity maxima, where extremes in seasonality favor increased weathering and dust flux (Woodard et al., 2011). Independent proxies (including Sr and Os isotope systems) have also suggested enhanced weathering rates during the PETM and some OAEs (Jones et al., 1994; McArthur et al., 2000; Jones and Jenkyns, 2001; Jenkyns, 2002; Bralower et al., 1997; Frija and Parente, 2008; Kelly et al., 2005).

A number of ‘hyperthermal’ events show the decrease in wt% $CaCO_3$ leading the peak of the CIE for individual sites. Zachos et al., 2005, explain the lead in carbonate reduction for the PETM as a result of carbonate burn-down or

cessation in carbonate deposition—either the peak of the CIE has dissolved or was never recorded. Hermoso et al., 2012, note a similar feature in a high-resolution record of the Toarcian, which they argue cannot be a result of burn-down because the site is shallow (~100 m) and wt% $CaCO_3$ never goes to zero. Instead, they interpret the lead in carbonate reduction as evidence of high CO_2 levels with relatively heavy isotopic composition occurring ~15 kyr before input of isotopically depleted CO_2. Leads in carbonate reduction also occur for the C22r-C21r events; based on the published age models, these leads are typically 8-15 kyr.

Earth system modeling suggests that such temporal offsets occur in sediment records when a single pulse of carbon is applied to the atmosphere-oceans, without requiring complete carbonate burn-down or CO_2 rises decoupled from isotopic change. We suggest that the lead in carbonate reduction is a result of carbonate neutralization/compensation and the weathering of carbonates. A pulse of isotopically depleted carbon to the oceans-atmosphere must mix through the oceans before it is recorded at the seafloor in either benthic foraminifera or bulk carbonates.

In contrast, decreases in wt% $CaCO_3$ are partly a function of lower carbonate export due to decreased carbonate saturation in the surface ocean. As a result, carbonate accumulation begins to recover while the $\delta^{13}C$ of carbonates is still decreasing. The result is an offset in the time of greatest reduction in carbonate accumulation and the point at which the whole ocean $\delta^{13}C$ reaches a

minimum. In sedimentary records where carbonate burn-down is unlikely to have occurred, explanation of temporal offsets thus does not require additional input of isotopically heavy CO_2 preceding the pulse of light CO_2.

4.7 Biotic change during CIEs

The co-occurrence of CIEs and mass extinctions is clearly the most extreme example of biotic change associated with these events. The P/T and T/J are two of the five major mass extinctions of the Phanerozoic (Raup and Sepkoski, 1984). The extreme degree of biotic change during these events is likely, in and of itself, to have influenced recorded $\delta^{13}C$, making it difficult to fully ascribe the CIEs associated with these events to carbon-input processes.

While the P/T and T/J are extreme examples, some degree of biotic change is common to many of the postulated 'hyperthermals.' The widespread extinction of benthic foraminifera is a well-known feature of the PETM (Kaiho et al., 1994; Thomas 2007). The Toarcian event has been linked to high rates of marine and continental extinction and is a large extinction event for bivalves (Little and Benton, 1995; Palfy and Smith, 2000; Aberhan and Baumiller 2003). High rates of extinction and turnover are also evident for other OAEs—Leckie et al., 2002, note the highest rates of tunover in calcareous nannoplankton during the Cretaceous at the Aptian and C/T events and Erbacher et al., 1996, demonstrate that the highest rates of turnover in radiolara during the Cretaceous also coincide with the OAEs.

For the smaller Paleogene events, there is some indication of biotic impacts (or associated change). The Dan-C2 event correlates with low diversity and genus richness in benthic foraminifera and the presence of opportunistic taxa (Alegret and Thomas, 2004; Coccioni 2010). Across the Dan-C2, LDE, and MPBE, nannofossil and foraminiferal assemblages shift from high-diversity to low-diversity, with increases in the relative abundance of taxa indicative of warm water, oligotrophic environments (Youssef Ali, 2009; Bornemann et al., 2009; Bernaola et al., 2007; Petrizzo, 2005). Significantly less data on biotic change exists for the late Paleocene-mid Eocene 'hyperthermals,' though Gibbs et al., 2012, demonstrates that the larger events (H1 or ELMO and I1) are associated with above-background variance in calcareous nannoplankton populations at ODP Site 1209, though no such indication of biotic change is apparent for the smaller events (including H2 and I2).

While there is no published biological or ecological data for many of the smaller Paleogene events, the Gibbs et al., 2012, study suggests a minimum CIE-size for detecting biotic effects. They suggest that CIEs smaller than 0.6‰ (in between the size of I1 and H2 recorded from ODP Site 1209) are not associated with perceivable biotic change. It is impossible to take a specific CIE-magnitude requirement for the recognition of biotic change from a single site, however, particularly because ODP Site 1209 has relatively low sedimentation rates (~1 cm/kyr), which suppresses the amplitude of high-frequency variability and thus may make events appear smaller (Westerhold et al., 2008).

Another complication arises from the fact that changing nannoplankton assemblages themselves can have an impact on $\delta^{13}C$ variability. For instance, Rickaby et al., 2007, postulate a linkage between secular trends in $\delta^{13}C$ over the past 1 Myr and shifts from high productivity assemblages dominated by calcareous nannoplankton to low productivity assemblages dominated by siliceous nannoplankton. Similar changes may account for at least part of the $\delta^{13}C$ signal recorded during a CIE—extracting the influence of similar population changes on carbon isotope records is therefore important for determining the mass of carbon transfer/input required to explain each event.

4.8 Anoxia and changes in productivity and organic matter burial

Deposition of sedimentary sections rich in organic matter indicates extensive anoxia during the P/T—widespread development of euxinic conditions has been suggested as a cause of the mass extinction at this time (Hallam and Wignall, 1997; Isozaki, 1997; Meyer and Kump, 2008). The CIEs associated with the Toarcian and Cretaceous OAEs appear to precede the deposition of black shales and organic-rich sediments indicative of widespread anoxia (Jenkyns, 2010).

While specific details of how anoxia developed are still widely debated, some have hypothesized that the preceding negative CIEs indicate carbon release and warming led to increased stratification, increased nutrient supply, and elevated productivity and/or enhanced organic matter burial, all of which lead

to oxygen depletion (Hesselbo et al., 2000; Jahren et al., 2001; Jenkyns et al., 2003; McElwain et al., 2005; Kuroda et al., 2007; Jenkyns, 2010). The Toarcian, Aptian, and C/T events all show evidence that, at least in some locations, euxinic conditions prevailed high in the water column, though there is clearly regional heterogeneity in the extent and severity of oxygen depletion (Jenkyns, 2010; Sinninghe Damste and Koster, 1998; Pancost et al., 2004; van Breugel et al., 2007; van Bentum et al., 2009). It is not clear that all the Cretaceous OAEs were global—in particular, the Albian OAE-1b may be a regional event of the Atlantic-Tethys (Jenkyns, 2003).

Similarly, some have suggested that the PETM represents an incipient ocean anoxic event, with clear evidence for anoxia in the Arctic, North Sea, and North African and North American continental margins (Speijer and Wagner, 2002; Sluijs et al., 2008; Cohen et al., 2007; John et al., 2008; Jenkyns, 2010). Increased organic matter and a lack of benthic microfossils indicate anoxia corresponding to the LDE in the Tethys Egypt margin (Speijer et al., 2003; Sprong et al., 2012). There is also evidence for anoxia in the Arctic during the ELMO event that suggests very similar environmental conditions to those prevailing during the PETM (Sluijs et al., 2008).

Further, the *Azolla* events of the early-middle Eocene, when the Arctic experienced massive, episodic blooms of the eponymous freshwater fern, are correlated with a highly stratified water column and high rates of organic matter burial (Brinkhuis et al., 2006). The absence of benthic microfossils and presence

of thin laminations in Arctic sediments from this interval suggest anoxic conditions (Brinkhuis et al., 2006). A minimum estimate for the duration of the *Azolla* blooms, from ~48.1-49.3 (Speelman et al., 2009), demonstrates that these events temporally coincide with a number of the C22r-C21r events. The CIEs themselves have not been identified from Arctic sedimentary sections, but this is owing to a lack of calcareous sediment, as well as the likelihood that bulk organic carbon isotopes largely record the presence or absence of *Azolla* rather than a global signal.

There is still debate whether anoxia during these events is a function of increased organic matter preservation or increased productivity. For the PETM, there have been suggestions of increased productivity facilitating excess CO_2 drawdown, but there is also evidence that increases in export production lagged the onset of the event by around 70 kyr (Bains et al., 2000; Torfstein et al., 2010). For the C/T event, increases in phosphorus accumulation rates and Ba/Al ratios suggest an increase in productivity (Mort et al., 2007; Kuypers et al., 2002). Erba et al., 2004, interpret changes in calcareous nannofossil assemblages preceding anoxia and the deposition of organic-rich sediments to infer high productivity during the Toarcian, Aptian, and C/T OAEs, and Browning and Watkins, 2008, use calcareous nannofossil assemblage change to infer increases in productivity across the Albian OAE as well. Meyer et al., 2011, use surface to deep $\delta^{13}C$ gradients to infer strong productivity at the end-Permian.

4.9 Importance of shallow epicontinental seas?

Basin geography—including sill depth, sea level, and connection to rivers—is significant for the development of localized anoxia and the formation of black shales. Today, anoxia develops in silled basins like the Black Sea, restricted basins such as the Cariaco in Venezuela and the Santa Barbara off California, fijords, and unmixed lakes, though not in the open ocean (Meyer and Kump, 2008). However, during the P/T, OAEs, and some hyperthermals, anoxia was clearly much more widespread. Meyer and Kump, 2008, suggest that the development of such widespread anoxia requires geography that favors extensive 'nutrient-trapping' regions—these are typically narrow oceans and epicontinental seas. Using the GENIE model, they demonstrate the large extent of such regions at the end Permian, a time of widespread and intense anoxia. Nutrient-trapping efficiency is similarly widespread during the Cretaceous, more limited at the PETM, and minimal in the modern (Meyer and Kump, 2008).

There is an interesting correlation between anoxia-favoring paleogeography and the occurrence and size of the CIEs described here. Over the Cenozoic, there is a clear trend towards opening seaways and a reduction in the extent of epicontinental seas. In particular, Arctic ventilation began sometime between the middle-Eocene to Miocene, with some evidence placing the end of Arctic isolation at ~36 Ma (O'Regen et al., 2011). The Arctic was the last large basin favorable to the development of anoxia during the Cenozoic. Its opening also roughly coincides with the date of the last hyperthermal, the MECO, at ~40

Ma.

We suggest that the anoxia-favoring geography is a necessary pre-condition for the occurrence of hyperthermal events, since this geography allows the development of a large organic carbon reservoir. Higgins and Schrag, 2006, hypothesize that dessication of organic matter following the isolation and uplift of an ~3 x 10^6 km^2 shallow epicontinental seaway could contribute the ~5000 Gt organic carbon over 10-30 kyr necessary to explain the PETM. They argue that the occurrence of multiple hyperthermals (citing the ELMO and X events) further complicates the methane hydrate hypothesis for hyperthermal generation by requiring either a larger than expected methane hydrate reservoir during such a warm background climate (which would reduce the hydrate stability zone) or a rapid rate of recharge following depletion events. In contrast, they suggest that additional hyperthermal events might be expected during periods of large epicontinental seas.

While Higgins and Schrag, 2006, suggest a tectonic mechanism for isolation and uplift of a shallow epicontinental sea to drive organic matter dessication, we suggest that tectonic uplift is not necessary to explain the link between the existence of epicontinetal seaways and hyperthermals in every event. For instance, during the *Azolla* events in the Arctic during the early-middle Eocene, cyclical stratification and subsequent oxygenation of deep waters, leading to the oxidation and release of both sedimentary organic carbon and dissolved organic carbon in the water column could occur as a result of changes

in the hydrology and freshwater input to the Arctic basin, changing sea level, or changing sill depth. Similarly, the build-up of and release of marine reservoirs of organic carbon could be strongly affected by changes in overturning circulation, which general circulation modeling results have linked to eccentricity--potentially explaining the link between eccentricity forcing and the timing of multiple hyperthermals in the late Paleocene-early Eocene (Lunt et al., 2011).

The existence of major epicontinental seas favorable to the build-up and storage of large quantities of organic matter may explain the dynamic carbon cycle response to orbital forcing before the existence of ice sheets. Further, the areal extent of epicontinental seaways may provide a limit on the potential magnitude of a given 'hyperthermal' event, with smaller events related to the progressive opening of narrow seaways throughout the early Cenozoic.

Moreover, the regularity of events (i.e. whether they occur at every eccentricity maxima) may be related to a combination of background climate and tectonic forcing, which together determines the sensitivity of the organic carbon reservoir to orbital forcing (in a method analogous to Lunt et al., 2011). In this conceptual framework, the proximity to some threshold determines the regularity of events, while simultaneously placing a constraint on the total size of each release event related to the potential rate of recharge. Organic carbon from epicontinetal seas need not be the exclusive carbon source during events; in particular, the largest events may have included terrestrial organic carbon oxidation and the release of some methane hydrates, but we suggest that

oxidation of organic carbon is a common factor among all events.

The existence of epicontinental seas also potentially influences the recovery from events. The same geography that dictates the build-up of large quantities of organic matter preceding an event would favor enhanced organic carbon burial following a release event. In fact, the release of nutrients during organic carbon oxidation might explain the unexpectedly rapid rates of CO_2 drawdown following hyperthermals by stimulating productivity. Reduced oxygen availability and increased demand in large, restricted basins, leading to enhanced organic carbon burial, represents a mechanism for the preferential removal of ^{12}C. For the Mesozoic CIEs, this negative feedback may have been sufficiently strong that the recoveries developed into full-blown ocean anoxic events. It is not uncommon for even the smallest hyperthermals to overshoot (reflected in $\delta^{13}C$ values becoming more positive following the recovery than before the onset of the event).

The importance of paleogeography in controlling the strength of recovery is evident in the differential strength of recovery with respect to event size between the Mesozoic CIEs and the PETM. For instance, the negative CIE that precedes the C/T OAE is significantly smaller than the PETM, but the C/T represents a major, global anoxic event, whereas anoxia during or immediately following the PETM negative CIE was regional. Demonstrated by Meyer and Kump, 2008, geography during the Mesozoic was more favorable to anoxia than at the PETM, thus explaining the difference in recoveries.

4.10 Concluding remarks: What is a hyperthermal event?

Qualitatively, the defining criteria for hyperthermal events are clear: a negative CIE accompanied by evidence of warming and dissolution and/or the reduced accumulation of carbonates that develops rapidly and occurs over a geologically short interval. Secondary evidence includes high rates of organic carbon burial, biotic turnover, and enhanced rates of weathering. It is substantially more difficult to develop a set of quantitative criteria for conclusively labeling an event as a hyperthermal. It is likely that improving resolution of $\delta^{13}C$ records from high resolution sites of the early Cenozoic and Mesozoic will lead to continuing identification of rapid, 1-2‰ excursions. Whether these should all qualify as individual “events” or simply be taken to reflect large variability in carbon cycling at orbital-scale cyclicity is unclear.

The temporal correlation between widespread shallow epicontinetal seas and hyperthermals, as well as the apparent orbital pacing of many of the Paleogene events, suggest that hyperthermals may be scaled responses to similar forcing mechanisms—with ultimate size controlled by the extent of the perturbable carbon reservoir. Alternatively, the largest events may represent a combination of feedbacks that lead to carbon release from additional reservoirs (such as methane hydrates), thereby accounting for the necessity of multiple pulses of carbon release for events with a long duration.

As proposed analogs for future global warming, research into hyperthermals will likely continue, with different events providing a ‘best match’

for the modern in different ways (i.e. similarity of continental configuration, background climate, rate of change, etc). It is important to continue considering the context provided by other identified events (not simply the PETM and/or Toarcian), as researchers continue to identify and describe these events.

Chapter 4, in part, is currently being prepared for submission for publication. I am the primary investigator and author of this paper in collaboration with co-author Richard Norris.

4.11 References

Aberhan, M., and T.K. Baumiller, (2003), Selective extinction among Early Jurassic bivalves: A consequence of anoxia, *Geology,* Vol. 31, No. 12 pp.1077-1080 doi: 10.1130/G19938.1.

Alegret, L., and E.Thomas, (2004), Benthic foraminifera and environmental turnover across the Cretaceous/Paleogene boundary at Blake Nose (ODP Hole 1049C, Northwestern Atlantic), *Palaeogeography, Palaeoclimatology, Palaeoecology*, Vol. 208, No. 1–2, pp. 59-83, doi:10.1016/j.palaeo.2004.02.028.

Alegret, L., and E. Thomas, (2005), Cretaceous/Paleogene boundary bathyal paleo-environments in the central North Pacific (DSDP Site 465), the Northwestern Atlantic (ODP Site 1049), the Gulf of Mexico and the Tethys: The benthic foraminiferal record, *Palaeogeography, Palaeoclimatology, Palaeoecology*. Vol. 224, No. 1–3, pp. 53-82, doi:10.1016/j.palaeo.2005.03.031.

Ando, A., Kaiho, K., Kawahata, H., and T. Kakegawa, (2008), Timing and magnitude of early Aptian extreme warming: Unraveling primary δ18O variation in indurated pelagic carbonates at Deep Sea Drilling Project Site 463, central Pacific Ocean*, Palaeogeography, Palaeoclimatology, Palaeoecology*. Vol. 260, No. 3–4, Pages 463-476, doi:10.1016/j.palaeo.2007.12.007.

Bailey, T. R., Y. Rosenthal, J. M. McArthur, B. van de Schootbrugge, and M. F. Thirlwall, (2003), Paleoceanographic changes of the Late Pliensbachian Early Toarcian interval: A possible link to the genesis of an oceanic anoxic event, *Earth Planetary Science Letters*, Vol. *212*, pp. 307–320, doi:10.1016/S0012821X(03)00278-4.

Bains, S., R. Corfield, and R. Norris, (1999), Mechanisms of climate warming at the end of the Paleocene, *Science*. Vol. 285, No., 5428, pp. 724–727, doi:10.1126/science.285.5428.724.

Bains, S., Norris, R.D., Corfield, R.M., and K.L. Faul, (2000), Termination of global warmth at the Palaeocene/Eocene boundary through productivity feedback, Nature, Vol. 407, pp. 171-174, doi:10.103/35025035.

Bellanca, A., Erba, E., Neri, R., Premoli Silva, I., Sprovieri, M., Tremolada, F., and D. Verga, (2002), Palaeoceanographic significance of the Tethyan 'Livello Selli' (Early Aptian) from the Hybla Formation, northwestern Sicily: biostratigraphy and high-resolution chemostratigraphic records, *Palaeogeography, Palaeoclimatology, Palaeoecology*. Vol. 185, No.1–2, pp.175-196, doi:10.1016/S0031-0182(02)00299-7.

Bernaola, G. J.I Baceta, X. Orue-Etxebarria, L. Alegret, M. Martin-Rubio, J. Arostegui, J. Dinares-Turell, (2007), Evidence of an abrupt environmental disruption during the mid-Paleocene biotic event (Zumaia section, western Pyrenees), *GSA Bulletin*. Vol. 119, No. 7-8 pp. 785-795, doi:10.1130/B26132.1.

Berner, R.A, (2003), The long-term carbon cycle, fossil fuels, and atmospheric composition, *Nature*, Vol. 426, pp. 323-326, doi:10.1038/nature02131.

Bird, M.L., J. Lloyd, and G.D. Farquhar, (1994), Terrestrial carbon storage at the LGM, *Nature*, Vol. 371, No. 566, doi:10.1038/371566a.

Bohaty, S.M., and Zachos, J.C, (2003), Significant Southern Ocean warming event in the late middle Eocene, *Geology*, Vol. 31, No. 11, pp. 1017-1020 doi:10.1130/G19800.1.

Bohaty, S.M., Zachos, J.C., Florindo, F., Delaney, (2009), Coupled greenhouse warming and deep-sea acidification in the middle Eocene, *Paleoceanography*, Vol. 24, PA2207, 16 pp., doi:10.1029/2008PA001676.

Bornemann, A., P. Schulte, J. Sprong, E. Steurbaut, M. Youssef, and R.P.

Speijer, (2009), Latest Danian carbon isotope anomaly and associated environmental change in the southern Tethys (Nile Basin, Egypt), *Journal of the Geological Society*, Vol. 166, pp. 1135-1142, doi:10.1144/001676492008104.

Bowen, G.J., Beerling, D.J., Koch, P.L., Zachos, J.C. & T. Quattlebaum, (2004). A humid climate state during the Palaeocene/Eocene thermal maximum. *Nature*, Vol. 432, pp. 495-499, doi:10.1038/nature03115.

Bowen, G.J., and Zachos. J.C, (2010), Rapid carbon sequestration at the termination of the Palaeocene-Eocene thermal maximum, *Nature Geoscience*, Vol. 3, pp. 866–869, doi:10.1038/ngeo1014.

Bralower, T.J., Thomas, D.J., Zachos, J.C., Hirschmann, M.M., Rohl, U., Sigurdsson, H., Thomas, E., and D.L. Whitney, (1997), High-resolution records of the late Paleocene thermal maximum and circum-Caribbean volcanism: Is there a casual link? *Geology*, Vol. 25, No. 11, doi:10.1130/0091-7613(1997).

Bralower, T.J., Premoli Silva, I., and M.J. Malone, (2006), Leg 198 synthesis: a remarkable 120-m.y. record of climate and oceanography from Shatsky Rise, northwest Pacific Ocean, *In* Bralower, T.J., Premoli Silva, I., and Malone, M.J. (Eds.), *Proceedings of the Ocean Drilling Program, Scientific Results,* 198: College Station, TX (Ocean Drilling Program), pp. 1–47. doi:10.2973/odp.proc.sr.198.101.2006.

Brinkhuis, H., Schouten, S., Collinson, M.E., Sluijs, A., Sinninghe Damsté, J.S., Dickens, G.R., Huber, M., Cronin, T.M., Onodera, J., Takahashi, K., Bujak, J.P., Stein, R., Van der Burgh, J., Eldrett, J.S., Harding, I.C., Lotter, A.F., Sangiorgi, F., van Konijnenburg-van Cittert, H., de Leeuw, J.W., Matthiessen, J., Backman, J., Moran, K., & the Expedition 302 Scientists, (2006), Episodic fresh surface waters in the Eocene Arctic Ocean, *Nature*, Vol. 441, pp. 606-609, doi:10.1038/nature04692.

Browning, E.L., and D. K. Watkins, (2008), Elevated primary productivity of calcareous nannoplankton associated with ocean anoxic event 1b during the Aptian/Albian transition (Early Cretaceous), *Paleoceanography*, Vol. 23, PA2213, doi:10.1029/2007A001413.

Clarke, L.J. and H.C. Jenkyns, (1999), New oxygen isotopic evidence for long term Cretaceous climate change in the Southern Hemisphere, *Geology*, Vol. 27, No. 8, pp. 699-702, doi: 10.1130/0091-7613.

Coccioni, R., Frontalini, F., Bancalà, G., Fornaciari, E., Jovane, L., and M. Sprovieri, (2010), The Dan-C2 hyperthermal event at Gubbio (Italy): Global implications, environmental effects, and cause(s), *Earth and Planetary Science Letters*, Vol. 297, No. 1–2, pp. 298-305, doi:10.1016/j.epsl.2010.06.031.

Cohen, A.S. Coe, A.L, and D.B. Kemp, (2007), The late Palaeocene-Early Eocene and Toarcian (Early Jurassic) carbon isotope excursions: a comparison of their time scales, associated environmental changes, causes and consequences, *Journal of the Geological Society London*, Vol. 164, pp. 1093-1108, doi:10.1144/0016-76492006-123.

Corsetti, F.A., Baud, A. Marenco, P.J., and S. Richoz, (2005), Summary of Early Triassic carbon isotope records, *Comptes Rendus Palevol*, Vol. 4, No. 6 7, pp. 473-486, doi:10.1016/j.crpv.2005.06.004.

Cramer, B.S., Wright, J.D., Kent, D.V., and M.P. Aubry. (2003). Orbital climate forcing of d13C excursions in the late Paleocene-early Eocene (chrons C24n-C25n), *Paleoceanography*, Vol. 18, No. 1097, 25 pp., doi:10.1029/2003PA000909.

Cui, Y., Kump, L.R., Ridgwell, A.J., Charles, A.J., Jinium, C.K, Diefendorf, A.F., Freeman, K.H., Urban, N.M., and I.C. Harding, (2011), Slow release of fossil fuel carbon during the Paleocene-Eocene Thermal Maximum, *Nature Geoscience,* Vol. 4, pp. 481-485, doi:10.1038/ngeo1179.

Curry, W.B., J.C. Duplessy, L.D. Labeyrie, N.J. Shackleton, (1988), Changes in the distribution of d13C of deep water TCO2 between the last glaciation and the Holocene, *Paleoceanography*, Vol. 3, pp. 317-341, doi:10.1029/PA003i003p00317.

Dickens, G., J. O'Neil, D. Rea, and R. Owen, (1995), Dissociation of oceanic methane hydrate as a cause of the carbon isotope excursion at the end of the Paleocene, *Paleoceanography,* Vol. 10, No. 6, pp. 965–971, doi:10.1029/95PA02087.

Diester-Haass, L., (1996), Late Eocene-Oligocene paleoceanography in the southern Indian Ocean (ODP Site 744), *Marine Geology*, Vol. 130, pp. 99 119,doi:10.1016/0025-3227(95)00128-X.

Dinarès-Turell, J., Stoykova, K., Baceta, J.I., Ivanov, M., and V. Pujalte, (2010), High-resolution intra- and interbasinal correlation of the Danian–Selandian transition (Early Paleocene): The Bjala section (Bulgaria) and the

Selandian GSSP at Zumaia (Spain), *Palaeogeography, Palaeoclimatology, Palaeoecology*, Vol. 297, No. 2, pp. 511-533, doi:10.1016/j.palaeo.2010.09.004.

Dunkley Jones, T., Ridgwell, A., Lunt, D.J., Maslin, M.A., Schmidt, D.N., and P.J. Valdes, (2010), A Palaeogene perspective on climate sensitivity and methane hydrate instability, *Philosophical Transactions of the Royal Society A*, Vol. 368, No. 1919, pp. 2395-2415, doi: 10.1098/rsta.2010.0053.

Edgar, K.M, P.A. Wilson, P.F. Sexton, Y. Suganuma, (2007), No extreme bipolar glaciation during the main Eocene calcite compensation shift, *Nature*, Vol. 448, pp. 908-911, doi:10.1038/nature06053.

Erba, E, (2004), Calcareous nannofossils and Mesozoic oceanic anoxic events, *Marine Micropaleontology*, Vol. 52, No. 1–4, pp. 85-106, doi:10.1016/j.marmicro.2004.04.007.

Erbacher, J., J. Thurow, and R. Littke, (1996), Evolution patterns of radiolara and organic matter variations: A new approach to identify sea-level changes in mid-Cretaceous pelagic environments, *Geology*, Vol. 24, No. 6, pp. 499 502, doi: 10.1130/0091-7613.

Farley, K.A., and S.F. Eltgroth, (2003), An alternative age model for the Paleocene Eocene thermal maximum using extraterrestrial 3He, *Earth and Planetary Science Letters,* Vol. 208, No. 3–4, pp. 135-148, doi:10.1016/S0012-821X(03)00017-7.

Flower, B., and J. Kennett, (1995), Middle Miocene deepwater paleoceanography in the southwest Pacific: Relations with East Antarctic Ice Sheet development, *Paleoceanography*, Vol. 10, No. 6, pp. 1095– 1112, doi:10.1029/95PA02022.

Frijia, G., and M. Parente, (2008), Strontium isotope stratigraphy in the upper Cenomanian shallow-water carbonates of the southern Apennines: Short term perturbations of 87Sr/86Sr during the oceanic anoxic event 2, *Palaeogeography, Palaeoclimatology, Palaeoecology,* Vol. 261, pp. 15 29, doi:10.1016/j.palaeo.2008.01.003.

Gale, A.S., H.C. Jenkyns, W.J. Kennedy, and R.M Corfield, (1993), Chemostratigraphy versus biostratigraphy: data from around the Cenomanian-Turonian boundary, *Journal of the Geological Society, London*, Vol. 150, pp 29-32. doi: 10.1144/gsjgs.150.1.0029

Gale, A.S., Kennedy, W.J., Burnett, J.A., Caron, M., and B.E. Kidd, (1996), The Late Albian to Early Cenomanian succession at Mont Risou near Rosans (Drôme, SE France): an integrated study (ammonites, inoceramids, planktonic foraminifera, nannofossils, oxygen and carbon isotopes), *Cretaceous Research*, Vol. 17, No. 5, pp. 515-606, doi:10.1006/cres.1996.0032.

Gibbs, S.J., P.R. Brown, B.H. Murphy, A. Sluijs, K.M. Edgar, H. Palike, C.T. Bolton, J.C. Zachos, (2012), Scaled biotic disruption during early Eocene global warming events, *Biogeosciences Discussions*, Vol. 9, pp. 1237 1257, doi:10.5194/bgd-9-1237-2012.

Hallam, A., and P.B Wignall, (1999), Mass extinctions and sea-level changes, *Earth Science Reviews*, Vol. 48, No. 4, pp. 217-250, doi:10.1016/S0012-8252(99)00055-0.

Hancock, H.J.L., and Dickens, G.R., (2005), Carbonate dissolution episodes in Paleocene and Eocene sediment, Shatsky Rise, west-central Pacific, *In* Bralower, T.J., Premoli Silva, I., and Malone, M.J. (Eds.), *Proceedings of the Ocean Drilling Program Scientific Results,* 198: College Station, TX (Ocean Drilling Program), pp. 1–24, doi:10.2973/odp.proc.sr.198.116.2005.

Hayes, J., H. Strauss, and A. Kaufman, (1999), The abundance of 13C in marine organic matter and isotopic fractionation in the global biogeochemical cycle of carbon during the past 800 ma, *Chemical Geology*, Vol. 161, pp. 103–125, doi:10.1016/S0009-2541(99)00083-2.

Haywood, A.M., A. Ridgwell, D.J. Lunt, D.J. Hill, M.J. Pound, H.J. Dowsett, A.M. Dolan, J.E. Francis, and M. Williams, (2011), Are there pre-Quaternary geological analogues for a future greenhouse warming? *Philosophical Transactions of the Royal Society A,* Vol. 369, No. 1938, pp. 933-956, doi: 10.1098/rsta.2010.0317.

Hermoso, M., L. Le Callonnec, F. Minoletti, M. Renard, and S. P. Hesselbo (2009), Expression of the Early Toarcian negative carbon-isotope excursion in separated carbonate microfractions (Jurassic, Paris Basin), *Earth Planet. Science Lett*ers, Vol. 277, pp. 194–203, doi:10.1016/j.epsl.2008.10.013.

Hermoso, M., Minoletti, F., Rickaby, R.E.M., Hesselbo, S.P., Baudin, F., and H.C. Jenkyns, (2012), Dynamics of a stepped carbon-isotope excursion: Ultra high-resolution study of Early Toarcian environmental change, *Earth and*

Planetary Science Letters, Vol. 319–320, pp. 45-54, doi:10.1016/j.epsl.2011.12.021.

Herrle, J.O., Pross, J., Friedrich, O., Kößler, P., and C. Hemleben, (2003), Forcing mechanisms for mid-Cretaceous black shale formation: evidence from the Upper Aptian and Lower Albian of the Vocontian Basin (SE France), *Palaeogeography, Palaeoclimatology, Palaeoecology*, Vol. 190, pp. 399-426, doi:10.1016/S00310182(02)00616-8.

Hesselbo, S. P., D. R. Gröcke, H. C. Jenkyns, C. J. Bjerrum, P. Farrimond, H. S. Morgans Bell, and O. R. Green, (2000), Massive dissociation of gas hydrate during a Jurassic oceanic anoxic event, *Nature*, Vol. 406, pp. 392 395, doi:10.1038/35019044.

Hesselbo, S.P., Robinson, S.A., Surlyk, F., and S. Piasecki, (2002), Terrestrial and marine extinction at the Triassic-Jurassic boundary synchronized with major carbon-cycle perturbation: A link to initiation of massive volcanism? *Geology*, Vol. 30, No. 3, pp. 251-254, doi: 10.1130/0091-7613(2002).

Hesselbo, S. P., H. C. Jenkyns, L. V. Duarte, and L. C. V. Oliveira, (2007), Carbon-isotope record of the Early Jurassic (Toarcian) oceanic anoxic event from fossil wood and marine carbonate (Lusitanian Basin, Portugal), *Earth Planetary Science Letters*, Vol. 253, pp. 455–470, doi:10.1016/j.epsl.2006.11.009.

Higgins, J.A., and D.P. Schrag, (2006), Beyond methane: Towards a theory for the Paleocene–Eocene Thermal Maximum*, Earth and Planetary Science Letters*, Vol. 245, No. 3–4, pp. 523-537, doi:10.1016/j.epsl.2006.03.009.

Honisch, B., Ridgwell, A., Schmidt, D.N., Thomas, E., Gibbs, S.J., Sluijs, A., Zeebe, R., Kump, L., Martindale, R.C., Greene, S.E., Kiessling, W., Ries, J., Zachos, J.C., Royer, D.L., Barker, S., Marchitto Jr., T.M., Moyer, R., Pelejero, C., Ziveri, P., Foster, G.L., and B. Williams, (2012), The Geological Record of Ocean Acidification, *Science,* Vol. 335, No. 6072, pp. 1058-1063, doi:10.1126/science.1208277.

Huber, B.T., R.M. Leckie, R.D. Norris, T.J. Bralower, and E. CoBabe, (1999), Foraminiferal assemblage and stable isotopic change across the Cenomanian-Turonian boundary in the subtropical North Atlantic, *Journal of Foraminiferal Research,* Vol. 29, No. 4, pp. 392-417, uri:http://hdl.handle.net/10088/7428.

Isozaki, Y., (1997), Permo-Triassic boundary superanoxia and stratified

superocean: records from the lost deep sea, *Science,* Vol. 276, No. 5310, pp. 235-238, doi:10.1126/scienc.276.5310.235.

Jahren, A. H., N. C. Arens, G. Sarmiento, J. Guerrero, and R. Amundson, (2001), Terrestrial record of methane hydrate dissociation in the Early Cretaceous, *Geology*, Vol. 29, pp.159–162, doi:10.1130/00917613(2001)029<0159:TROMHD>2.0. CO;2.\

Jenkyns, H. C., and C. J. Clayton, (1997), Lower Jurassic epi- continental carbonates and mudstones from England and Wales: Chemostratigraphic signals and the early Toarcian anoxic event, *Sedimentology*, Vol. 44, pp. 687–706, doi:10.1046/ j.1365-3091.1997.d01-43.x.

Jenkyns, H. C., D. R. Gröcke, and S. P. Hesselbo, (2001), Nitrogen isotope evidence for water mass denitrification during the early Toarcian oceanic anoxic event, *Paleoceanography*, Vol. 16, pp. 593–603, doi:10.1029/2000PA000558.

Jenkyns, H. C., C. E. Jones, D. R. Gröcke, S. P. Hesselbo, and D. N. Parkinson, (2002), Chemostratigraphy of the Jurassic System: Applications, limitations and implications for palaeoceanography, *Journal of the Geological Society,* Vol. 159, No. 4, pp 351-378, doi:10.1144/0016-764901-130.

Jenkyns, H.C., (2003), Evidence for rapid climate change in the Mesozoic Palaeogene greenhouse world. *Philosophical Transactions of the Royal Society London*, Vol. 361, No. 1810, pp. 1885-1916, doi:10.1098/rsta.2003.1240.

Jenkyns, H.C., (2010), Geochemistry of ocean anoxic events. *Geochemistry, Geophysics, Geosystems*, Vol 11, Q03004, 30 pp., doi:10.1029/2009GC002788.

John, C.M., Bohaty, S.M., Zachos, J.C., Sluijs, A., Gibbs, S., Brinkhuis, H., and T.J. Bralower, (2008), North American continental margin records of the Paleocene-Eocene thermal maximum: implications for global carbon and hydrological cycling, *Paleoceanography*, Vol. 23, PA2217, 20 pp., doi:10.1029/2007PA001465.

Jones, C. E., and H. C. Jenkyns, (2001), Seawater strontium isotopes, oceanic anoxic events, and seafloor hydrothermal activity in the Jurassic and Cretaceous, *American Journal Science*, Vol. 301, No. 2, pp. 112–149, doi:10.2475/ajs.301.2.112.

Jones, C. E., H. C. Jenkyns, and S. P. Hesselbo, (1994), Strontium isotopes in Early Jurassic seawater, *Geochimica Cosmochimica Acta*, Vol. 58, pp. 1285–1301, doi:10.1016/0016-7037 (94)90382-4.

Kaiho, K., and T. Hasegawa, (1994), End-Cenomanian benthic foraminiferal extinctions and oceanic dysoxic events in the northwestern Pacific Ocean, *Palaeogeography, Palaeoclimatology, Palaeoecology*, Vol. 111, No.1–2, pp. 29-43, doi:10.1016/00310182(94)90346-8.

Kaiho, K., Arinobu, T., Ishiwatari, R., Morgans, H.E.G., Okada, H., Takeda, N., Tazaki, K., Zhou, G., Kajiwara, Y., Matsumoto, R., Hirai, A., Niitsuma, N., and H. Wada, (1996), Latest Paleocene benthic foraminiferal extinction and environmental changes at Tawanui, New Zealand, *Paleoceanography*, Vol. 11, No. 4, pp. 447–465, doi:10.1029/96PA01021.

Kelly, D.C., Zachos, J.C., Bralower, T.J., and S.A. Schellenberg, (2005), Enhanced terrestrial weathering/runoff and surface ocean carbonate production during the recovery stages of the Paleocene-Eocene thermal maximum, *Paleoceanography*, Vol. 20, PA4023, 11 pp., doi:10.1029/2005PA001163.

Kemp, D. B., A. L. Coe, A. S. Cohen, and L. Schwark, (2005), Astronomical pacing of methane release in the early Jurassic period, *Nature*, Vol. 437, pp. 396-399, doi:10.1038/nature04037.

Kennedy, M.J., Christie-Blick, N., and L.E. Sohl, (2001), Are Proterozoic cap carbonates and isotopic excursions a record of gas hydrate destabilization following Earth's coldest intervals? *Geology*, Vol. 29, No. 5, doi:10.1130/ 0091-7613(2001).

Kennett, J. P., and L. D. Stott, (1991), Abrupt deep-sea warming, palaeoceanographic changes, and benthic extinctions at the end of the Paleocene, *Nature*, Vol. 353, pp. 225–229, doi:10.1038/353225a0.

Kidder, D.L., and T.R. Worsley, (2004), Causes and consequences of extreme PermoTriassic warming to globally equable climate and relation to the PermoTriassic extinction and recovery, *Palaeogeography, Palaeoclimatology, Palaeoecology*, Vol. 203, No. 3–4, pp. 207-237, doi:10.1016/S0031-0182(03)00667-9.

Korte, C., Hesselbo, S.P., Jenkyns, H.C., Rickaby, R.E.M., and C. Spotl, (2009), Palaeoenvironmental significance of carbon- and oxygen-isotope stratigraphy of marine Triassic-Jurassic boundary sections in SW Britain.

Journal of the Geological Society, Vol. 166, pp. 431-445, doi: 10.1144/ 001676492007-177.

Korte, C., and H.W. Kozur, (2010), Carbon-isotope stratigraphy across the Permian Triassic boundary: A review*, Journal of Asian Earth Sciences,* Vol. 39, No. 4, pp. 215-235, doi:10.1016/j.jseaes.2010.01.005.

Kump, L.R., (1991), Interpreting carbon-isotope excursions: Strangelove oceans. *Geology*, Vol. 19, No. 4, pp. 299-302, doi: 10.1130/0091-7613(1991).

Kump, L. R., and M.A. Arthur, (1999), Interpreting carbon-isotope excursions: carbonates and organic matter, *Chemical Geology*, Vol. 161, No. 1-3, pp. 181-198, doi:10.1016/S00092541(99)00086-8.

Kuroda, J., Ogawa, N.O., Tanimizu, M., Coffin, M.F., Tokuyama, H., Kitazato, H., and N. Ohkouchi, (2007), Contemporaneous massive subaerial volcanism and late cretaceous Oceanic Anoxic Event 2, *Earth and Planetary Science Letters*, Vol. 256, No. 1–2, pp. 211-223, doi:10.1016/j.epsl.2007.01.027.

Kuypers, M. M. M., R. D. Pancost, I. A. Nijenhuis, and J. S. Sinninghe Damsté, (2002), Enhanced productivity led to increased organic carbon burial in the euxinic North Atlantic basin during the late Cenomanian oceanic anoxic event, *Paleoceanography*, Vol. 17, No. 4, pp. 1051, doi:10.1029/2000PA000569.

Leckie, R.M., T.J. Bralower, R. Cashman, (2002), Oceanic anoxic events and plankton evolution: Biotic response to tectonic forcing during the mid Cretaceous, *Paleoceanography*, Vol. 17, pp. 1041, doi:10.1029/2001PA000623.

Li, Y.X., Bralower, T.J., Montañez, I.P., Osleger, D.A., Arthur, M.A., Bice, D.M., Herbert, T.D., Erba, E., and I. Premoli Silva, (2008), Toward an orbital chronology for the early Aptian Oceanic Anoxic Event (OAE1a, 120 Ma), *Earth and Planetary Science Letters*, Vol. 271, No. 1–4, pp. 88-100, doi:10.1016/j.epsl.2008.03.055.

Little, C.T.S., and M.J. Benton, (1995), Early Jurassic mass extinction: A global long-term event, *Geology*, Vol. 23, No. 6, pp. 495-498, doi: 10.1130/00917613(1995) 023<0495:EJMEAG> 2.3.CO;2.

Littler, K., Zachos, J.C., Kersey, A., Roehl, U., and T. Westerhold, (2011), A high-resolution benthic stable-isotope record for the South Atlantic: implications for orbital scale changes in Late Paleocene-Early

Eocene climate and circulation, AGU Fall Meeting 2011, PP22A-05, San Francisco, CA.

Lourens, L.J., Sluijs, A., Kroon, D., Zachos, J.C., Thomas, E., Röhl, U., Bowles, J., & I. Raffi, (2005), Astronomical pacing of late Palaeocene to early Eocene global warming events, *Nature,* Vol. 435, pp. 1083-1087 doi:10.1038/nature03814.

Lunt, D.J., Ridgwell, A. and Sluijs, A. Zachos, J., Hunter, S., and A. Haywood, (2010), Orbital pacing of methane hydrate destabilization during the Paleogene. *Nature Geoscience,* Vol. 4, pp. 775–778 doi:10.1038/ngeo1266.

McArthur, J. M., D. T. Donovan, M. F. Thirlwall, B. W. Fouke, and D. Mattey, (2000), Strontium isotope profile of the early Toarcian (Jurassic) oceanic anoxic event, the duration of ammonite biozones, and belemnite palaeotemperatures, *Earth and Planetary Science Letters*, Vol. *179*, pp. 269–285, doi:10.1016/S0012-821X(00)00111-4.

McElwain, J. C., J. Wade-Murphy, and S. P. Hesselbo, (2005), Changes in carbon dioxide during an oceanic anoxic event linked to intrusion into Gondwanan corals, *Nature*, Vol. 435, pp. 479–482, doi:10.1038/nature03618.

Menegatii, A.P., H. Weissert, R.S. Brown, R.V. Tyson, P. Farrimond, A. Strasser., M. Caron, (1998). High-resolution d13C stratigraphy through the Early Aptian “Livello selli” of the Alpine Tethys, *Paleoceanography*, Vol. 13, No. 5, pp. 530, doi:10.1029/98PA01793.

Meyer, K.M., and L.R. Kump, (2008), Oceanic Euxinia in Earth History: Causes and Consequences. *Annual Review of Earth and Planetary Sciences*, Vol. 35, pp. 251-288, doi:10.1146/annurev.earth.36.031207.124256.

Meyer, K.M., Yu, M., Jost, A.B., Kelley, B.M., and J.L. Payne, (2011), δ13C evidence that high primary productivity delayed recovery from end Permian mass extinction, *Earth and Planetary Science Letters*, Vol. 302, No. 3–4, pp. 378-384, doi:10.1016/j.epsl.2010.12.033.

Mix, A.C., Le, J., and N.J. Shackleton, (1995), Benthic foraminiferal stable isotope stratigraphy of Site 846: 0–1.8 Ma. *In* Pisias, N.G., Mayer, L.A., Janecek, T.R., Palmer-Julson, A., and van Andel, T.H. (Eds.), *Proceedings of the Ocean Drilling Program, Scientific Results,* 138: College Station, TX (Ocean Drilling Program), pp. 839–854,

doi:10.2973/odp.proc.sr.138.160.1995.

Mort, H.P., T. Adatte, K.B. Follmi, G. Keller, P. Steinmann, V. Matera, Z. Berner, D. Stuben, (2007), Phosphorus and the roles of productivity and nutrient recycling during oceanic anoxic event 2, *Geology*, Vol. 35, No. 6, pp. 483-486, doi:10.1130/G23475A.

Murphy, B.H., Farley, K.A., and J.C. Zachos, (2010),An extraterrestrial 3He based timescale for the Paleocene–Eocene thermal maximum (PETM) from Walvis Ridge, IODP Site 1266, *Geochimica et Cosmochimica Acta*, Vol. 74, No. 17, pp. 5098-5108, doi:10.1016/j.gca.2010.03.039.

O'Regan, M., Williams, C.J., Frey, K.E., and M. Jakobsson, (2011), A synthesis of the long-term paleoclimatic evolution of the Arctic, *Oceanography*, Vol. 24, No. 3, pp. 66-80, doi:10.5670/oceanog.2011.57.

Pagani, M., Pedentchouk, N., Huber, M., Sluijs, A., Schouten, S., Brinkhuis, H., Sinninghe Damsté, J.S., Dickens, G.R., Expedition 302 Scientists & Backman, J., Clemens, S., Cronin, T., Eynaud, F., Gattacceca, J., Jakobsson, M., Jordan, R., Kaminski, M., King, J., Koc, N., Martinez, N.C., McInroy, D., Moore Jr, T.C., O'Regan, M., Onodera, J., Pälike, H., Rea, B., Rio, D., Sakamoto, T., Smith, D.C., St John, K.E.K., Suto, I., Suzuki, N., Takahashi, K., Watanabe M., & M. Yamamoto for Expedition 302 Scientists, (2006), Arctic hydrology during global warming at the Palaeocene/Eocene Thermal Maximum, *Nature,* Vol. 442, pp. 671-675 doi:10.1038/nature05043.

Pálfy, J., and P. L. Smith, (2000), Synchrony between Early Jurassic extinction, oceanic anoxic event, and the Karoo- Ferrar flood basalt volcanism, *Geology,* Vol. 28, pp. 747–750, doi:10.1130/0091.7613(2000)28<747:SBEJEO>2.0.CO;2.

Palfy, J. A. Demeny, J. Haas, M. Hetenyi, M..J. Orchad, I. Veto, (2001), Carbon isotope anomaly and other geochemical changes at the Triassic-Jurassic boundary from a marine section in Hungary, *Geology*, Vol. 29, No. 11, pp. 1047-1050, doi: 10.1130/0091-7613(2001).

Palike, H., Norris, R.D., Herrle, J.O., Wilson, P.A., Coxall, H.K., Lear, C.H., Shackleton, N.J., Tripati, A.K., and B.S. Wade, (2006), The Heartbeat of the Oligocene Climate System, *Science,* Vol. 314, No. 5807, pp. 1894-1898, doi:10.1126/science.1133822

Panchuk, K., (2007), Investigating the Paleocene/Eocene Carbon Cycle

Perturbation: An Earth System Model Approach, Ph.D. Dissertation, The Pennsylvania State University.

Panchuk, K., Ridgwell, A. and L.R. Kump, (2008), Sedimentary response to Paleocene-Eocene Thermal Maximum carbon release: A model-data comparison, *Geology,* Vol. 36, No.4, pp. 315-318, doi: 10.1130/G24474A.1.

Pancost, R. D., N. Crawford, S. Magness, A. Turner, H. C. Jenkyns, and J. R. Maxwell, (2004), Further evidence for the development of photic-zone euxinic conditions during Mesozoic oceanic anoxic events, *Journal of the Geological Society*, Vol. 161, No. 3, pp. 353– 364, doi:10.1144/0016764903-059.

Payne, J.L., D.J. Lehrmann, J. Wei, M.J. Orchard, D.P. Schrag, and A.H. Knoll, (2004), Large perturbations of the carbon cycle during recovery from the end Permian extinction, *Science,* Vol. 305, No. 5683, pp. 506-509, doi:10.1126/science.1097023.

Payne, J.L., and L.R. Kump, (2007), Evidence for recurrent Early Triassic massive volcanism from quantitative interpretation of carbon isotope fluctuations, *Earth and Planetary Science Letters*, Vol. 256, No. 1–2, pp. 264-277, doi:10.1016/j.epsl.2007.01.034.

Petrizzo, M.R., (2005), An early late Paleocene event on Shatsky Rise, northwest Pacific Ocean (ODP Leg 198): evidence from planktonic foraminiferal assemblages. *In* Bralower, T.J., Premoli Silva, I., and Malone, M.J. (Eds.), *Proceedings of the Ocean Drilling Program, Scientific Results,* 198: College Station, TX (Ocean Drilling Program), pp. 1–29. doi:10.2973/odp.proc.sr.198.102.2005.

Quillévéré, F., Norris, R.D., Kroon, D., and P. A. Wilson, (2008), Transient ocean warming and shifts in carbon reservoirs during the early Danian, *Earth and Planetary Science Letters*, Vol. 265, No. 3–4, pp. 600-615, doi:10.1016/j.epsl.2007.10.040.

Raup, D.M., and J.J. Sepkoski Jr., (1984), Periodicity of extinctions in the geologic past. *Proceedings of the National Academy of Sciences*, Vol. 81 No. 3, pp. 801-805, doi:10.1073/pnas.81.3.801.

Ridgwell, A., and R.E. Zeebe, (2005), The role of the global carbonate cycle in the regulation and evolution of the Earth system, *Earth and Planetary Science Letters*, Vol. 234, No. 3–4, pp. 299-315,

doi:10.1016/j.epsl.2005.03.006.

Rickaby, R.E.M., Bard, E., Sonzogni, C., Rostek, F., Beaufort, L., Barker, S., Rees, G., and D.P. Schrag, (2007), Coccolith chemistry reveals secular variations in the global ocean carbon cycle?, *Earth and Planetary Science Letters*, Vol. 253, No. 1–2, pp. 83-95, doi:10.1016/j.epsl.2006.10.016.

Robinson, S.A., (2010), Shallow-water carbonate record of the Paleocene Eocene Thermal Maximum from a Pacific Ocean guyot, *Geology*, Vol. 39, No. 1, pp. 51-54, doi: 10.1130/G31422.1.

Rohl, U., Westerhold, T., Bralower, T.J., and J.C. Zachos, (2007). On the duration of the Paleocene-Eocene thermal maximum. *Geochemistry, Geophysics, Geosystems*. Vol 8, Q12002, 13 pp., doi:10.1029/2007GC001784.

Ruhl, M., Bonis, N.R., Reichart, G.J., Sinninghe Damste, J.S., and W.M. Kurschner, (2011), Atmospheric carbon injection linked to end-Triassic mass extinction, *Science,* Vol. 333, No. 6041, pp. 430-434, doi:10.1126/science.1204255.

Ruhl., M., and W.M. Kurschner, (2011), Multiple phases of carbon cycle disturbance from large igneous province formation at the Triassic-Jurassic transition, *Geology*, Vol. 39, No. 5, pp. 431-434, doi: 10.1130/ G31680.1.

Russon, T., Paillard, D., and M. Elliot, (2010), Potential origins of 400-500 kyr periodicities in the ocean carbon cycle: A box model approach. *Global Biogeochemical Cycles,* Vol. 24, GB2013, 16 pp., doi:10.1029/2009GB003586.

Scholle, P.A., and M. A. Arthur, (1980), Carbon isotope fluctuations in Cretaceous pelagic limestones; potential stratigraphic and petroleum exploration tool. *AAPG Bulletin*, Vol. 64, No. 1, pp. 67-87, doi:10.1306/2F91892D-16CE-11D7-8645000102C1865D.

Schouten, S., Woltering, M., Irene, W., Rijpstra, C., Sluijs, A., Brinkhuis, H., and J.S. Sinninghe Damsté, (2007), The Paleocene–Eocene carbon isotope excursion in higher plant organic matter: Differential fractionation of angiosperms and conifers in the Arctic, *Earth and Planetary Science Letters*, Vol. 258, No. 3–4, pp. 581-592, doi:10.1016/j.epsl.2007.04.024.

Sexton, P.N., Norris, R.D., Wilson, P.A., Palike, H., Westerhold, T., Rohl, U., Bolton, C.T., and S. Gibbs, (2011), Multiple Eocene 'hyperthermal' events

driven by ocean ventilation, *Nature,* Vol. 471, pp. 349-353, doi:10.1038/nature09826.

Shackleton, N.J., (1985), Oceanic carbon isotope constraints on oxygen and carbon dioxide in the Cenozoic atmosphere, In: Sundquist, E., and W.S. Broecker, (Eds.), The Carbon Cycle and Atmospheric CO2: Natural Variations Archean to Present. American Geophysical Union, Washington, DC, pp. 412–417.

Shackleton, N., (1987), The carbon isotope record of the Cenozoic: History of organic carbon burial and of oxygen in the ocean and atmosphere, In: Brooks, J., and A. Fleet (Eds.), Marine Petroleum Source Rocks, Geological Society Special Publication, Vol. 26, pp. 423 – 434, Geological Society, London.

Sigman, D.M., and E.A. Boyle, (2000), Glacial/interglacial variations in atmospheric carbon dioxide*, Nature*, Vol. 407, doi:10.1038/35038000.

Sinninghe Damsté, J. S., and J. Köster, (1998), A euxinic southern North Atlantic Ocean during the Cenomanian–Turonian oceanic anoxic event, *Earth and Planetary Science Letters*, Vol. 158, pp. 165–173, doi:10.1016/S0012-821X(98)00052-1.

Sluijs, A., Schouten, S. Pagani, M., Woltering M., Brinkhuis, H., Sinninghe Damsté, J.S., Dickens, G.R., Huber, M., Reichart, G.J., Stein, R., Matthiessen, J., Lourens, L.J., Pedentchouk, N., Backman, J., Moran K., & the Expedition 302 Scientists, (2006), Subtropical Arctic Ocean Temperatures during the Palaeocene/Eocene thermal maximum, *Nature,* Vol. 441, pp. 610-613, doi:10.1038/nature04668.

Sluijs, A., Rohl, U., Schouten, S., Brumsack, H.J., Sangiorgi, F., Sinninghe Damste, J.S., and H. Brinkhuis, (2008) Arctic late Paleocene-early Eocene paleoenvironments with special emphasis on the Paleocene-Eocene thermal maximum (Lomnosov Ridge, Integrated Ocean Drilling Program Expedition 302), *Paleoceanography*, Vol. 23, PA1S11, 17 pp., doi:10.1029/2007PA01495.

Sluijs, A., Schouten, S., Donders, T.H., Schoon, P.L., Rohl., U., Reichart, G., Sangiorgi, F., Kim, J.H, Sinninghe Damste, J.S., ad H. Brinkhuis, (2009), Warm and wet conditions in the Arctic region during Eocene Thermal Maximum 2, *Nature Geoscience*, Vol. 2, No. 11, pp. 777-780, doi.10.1038/ngeo668.

Speelman, E.N., Van Kempen, M.M.L., Barke, J., Brinkhuis, H., Reichart, G.J., Smolders, A.J.P., Roelofs, J.G.M.,Sangiogi, F., De Leeuw, J.W., Lotter, A.F., and J.S. Sinninghe Damste, (2009), The Eocene Arctic Azolla bloom: environmental conditions, productivity and carbon drawdown, *Geobiology*, Vol. 7, No. 2, pp. 155-170, doi:10.1111/j.1472-4669.2009.00195.x.

Speijer, R. P., and T. Wagner, (2002), Sea-level changes and black shales associated with the Late Paleocene Thermal Maximum (LPTM): Organic geochemical and micropaleontologic evidence from the southern Tethyan margin (Egypt– Israel), In *Catastrophic Events and Mass Extinctions: Impacts and Beyond*, C. Koeberl and K. G. MacLeod (Eds.), Special Paper of the Geological Society of America, No. 356, pp. 533–549.

Speijer, R.P., (2003), Danian-Selandian seal-level change and biotic excursion on the southern Tethyan margin (Egypt), *Geolgocical Society of America Special Paper,* No. 369, In *Causes and Consequences of Globally Warm Climates in the Early Paleogene*, Wing, S.L, Gingerich, P.D., Schmitz, B., and E. Thomas (Eds.), pp 275.

Spero, H. J., J. Bijma, D. W. Lea, and B. E. Bemis, (1997), Effect of seawater carbonate concentration on foraminiferal carbon and oxygen isotopes, *Nature*, Vol. 390, pp. 497–500, doi:10.1038/37333.

Sprong. J., M.A. Youssef, A. Bornemann, P. Schulte, E. Steurbaut, P. Stassen, T.J. Kouwenhoven, and R.P. Speijer, (2011), A multi-proxy record of the latest Danian Event at Gebel Qreiya, Eastern Desert, Egypt, *Journal of Micropalaeontology*, Vol. 30, pp. 167-182, doi: 10.1144/ 0262-821X10-023.

Sprong, J., Kouwenhoven, T.J., Bornemann, A., Schulte, P., Stassen, P., Steurbaut, E., Youssef, M., and R.P. Speijer, (2012), Characterization of the Latest Danian Event by means of benthic foraminiferal assemblages along a depth transect at the southern Tethyan margin (Nile Basin, Egypt), *Marine Micropaleontology*, Vol. 86–87, pp. 15-31, doi:10.1016/j.marmicro.2012.01.001.

Stap, L., Sluijs, A., Thomas, E., and L. Lourens, (2009), Patterns and magnitude of deep sea carbonate dissolution during Eocene Thermal Maximum 2 and H2, Walvis Ridge, southeastern Atlantic Ocean, *Paleoceanography,* Vol. 24, PA1211, 13 pp., doi:10.1029/2008PA001655.

Stap, L., L.J. Lourens, E. Thomas, A. Sluijs, S. Bohaty, and J.C. Zachos, (2010), High-resolution deep-sea carbon and oxygen isotope records of Eocene

Thermal Maximum 2 and H2, *Geology*, Vol. 38, No. 7, pp. 607-610, doi:10.1130/G30777.1.

Thomas, D.J., Bralower, T.J., and J.C. Zachos, (1999), New evidence for subtropical warming during the Late Paleocene thermal maximum: Stable isotopes from Deep Sea Drilling Project Site 527, Walvis Ridge, *Paleoceanography*, Vol. 14, No. 5, pp. 561, doi:10.1029/1999PA900031.

Thomas, E., Zachos, J. C., and T.J. Bralower, (2000), Deep-sea environments on a warm earth: latest Paleocene-early Eocene, In *Warm Climates in Earth History*, pp. 132-160.

Thomas, D. J., J. C. Zachos, T. J. Bralower, E. Thomas, and S. Bohaty, (2002), Warming the fuel for the fire: Evidence for the thermal dissociation of methane hydrate during the Paleocene–Eocene Thermal Maximum, *Geology*, Vol. 30, pp. 1067– 1070, doi:10.1130/0091-7613(2002)030<1067:WTFFTF>2.0.CO;2.

Thomas, E., (2007), Cenozoic mass extinctions in the deep sea: What perturbs the largest habitat on Earth? In Monechi, S., Coccioni, R., and M.R. Rampino, M.R., (Eds.), *Large Ecosystem Perturbations: Causes and Consequences*. The Geological Society of America Special Paper, No. 424, pp 1-23, doi:10.1130/2007.2424(01).

Torfstein, A., Winckler, G., and A. Tripati, (2010), Productivity feedback did not terminate the Paleocene-Eocene Thermal Maximum, *Climates of the Past*, Vol. 6, pp. 265-272, doi:10.5194/cp-6-265-2010.

Van Bentum, E., A. Hetzel, H.-J. Brumsack, A. Forster, G. J. Reichert, and J. S. Sinninghe-Damsté, (2009), Reconstruction of water column anoxia in the equatorial Atlantic during the Cenomanian-Turonian oceanic anoxic event using bio- marker and trace metal proxies, *Palaeogeography, Palaeoclimatology, Palaeoecology*, Vol. 280, pp. 489–498, doi:10.1016/j.palaeo.2009.07.003.

Van Breugel, Y., S. Schouten, H. Tsikos, E. Erba, G.D. Price, and J.S. Sinninghe Damste, (2007), Synchronous negative carbon isotope shifts in marine and terrestrial biomarkers at the onset of Aptian oceanic anoxic event 1a: Evidence for the release of methane into the atmosphere. Chapter 6: PhD thesis. Causes for negative carbon isotope anomalies in Mesozoic marine sediments: Constraints from modern and ancient anoxic settings. Utrecht University.

Van de Schootbrugge, B., J.L., Payne, A. Tomasovych, J. Pross, J. Fiebig, M. Benbrahim, K.B. Follmi, T.M. Quan, (2008), Carbon cycle perturbation and stabilization in the wake of the Triassic-Jurassic boundary mass-extinction event, *Geochemistry Geophysics Geosystems*, Vol. 9, Q04028, 16 pp., doi:10.1029/2007GC001914.

Veizer, J., Ala, D., Azmy, K., Bruckschen, P., Buhl, D., Bruhn, F., Carden, G.A.F., Diener, A., Ebneth, S., Godderis, Y., Jasper, T., Korte, C, Pawellek, F., Podlaha, O.G., and H. Strauss, (1999) 87Sr/86Sr, δ13C and δ18O evolution of Phanerozoic seawater, *Chemical Geology*, Vol. 161, No. 1–3, pp. 59-88, doi:10.1016/S00092541(99)00081-9.

Voigt, S., Gale, A.S., and T. Voigt, (2006), Sea-level change, carbon cycling and palaeoclimate during the Late Cenomanian of northwest Europe; an integrated palaeoenvironmental analysis, *Cretaceous Research*, Vol. 27, No. 6, pp. 836-858, doi:10.1016/j.cretres.2006.04.005.

Wagner, T., Wallmann, K., Herrle, J.O., Hofmann, P., and I. Stuesser, (2007), Consequences of moderate ~25,000 yr lasting emission of light CO2 into the mid-Cretaceous ocean, *Earth and Planetary Science Letters*, Vol. 259, No. 1–2, pp. 200-211, doi:10.1016/j.epsl.2007.04.045.

Wagner, T., J.O. Herrle, J.S. Sinninghe Damste, S. Schouten, I. Stussor, and P. Hoffman, (2008), Rapid warming and salinity changes of Cretaceous surface waters in the subtropical North Atlantic, *Geology*, Vol. 36, No. 3, pp. 203-206, doi: 10.1130/G24523A.1.

Westerhold, T., Rohl, U., Laskar, J., Raffi, I., Bowles, J., Lourens, L.J., and J.C. Zachos, (2007), On the duration of magnetochrons C24r and C25n and the timing of early Eocene global warming events: Implications from the OceanDrilling Program Leg 208 Walvis Ridge depth transect, *Paleoceanography*, Vol. 22, PA2201, 19 pp., doi:10.1029/2006PA001322.

Westerhold, T., Röhl, U., Raffi, I., Fornaciari, E., Monechi, S., Reale, V., Bowles, J., and H.F. Evans, (2008), Astronomical calibration of the Paleocene time, *Palaeogeography, Palaeoclimatology, Palaeoecology*, Vol. 257, No.4, pp. 377-403, doi:10.1016/j.palaeo.2007.09.016.

Westerhold., T., and U. Rohl, (2009), High resolution cyclostratigraphy of the early Eocene - new insights into the origin of the Cenozoic cooling trend. *Climates of the Past*, Vol. 5, pp. 309-327, doi:10.5194/cp-5-309-2009.

Westerhold, T., U. Röhl, B. Donner, H. K. McCarren, and J. C. Zachos, (2011), A

complete high-resolution Paleocene benthic stable isotope record for the central Pacific (ODP Site 1209), *Paleoceanography*, Vol. 26, PA2216, doi:10.1029/2010PA002092.

Wilson, P.A., and R.D. Norris, (2001), Warm tropical ocean surface and global anoxia during the mid-Cretaceous period, *Nature*, Vol. 412, pp. 425-429, doi:10.1038/35086553.

Woodard, S.C., D.J. Thomas, S. Hovan, U. Rohl, and T. Westerhold, (2011) Evidence for orbital forcing of dust accumulation during the early Paleogene greenhouse. *Geochemistry, Geophysics, Geosystems*, Vol. 12, No. 2, Q02007, doi:10.1029/2010GC003394.

Woodruff, F., and S. Savin, (1991), Mid-Miocene isotope stratigraphy in the deep sea: High-resolution correlations, paleoclimatic cycles, and sediment preservation, *Paleoceanography*, Vol. 6, No. 6, pp. 755–806, doi:10.1029/91PA02651.

Wortmann, U.G.,Herrle, J.O., and H. Weissert, (2004), Altered carbon cycling and coupled changes in Early Cretaceous weathering patterns: Evidence from integrated carbon isotope and sandstone records of the western Tethys, *Earth and Planetary Science Letters*, Vol. 220, No. 1–2, pp. 69-82, doi:10.1016/S0012-821X(04)00031-7.

Youssef Ali, M., (2009), High resolution calcareous nannofossil biostratigraphy and paleoecology across the Latest Danian Event (LDE) in central Eastern Desert, Egypt, *Marine Micropaleontology*, Vol. 72, No. 3–4,pp. 111-128, doi:10.1016/j.marmicro.2009.03.007.

Zachos, J., T. Quinn, and K. Salamy, (1996), High-resolution (104 years) deep sea foraminiferal stable isotope records of the Eocene-Oligocene climate transition, *Paleoceanography*, Vol. 11, No. 3, pp. 251– 266, doi:10.1029/96PA00571.

Zachos, J.C., M. Pagani, L. Sloan, E. Thomas, and K. Billups, (2001), Trends, Rhythms, and Aberrations in Global Climate 65 Ma to Present, *Science,* Vol. 292, No. 5517, pp. 686-693, doi:10.1126/science.1059412**.**

Zachos, J.C., Rohl, U., Schellenberg, S.A., Sluijs, A., Hodell, D.A., Kelly, D.C., Thomas, E, Nicolo, M.,Raffi, I., Lourens, L.J., McCarren, M., and D. Kroon, (2005), Rapid acidification of the ocean during the Paleocene-Eocene Thermal Maximum, *Science,* Vol. 308, No. 5728, pp. 1611-1615 doi:10.1126/science.1109004.

Zachos, J.C., S. Schouten, S. Bohaty, T. Quattlebaum, A. Sluijs, H. Brinkhuis, S.J. Gibbs, and T.J. Bralower (2006), Extreme warming of the mid-latitude coastal ocean during the Paleocene-Eocene Thermal Maximum: Inferences from TEX86 and isotope data, *Geology*, Vol. 34, No. 9, doi:10.1130/ G22522.1.

Zachos., J.C., Bohaty, S.M., John, C.M., McCarren, H., Kelly, D.C., and T.Nielson, (2007), The Palaeocene-Eocene carbon isotope excursion: constraints from individual shell planktonic formanifer records. *Philosophical Transactions of the Royal Society*, Vol. 365, No. 1856, pp. 1829-1842, doi:10.1098/rsta.2007.2045.

Zachos, J.C., McCarren, H., Murphy, B., Röhl, U., and T. Westerhold, (2010), Tempo and scale of late Paleocene and early Eocene carbon isotope cycles: Implications for the origin of hyperthermals, *Earth and Planetary Science Letters*, Vol. 299, No. 1–2, pp. 242-249, doi:10.1016/j.epsl.2010.09.004.

Zeebe, R. E., J. C. Zachos, and G. R. Dickens, (2009), Carbon dioxide forcing alone insufficient to explain Palaeocene– Eocene Thermal Maximum warming, *Nature Geoscience*, Vol. 2, pp. 576–580, doi:10.1038/ngeo578.

CHAPTER 5

Evaluating the Sedimentary Record of a Small Eocene Hyperthermal using an Earth System Model of Intermediate Complexity

Hyperthermal events, or episodes of abrupt global warming associated with the massive injection of carbon into the oceans and atmosphere, provide possible analogs for future climate change. However, the use of these events to understand climate sensitivity and carbon cycle feedbacks is complicated by uncertainties in their true magnitude, rate, and duration. Here, we use an Earth system model of intermediate complexity to assess the likely magnitude and rate of carbon input associated with a small hyperthermal event from the early-middle Eocene. We use an iterative method, combined with a sediment model simulating the formation and mixing of deep-sea sediment cores, to back out the likely magnitude of the carbon cycle perturbation in the atmosphere and ocean. We find that the method depends on generating a close match between the model site and the site from which the data derives. Our method provides a quantitative estimate of the degree to which sediment mixing has biased the apparent magnitude and duration of an event. In particular, we show that an event characterized by a $\delta^{13}C$ excursion of 0.6-0.95‰ in the deep sea is consistent with an atmospheric CO_2 $\delta^{13}C$ excursion of 1.6‰. We assess controls inter-site variation of event shape in model sediments and find that sedimentation rate is strongest determinant of event size, with higher sedimentation rate sites recording atmospheric and ocean signals more accurately. Our revised estimate for the true size of an event increases calculations of the required rate and total magnitude of carbon input by approximately 84%.

5.1 Introduction

Earth system models of intermediate complexity offer the possibility to assess the carbon cycle and climate implications of events identified in the paleo-record. Whereas highly complex coupled general circulation models (GCMs) represent the most advanced state of knowledge about the operation of the modern climate system, these models are often inappropriate for investigating paleo-events, where insufficient data exists to constrain important model parameters, and high computational demand means experiments with a long duration (thousands of years) are impossible. Earth system models, by contrast, combine simplified ocean and atmosphere dynamics with representations of biogeochemical cycles, sediments, and weathering, and can accommodate experiments of 10^5 model-years.

Researchers have used multiple models (from box models to GCMs) in order to investigate the causes and consequences of the Paleocene/Eocene Thermal Maximum (PETM; ~56 Ma). In particular, studies by have used the Grid-Enabled Earth System model (GENIE) to diagnose the likeliest mass and isotopic composition of a carbon input necessary to generate the PETM (by Panchuk et al., 2008) and have also calculated the likely rate and duration of carbon input (Cui et al., 2011). Additionally, Panchuk, 2007, used GENIE-1 to assess causes for differences in the size of the carbon isotope excursion (CIE) between various deep-sea records of the PETM. However, there is no published application of Earth system models to assess the other, smaller hyperthermal events of the

Paleocene and Eocene. Very few modeling studies have addressed the myriad climate-carbon cycle events occurring in these epochs.

Not only is it possible to adapt methods used for studying the PETM to the analysis of these smaller events, it is also possible to use these events to test the functioning of Earth system models over a larger range of scenarios. Assessing a multitude of events allows comparison of the impacts on the climate, biogeochemistry, and sediments of various forcings and indicates the fidelity of the model at reproducing various paleo-records. Such analysis has the potential to provide clues as to what factors most influence the record of various tracers in the sediments, which scenarios are most similar to modern climate change, and what significant components may be missing from the model.

This study has three primary aims: to assess the 'true' magnitude of CIEs recorded from the early-middle Eocene, to diagnose the likely rate and duration of carbon input necessary to generate these events, and to understand the factors that control the sedimentary expression of these events across different sites.

5.2 Methods

As a result of studies of the PETM, GENIE has been optimized for studying the late Paleocene/early Eocene. The version of GENIE used for PETM experiments by Panchuk et al., 2008, Ridgwell and Schmidt 2010, and Cui et al., 2011 is GENIE-1, which includes C-GOLDSTEIN—a fast climate model with a

frictional geostrophic ocean, a one-layer energy and moisture balance atmosphere, and a thermodynamic sea ice model (Edwards and Marsh, 2005; Hargreaves et al., 2004; Ridgwell et al., 2007), BIOGEM—an ocean biogeochemistry model, ATCHEM—an atmospheric chemistry model, SEDGEM—a model representing the delivery of sediments to the deep sea, and ROCKGEM—a model to calculate the supply of weathering products from the land to the ocean. (Ridgwell and Hargreaves, 2007; Ridgwell et al., 2007). For this study, we use cGENIE, a developmental offshoot of GENIE-1 maintained by A. Ridgwell at the University of Bristol.

The SEDGEM model provides the most significant advantage over other models for this study; in particular, SEDGEM allows the creation of virtual sediment cores, or stacked records of deep-sea sediment, which we can directly compare to sediment core data (Ridgwell and Hargreaves, 2007). SEDGEM links to the biogeochemistry module through the preservation and/or dissolution of carbonate. In BIOGEM, export production of particulate organic carbon (POC) is calculated from surface nutrient concentrations (phosphate), and carbonate flux is related to the export POC flux using a thermodynamic modifier of carbonate production based on the ambient saturation state of seawater with respect to calcite (Ridgwell et al., 2007). In contrast, remineralization depends on the saturation state, the length scale (with a calibrated value of 600 m), a calibrated scalar, and the depth below the euphotic zone (Ridgwell et al., 2007).

Carbonate reaching the seafloor can be buried or dissolved, according to the calculated dissolution flux from the oxic-only component of the dissolution model of Archer 1991 (Ridgwell and Hargreaves, 2007). The dissolution flux is highly dependent on the rain ratio of carbonate to POC, which is a user-imposed constraint in cGENIE. Any organic carbon that reaches the seafloor is remineralized there, so the only preserved components in the sediment model are carbonate and detrital material, which is another imposed condition.

For this study, we use a detrital flux that has been determined by an ensemble of runs to select the best fit to documented late-Paleocene wt% carbonate distributions (Chun, unpublished data) (Figure 5-1). We use a rain ratio generated to best match sites from which we have data on wt% $CaCO_3$ for the early-middle Eocene, which falls within the range used for simulations of the late Paleocene (between 0.15-0.2). As a result, we use a spatially varying detrital flux fit, where detrital flux is specified at each ocean grid-cell, and a rain ratio of 0.175 (Figure 5-2). In steady state, we force the model to maintain an atmospheric concentration of 3X pre-industrial CO_2 (834 ppm) and a CO_2 $\delta^{13}C$ of -4.9‰.

Sediments accumulate in a 5 cm-thick surface layer, where dissolution flux calculations mostly occur. According to the mass balance calculated in this surface layer (of constant thickness), the underlying first layer in the sediment stack can vary from 0-1 cm. The other layers in the sediment stack are all 1-cm thick, and diffusive transfer between the layers results in mixing or ‘bioturbation’ of the sediment column that decreases with depth with an e-folding length of

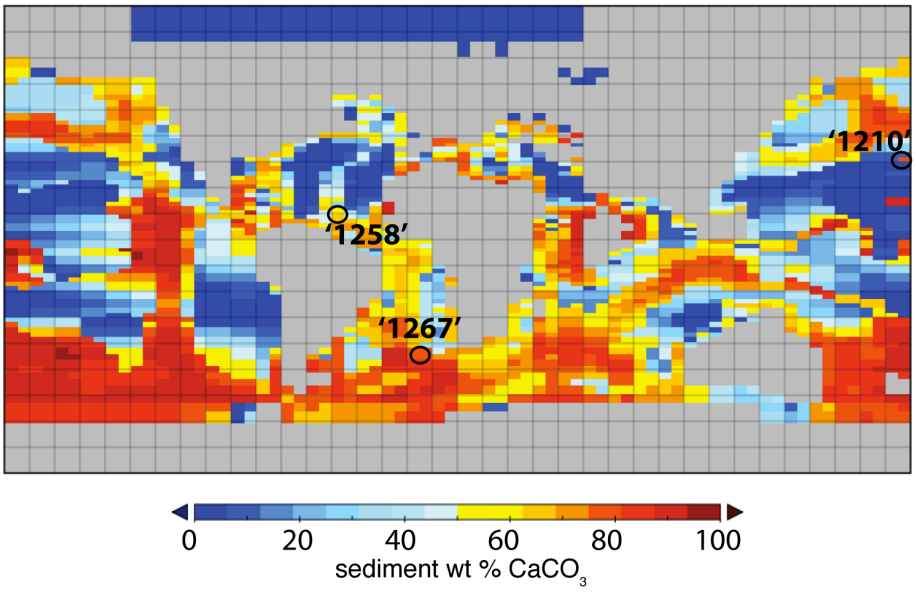


Figure 5-1. Seafloor carbonate distribution used as the initial condition for all subsequent experiments. Locations of three model sites (selected to approximate ODP Site 1258 in the equatorial Atlantic, ODP Site 1267 in the South Atlantic, and ODP Site 1210 in the Central Pacific) are shown in open black circles corresponding to their grid location. All three sites have carbonate greater than 50% at the start of the experiment and are thus inferred to be above the carbonate compensation depth.

1-cm (Ridgwell and Hargreaves, 2007). As carbonate is deposited to the sediment column, it is tagged with an 'age' (or the model year in years before present), with the resulting age of a layer in the sediment column equal to the average of the tagged ages of all the carbonate which makes up that layer (Ridgwell and Hargreaves, 2007). As a result of homogenization of sediments in the core-top layer, as well as bioturbation further down-core, the core-top age will always be slightly older than the model time (Figure 5-3). These functions of SEDGEM allow for the creation of time-series of core properties, which can be correlated with model time in order to assess the relative timing of signals

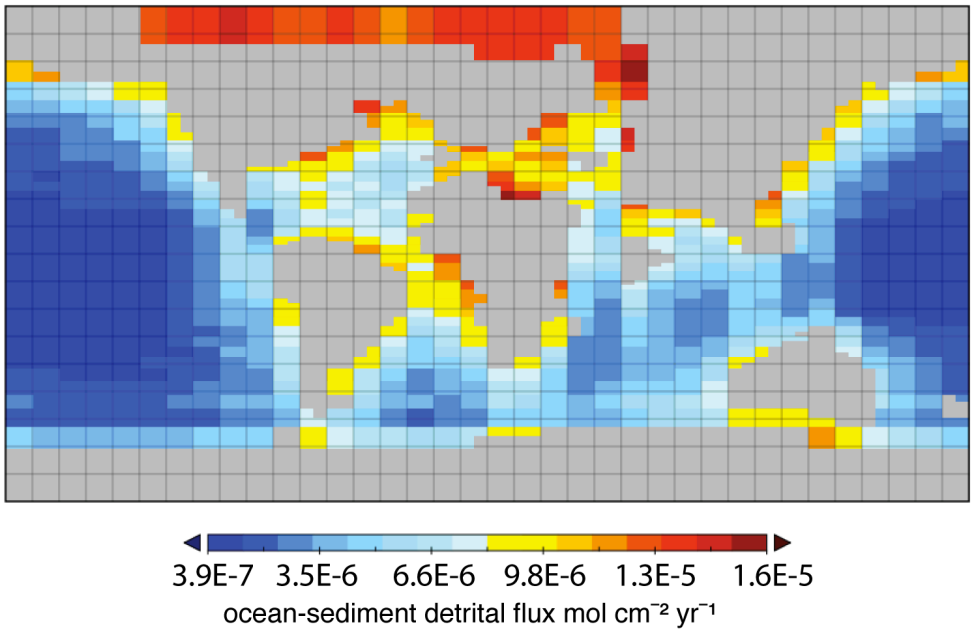


Figure 5-2. Spatially prescribed detrital flux forcing (in mol cm^{-2} yr^{-1}) used to generate initial conditions for all subsequent experiments. This detrital flux fit identifies the detrital flux at each sediment grid point (72x72). Together, sediment carbonate content plus the detrital component must equal 100%.

recorded in sediments with those recorded in ocean and atmosphere biogeochemistry. Additionally, it is possible to compare cores from specific-grid points to their data equivalent, but due to uncertainties in bathymetry, these cores are not always in the exact same locations as the calculated paleo-coordinates for a given site.

For this study we use a configuration of the Eocene similar to that of Ridgwell and Schmidt (2010), but with differences in the detrital flux and rain ratio described above. This version of cGENIE has a reduced solar constant of 0.46%,

an early Eocene continental configuration and bathymetry, annual average surface ocean wind stress and wind speed, zonally and annually averaged

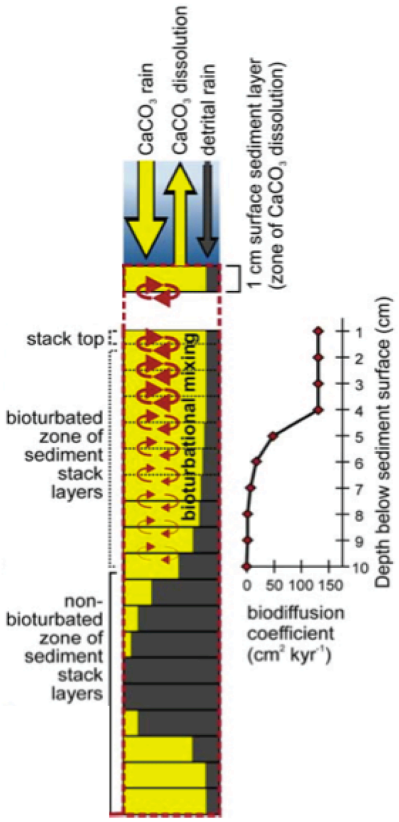


Figure 5-3. Model schematic (from Ridgwell, 2007) of the GENIE SEDGEM model. The balance between carbonate accumulation/dissolution is calculated in the surface sediment layer of constant 1 cm thickness. Below this layer is the top of the sediment stack, which may grow or shrink depending on the mass balance calculated from the surface sediment layer. Bioturbation in the sediment stack is modeled as mixing between adjacent layers. Bioturbation intensity decreases with depth in the sediment stack, with deeply buried sediments no longer bioturbated. In the model schematic, yellow indicates carbonate and grey indicates detrital material, which together equal 100% of sediment content (particular organic carbon is not preserved in the sediments, but remineralized at the sediment surface).

albedo re-gridded from the coupled GCM HADCM3L (Tindall et al., 2010) forced at x3CO_2, a 1% decrease in mean ocean salinity (to represent an ice-free world), an increase in the air-sea gas transfer coefficient (from 0.31 to 0.52), and the following initial carbon cycle conditions: Ca^{2+} of 18.22 mmol/kg, Mg^{2+} of 29.89 mmol/kg, SO_4^{2-} of 15 mmol/kg, and alkalinity of 2,075 μmol/kg, which produces ocean dissolved inorganic carbon (DIC) of 2,081 μmol/kg, a global deep-sea sediment burial rate of 16.8 Tmol Ca^{2+}/yr, and mean $CaCO_3$ content below 176 m of 38.38%. Finally, there is a prescribed weathering rate of 10 Tmol of $CaCO_3$ per year with $\delta^{13}C$ of 2.0 ‰ (equivalent to 20 Tmol HCO_3^- yr^{-1}), which is midway between the shallow and deep CCD options from Cui et al., 2011 of 9 Tmol HCO_3^- yr^{-1} and 32 Tmol HCO_3^- yr^{-1}.

For each experiment, the first step is to calculate the steady state composition of the climate and carbon cycle with a fixed weathering input. We use the 'first-guess closed system spin-up' methodology, where cGENIE is run as a closed system for 25 kyr, with a solute input applied to the ocean but balanced by subtraction from ocean cells overlying sediments and bioturbation is set 'off.' Next, we run an open spin-up for 50 kyr, where the prescribed weathering flux is revised based on the diagnosed global $CaCO_3$ burial rate from the closed system spin-up and bioturbation is set 'on.' In addition to bringing the system to steady state, with solute input due to weathering balancing the carbonate burial in deep sea sediments, these spin-ups are run to provide a sufficient sediment column to

perturb during experiments (i.e. if an experiment causes dissolution, there will always be older carbonate to dissolve).

The initial motivation for this study is work by Cui et al., 2011, who developed a methodology to diagnose the rate of carbon input during the PETM by forcing the model atmospheric CO_2 $\delta^{13}C$ to follow a prescribed curve. They assumed that a record they had generated of total organic carbon $\delta^{13}C$ represented the CIE seen by the atmosphere during the PETM. They adjusted their record to atmospheric values (relative to -6.5‰) and forced the atmosphere pCO_2 $\delta^{13}C$ to match this curve by either adding or removing carbon with a specified isotopic composition from the atmosphere. They found two best fits to their data—in one experiment they used a carbon input with $\delta^{13}C$ of -60 ‰ (methane) and a shallow CCD (caused by lower weathering input from rivers of 9 Tmol HCO_3^- yr^{-1}), and in the other they used carbon with $\delta^{13}C$ of -25 ‰ (organic carbon) and a deeper CCD (weathering input of 32 Tmol HCO_3^- yr^{-1}).

For the smaller hyperthermal events of the early-middle Eocene, there are relatively few records compared to the PETM, and these are primarily from deep-sea sites. As a result, our best records for the CIEs during these events come from benthic foraminifera. These records are usually highly influenced by preservational effects including bioturbation, sedimentation rate, and dissolution.

For the PETM, the wide range of shapes and sizes among CIEs from various sites demonstrates how much a given sediment record of an event may differ from the actual event in the atmosphere and surface ocean. However,

SEDGEM has the ability to simulate many of these factors, with bioturbation modeled as diffusive transfer between adjacent sediment layers, dissolution flux of carbonate calculated according to the oxic-only model of Archer (1991, 1996), and sedimentation rates spatially variable based on the productivity and chemistry of the overlying water column modeled by BIOGEM.

In addition, it is possible to approximate actual sediment cores to their model-equivalent. Here, we use these aspects of cGENIE to 'back out' the likely magnitude of the CIE in the atmosphere by combining the method of Cui et al., 2010, with an iterative process to calculate the difference between the CIE applied to that atmosphere and that recorded in the sediments.

We start by forcing the atmospheric CO_2 $\delta^{13}C$ in the model to follow a curve generated from the benthic foraminiferal $\delta^{13}C$ record, adjusted relative to a starting value of -4.9‰. For this experiment, we have selected event C22nH3 from Sexton et al., 2011, recorded at Demerara Rise in the equatorial Atlantic, ODP Site 1258 (Figure 5-4). C22nH3 occurred at ~49.2 Ma and lasted for ~36 kyr (defined as starting at the point at which values begin to decrease towards the peak of the excursion and ending where $\delta^{13}C$ returns to a value approximately as heavy as the starting value). ODP 1258 has a paleodepth for the Eocene of ~3000 m with pre-event wt% $CaCO_3$ of 52% and a sedimentation that reaches a maximum of 2-2.5 cm/kyr. The CIE recorded at 1258 for C22nH3 has a magnitude of 0.95‰ with the peak occurring 15 kyr after the onset of the event and sample spacing of 3-5 kyr.

We run the model for 55 kyr, forcing the atmospheric CO_2 $\delta^{13}C$ to match the prescribed curve for 36 kyr and then remaining at the final value for the duration of the run. The extra run time (as opposed to stopping at 36 kyr) is necessary in order to ensure sufficient time to record the entire excursion in the sediments, given the delay in transmitting the signal from the surface to the deep ocean and the possibility that the excursion is smeared out in the sediments. In order to more accurately reproduce the paleo-record in the model sediments, we have developed planktonic and benthic foraminiferal tracers that form from

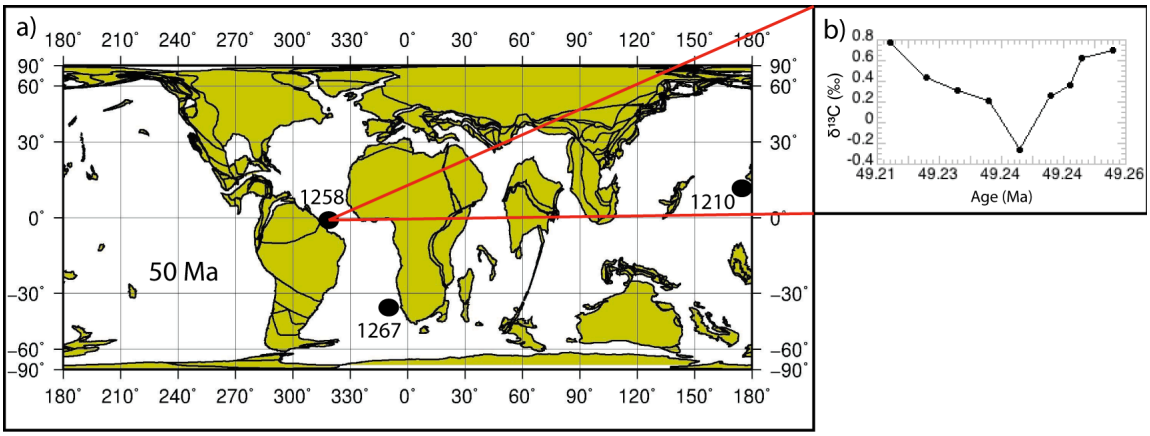


Figure 5-4. a) 50 Ma reconstruction showing location of ODP Site 1258, ODP Site 1267, and ODP 1210, three sites used for comparison to GENIE model results. b) Benthic foraminiferal $\delta^{13}C$ record for event C22nH3 from ODP Site 1258 (data from Sexton et al., 2011). This record is the source of the curve used to force atmospheric CO_2 $\delta^{13}C$ (after adjusting to atmospheric values by setting the onset at -4.9‰).

the surface and benthic DIC pools, respectively. This newly formed calcite has a $\delta^{13}C$ equal to that of the DIC pool, plus a positive fractionation factor that

increases with temperature. We must specify the $\delta^{13}C$ of the carbon input, which we assign as -25‰ (organic carbon) consistent with the hypothesis for the source of carbon from Sexton et al., 2011.

We assess the sedimentary CIE generated by forcing the atmosphere with a -0.95‰ excursion using a model sediment core corresponding to Site 1258 in the model, with a paleodepth of 2500 m, an initial wt% $CaCO_3$ of 55% and a sedimentation rate of ~2.5 cm/kyr (Figure 5-5). We plot model sediment core results as benthic foraminiferal $\delta^{13}C$ against $CaCO_3$ age in yr BP. For comparison with the record of CO_2 $\delta^{13}C$ applied to the atmosphere, we assign the start of the excursion using an ash tracer in SEDGEM, where a pulse of ash, as a tracer of mixing, is applied to the sediments at the start of each run.

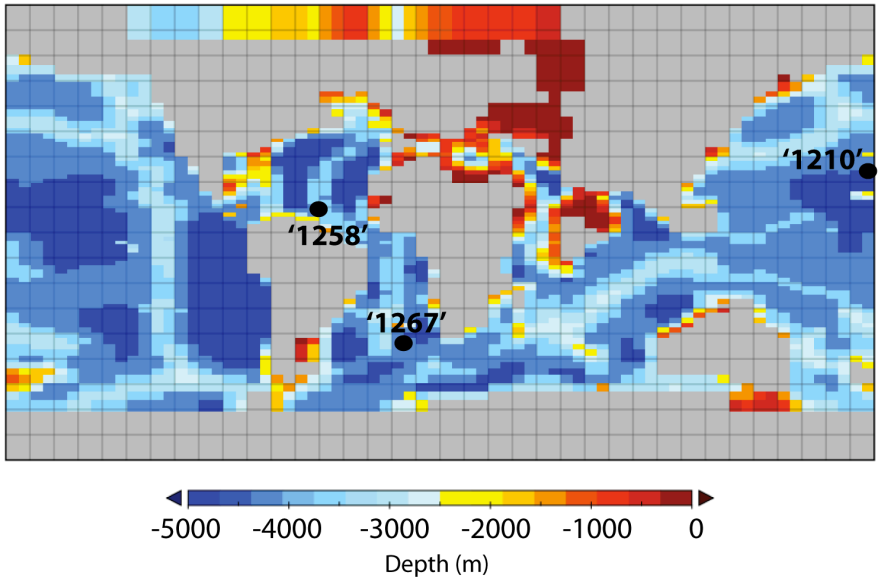


Figure 5-5. Locations of model sites used in this study plotted against model depth. '1258' has a depth of 2500 m, '1267' has a depth of 3000 m, and '1210' has a depth of 2400 m.

The deepest model sediment core interval containing ash indicates the deepest point to which material dating from the start of the run has mixed. We define the end of the excursion when $\delta^{13}C$ values have reached their most positive ratios. By this method, we can compare the magnitude, duration and relative timing of the CIE in the model sediment core benthic foraminiferal record to the atmosphere.

We calculate the difference between the excursion magnitude in the data and in the model sediment core benthic record in order to derive the new excursion to be applied to the atmosphere in the subsequent experiment. First, we assess the difference in the timing of the peak excursion and the overall excursion duration in the model sediment core compared to the model atmosphere. After forcing atmospheric CO_2 $\delta^{13}C$ with the original curve, the resulting sediment core benthic foraminiferal $\delta^{13}C$ record shows the peak of the excursion occurring over 19 kyr after the start of the event and an overall event duration of ~48 kyr.

We determine the new timescale of the atmospheric forcing by calculating the difference between these times:

$$t_{peak(new)} = \frac{t_{peak(initial)}^{2}}{t_{peak(sedcore)}}$$

where $t_{peak(initial)}$ is the time of the peak in the original forcing (15 kyr), $t_{peak(sedcore)}$ is the time of the peak in the model sediment core, and $t_{peak(new)}$ is the timing of the peak in the new forcing. Similarly, to calculate the new duration of the forcing:

$$T_{(new)} = \frac{T_{(initial)}^2}{T_{(sedcore)}}$$

where $T_{(initial)}$ is the total duration of the original forcing (36 kyr), $T_{(sedcore)}$ is the total duration of the carbon isotope excursion in the model sediment core, and $T_{(new)}$ is the total duration of the new forcing.

Our subsequent runs alter only the timing, not the magnitude of the original forcing, so we use the modified time of the peak and total duration as tie points to calculate new times for each δ-value. Altering timing alone is important, since changes in the rate of onset influence the magnitude of the excursion recorded in the sediment core—an event with the same magnitude but more rapid onset will result in a smaller recorded $\delta^{13}C$ excursion.

After iteratively altering the timing of the atmospheric forcing in order to achieve a model sediment core result with the peak in the benthic foraminiferal $\delta^{13}C$ tracer at approximately 15 kyr and a total duration of ~36 kyr (in this case, three runs were necessary), we begin to modify the magnitude of the $\delta^{13}C$ excursion. We modified the magnitude of the run in an analogous method to the timing modification:

$$CIE_{(new)} = \frac{CIE_{(initial)}^2}{CIE_{(time\text{-}modified\ sedcore)}}$$

where $CIE_{(new)}$ is the new magnitude of the CIE to be applied to atmospheric CO_2 $\delta^{13}C$, $CIE_{(initial)}$ is the original magnitude of the CIE (0.95‰), and $CIE_{(time\text{-}modified\ sedcore)}$ is the CIE magnitude in the model sediment core after adjusting the timing. Again we use the new magnitude and linearly interpolate to generate the new

forcing curve. We iteratively repeat this process to derive a 0.95‰ excursion in the benthic foraminiferal $\delta^{13}C$ tracer of the model sediment core. The curve applied to the atmosphere to generate this sediment core CIE is our 'backed out' or approximated true CIE (Figure 5-6).

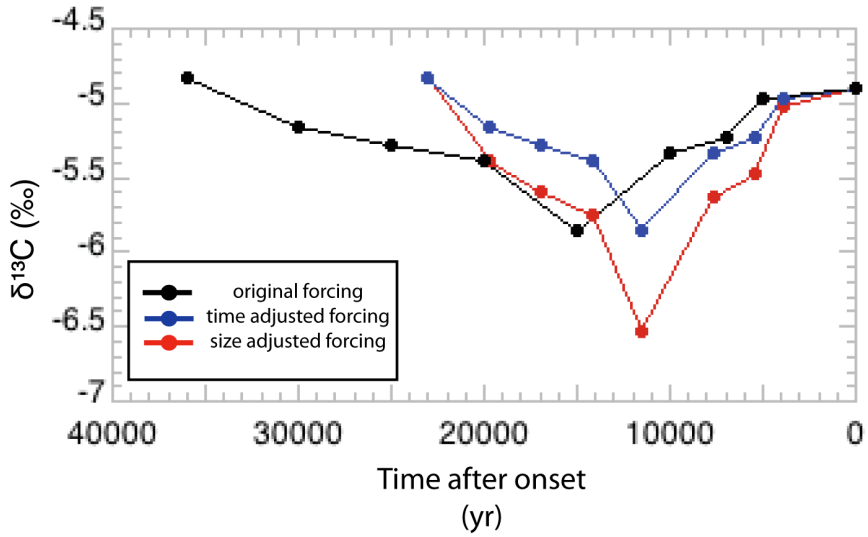


Figure 5-6. Illustration of the iterative process of backing out the 'true' atmospheric CO_2 $\delta^{13}C$ excursion using the benthic foraminiferal $\delta^{13}C$ record from ODP Site 1258 (black line) adjusted to atmospheric values. The blue curve represents time-modification of the forcing only (where same magnitude excursion as the initial forcing is applied, but altered to produce correct timing of the peak and total duration of the event in the '1258' model sediment core). The red curve represents both time-modification and magnitude-modification (where the curve is now altered to produce a 0.95‰ excursion in the '1258' model sediment core). The red curve is the final forcing applied to the atmosphere; all described model results are derived from the experiment using this curve.

While we only use one site for this exercise (1258 and its model-equivalent) because we have the highest resolution benthic record from this site, it is possible to repeat this exercise using data from another site, as long as there

is approximate match between the model site and the actual site (in terms of paleodepth, sedimentation rate, and wt% $CaCO_3$).

5.3 Results

Applying a -0.95‰ excursion to the atmosphere results in a benthic foraminiferal CIE in our selected model sediment core (to approximate ODP Site 1258) of -0.65‰. By following the iterative method described above, we generate a 0.95‰ excursion in the model sediment core benthic foraminiferal $\delta^{13}C$ by applying a -1.60‰ excursion to the atmosphere. The -1.60‰ excursion represents the approximated 'true' excursion size, from which we calculate the required carbon input and compare inter-site characteristics of CIE shape.

5.3.1 Excursion in BIOGEM

With an atmospheric CO_2 CIE of -1.60‰, the CIE in average surface DIC $\delta^{13}C$ is 1.88‰ and 1.71‰ in average benthic DIC $\delta^{13}C$. The enhanced magnitude of the excursion in DIC compared to the atmosphere is a result of changing fractionation between dissolved CO_2 and DIC from the onset to the peak of the event. As the model progressively adds more CO_2 to the atmosphere, surface ocean temperature rises, and excess CO_2 dissolves in the surface ocean, lowering pH and increasing the fraction of HCO_3^- in DIC but decreasing the fraction of CO_3^{2-}. Fractionation between dissolved CO_2 and total DIC depends on

the relative proportion of the different carbon species in seawater (CO_2, HCO_3^-, and CO_3^{2-}) as well as temperature (the fractionation scheme during air-sea gas transfer follows that of Marchal et al., 1998), so by the peak of the event, there is smaller fractionation between atmospheric CO_2 $\delta^{13}C$ and surface DIC $\delta^{13}C$ than at the onset. As a result, the excursion magnitude is larger in DIC than in the atmosphere.

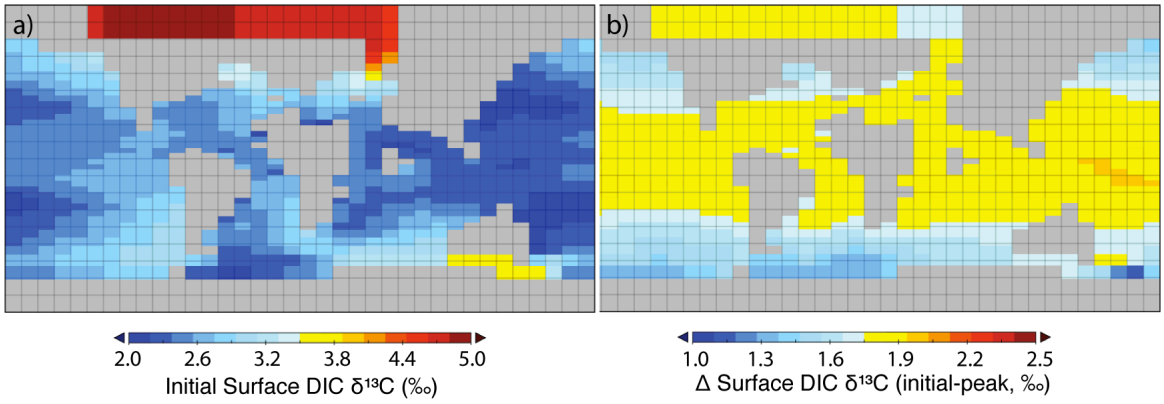


Figure 5-7. a) Distribution of initial surface dissolved inorganic carbon $\delta^{13}C$. Differences in values are largely a function of surface productivity, estimated from available surface nutrient concentrations and limited by the annual strength of local insolation, so areas with higher δ-values correspond to greater surface productivity. b) Global distribution of the size of the carbon isotope excursion in surface DIC $\delta^{13}C$. The excursion magnitude ranges from -1.0‰ to -2.0‰, compared to a -1.6‰ excursion in atmospheric CO_2.

Panchuk (2007) noted that the magnitude of the CIE in surface DIC is not globally homogenous, but varies based on the initial surface DIC $\delta^{13}C$, explaining that the range of excursion sizes is a function of the difference between the mass of carbon added and the total mass of carbon in the exogenic system after the addition. Another factor in the size of the excursion at a given site is that sites with a higher initial DIC $\delta^{13}C$ experience greater fractionation between dissolved

CO_2 and DIC, so the reduction in fractionation is more pronounced compared to sites where CO_2 to DIC fractionation is smaller (Figure 5-7).

5.3.2 Excursion in SEDGEM

Calcite (including the benthic and planktonic foraminiferal tracers) forms from the DIC pool. However, the magnitude of the excursion in calcite recorded in SEDGEM is not equivalent to the DIC CIE—excursion magnitudes across core-top calcite are smaller than in DIC, with a range from 0.00-1.00‰ (Figure 5-8). The range in recorded excursion sizes is a result of the range in size of the DIC excursion as well as different model site characteristics (e.g. depth and sedimentation rate).

The excursion magnitudes are smaller in core-top calcite compared to DIC because of temperature dependent fractionation during the formation of calcite from HCO_3^- (Panchuk 2007) and mixing at the sediment surface. At higher temperatures, fractionation between calcite and bicarbonate is reduced, so the CIE is reduced in $CaCO_3$ relative to the DIC pool. Model sediment core-top records record tracer properties in the top layer of carbonate before the layer is transferred to the sediment stack, and all tracer values are homogenized in the 5 cm-thick core top. This homogenization means that newly deposited carbonate is constantly mixed with older, isotopically heavier material, damping the apparent size of the excursion.

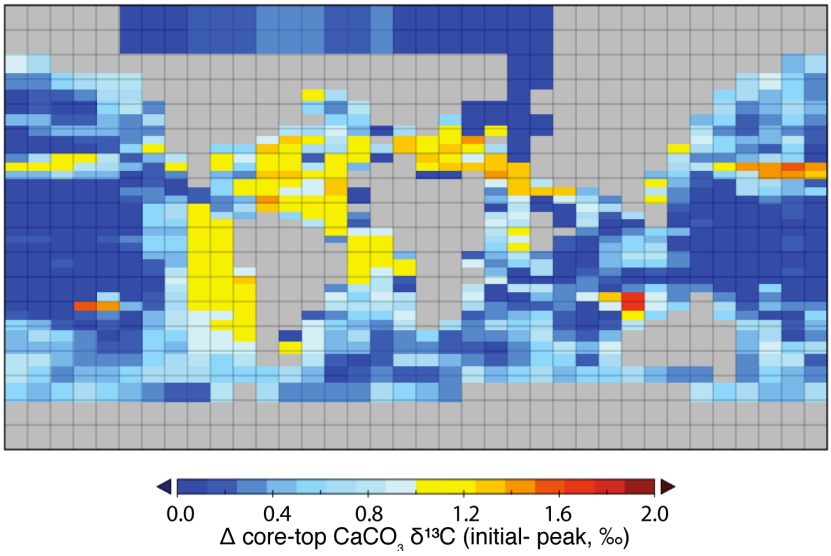


Figure 5-8. Global distribution of the size of the carbon isotope excursion in core-top sediment $CaCO_3$. The target was to generate a CIE of 0.95‰ at model site '1258.' A 0.95‰ CIE is approximately the median size of those recorded globally. Some sites record no CIE—these are sites with very low carbonate content. There are also very few spots where the recorded CIE approximates the atmospheric CO_2 excursion magnitude of 1.6‰.

Comparison of model sediment core results with sediment core-top records provides an indication of the relative importance of bioturbation within the sediment core in reducing the apparent magnitude of the CIE. In experiments modeling the PETM CIE, Panchuk (2007) suggested that the core-top and sediment core $\delta^{13}C$ excursions are of the same magnitude, but this is not consistent with what we find here. In contrast, we find that the core-top and sediment core CIEs can differ greatly.

Bioturbation in the sediment core is modeled as a biodiffusion rate that decreases with an e-folding depth of 1 cm—this depth profile of mixing intensity is the same globally (Ridgwell, 2001; Ridgwell, 2007). However, sedimentation

rates vary from site to site in the model, so the relative range of $\delta^{13}C$ values across which mixing takes place varies depending on the sedimentation rate at a given site. With the carbonate age tracer, it is possible to calculate the sedimentation rate for each sediment core. The core-top record from our model-site corresponding to ODP Site 1258 has a CIE of 1.78‰ in bulk $CaCO_3$ $\delta^{13}C$ compared to an excursion of 1.10‰ in bulk $CaCO_3$ $\delta^{13}C$ in the model sediment core; the sediment core sedimentation rate is 2.5 cm/kyr, similar to the sedimentation rate at ODP Site 1258 (Figure 5-9).

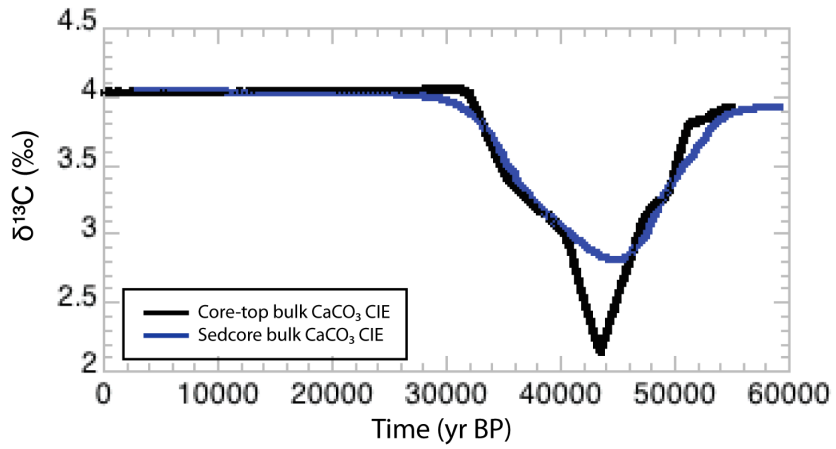


Figure 5-9. Comparison of core-top CIE (black line) and sediment core CIE (blue line) from model site '1258.' The core-top CIE is larger in magnitude than the atmospheric CO_2 CIE but closely approximates the CIE in benthic DIC of the overlying water column at this site. The difference in these two curves is a result of bioturbation between buried sediment layers.

In addition to the sediment core records from the model-site equivalent to ODP Site 1258, we can also compare model sediment core records for other sites from which we have data for this event. These are ODP Site 1210 in the

central Pacific (paleodepth ~2000 m) and ODP Site 1267 in the southern Atlantic (paleodepth ~3000 m). The cores that most closely match these sites are at depths of 2400 m and 3000 m, respectively. The CIE recorded in these two model sites is smaller than that recorded in the model sediment core '1258.' In model sediment core '1210' the benthic foraminiferal CIE is -0.66, and in model sediment core '1267,' the benthic foraminiferal CIE is -0.75‰. Both sites have higher initial wt% $CaCO_3$ compared to model sediment core '1258' and lower sedimentation rates (0.8 cm/kyr at site '1210 and and 1.7 cm/kyr at site '1267').

The CIE in sediment core '1267' is similar to preliminary data for C22nH3 from ODP Site 1267, which show a benthic foraminiferal CIE of approximately -0.6‰ (Figure 5-10). Comparing the sediment core bulk $CaCO_3$ $\delta^{13}C$ excursions to the core-top bulk $CaCO_3$ $\delta^{13}C$ excursions from these model sites shows larger differences compared to that for model site '1258,' consistent with the relative difference in sedimentation rate. At model site '1210', the difference in $\delta^{13}C$ excursion size between the model core-top and model sediment core records is 1.13‰. With an intermediate sedimentation rate, model site '1267' falls in between with a difference of 1.05‰.

The wt% $CaCO_3$ decrease and CIE size do not obviously co-vary in data for C22nH3 from our three sites, and in the model results, the order of the CIE size across the sediment cores from the three sites is consistent with the initial wt% $CaCO_3$ but not the magnitude of the normalized decrease in wt% $CaCO_3$ across each event.

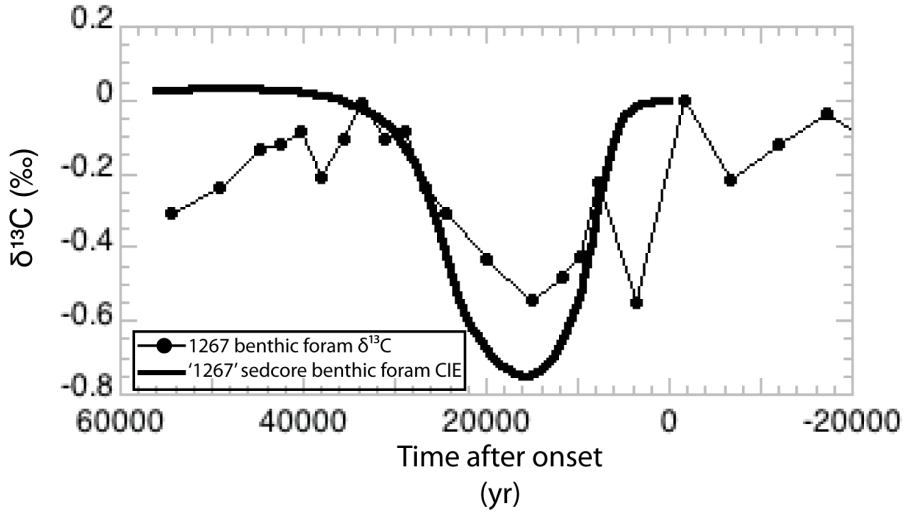


Figure 5-10. Sediment core benthic foraminiferal $\delta^{13}C$ record for model site '1267' (black line) plotted against actual ODP Site 1267 benthic foraminiferal $\delta^{13}C$ data (black dotted line). Actual Site 1267 data is plotted on an age model developed by tuning % $CaCO_3$ records from ODP Site 1267 to ODP Site 1258, with year zero assigned to the age from the ODP Site 1258 benthic foraminiferal $\delta^{13}C$ record where values begin to descend towards the $\delta^{13}C$ nadir. The ~0.2‰ difference between the data and model-derived CIEs is likely a result of the relatively high sedimentation rate in cGENIE for model site '1267.' Both records (data and model) have been adjusted to relative to 0‰ for ease of comparison.

Normalized change in wt% $CaCO_3$, after Panchuk (2007) is defined as:

$$\Delta_n CaCO_3 = \frac{CaCO_{3initial} - CaCO_{3final}}{CaCO_{3initial}}$$

The sediment core with the lowest initial wt% $CaCO_3$ (sediment core '1258') records the largest CIE, but the largest $\Delta_n CaCO_3$ occurs at '1267' with a slightly smaller CIE. In general, we expect an inverse relationship between initial carbonate wt% and normalized carbonate decrease because greater initial

carbonate increases buffering capacity. In the core-top records, where all the sites show relatively similar CIEs in bulk $CaCO_3$, the CIE size is largely a function of the CIE of DIC in the overlying water column and not much influenced by sedimentary characteristics of the site (Figure 5-11).

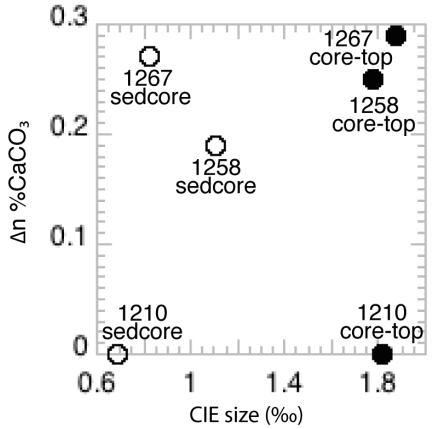


Figure 5-11. CIE size versus normalized change in wt% $CaCO_3$ for the three model sites, both core-top (closed circles) and sediment core (open circles). Core-top records show less variability in CIE size than do sediment core records. Core-top records also show slightly larger normalized wt% $CaCO_3$ changes compared to sediment cores, since mixing within the sediment stack can mix up $CaCO_3$ from adjacent sediment layers to mask the full extent of reduced $CaCO_3$ accumulation and/or dissolution.

As a result of the inconsistent relationship between CIE size and wt% $CaCO_3$, we infer that the extent of bioturbation is the most important factor in determining the sediment core CIE size. Furthermore, the sedimentation rate (and extent of mixing) can influence the amount of $CaCO_3$ that dissolves, since more extensive bioturbation can deliver more old $CaCO_3$ to the sediment surface to dissolve (Panchuk, 2007), which means that sedimentation rate effects the

magnitude of the normalized % $CaCO_3$ decrease in addition to the CIE size (explaining differences in Δ_n $CaCO_3$ between model core-top and sediment core records).

5.3.3 Timing of the CIE

In addition to the overall magnitude of the CIE, the rate of onset and timing of the peak are important factors in the shape of the recorded event. The peak of the excursion is approximately synchronous in surface DIC $\delta^{13}C$ and in the core-top carbonate at all three sites (Figure 5-12a). Though the excursion is slightly delayed in benthic DIC, most of the core-top carbonate has an isotopic value set when carbonate forms nearer to the ocean surface. However, once a new storage layer at the surface is transferred into the sediment stack, it will begin mixing with sediments in the layer below. In other words, once the core-top layer with the 'peak' values is transferred into the sediment stack, mixing will push the signal into older material. As a result, within the sediment cores, the peak of the CIE is consistently earlier than the peak in DIC. Bioturbation also means that the entire excursion looks spread out over a greater duration in the sediment core compared to DIC (Figure 5-12b).

The relative lag in the core-top peak and lead in the sediment core peak is also related to the sedimentation rate at each model site. The greatest delay in the core-top peak occurs at '1258,' with the highest sedimentation rate, and the

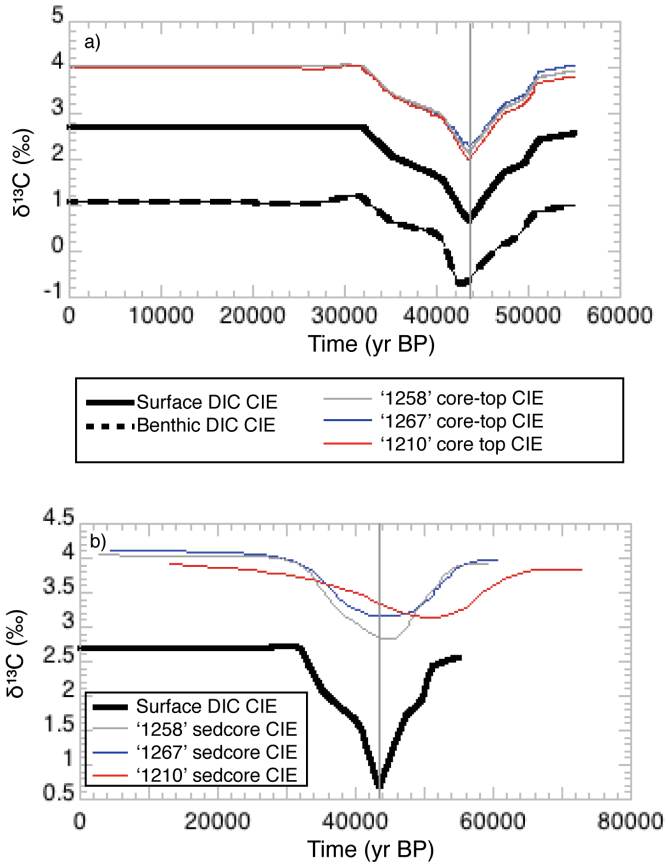


Figure 5-12. a) CIE recorded in surface (solid black line) and benthic (dashed black line) DIC and in core-top records for '1258' (grey line), '1267' (blue line), and '1210' (red line). Vertical grey line shows the timing of the peak in surface DIC $\delta^{13}C$. Benthic DIC CIE peak lags surface DIC CIE slightly; core-top CIE peaks are synchronous with surface DIC CIE peak. b) CIE recorded in surface DIC (solid black line) and in model sediment cores for '1258' (grey line), '1267' (blue line), and '1210' (red line). Vertical grey line shows the timing of the peak in surface DIC $\delta^{13}C$. The peak in model sediment cores leads the DIC CIE peak at all three sites. The lead is greatest at '1210' (red line) with the lowest sedimentation rate.

smallest delay occurs at '1210,' with the lowest. In the sediment core, the higher the sedimentation rate, the smaller the impact of 'smearing,' and so the smaller the lead in the apparent timing of the peak compared to DIC. Additionally, the high sedimentation rate sites show a shorter duration between onset and peak

compared to the low sedimentation rate sites, and the overall event duration is shorter in the high sedimentation rate sites.

Another consistent feature of the relative timing of the CIE peak in the sediment core records is that it consistently lags the minima in wt% carbonate (Figure 5-13). Of the three sites observed, wt% carbonate never goes to zero, even in the core-top records (it is important to distinguish between core-top and sediment core carbonate records because sediment cores can record non-zero wt% $CaCO_3$ even when no carbonate reaches the seafloor as a result of bioturbation, which brings old carbonate to the surface, e.g. Panchuk, 2007). As a result, the lag of the CIE with respect to the wt% $CaCO_3$ minima is not because there is no carbonate with which to record the most negative isotopic values, which might occur with greater carbon release (such as at the PETM). In the model, the surface CO_3^{2-} concentration reaches a minimum before surface DIC $\delta^{13}C$ reaches its most negative value. Translated to the sediments, this means that the minimum in carbonate export production occurs before the isotopically depleted carbon mixes through the whole ocean.

5.3.4 Diagnosed Carbon Input

In our final iteration of the atmospheric pCO_2 $\delta^{13}C$ inversion, atmospheric CO_2 increases from 834 to a peak of 1,219 ppm. The total amount of carbon ($\delta^{13}C$ = -25‰) added to the atmosphere is 2,349 Pg C, with a maximum rate of

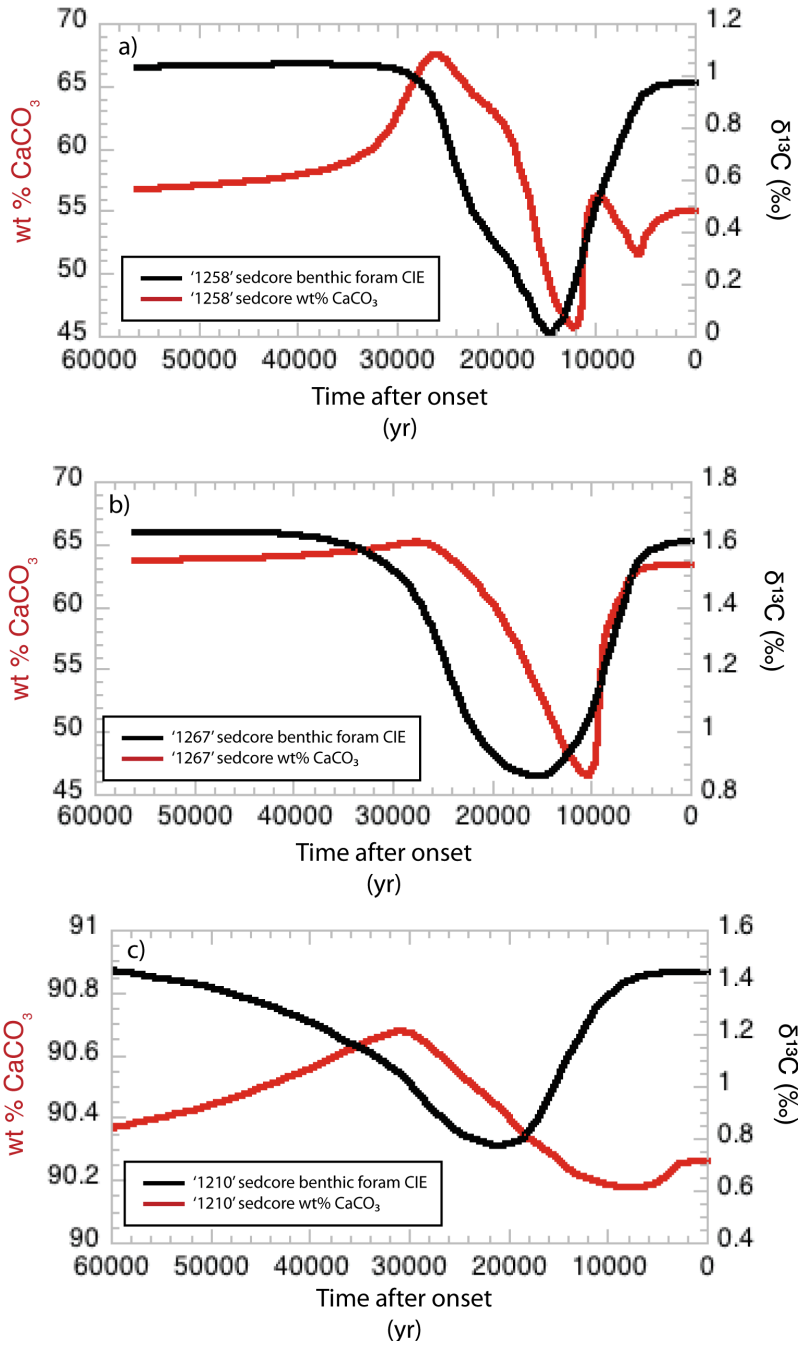


Figure 5-13. Records of model sediment core benthic foraminiferal $\delta^{13}C$ plotted against model sediment core wt% $CaCO_3$ for a) model site '1258,' b) model site '1267,' and c) model site '1210.' In each model sediment core, the minimum in wt% $CaCO_3$ occurs before the peak of the CIE.

0.42 Pg C/yr. In contrast, to generate the first iteration, the total carbon addition is 1,275 Pg with a maximum addition rate of 0.25 Pg/yr, suggesting that the iterative method of backing out the 'true' sediment excursion results in a 84% increase in the magnitude of the required carbon input. However, in order to generate a sediment core CIE with a 36 kyr duration, atmospheric CO_2 only stays at its maximum of ~1400 ppm for ~200 years, and then begins to decline more rapidly than it rose, with a maximum carbon removal rate reaching 0.58 Pg/yr (Figure 5-14). Atmospheric CO_2 concentration levels out at 730 ppm (lower than the initial concentration). Effectively, it requires a larger perturbation to the carbon cycle to recover from the event than it does to generate it (i.e. rate of removal is greater than rate of addition). The diagnosed rate of addition is significantly smaller than that for the PETM (~1.7 Pg/yr), though the removal rate is comparable (Cui et al., 2011).

It is possible to compare this inversion experiment (forcing the atmosphere to follow the prescribed -1.60 ‰ excursion), with a similar 'flux-forcing' experiment in cGENIE—applying a pulse of carbon calculated to generate a ~1.60‰ excursion in the total carbon reservoir (excluding terrigenous carbon, which is not represented). According to isotopic mass balance:

$$M_p = M_T * \frac{(\delta_T - \delta_{T'})}{(\delta_T - \delta_p)}$$

where M_T and M_p are the mass of carbon in the total exogenic system and the mass of the carbon pulse and δ_T, $\delta_{T'}$, and δ_p are the $\delta^{13}C$ of the total carbon

reservoir before and after the pulse, and the $\delta^{13}C$ of the added carbon, a -1.60% excursion requires a carbon addition of ~2,000 Pg C. Applying this pulse evenly over 12 kyr (the time of the intended CIE peak) at a rate of around 0.2 Pg C/yr

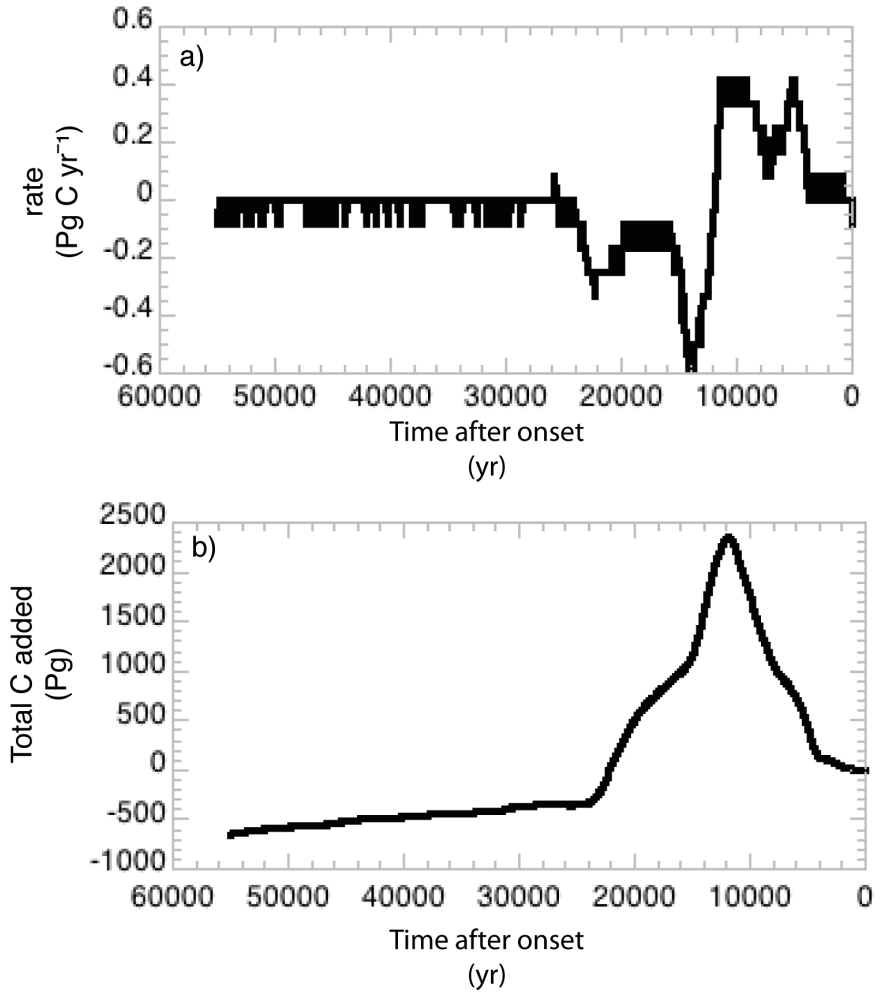


Figure 5-14. a) Diagnosed rate of carbon addition/removal in Pg yr^{-1} when forcing atmospheric CO_2 $\delta^{13}C$ to match the 1.60‰ excursion. b) Total carbon added to generate the 1.6‰ CIE. Compare to rates of 1.7 Pg yr^{-1} and 12,500 Pg total carbon if organic carbon is used to generate the PETM (Cui et al., 2011).

causes atmospheric CO_2 concentrations to rise and $\delta^{13}C$ of CO_2 and DIC, and sedimentary $CaCO_3$ content to decrease, but all these time-series show a long tail, with the recovery of isotopes much slower than the recovery of CO_2 and sedimentary $CaCO_3$ content (Figure 5-15).

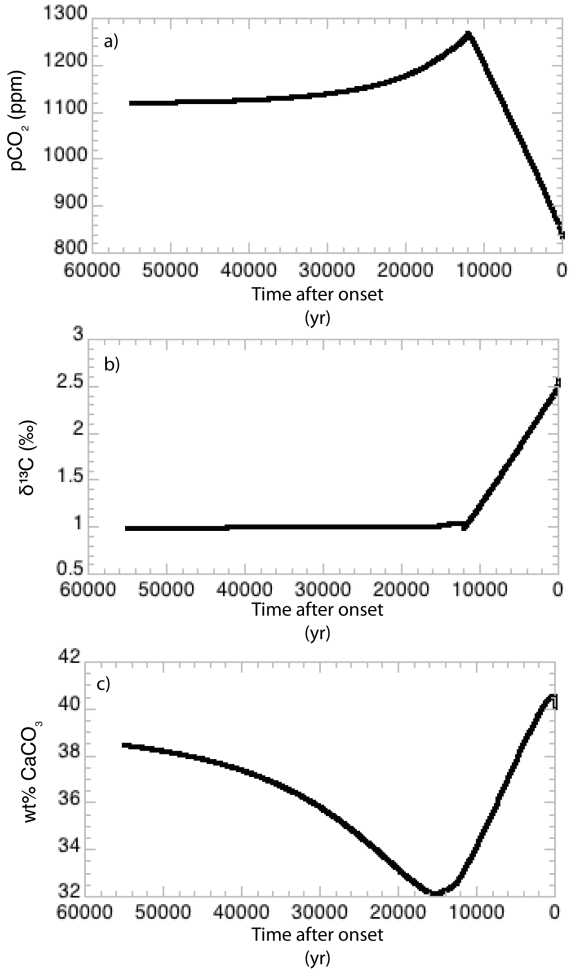


Figure 5-15. Results of flux forcing experiment, where a pulse of organic carbon (-25‰) is applied to the atmosphere at a constant rate over 12 kyr, after which the model continues to run without a carbon input for the remaining duration (55 kyr total). a) Change in atmospheric pCO_2 concentration (ppm). b) Carbon isotope excursion in surface DIC. c) Global decrease in sedimentary wt% $CaCO_3$.

This result is typical of CO_2 injection experiments in general, both for PETM simulations (e.g. Panchuk 2007; Panchuk et al., 2008; Cui et al., 2011) as well as modern fossil fuel emissions experiments (Ridgwell et al., 2007; Archer et al., 2009). The long tail in atmospheric CO_2 concentration is a result of the slow rate of carbonate compensation in drawing excess CO_2 from the atmosphere. The difference between the rate of recovery in the flux experiment and the rate of recovery in our inversion experiment represents cumulative drawdown processes not explicitly modeled in cGENIE. While the maximum rate of removal exceeds the maximum rate of addition in our inversion experiment, the removal rate never exceeds the addition rate in the flux experiment.

5.4 Discussion

The primary purpose of this study is to use cGENIE to analyze the smaller hyperthermal events identified from the early to middle Eocene. We select one event, C22nH3, as the target carbon isotope excursion because we have relatively high-resolution benthic foraminiferal data from this event (~5 kyr resolution) and because this event (~1.0 ‰) has a magnitude that is a rough average of the sizes represented among the CIEs identified from the Paleogene (compared to those identified by Cramer et al., 2003; Zachos et al., 2010). Very few of the smaller CIEs of the Paleogene have published foraminiferal isotope records.

The exceptions are the hyperthermal events of Sexton et al., (2011), from which we obtain the record for C22nH3, and the Stap et al., (2010) record of the Elmo (or ETM-2) and H2 events. However, comparison of Elmo with the other hyperthermal events indicates that it is the second largest event (after the PETM). All other isotopic records for identified CIEs come from bulk carbonate samples (see Chapter 3).

5.4.1 Backing out the CIE magnitude

Our first aim is to assess the approximate true magnitude of the CIE during C22nH3. The advantage of benthic foraminiferal data for this exercise is that benthic foraminifera provide the most accurate signal of DIC $\delta^{13}C$ (though offset due to vital effects), and thus CO_2 $\delta^{13}C$ (though DIC $\delta^{13}C$ is more spatially variable than CO_2 $\delta^{13}C$ as a result of photosynthesis and air-sea mixing) (Gruber et al., 1999; Lynch-Stieglitz et al., 1995; Tipple et al., 2010).

Planktonic foraminferal $\delta^{13}C$ is influenced by photosynthesis, depth-habitat, seasonal variability, preservation-effects, and individual specimen size (due to photosymbionts) (Tipple et al., 2010). While both planktonic and benthic foraminifera are subject to diagenesis after burial (or recrystallization and the incorporation of secondary calcite), these factors are likely less significant for benthics, owing to their heavily calcified skeletons (Tipple et al., 2010).

cGENIE has benthic and planktonic foraminiferal tracers, but the planktonic tracer does not capture the full range of controls on the actual $\delta^{13}C$ recorded by individual species of planktonics—it simply forms calcite with a temperature dependent fractionation step from the surface DIC pool. The benthic tracer does not capture species-specific vital effects either (which is why we assess the relative magnitude of CIEs generated in this model tracer rather than the specific $\delta^{13}C$-values), but for the reasons mentioned above, we expect that this failure will be less critical for benthics compared to planktonics.

cGENIE also has a tracer for the $\delta^{13}C$ of bulk carbonate, but this model-version cannot be expected to accurately represent measurements of bulk $CaCO_3$ $\delta^{13}C$. While GENIE generates carbonate from the global DIC pool, actual bulk carbonate $\delta^{13}C$ measurements incorporate many unidentified species of calcareous nannoplankton, the relative proportions of which may vary during episodes of environmental change, and whose fractionation with respect to DIC is not well understood.

The difference between measurements of the $\delta^{13}C$ of bulk carbonate, benthic foraminifera, and planktonic foraminifera for C22nH3 compared to the model-derived sedimentary records from our inversion experiment reflect the advantage of using the benthic foraminiferal record to assess the true size of the CIE. While the observed benthic foraminiferal CIE is -0.95‰, the CIE in planktonic foraminifera is slightly smaller (-0.83‰), and the bulk CIE is the smallest (-0.6‰). This pattern of relative size is not matched in the model output,

where the planktonic foraminiferal tracer records the largest excursion, followed by bulk carbonate, and the benthic foraminiferal tracer records the smallest. In the data, we infer that the large magnitude of the excursion in benthic foraminifera reflects the close approximation to DIC. In contrast, in the model, the large magnitude of the planktonic foraminiferal CIE reflects the fact that the greatest excursion occurs in surface ocean DIC. The bulk carbonate CIE recorded in the data is likely the smallest because changes in species composition, and thus the relative fractionation between carbonate and the DIC from which it forms, has dampened some of the excursion in a method that cannot be easily reproduced by cGENIE.

Using the extent of mixing calculated in the model sediment core that most closely correlates to the site from which our isotopic records derive, we are able to back out the magnitude of a CIE in atmospheric CO_2 $\delta^{13}C$ that would generate a benthic foraminiferal $\delta^{13}C$ excursion in our target model sediment core of -0.95‰. The calculated atmospheric CO_2 CIE is 1.6‰. The difference between the two excursion sizes is relatively small compared to the difference between the excursion in the atmosphere and the other model sediment cores; this is a result of the high sedimentation rate at the model site used (~2.5 cm/kyr) and therefore the relatively low impact of mixing in 'smearing' the record. Still, this model sedimentation rate is probably slightly too high based on age models developed for ODP Site 1258 in this interval (Sexton et al., 2006; Westerhold et al., 2009), so our 'true' excursion is still a minimum estimate. For instance, if we

used our method to ‘back out’ the true magnitude on a site with a lower sedimentation rate of ~1.7 cm/kyr (our model site ‘1267’), while the site is not in the right location and has too high much preserved carbonate, the resulting atmospheric CIE would be larger.

A caveat to this exercise of backing out the true CIE size, then, is that it is important to match details of the model sites to the data as closely as possible. Sedimentation rate is largely a function of the productivity of the overlying water column and the applied detrital flux fit, so varying the 2D spatially prescribed detrital flux field can result in variations of the sedimentation rate. To vary the initial wt% carbonate, we can vary either the rain ratio of $CaCO_3$ to POC or the weathering flux of bicarbonate, where a higher rain ratio and/or greater flux of bicarbonate will effectively deepen the CCD and increase the total $CaCO_3$ preserved at each site. We do not have nearly as many sites to provide information for the early-middle Eocene as for the late Paleocene, and the bathymetry is also set for the late Paleocene, so our values for the detrital, rain ratio, and weathering parameters are best guesses from an ensemble meant to match the late Paleocene. Initial conditions at the three model sites that we describe here do not perfectly describe available data, but tuning model parameters to yield perfect matches at these sites (especially by altering bathymetry from the late Paleocene configuration), is not justified by the relatively small number of datasets used to constrain initial configurations compared to the late Paleocene.

Even without a perfect match between model and data site characteristics, our method still reveals the best possible guess for the $\delta^{13}C$ of atmospheric CO_2 suggested by the available sedimentary records. It is possible to repeat this exercise for the same event (C22nH3), but using records from a different site, to back out a similar CIE in the atmosphere. For instance, preliminary benthic data from ODP Site 1267 suggests a negative excursion of ~0.6‰ for C22nH3, in comparison with the -0.95‰ excursion recorded at ODP 1258. This difference is similar to the model difference between the CIE in sedcore '1258' and '1267' (0.95 vs. 0.75‰).

The slightly larger size of the model-derived CIE compared to the measured CIE is likely a result of the slightly high sedimentation rate estimated for the site (model sedimentation rate of 1.7 cm/kyr compared to ~1 cm/kyr actual sedimentation rate). However, the larger difference between the atmospheric CIE and the modeled benthic foraminiferal CIE at model site '1267' suggests that if we forced the model to match the -0.6‰ excursion initially, and then backed out the true excursion using the sediment core '1267' record, the true excursion would differ from the initial excursion by a larger amount than the difference between the backed-out atmospheric CIE using the '1258' data and the original 0.95‰ CIE. Thus, we would converge on a similar 'true' excursion magnitude.

5.4.2 Diagnosing carbon input and removal

The second goal of this study is to diagnose the rate and duration of the carbon input during a smaller 'hyperthermal' event. Unfortunately, we do not yet have sufficient information for the change in CCD during these events to constrain the isotopic composition of the input in a manner analogous to that of Panchuk et al., 2008. The three sites from which we have data for C22nH3 fall in a ~1000 m depth range and appear to be above the CCD for the entire event, based on the operational definition that a site is above the CCD if it preserves greater than 10% carbonate (Ridgwell and Zeebe, 2005; Goodwin and Ridgwell, 2010). Data from the actual sites shows that, in the Atlantic, wt% $CaCO_3$ drops to 42% at ODP Site 1258 and 62% at Site 1267 (both sites at ~3000 m paleodepth), while in the Pacific, wt% $CaCO_3$ never falls below 92% at ODP Site 1210 (paleodepth ~2000 m). While a site could presumably stop accumulating carbonate during an event as the CCD shoaled and yet never have wt% $CaCO_3$ fall to zero because mixing continued to deliver older, already deposited carbonate to the sediment surface, wt% $CaCO_3$ seems sufficiently high for this not to be the case. Still, the narrow depth range of our sites means we have insufficient information on the depth of the CCD or the extent of shoaling. Without this information, we are lacking a critical variable to calculate the likeliest mass of carbon input. As a result, a variety of carbon inputs of varying isotopic compositions could account for the -1.60‰ excursion.

Fortunately, flux-forcing experiments do provide some bounds on the feasible mass (and thus isotopic composition) of the carbon pulse. To generate a -1.60‰ excursion with methane ($\delta^{13}C$= -60‰) requires a pulse of ~900 Pg C. Such a small carbon pulse does not generate decreases in wt% $CaCO_3$ at our model sites that are as large as those in the actual sites. In contrast, using volcanic CO2 ($\delta^{13}C$=-5‰) requires a pulse of more than 11,000 Pg C and takes wt% $CaCO_3$ close to zero in our model sediment cores. These are not strictly quantitative bounds on the pulse size, but they suggest that organic carbon ($\delta^{13}C$=-25‰), or perhaps carbon from a mixture of sources with an intermediate $\delta^{13}C$, is most consistent with observations.

The diagnosed rate of carbon input is a maximum of 0.42 Pg C/yr, and the pulse has a symmetrical shape, with the total carbon input occurring in a pulse spread over ~8 kyr, and the maximum addition rate maintained for ~1.5 kyr (Figure 5-14). This rate of input is just a quarter of that diagnosed by Cui et al., 2011, for the PETM of 1.7 Pg/yr, though the PETM CIE they generate is around 2.5 times the size of the CIE for C22nH3, demonstrating a non-linear relationship between CIE size and the rate of carbon input required.

Both the PETM and C22nH3 carbon input curves show two distinct peaks of addition. For the PETM, the second peak in input rate is much greater than the first, whereas for C22nH3, the input rate peaks twice at the same rate. In contrast to our experiment, where we force the atmosphere to the $\delta^{13}C$ minimum at 11.5 kyr, the curve used for the PETM simulation does not reach the atmospheric CO_2

$\delta^{13}C$ minima until 20 kyr after values have begun to decline. However, both pulse shapes appear consistent with hypotheses that favor multiple injections of CO_2 into the atmosphere, possibly from different sources as a result of carbon cycle feedbacks due to warming. In fact, during the onset of the PETM, the input rate hits a value 0.4 Pg/yr and maintains this rate for a few thousand years. Given that this input rate is roughly comparable to the input rate for C22nH3, it is plausible to interpret the pulses of carbon responsible for generating the smaller CIEs of the Paleogene as comparable to the early stages of the PETM. Whereas negative feedbacks were apparently able to halt the carbon input and begin the recovery from these small events, during the PETM, the input rate only accelerated, perhaps because there was a greater reservoir of carbon available for perturbation.

In comparison, the maximum rate of carbon removal during the recovery of C22nH3 diagnosed in our experiment is similar to the PETM, at 0.5 Pg/yr (Cui et al., 2011). For the PETM, this asymmetry between the rate of C-input and the rate of removal reflects the long tail of negative $\delta^{13}C$ values recorded for the PETM, with a complete recovery achieved ~150 kyr after the onset (Cui et al., 2011). In our experiment, the rate of removal hits its maximum shortly after the most negative isotopic values are reached (just as in the PETM simulation), and removal of excess carbon is complete by 25 kyr after the event onset (Figure 5-14).

A rate of removal that can draw-down CO_2 to levels lower (in this case) than at the onset of the event is not achieved in flux experiments where the atmosphere is not explicitly forced to remove isotopically light CO_2 from the atmosphere in order to rapidly return $\delta^{13}C$ to heavier values. In their study of the PETM, Cui et al., 2011, noted that enhanced silicate weathering could lead to more rapid CO_2 drawdown, though this would not change the isotopic composition of surface ocean DIC, and thus could not remove the long tail in the isotopic time-series. Additionally, silicate weathering operates on a longer timescale (hundreds of thousands of years) compared to carbonate compensation (Ridgwell and Hargreaves, 2007; Goodwin and Ridgwell, 2010), and so could not explain the rapid recovery in CO_2 concentration either.

As a result, Cui et al. invoke excess organic carbon drawdown as the mechanism responsible for relatively rapid recovery of isotopes in records of the PETM compared to model simulations. Bowen and Zachos, 2010, suggested that the rapid rate of recovery post-PETM could be explained partially by differences from modern in the total mass of the Paleocene exogenic carbon reservoir or the rate of fluxes into/out of the lithosphere. However, their analysis of proxy-data on the Paleocene carbon cycle suggested that the mass of the exogenic carbon reservoir was no less than ~75% of its modern size and flux rates (on the basis of carbonate accumulation) were not obviously greater than modern. As a result, they hypothesized that enhanced organic carbon burial was necessary to explain

the rapid rate of recovery, which would preferentially remove isotopically light carbon from the exogenic system.

Ridgwell and Hargreaves, 2007, describe the role of ocean-sediment feedbacks in GENIE in controlling the long-term (tens of thousands of years) model response to a carbon input. Dissolution of deep-sea carbonates and the imbalance in weathering and sedimentation as a result of declining carbonate burial cause a drawdown in CO_2 beyond simple redistribution of carbon between the atmosphere and ocean. Goodwin and Ridgwell, 2010, calculate that 6-10% of carbon emissions will remain in the ocean after a new steady state is reached following carbonate compensation.

However, cGENIE does not currently include a scheme for the preservation of organic carbon in the sediments—all organic carbon that escapes degradation in the water column is simply remineralized when it reaches the sediments (Ridgwell, 2007; Ridgwell and Hargreaves, 2007). Ongoing additions of sedimentary organic carbon preservation in cGENIE may soon enable direct calculation of the excess removal of light carbon through, for instance, changes in deep ocean redox conditions and/or increasing productivity. However, since our inversion experiment only allows the model to add or subtract CO_2 with $\delta^{13}C$ of -25‰, we are effectively constraining the preferential extraction from light carbon from the system as no greater than 0.5 Pg/yr.

In order to match the prescribed isotopic curve, CO_2 removal begins as soon as the atmospheric CO_2 hits the $\delta^{13}C$ minima. The forced CO_2 extraction

prevents DIC from increasing by as much as it normally would—in the flux forcing experiment, DIC increases by more than the size of the carbon pulse as a result of the dissolution of old carbonates (e.g. Panchuk et al., 2007) and the reduction in carbonate burial and build up of weathering products in the ocean (Figure 5-16). These processes (sea-floor carbonate neutralization and terrestrial carbonate neutralization, respectively) normally allow atmospheric CO_2 to decrease by more than ocean invasion only (which occurs due to the difference in partial pressure of CO_2 across the air-sea interface as a result of the carbon pulse). A few tens of thousands of years after the cessation of the carbon pulse,

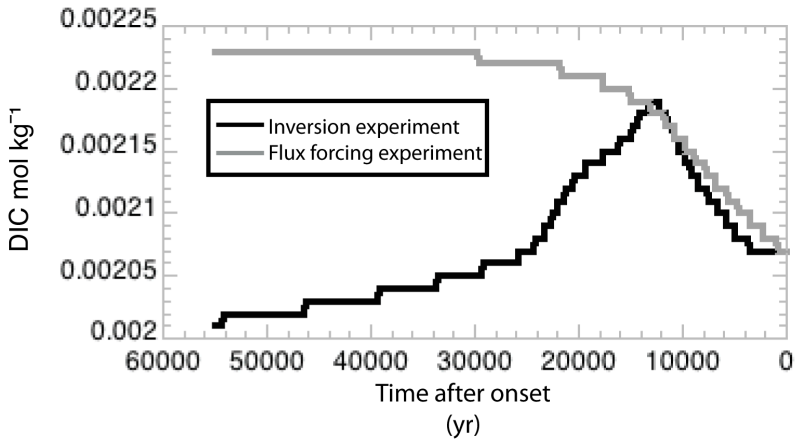


Figure 5-16. Comparison of the global ocean DIC concentration during the inversion experiment, where the atmosphere CO_2 is forced to match a specified curve by either adding or removing CO_2 (black line), and during the flux forcing experiment, where a pulse of CO_2 is applied to the atmosphere at a constant rate over 12 kyr (grey line). Without artificially forcing the removal of excess CO_2, global DIC concentration continues to rise as dissolved carbonate and weathering products accumulate in the ocean.

DIC levels out at a concentration higher than its initial state, though [CO_3^{2-}] recovers to approximately its initial value and so has the mean sediment surface wt% carbonate (Goodwin and Ridgwell, 2010).

In our inversion experiments, however, the forced removal of carbon means that while DIC continues to increase for ~2 kyr after the forced CO_2 extraction has already begun, it then decreases for the remainder of the experiment (Figure 5-16). This forced removal prevents carbonate compensation from occurring normally, so preferential organic carbon burial does not have to account for the entire 0.5 Pg/yr removal rate.

The rate of recovery of DIC $\delta^{13}C$ in the flux experiment is relatively slow compared to the recovery of atmospheric CO_2 concentration (Figure 5-15). In the flux experiment, DIC $\delta^{13}C$ recovers at a linear rate of ~0.003‰/kyr compared to the >0.1‰/kyr rate from our inversion experiment. In the flux experiment, DIC $\delta^{13}C$ recovers only because of the continual addition of weathering $CaCO_3$ products with a $\delta^{13}C$ of 2.0‰ after addition of the light carbon has stopped, while carbonate continues to precipitate from the depleted DIC pool. Even if the rate of CO_2 removal from the atmosphere were increased by enhanced weathering, unless the removal process preferentially selected isotopically light carbon, it would not be possible to greatly increase the rate of DIC $\delta^{13}C$ recovery—therefore is it the rate of recovery of carbon isotopes, more than the rate of recovery of CO_2 concentrations, which requires an additional carbon sequestration mechanism.

5.4.3 Factors controlling sedimentary CIE expression

The third priority of this study is to assess the factors that control the shape of the carbon isotope excursion eventually recorded in the sediments. Panchuk, 2007, addressed a similar issue using flux experiments with carbon pulses of varying isotopic composition to generate the PETM. Her primary conclusions included 1) that there is no simple relationship between either initial wt% carbonate or the extent of carbonate decrease and CIE size and 2) that the rate of recovery of the saturation state of seawater with respect to calcite and the extent of bioturbation were key factors in controlling CIE shape. Panchuk's study evaluated how different size carbon pulses could affect the sedimentary signal, with pulses varying from 2,300 to 70,000 Pg of carbon. Consequently, the results mostly focused on the role that dissolution plays in altering records of the CIE. When pulses of carbon are large enough to cause significant dissolution, they introduce intervals in which it is not possible to record the changing isotopic composition of seawater—bioturbation can mask this signal by making it appear that a record is continuous by mixing previously deposited carbonate to the sediment surface (Panchuk, 2007). This issue has long presented difficulties for researchers trying to generate a record of the onset of the PETM, determine its rapidity, and assess the true CIE magnitude.

In contrast, the smaller CIEs of the Paleogene are often insufficiently large to cause major dissolution of carbonates throughout the deep-sea. A pulse of ~900 Pg of carbon (if in the form of methane) could have generated a 1.60‰

CIE, and our inversion experiment, using organic carbon ($\delta^{13}C$ of -25‰), requires approximately the same amount of carbon as the smallest possible PETM carbon pulse used by Panchuk, 2007. At 2000 m, our record from the Pacific still shows wt% $CaCO_3$ at the peak of the event of around 88%. The largest normalized wt% $CaCO_3$ decrease during C22nH3 is less than 0.4, where at the same site during the PETM, all carbonate was lost. The advantage of the smaller pulse size required to generate our event is that we can largely remove the influence of extensive carbonate dissolution on the recorded CIE.

As a result, the most critical factor in determining the size and shape of our event is sedimentation rate, which controls the extent of bioturbation. By applying a prescribed isotopic curve to the atmosphere and assessing the resulting sediment records, we find that sites with the highest sedimentation rates most closely record the 'true' CIE magnitude. It is possible to remove the influence of other environmental factors that vary between sites by comparing the core-top and model sediment core records for a given site. Across sites, the core-top CIE varies in size because DIC $\delta^{13}C$ is not globally homogenous, but varies depending on productivity at the surface and patterns of deep-ocean overturning. Within a given site, the difference between the CIE magnitude recorded in the model sediment core and core-top is a function of sedimentation rate—the lower the sedimentation rate, the larger the difference between the CIE magnitude in the core-top bulk $CaCO_3$ $\delta^{13}C$ tracer and the model sediment core bulk $CaCO_3$ $\delta^{13}C$ tracer.

The sedimentation rate (and extent of mixing) also controls the timing of the CIE at each site. When sedimentation rate is low, bioturbation more effectively 'smears out' the CIE, resulting in an apparently longer event. However, mixing means the peak is advanced in the model sediment core relative to DIC. These effects are therefore more extreme at sites with low sedimentation rate—a lower rate means a longer apparent event and an apparently earlier CIE peak. Furthermore, the apparent rate of onset varies across sites, with the low sedimentation rate sites showing $\delta^{13}C$ begin to decrease first, but at slower rate, compared to higher sedimentation rate sites. This result has implications for attempts to tune inter-site records of CIEs. Such tuning is typically accomplished by one of two methods—either aligning the peaks at each site, or the onsets. Our results suggest that for a given, globally contemporaneous event, records of both the time of onset and time of peak will vary as a function of sedimentation rate (not including any effects of overturning circulation). Aligning records with different sedimentation rates can therefore introduce a few thousand years of error into age models created by assigning an absolute age to an isotopic event.

5.4.4 Leads and lags in carbonate burial and $\delta^{13}C$

Model results from every site, as well as all our collected data for event C22nH3, show minima in wt% carbonate preceding the peak of the CIE. The lead is more pronounced for sites with higher sedimentation rates (less affected by

mixing). This lead is also present in the relative timing of the point at which undersaturation in the carbonate ion is greatest compared to the CIE in DIC.

Since bicarbonate is by far the largest constituent of the DIC pool, its isotopic composition mostly determines the isotopic composition of DIC. However, as CO_2 hydrolysis adds bicarbonate to the DIC pool, and free hydrogen ions cause a reduction in carbonate ion, the large size of the bicarbonate pool means that changing its isotopic composition proceeds more slowly than the rate at which the carbonate ion concentration falls. The minima in $[CO_3^{2-}]$ occurs a few hundred years before the minima in surface ocean DIC $\delta^{13}C$, but the effect is pronounced in the sediment core records because the minima in $[CO_3^{2-}]$ immediately materializes as a reduction in carbonate export, while the $CaCO_3$ $\delta^{13}C$ minima requires the depleted carbon to fully mix through the ocean DIC pool.

The temporal offset between wt% $CaCO_3$ and $\delta^{13}C$ also has important implications for tuning of records. It is not uncommon to tie physical property records (including wt% $CaCO_3$) to isotope records; for instance, tying minima in wt% $CaCO_3$ at ODP Sites 1210 and 1267 to CIEs at ODP Site 1258 is the method used by Sexton et al., 2011, to develop inter-site correlations. Using age models developed from these correlations to plot isotope data reveals offsets in the timing of the CIE at each site. These results suggest that both sedimentation rate differences between sites, and lags between features in wt% $CaCO_3$ and isotope records from a single site have strong impacts on inter-site correlation.

5.5 Conclusions

Records of past carbon cycle events recorded at individual sites are heavily biased by site-specific preservational effects, but this does not mean that they are useless for providing information about the global events they partially record. Earth system models, with representations of climate, biogeochemistry, and the formation of deep-sea sediment records are important tools for extracting useful information from these datasets. The cGENIE model allows us to generate a quantitative estimate for the true magnitude of the carbon isotope excursion that characterizes C22nH3 by removing the influence of sediment mixing in smearing the excursion in the sediments—reducing its magnitude and increasing its apparent duration. The factors influencing the preservation of smaller CIEs, like C22nH3, may be less complicated than for the PETM, since dissolution was not nearly as extensive during these events. As a result, it appears that sedimentation rate most strongly influences the details of the excursion recorded at a single site, after accounting for spatial differences in DIC $\delta^{13}C$ as a result of productivity and circulation.

An improved assessment of the true magnitude of the isotopic excursion in the atmosphere allows us to predict the likeliest rate and shape of both carbon release and sequestration. Carbon input required to generate these events is much slower than the rate of fossil fuel release due to anthropogenic emissions today, and slower than the rate predicted for the PETM as well. As a result, it does not appear that these events are particularly good analogs for the modern

in terms of their rate of onset—though their total size would be roughly equivalent to a relatively optimistic scenario of future fossil fuel release, where carbon emissions are kept below 2000 Gt C.

However, the rapidity of recovery from these events is more rapid that can be explained by enhanced ocean sequestration and carbonate compensation alone. In particular, our results support the hypothesis proposed for the PETM that these events caused some change in productivity and/or ocean redox conditions which favored the preferential removal of organic carbon. The rate of carbon removal predicted from this experiment is roughly equivalent to that predicted for the PETM—information that may be used to test ongoing improvements to models of organic carbon preservation and burial, and ultimately help improve understanding of negative feedbacks that may speed-up recovery from carbon cycle perturbations.

Chapter 5, in part, is currently being prepared for submission for publication. I am the primary investigator and author of this paper in collaboration with Andy Ridgwell.

5.6 References

Archer, D., (1991), Modeling the calcite lysocline, *Journal of Geophysical Research*, Vol. 96, No. C9, pp.17,037-17,050, doi:10.1029/91JC01812.

Archer, D., (1996), A data-driven model of the global calcite lysocline, *Global Biogeochemical Cycles*, Vol. 10, No. 3, pp. 511-526, doi:10.1029/96GB01521.

Archer, D., Eby, M., Brovkin, V., Ridgwell, A., Cao, L., Mikolajewicz, U., Caldeira, K., Matsumoto, K., Munhoven, G., Montenegro, A., and K. Tokos, (2009), Atmospheric lifetime of fossil fuel carbon dioxide, *Annual Reviews of Earth and Planetary Sciences*, Vol. 37, pp. 114-134, doi:10.1146/annurev.earth.031208.100206.

Bowen, G.J., and J.C. Zachos, (2010), Rapid carbon sequestration at the termination of the Palaeocene-Eocene thermal maximum, *Nature Geoscience*, Vol. 3, pp. 866–869, doi:10.1038/ngeo1014.

Cramer, B.S., Wright, J.D., Kent, D.V., and M.P. Aubry, (2003), Orbital climate forcing of d13C excursions in the late Paleocene-early Eocene (chrons C24n-C25n), *Paleoceanography*, Vol. 18, No. 1097, 25 pp., doi:10.1029/2003PA000909.

Cui, Y., Kump, L.R., Ridgwell, A.J., Charles, A.J., Jinium, C.K, Diefendorf, A.F., Freeman, K.H., Urban, N.M., and J.C. Harding, (2011), Slow release of fossil fuel carbon during the Paleocene-Eocene Thermal Maximum, *Nature Geoscience*, Vol. 4, pp. 481-485, doi:10.1038/ngeo1179.

Edwards, N.R., and R. Marsh, (2005), Uncertainties due to transport-parameter sensitivity in an efficient 3-D climate model, *Climate Dynamics*, Vol. 24, No., 4, pp. 415-433, doi:10.1007/s00382-004-0508-8.

Goodwin, P., and A. Ridgwell, (2010), Ocean-atmosphere partitioning of anthropogenic carbon dioxide on multimillenial timescales, *Global Biogeochemical Cycles*, Vol. 24, GB2014, 13 pp., doi:10.1029/2008GB003449.

Gruber, N., Keeling, C.D., Bacastow, R.B., Guenther, P.R., Lueker, T.J., Wahlen, M.,Meijer, H.A.J., Mook, W.G. and T. F. Stocker, (1999), Spatiotemporal patterns of carbon-13 in the global surface oceans and the oceanic Suess effect, *Global Biogeochemical Cycles*, Vol.13, pp. 307–335, doi:10.1029/1999GB900019.

Hargreaves, J.C., Annan, J.D., Edwards, N.R., and R. Marsh, (2004), An efficient climate forecasting method using an intermediate complexity Earth System Model and the ensemble Kalman filter, *Climate Dynamics*, Vol. 23, No. 7-8, pp. 745-760, doi:10.1007/s00382-004-0471-4.

Lynch-Stieglitz, J., Stocker, T.F., Broecker, W.S., and R. G. Fairbanks, (1995), The influence of air-sea exchange on the isotopic composition of oceanic carbon: Observations and modeling, *Global Biogeochemical Cycles*, Vol. 9, pp. 653–665, doi:10.1029/95GB02574.

Marchal, O., Stocker, T.F., and F. Joos, (1998), A latitude-depth, circulation biogeochemical ocean model for paleocliamte studies: Development and sensitivities,*Tellus B:Chemical and Physical Meteorology*, Vol. 50, No. 3, pp. 290-316, doi:10.1034/j.1600-0889.1998.t01-2-006.x.

Panchuk, K., (2007), Investigating the Paleocene/Eocene Carbon Cycle Perturbation: An Earth System Model Approach, Ph.D. Dissertation, The Pennsylvania State University.

Panchuk, K., Ridgwell, A. and L.R. Kump, (2008), Sedimentary response to Paleocene-Eocene Thermal Maximum carbon release: A model-data comparison, *Geology,* Vol. 36, No. 4, pp. 315-318, doi:10.1130/G24474A.1.

Ridgwell., A., (2001), Glacial-interglacial perturbations in the global carbon cycle, Ph.D. thesis, University of East Anglia at Norwich, Norwich, U.K.

Ridgwell, A., and R.E. Zeebe, (2005),The role of the global carbonate cycle in the regulation and evolution of the Earth system, *Earth and Planetary Science Letters*, Vol. 234, No. 3–4, pp. 299-315, doi:10.1016/j.epsl.2005.03.006.

Ridgwell, A., (2007), Interpreting transient carbonate compensation depth changes by marine sediment core modeling, *Paleoceanography*, Vol. 22, PA4102, doi:10.1029/2006PA001372.

Ridgwell, A., and J.C. Hargreaves, (2007), Regulation of atmospheric CO_2 by deep-sea sediments in an Earth system model, *Global Biogeochemical Cycles*, Vol. 21, GB2008, 14 pp., doi:10.1029/2006GB002764.

Ridgwell, A., Zondervan, I., Hargreaves, J.C., Bijma, J., and T.M. Lenton, (2007), Assessing the potential long-term increase of fossil fuel uptake due to CO_2-calcification feedback*, Biogeosciences*, Vol. 4, pp. 481-492, www.biogeosciences.net/4/481/2007.

Ridgwell, A., and D.N. Schmidt, (2010), Past constraints on the vulnerability of marine calcifiers to massive carbon dioxide release, *Nature Geoscience*, Vol. 3, pp. 196-200, doi:10.1038/ngeo755.

Sexton, P.F., Wilson, P.A., and R.D. Norris, (2006), Testing the Cenozoic multisite composite $\delta^{18}O$ and $\delta^{13}C$ curves: New monospecific Eocene records from a single locality, Demerara Rise (Ocean Drilling Program Leg 207), *Paleoceanography*, Vol. 21, PA2019, 17 pp., doi:10.1029/2005PA001253.

Sexton, P.N., Norris, R.D., Wilson, P.A., Palike, H., Westerhold, T., Rohl, U., Bolton, C.T., and S. Gibbs, (2011), Multiple Eocene 'hyperthermal' events driven by ocean ventilation, *Nature,* Vol. 471, pp. 349-353, doi:10.1038/nature09826.

Stap, L., L.J. Lourens, E. Thomas, A. Sluijs, S. Bohaty, and J.C. Zachos, (2010), High-resolution deep-sea carbon and oxygen isotope records of Eocene Thermal Maximum 2 and H2, *Geology,* Vol. 38, No. 7, pp. 607-610, doi:10.1130/G30777.1.

Tindall, J., Flecker, R., Valdes, P., Schmidt, D.N., Marwick, P., and J. Harris, (2010), Modelling the oxygen isotope distribution of ancient seawater using a coupled ocean-atmosphere GCM: Implications for reconstructing early Eocene climate, *Earth and Planetary Science Letters*, Vol. 292, Number 3-4, pp. 265-273, doi:10.1016/j.epsl.2009.12.049.

Tipple, B.J., Meyers, S.R., and M. Pagani, (2010), Carbon isotope ratio of Cenozoic CO_2: A comparative evaluation of available geochemical proxies, *Paleoceanography*, Vol. 25, No. 3, PA3202, doi:10.1029/2009PA001851.

Westerhold., T., and U. Rohl, (2009), High resolution cyclostratigraphy of the early Eocene - new insights into the origin of the Cenozoic cooling trend, *Climates of the Past,* Vol. 5, pp. 309-327, doi:10.5194/cp-5-309-2009.

Zachos, J.C., McCarren, H., Murphy, B., Röhl, U., and T. Westerhold, (2010), Tempo and scale of late Paleocene and early Eocene carbon isotope cycles: Implications for the origin of hyperthermals, *Earth and Planetary Science Letters*, Vol. 299, No. 1–2, pp. 242-249, doi:10.1016/j.epsl.2010.09.004.

CHAPTER 6

Conclusion to the Dissertation

The unifying goal of this dissertation has been to understand the Earth system during greenhouse climates—intervals when the Earth had no large, permanent ice sheets. The icehouse conditions that exist today characterized the past ~30 million years, but for hundreds of millions of years before that, the Earth was generally a much warmer place. In comparison, roughly the entire existence of humans has occurred in the past two to three million years while the Earth oscillated between glacial and interglacial periods marked by the waxing and waning of ice sheets' total extent in the Northern hemisphere.

Anthropogenic climate change not only threatens to disrupt modern societies—it may shift the Earth into a state similar to one last seen tens of millions of years ago. While the deep past is undoubtedly an imperfect analog for the future, fully comprehending the potential impacts of fossil fuel emissions requires an understanding of past greenhouse climates.

Despite the clear need to study warm intervals in Earth history, the majority of paleoclimate research has focused on the more recent past—particularly the Holocene and the glacial-interglacial transitions. In the most recent report from the Intergovernmental Panel on Climate Change, only a single column on a single page was devoted to climate prior to the Pliocene (around 3 Ma). The primary reason for this lack of attention is the quantity and quality of available data. Moving further back in time, records become scarce, resolution is generally worse, and proxies and time-scales become more uncertain. It is difficult to imagine achieving anything similar to the reconstructions of surface

temperature for the past two millennia from Mann et al., 2008, for intervals in the early Cenozoic.

I summarize major conclusions from this dissertation below. Overall there are two major themes throughout the previous chapters. First, I address 'big picture' questions about characteristics of a warm world. Chapter 2 provides information helpful in reconstructing deep-ocean circulation from the Paleocene greenhouse, while Chapters 3 and 4 address the ubiquity of abrupt warming events from the Jurassic through the Eocene. Second, I critically assess how well individual records record abrupt climatic variability through the use of data and modeling. This question is particularly pertinent for deep-time paleoclimatology, where descriptions of an event often hinge on very few datasets. A major goal in Chapters 3 and 5 is to move beyond the traditional, qualitative description of records of abrupt climatic transitions called hyperthermals to a more quantitative approach. While spatial and temporal coverage of these events must improve to allow the development of more useful model simulations, an interdisciplinary model-data approach at the early stages of study (as exemplified in this dissertation) can help suggest which types of datasets to target.

6.1 Major conclusions

1. An updated global composite of benthic foraminiferal carbon isotopes, with new data from a high latitude Southern Pacific site, suggests that deep waters formed in the Pacific sector of the Southern Ocean around

Antarctica at least intermittently during the Paleocene epoch. The most likely site of deep-water formation in this area is the Ross Sea.

2. Very high-resolution stable isotope records from multiple sites demonstrate that at least 5 of the hyperthermals identified from Sexton et al., 2011, were global events.
3. Comparative analysis of multi-site records of multiple hyperthermals from the late Paleocene through early-middle Eocene suggests similarity between most of these events, with the PETM and Elmo events appearing as clear outliers in terms of magnitude and duration.
4. A new method for determining the significance of an individual 'event' based on the amplitude of variability preserved at each site suggests that a number of previously identified hyperthermals are not obviously distinct from background variability.
5. Adaptation of a threshold model from Lunt et al., 2011, suggests a common mechanism could be responsible for the sequence of hyperthermals from the late Paleocene through the early-middle Eocene.
6. For small hyperthermals, there is a consistent offset in the timing of lowest carbonate content compared to the most negative isotopic values preserved. This is consistent with model results of the consequences of a pulse of carbon released to the atmosphere and oceans, suggesting that the lead in wt% $CaCO_3$ minima is likely a result of decreased carbonate

production and export, rather than an indication of separate episodes of carbon release.

7. Synthesis of carbon isotope excursions from ~250-44 Ma reveals 28 events that show clear bulk carbonate excursions at multiple sites coincident with evidence for warming. These events exhibit additional commonalities, with events generally corresponding to evidence for dissolution of carbonates, increases in weathering, and biotic change.
8. A newly developed iterative inversion method suggests an estimate for the true size of the carbon isotope excursion associated with a modestly sized early-middle Eocene hyperthermal. We demonstrate that a sedimentary record of a carbon isotope excursion of 0.95‰ from a single site is most consistent with an excursion of 1.6‰ in atmospheric pCO_2.
9. We show that a primary control on the recorded magnitude of small hyperthermals is the sedimentation rate, which controls the extent to which a record is mixed. For these smaller events, dissolution is not a major factor in altering the preserved sedimentary record.
10. Differences in sedimentation rate between sites can alter the apparent relative timing of a globally synchronous event at each site, suggesting that tuning records based on the assumption that events should appear synchronous can add bias to age models.
11. We demonstrate that climate feedbacks, ocean invasion, and carbonate compensation alone are insufficient to account for the rapid recovery from

small hyperthermal events, similar to suggestions that additional mechanisms of carbon drawdown are necessary to explain the PETM recovery.

6.2 References

Mann, M.E., Zhang, Z., Hughes, M.K., Bradley, R.S., Miller, S.K., Rutherford, S., and F. Ni, (2008), Proxy-based reconstructions of hemispheric and global surface temperature variations over the past two millennia, *Proceedings of the National Academy of Sciences*, Vol. 105, No. 36, pp. 13252-13257, doi:10.1073/pnas.0805721105.

Sexton, P.N., Norris, R.D., Wilson, P.A., Palike, H., Westerhold, T., Rohl, U., Bolton, C.T., and S. Gibbs, (2011), Multiple Eocene 'hyperthermal' events driven by ocean ventilation, *Nature,* Vol. 471, pp. 349-353, doi:10.1038/nature09826.

Solomon, S., Qin, D., Manning, M., Chen, Z., Marquis, M., Aeryt, K.B., Tignor, M., and H.L. Miller (eds.), 2007, Contribution of Working Group I to the Fourth Assessment Report of the Intergovernmental Panel on Climate Change, 2007, Cambridge University Press, Cambridge, United Kingdom and New York, NY, USA.